THE REPUBLIC OF TURKEY
ERCİYES UNIVERSITY
GRADUATE SCHOOL OF NATURAL AND APPLIED SCIENCES
DEPARTMENT OF TEXTILE ENGINEERING

DEVELOPMENT AND CHARACTERIZATION OF THERMAL AND STRUCTURAL PROPERTIES OF TEXTILE FIBERS

Prepared by
Md. Mahbubor Rahman

Supervised by
Prof. Dr. İsmail KARACAN

PhD Thesis

December 2021
KAYSERİ

THE REPUBLIC OF TURKEY
ERCİYES UNIVERSITY
GRADUATE SCHOOL OF NATURAL AND APPLIED SCIENCES
DEPARTMENT OF TEXTILE ENGINEERING

DEVELOPMENT AND CHARACTERIZATION OF THERMAL AND STRUCTURAL PROPERTIES OF TEXTILE FIBERS

(PhD Thesis)

Prepared by
Md. Mahbubor Rahman

Supervised by
Prof. Dr. İsmail KARACAN

December 2021
KAYSERİ

COMPLIANCE WITH SCIENTIFIC ETHICS

I declare that all information in this study has been obtained in accordance with academic and ethical rules. At the same time, as required by these rules and conduct, I declare that I have fully cited and referenced all materials and results that are not at the core of this work.

Md. Mahbubor Rahman
Signature

APPROVAL OF COMPLIANCE WITH THE DIRECTIVES

The PhD thesis entitled **"Development and Characterization of Thermal and Structural Properties of Textile Fibers"** has been prepared in accordance with the Erciyes University Graduate Thesis Proposal and Thesis Writing Directive.

Prepared by
Md. Mahbubor Rahman
Signature

Supervised by
Prof. Dr. İsmail KARACAN
Signature

Head
Department of Textile Engineering, Erciyes University
Prof. Dr. Abdulkadir BİLİŞİK
Signature

ACKNOWLEDGMENTS

First and foremost, I would like to express my sincere gratitude to my supervisor Professor Dr. İsmail KARACAN, for his relentless encouragement, constructive guidance, and words of motivation throughout this research period and moreover for the inspiration he provided to ensure the completion of this work. His expertise, availability to discuss ideas, and willingness to give of his knowledge were instrumental. I appreciate all his contributions of time, ideas, and thinking to make my PhD experience productive and stimulating. The joy and enthusiasm he has for the research were contagious and motivational for me, even during tough times in the PhD pursuit.

I would like to express my heartfelt gratitude to the authority of the Higher Education Council of Turkey (YÖK) for offering me the YÖK scholarship that made my PhD research work convenient here. I would also like to thank the authority of Erciyes University, Turkey, for giving me the opportunity to participate in the PhD program.

I gratefully acknowledge the members of my PhD thesis monitoring committee Professor Dr. İlhan ÖZEN and Professor Dr. Mustafa Serdar ÖNSES, for their insightful comments and encouragement throughout my PhD work. My sincere thanks also go to the other members of the jury Professor Dr. Ertuğrul ŞAHMETLİOĞLU, and Associate Professor Dr. Hüseyin BENLİ, who have agreed to evaluate this work in their busy schedule and gave me valuable feedback on the preliminary version of this thesis.

My sincere thanks to Kemal Şahin Tunçel for his endless support from the very beginning of my PhD research work, and also for the scientific and non-scientific discussions we have made. I would also like to thank Tuba Demirel for her friendly and cooperative approach to different issues throughout this period.

Last but not least, I would like to express my thanks to my loving family members for all their heartfelt prayers, love, and encouragement. Especially I am deeply thankful to my amazing wife Jannat, my five-year-old son Muntasir, and my parents for their all-time supportive, encouraging, and patient backing in a foreign country all over my PhD period.

Md. Mahbubor Rahman
December 2021, KAYSERİ

DEVELOPMENT AND CHARACTERIZATION OF THERMAL AND STRUCTURAL PROPERTIES OF TEXTILE FIBERS

Md. Mahbubor Rahman

Erciyes University, Graduate School of Natural and Applied Sciences
PhD Thesis, December 2021
Supervisor: Prof. Dr. İsmail KARACAN

ABSTRACT

The thermal oxidative stabilization of the precursor fiber is one of the most important steps to make it resistant to tolerate high temperatures in the subsequent stages like carbonization and activation phase of carbon fiber and activated carbon fiber manufacturing. This research aims to accelerate the stabilization process by utilizing different chemical pretreatments and different stabilization techniques, which are expected to optimize costs by lowering carbon fiber manufacturing duration. The impregnation of 15% ammonium persulfate aqueous solution with PAN multifilaments was performed, followed by a multistep thermal oxidative stabilization (TOS) process. The influence of the impregnation of phosphoric acid, boric acid, and urea as eco-friendly chemicals and the TOS process on the properties of polyamide 66 multifilament were analyzed at temperatures up to 245 °C for different stabilization periods. An investigation on the effect of sodium metasilicate pentahydrate and urea impregnation on the thermal-oxidative stabilization of eco-friendly jute fibers was undertaken. The transformations of structural and thermal properties of bamboo precursor fiber impregnated with DAP, sodium metasilicate, and urea throughout the oxidative thermal stabilization process were studied. The oxidative thermal stability of plant-based microcrystalline flax fiber was developed by incorporating DAP, boric acid, and urea followed by a multistep thermal oxidation process. The physical, mechanical, structural, and thermal characterization of the original and thermally stabilized samples were performed utilizing a set of measurements, including volume density, linear density, fiber thickness, flame test, tensile strength, tensile modulus, extension at break, DSC, TGA, XRD, FT-IR, SEM, and elemental analysis.

Keywords: Polyacrylonitrile, Polyamide 66, Jute, Bamboo, Flax, Thermal oxidative stabilization, Structural and thermal characterization.

TEKSTIL ELYAFIN TERMAL VE YAPISAL ÖZELLIKLERININ GELIŞTIRILMESI VE KARAKTERIZE EDILMESI

Md. Mahbubor Rahman

Erciyes Üniversitesi, Fen Bilimleri Enstitüsü
Doktora Tezi, Aralik 2021
Danışman: Prof. Dr. İsmail KARACAN

ÖZET

Karbon lif ve aktif karbon lif üretiminin karbonizasyon ve aktivasyon işlemlerinde yüksek sıcaklıklar tolere edilerek öncül lifleri kararlı hale getiren en önemli adım termal oksidatif stabilizasyon işlemidir. Bu çalışmada, karbon lif üretim süresini ve maliyetleri azaltmak için farklı kimyasal ön işlemleri ve farklı stabilizasyon teknikleri kullanılarak stabilizasyon sürecini hızlandırmak amaçlanmıştır. PAN multifilamentleri %15'lik amonyum persülfat sulu çözeltisinde emdirilmesinden sonra çok aşamalı bir termal oksidatif stabilizasyon (TOS) işlemi uygulanmıştır. Poliamid 66 multifilamanın özelliklerine çevre dostu kimyasallar olan fosforik asit, borik asit ve ürenin emdirme etkisinin ve TOS işleminin farklı stabilizasyon sürelerinde 245 °C 'ye kadar sıcaklıklarda analiz edilmiştir. Jüt lifleri, çevre dostu Sodyum metasilikat pentahidrat ve üre kimyasalları ile emdirilesi ile termal-oksidatif stabilizasyon üzerindeki etkisinin araştırılması gerçekleştirilmiştir. Oksidatif termal stabilizasyon süreci boyunca DAP, sodyum metasilikat ve üre ile emdirilmiş bambu öncül elyafın yapısal ve termal özelliklerinin dönüşümleri incelenmiştir. DAP, borik asit ve üre kimyasalları ve çok aşamalı bir termal oksidasyon işlemi beraber kullanılarak bitki bazlı mikro kristal keten lifinin oksidatif termal stabilitesi geliştirilmiştir. Ham ve termal olarak stabilize edilmiş numunelerin fiziksel, mekanik, yapısal ve termal karakterizasyonu, hacim yoğunluğu, iplik numarası ölçümü, lif kalınlığı, alev testi, gerilme mukavemeti, gerilme modülü, kopma uzaması, DSC, TGA, XRD, FT-IR, SEM, ve element analizi analizleri dahil olmak üzere bir dizi ölçüm kullanılarak gerçekleştirilmiştir.

Anahtar Kelimeler: Poliakrilonitril, Poliamid 66, Jüt, Bambu, Keten, Termal oksidatif stabilizasyon, Yapısal ve termal karakterizasyon.

ABBREVIATIONS

CF	Carbon Fiber
ACF	Activated Carbon Fiber
PAN	Polyacrylonitrile
PA66	Polyamide 66
TOS	Thermal Oxidative Stabilization
DSC	Differential Scanning Calorimetry
TGA	Thermogravimetric Analysis
XRD	X-ray Diffraction
FT-IR	Fourier Transform Infrared
SEM	Scanning Electron Microscopy
APS	Ammonium Persulfate
DAP	Di-Ammonium Phosphate
PBU	Phosphoric Acid – Boric acid – Urea
SMSPH-U	Sodium Metasilicate Pentahydrate – Urea
DAP-SMSU	Di-Ammonium Phosphate –Sodium Metasilicate – Urea
DAP-BAU	Di-Ammonium Phosphate –Boric Acid – Urea
CAGR	Compound Annual Growth Rate
CFRP	Carbon Fiber Reinforced Plastic
CPS	Counts Per Second

CONTENTS

DEVELOPMENT AND CHARACTERIZATION OF THERMAL AND STRUCTURAL PROPERTIES OF TEXTILE FIBERS

CHAPTER 3
MATERIALS AND METHODS

CHAPTER 4
RESULTS AND DISCUSSION

CHAPTER 5
CONCLUSION AND SUGGESTIONS

LIST OF TABLES

LIST OF FIGURES

CHAPTER 1
INTRODUCTION

1.1 Background

Together with the numerous benefits that synthetic polymeric materials provide to society in daily living, there is one apparent drawback associated with the higher flammability of many of them. Practical necessities and basic science both explain the recent growth in the significance of the thermal properties of materials. The research for heat-conducting and flame-retardant materials has become essential in the development of next-generation facilities [1]. The ability of a material to conduct heat is influenced by its atomic structure, and understanding of thermal properties can reflect back on the features of other materials. When materials are organized on a nanometer scale, their thermal properties change [2].

Carbon fibers are ultra-lightweight materials containing at least 90% carbon content with having high conductivity and thermal resistance derived from the controlled pyrolysis of specific textile fibers [3]. Carbon fibers are microscopic fibers with a diameter of 5–10 micrometers mainly composed of carbon atoms linked together to form a continuous chain. The carbon fibers are stiff, robust, and light, and are utilized in a variety of procedures to make high-quality building materials. The carbon fiber material is available in a number of "raw" building blocks, including yarns, unidirectional weaves, braids, and a variety of others, which are then utilized to make reinforced composites.

Carbon fiber has properties similar to steel and has a weight similar to that of plastic. Carbon fiber has a substantially greater strength-to-weight ratio than steel or plastic. In engineering, the utility of a material is typically measured in terms of strength-to-weight ratio and stiffness-to-weight ratio, especially in structural design, where added weight might result in higher lifespan costs or poor performance [4]. Carbon fiber production is likely to rise as a result of its extensive use in high-volume industrial applications; as a result, the procedures for synthesizing carbon fibers, as well as the precursors utilized in their manufacture, must be studied for their structures and other properties. Carbonization of organic fibers is the most practical approach in producing carbon fibers; however, because of the outstanding mechanical performance and high yield, the majority of carbon fibers are now derived from polyacrylonitrile (PAN) precursor [5].

Three major steps involved in transforming precursor fibers to carbon fibers are stabilization, carbonization, and graphitization, each of which comprises multiple chemical reactions. The stabilization process entails heating the precursor fibers in the air at 200-300 °C, in which a series of chemical processes convert them into structures that can resist the high temperatures necessary for carbonization, graphitization, and activation without decomposition. Even though it is thought that multiple reactions occur in the stabilization phase, the ultimate result is the conversion of polymer chains into ladder-like structures [6]. The stabilized ladder-like structured precursor fibers are heated to a temperature of 1000-1700 °C [7] during the carbonization stage, transforming ladder-like structures into the resultant carbon fiber microstructure, which is made up of graphitic sheets. Subsequently, the fibers are heated to 2500- 3000 °C during the graphitization phase to achieve high modulus fibers [8].

1.2 Scope of the Research

In the coming years, new emission regulations for the automobile and aerospace industries will provide particular challenges. To meet the stated environmental emission objectives, a considerable reduction in carbon dioxide emissions is required [9]. The instrumental weight will be one of the decisive elements in meeting the emission objectives. Unfortunately, during the last few decades, the weight of automobiles has

increased. Higher safety requirements, greater quality, and more interior and comfort have resulted in the higher weight of the vehicles and other utilities.

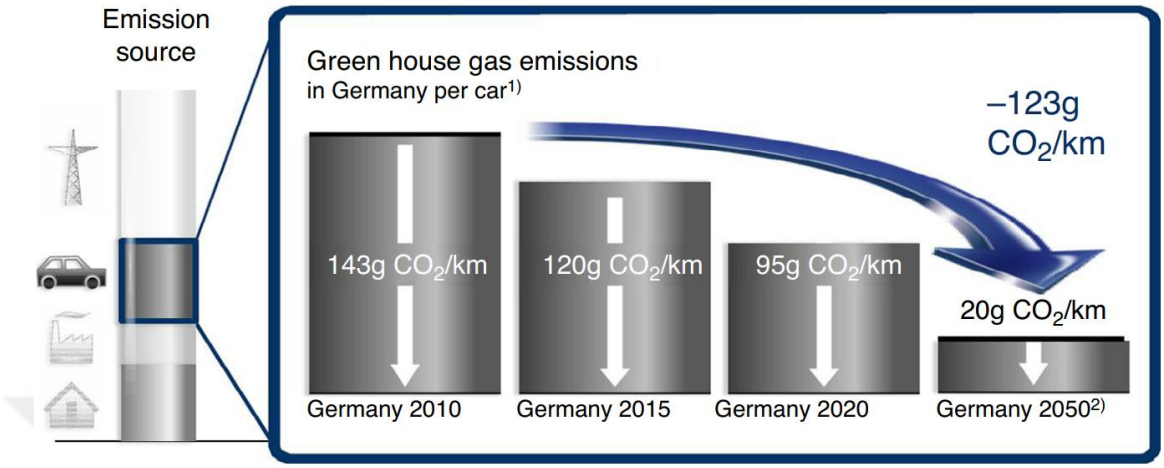

Figure 1.1 CO_2 emission standards in Germany.

Almost every automobile generation has seen an increase in weight. For instance, heavier high-performance chassis result from stronger body modifications for safety purposes. To maintain the car's dynamic performance, higher-performance engines with higher gas consumption are required, resulting in larger, heavier tanks. This cycle might be extended, leading to the basic principle of the "weight spiral," as shown in Figure 1.2 [10].

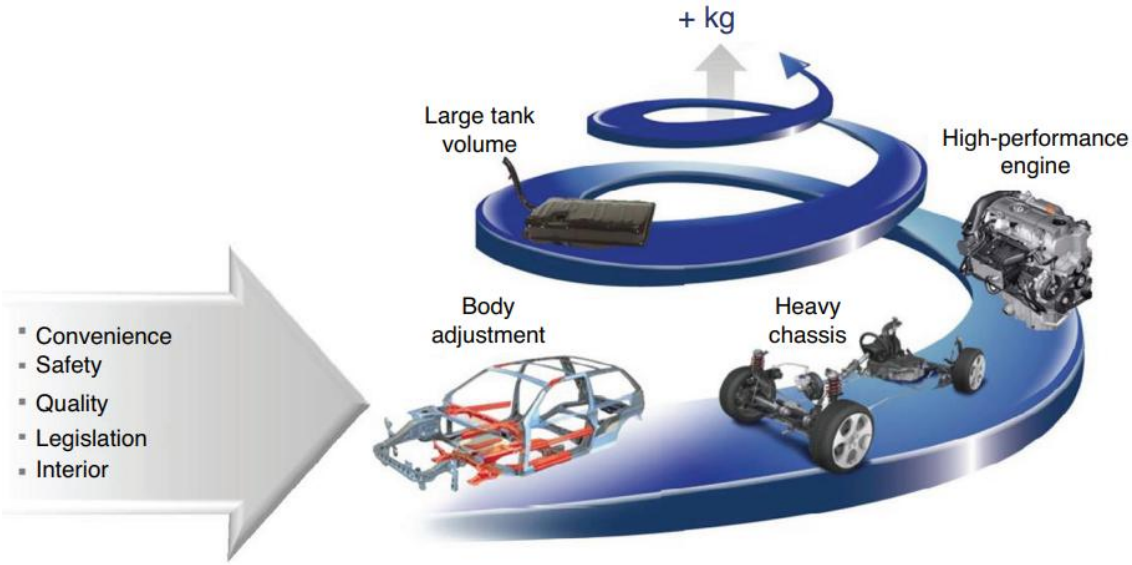

Figure 1.2 Principle of "weight spiral"[10].

One of the most important aspects of meeting emission regulations is lightweight design. To meet the new emission requirements, however, weight reductions of 50% or more in some components of the automobile would be required. Lightweight designs based on steel or aluminum structure would not attain such significant weight reduction. Figure 1.3 represents the structural potential of carbon fiber-reinforced composites in lightweight construction and the associated economic considerations that might be obtained by replacing a steel component with carbon fiber reinforced composites [10].

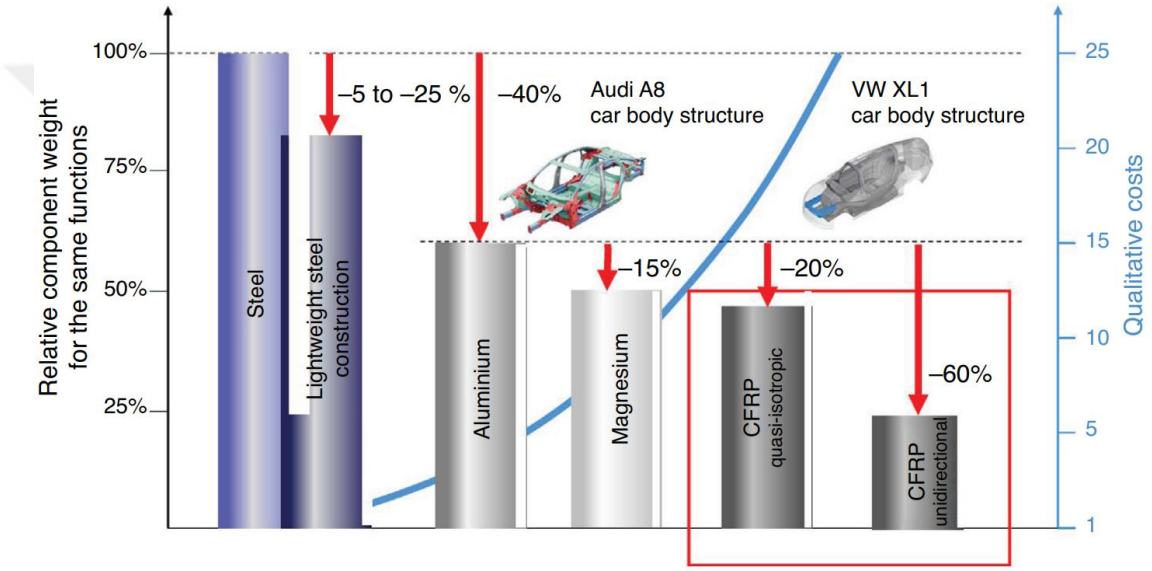

Figure 1.3 Potential of lightweight material substitution in structural applications.

Carbon fiber reinforced plastic (CFRP) is one viable means of reducing the challenge of weight reduction. With carbon fiber reinforced composites, component weight might be reduced by up to 60% with maintaining the same functionality [11]. To meet future emission requirements, it is inevitably essential to reverse the "weight spiral." Figure 1.4 depicts how the "weight spiral" might well be reversed. Lighter chassis are the result of lighter body adjustments, while lighter vehicles are the result of a combination of engine downsizing and tank volume reduction.

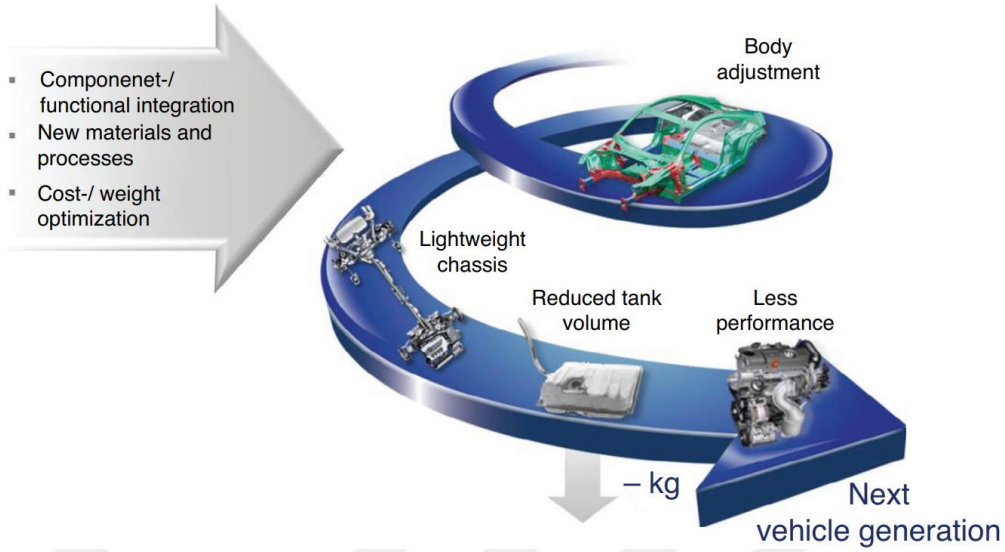

Figure 1.4 Reversing of "weight spiral" [10].

Customers in the aerospace and automobile industries benefit greatly from lightweight construction. In this context, the potential advantages of lightweight construction utilizing carbon fiber reinforced polymers are reduced fuel consumption, increased range, and improved vehicle driving dynamics. The lightweight construction impacts by lowering the weight of a car by 100 kg imply a decrease in fuel consumption of 0.3 liters per 100 km for a conventional engine or a range extension of 100 km for an electric engine drive [12, 13]. Carbon-based materials have now attracted great attention due to their numerous potential applications. Carbon fibers are extremely strong, stiff, and light, allowing them to improve performance in a variety of applications, including aircraft, sports, automotive, wind energy, oil and gas, infrastructure, military, and semiconductors. Carbon fibers, on the other hand, are limited in their usage in cost-sensitive, large-volume industrial applications due to their comparatively high cost [14].

Understanding the relationship between processing parameters, microstructure, and resultant characteristics is necessary for the development of high-strength carbon fibers. Intensive research of the microstructure of precursor fibers have all suggested that the fibers are comprised up of long and oriented graphitic 'turbostratic' layers, with voids interrupting the consistency along the fiber axis. The carbon fibers were reported to contain folded layers in the transverse cross-section, features specified by the processing parameters, and a variety of original precursors. As a result, different proposed patterns of the inner structure of these fibers have been observed [15–17].

Despite all this advancement, whilst commercial carbon fibers may attain a modulus comparable to that of ideal graphite, even the most advanced high-strength fibers have values that are less than 10% of that of ideal graphite strength [18]. The microstructure imperfections restrict the fiber strength, and the impact of process parameters on the resultant microstructure and features can be used to estimate the magnitude of these defects.

Carbon fiber reinforced composites are a promising component of the twenty-first century because they are lightweight, high-performance materials with excellent mechanical characteristics. Despite continued industry expansion, though, the usage of carbon fiber composites has mostly been restricted to low volume, high-cost applications, such as aircraft, high-performance luxury cars, and so on [19][20]. This is largely owing to the high manufacturing costs of carbon fiber, which are derived from expensive raw materials [21].

Completely new applications, as well as considerable improvements in current composite materials for lightweight usage, are accessible with specific control of attributes from the molecular structure to the composite. These comprise next-generation energy storage devices, adsorptive fibers for high-pressure hydrogen tanks, improved gas diffusion structures for fuel cells [22], new crash-absorbing systems in automobiles [23], cell-compatible fibers, and so on. Low-cost carbon fibers are especially attractive as reinforcing structures for wind turbine rotor blades [27] or carbon composites, where environmental and economic considerations play a significant role in the carbon fiber quantities required. Nevertheless, fundamental research is required before multifunctional carbon fiber can be used in resource-efficient intelligent building approaches on a wide scale. This is where novel techniques come into play, beginning with precursor material research and development and progressing through precursor fiber spinning stages, targeted stabilization, carbonization, graphitization, surface modification, and eventually developing ultimate composite materials [24]. This gives crucial insights throughout the whole production system, as well as the necessary requirements for multifunctional materials. Therefore, future versatile constructions with specified controllable features like strength, stiffness, ductility, energy storage, absorption capacity, and also electrical and thermal conductivities would have considerably enhanced resource efficiency.

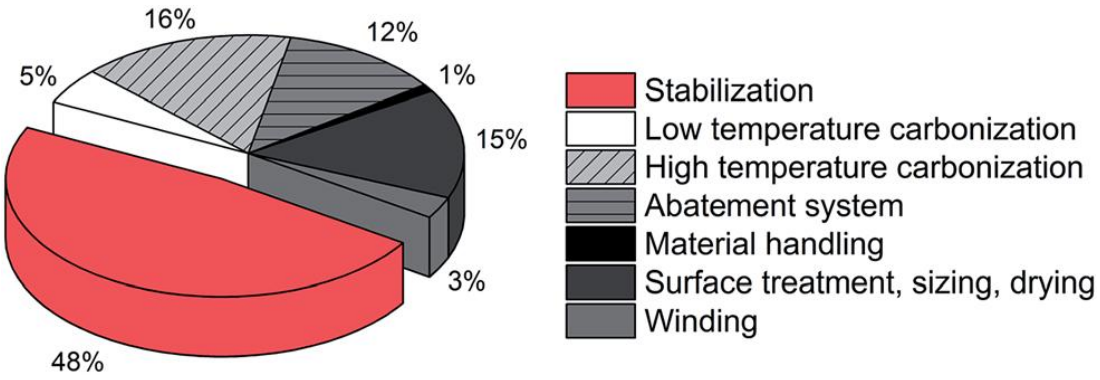

Figure 1.5 Energy consumption in different stages of carbon fiber manufacture [25].

Fiber heat treatment (stabilization and carbonization) accounts for 69% of energy cost, with stabilization accounting for 48% (Figure 1.5). As a result, stabilization is the most time and energy-intensive stage in the carbon fiber production process. As a result, this stage offers the greatest potency for optimization, resulting in lower costs and lesser environmental impacts [26–28]. Despite of having a number of variables in carbon fiber manufacturing, even a small change in processing temperatures might have a significant worldwide impact. The overall environmental impact of lowering energy consumption in carbon fiber manufacturing is two-fold. There is an immediate direct benefit from being used less energy in the manufacturing process. Second, the lower cost of these materials will allow them to be used in high-volume automotive light-weighting purposes, lowering CO_2 emissions from mass transportation [20, 21].

1.3 Research Objectives

The most natural and synthetic-based textile materials that we use on a daily basis have a critical combustion property that poses a significant risk of catching fire. Amount of heat generated on combustion, flame spread, rate of heat emission, ease of extinction, ignitability, flammability of the volatile stuff produced, smoke toxicity, smoke obscuration all contribute to the fire danger [29]. With the rise of industrialization, the expansion of mass communities, and technological advancement, fire danger has become a critical issue to address. One of the most important issues influencing the increased usage of composites in engineering constructions is ensuring flame retardancy.

Carbon fiber is a high-performance material with outstanding tensile characteristics, low densities, high thermal and chemical stability, excellent thermal and electrical conductivities, and, most importantly, flame retardancy. Before the carbonization stage in carbon fiber manufacturing, the precursor fibers undergo oxidative stabilization, which turns them into an infusible and non-flammable condition. This is one of the most crucial steps in defining the mechanical characteristics of final carbon fibers, yet the most frequent thermal treatment (200 to 300 °C) of precursor fibers without any chemical integration wastes a lot of processing time, money, and energy. As a result, more appropriate stabilization methods for precursor fibers with decreased processing time and energy cost are expected to find out.

The main focus of this study was to establish optimum approaches for the thermal stabilization of the precursor fibers. Within the scope of this thesis, it is aimed to obtain complete thermal stability on different textile fibers (both natural and synthetic) without losing too much tensile strength within the quickest possible time by modifying them with various chemicals or chemical compositions prior to the thermal stabilization. Physical, mechanical, thermal, and structural properties would be characterized by means of different characterization tools, including fiber thickness, linear density, volume density, flame test, tensile testing, X-ray diffraction (XRD), differential scanning calorimetry (DSC), thermogravimetric analysis (TGA), Fourier transform infrared (FT-IR) spectroscopy, elemental analysis, and scanning electron microscopy (SEM).

1.4 Research Methodology

Different thermoplastic and thermosetting polymeric textile fibers including, polyacrylonitrile multifilament, polyamide 66 multifilament, jute fiber, bamboo fiber, and flax fiber were utilized in this study as precursor fibers to obtain thermal stability in the queue of carbon fiber and activated carbon fiber manufacturing. For synthetic polymeric fibers, a suitable spinning method (from melt, dry or wet spinning) is followed to obtain in filament or fiber form. The melt spinning process is applied for thermoplastic polymers, and for thermosetting polymers, the dry and wet spinning process is utilized.

Figure 1.6 Working flowchart for synthetic fibers (in this study, PAN and PA66 multifilaments).

Pretreatment with different chemicals or chemical compositions was trialed in order to achieve thermal stability in the fibers, and the best options were chosen among them for further stages. For chemical pretreatment, the chemical compositions were finalized on the basis of flame retardancy, TOS accelerating property, tensile properties retaining property, etc. Chemical integrated fiber samples were undergone an oxidative thermal stabilization process in the air atmosphere following different stabilization techniques (Figure 1.6). Different stabilization approaches were also materialized by altering the stabilization variables like treatment time, temperature, heating rate, etc. Multistep stabilization strategies were preferred in maximum cases as it retains higher tensile properties in the precursor samples after achieving complete thermal stability.

In this work, differential scanning calorimetry (DSC), thermogravimetric analysis (TGA), X-ray diffraction (XRD), infrared (IR) spectroscopy techniques, elemental analysis, and scanning electron microscopy (SEM) were utilized to accomplish structural characterization of the raw, and chemical treated and thermally stabilized samples. Characterization of physical changes was accomplished by observing fiber burning behavior, change of color, linear density, fiber density, fiber thickness, and mechanical properties for the different stabilization periods.

CHAPTER 2
GENERAL INFORMATION AND LITERATURE STUDY

2.1 Carbon Fiber and Activated Carbon Fiber

2.1.1 Carbon Fiber

Carbon fiber is defined as a fiber that has at least 90% carbon content by weight, whereas graphite fiber contains at least 99% carbon [30]. In the absence of oxidizing agents, carbon fibers exhibit great tensile properties, outstanding electrical and thermal conductivities, low densities, high chemical and thermal stabilities, and excellent creep resistance. Carbon fibers offer a high tensile strength of up to 7 GPa, excellent creep resistance, low density (ρ = 1.75–2.00 g.cm^{-3}), and high moduli of up to 900 GPa. Carbon fiber, in the form of woven textiles as well as continuous or chopped fibers, is ideal for use in composites due to its high mechanical properties [31]. Compression molding, pultrusion, vacuum bagging, tape winding, liquid molding, injection molding, and filament winding are all methods that may be used to manufacture composite materials.

The carbon fiber manufacturing industry has been growing progressively in recent years to meet the demand of different high-tech sectors including, aerospace (aircraft and space systems), turbine blades, military, construction, sporting goods, pressure vessels, lightweight cylinders, automobile, medical, off-shore tethers, drilling risers, among others [32, 33]. Carbon fiber reinforced polymeric composites enable considerable weight reduction in the automobile sector, which is essential for battery-powered vehicles [31]. Body components (front end, deck lids, doors, bumpers, hoods, etc.), suspension systems (e.g., leaf springs), chassis and drive shafts, and so on may all be of reduced weight by utilizing carbon fibers.

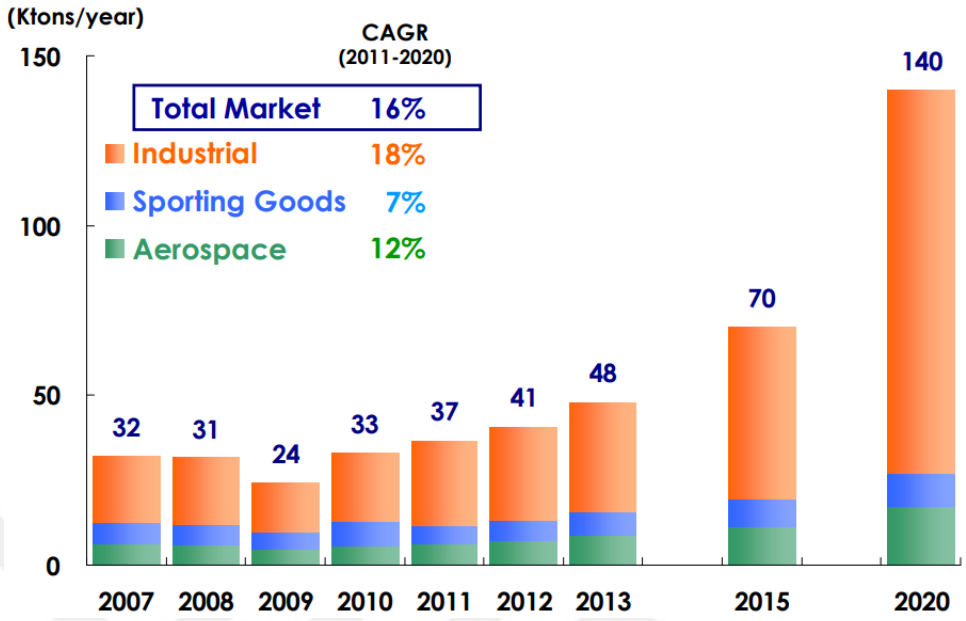

Figure 2.1 Carbon fibers market trends and compound annual growth rate (CAGR) of carbon fiber [34].

Carbon fiber utilization in both manufacturing and consumption is expected to rise steadily in the future. In reality, most carbon fiber producers are planning to expand in order to satisfy market demand. However, the expensive cost of carbon fiber and the absence of high-speed composite fabrication techniques have hampered its widespread use in the automobile sector [32].

2.1.2 Activated Carbon Fiber

Activated carbon fibers (ACFs) have greater surface reactivity, broad surface area, high porosity, and better distributions of pore size, making them particularly effective and adaptable adsorbents [35]. Due to the superior performance in terms of desorption properties and adsorption rate, as well as ease of operation, ACFs are the viable substitute for powder-based and granular activated carbons [36].

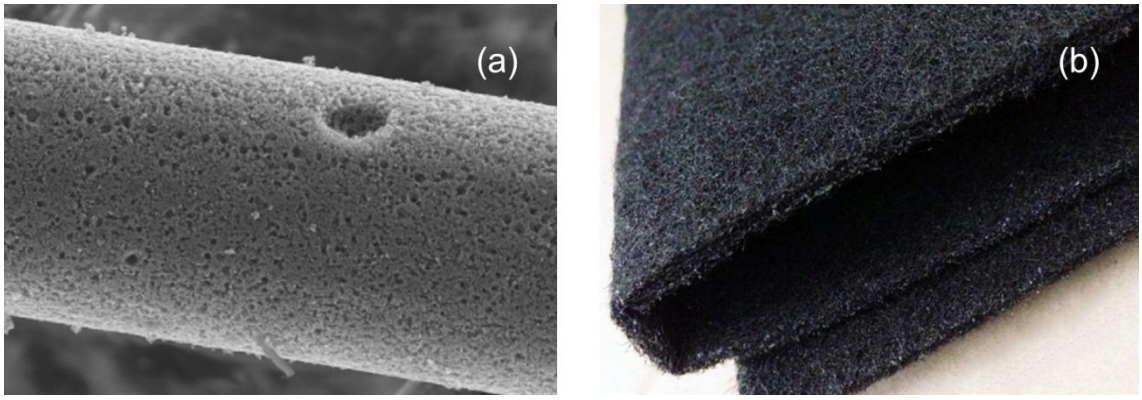

Figure 2.2 (a) SEM image of activated carbon fiber, and (b) Activated carbon cloth.

The physical or chemical activation process could be used to produce activated carbon fiber. This physical activation process consists of the precursor carbonization at 600-900 °C in an inert atmosphere to develop char that is then activated utilizing CO_2 and vapor as oxidizing gases at 600-1200 °C. The precursors are incorporated with the oxidizing chemicals like $ZnCl_2$, K_2CO_3, $AlC1_3$, Na_2HPO_4, and H_3PO_4, and afterward, heated in the inert environment like nitrogen or argon gases in the chemical activation method [37]. The chemical activation process was mentioned to offer greater surface area than the physical activation in many researches [38–42]. Chemically activated carbon has a greater adsorption propensity, and pores are mostly micropores, while physically activated carbon has predominant mesopores.

ACFs are available in different forms, including nonwoven, woven, and knitted structures to apply for different purposes [43, 44]. In medical and industrial applications, ACFs are favored in the construction of membranes for purification and separation purposes due to their ease of handling. At present, ACFs are widely used in producing high-quality drinking water, wastewater treatment plants, pharmaceutical and electronics industries, gas separation, controlled drug release, hemodialyzers, etc. [45]. Adsorption methods using activated carbon fiber are also used to remove contaminants like pesticides from wastewater [46, 47].

2.2 Structure and Properties of Carbon Fiber

Carbon fibers have an atomic structure identical to graphite, with carbon atom layers organized in a consistent hexagonal pattern, as illustrated in Figure 2.3. Layer patterns

in carbon fiber can be graphitic, turbostratic, or hybrid in structure, based on the precursor materials and production techniques. The layer patterns in graphitic crystalline areas are placed parallel to each other in a regular pattern. The atoms in a plane are covalently conjugated by sp^2 bonding, and the coupling between the layers is mediated by Van der Waals forces, which are relatively weak. The distance between two graphene sheets (d_{002}) in a single graphitic crystal is around 0.335 nm. These single crystals' elastic constants were determined [30]. C_{11} and C_{33} are 1,060 GPa and 36.5 GPa, respectively, but C_{44} for shearing is just 4.5 GPa. A stack of turbostratic layers, on the other hand, is the fundamental structural unit of different carbon fibers. The parallel graphene sheets are arranged unevenly or randomly tilted, folded, or split in a turbostratic structure. The presence of sp^3 bonding and uneven packing has been shown to raise *d*-spacing to 0.344 nm [33, 48, 49]. The turbostratic crystallites had L_c (crystallite height) of minimum 12 layer planes and L_a (crystallite width) of 6–12 nm, according to Johnson and Watt [50], who explored the crystallite structure of a PAN carbon fiber heated to 2500 °C.

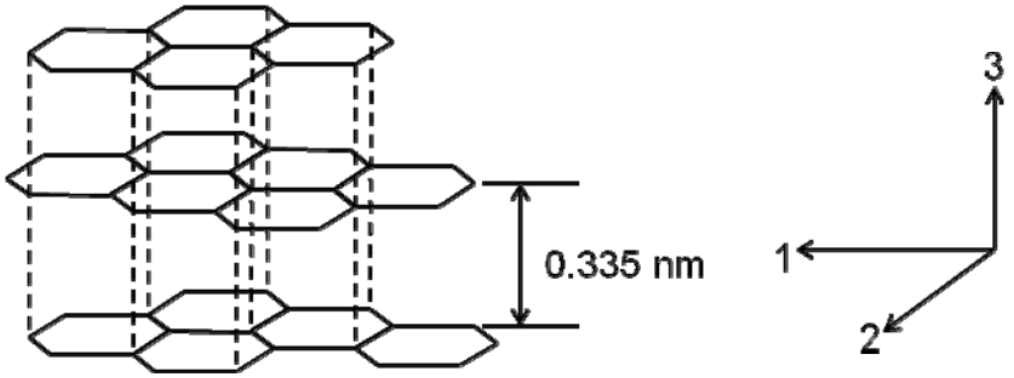

Figure 2.3 Structure of graphitic crystals and crystal directions.

X-ray diffraction was used to determine the optimum orientation of layers of hexagonal carbon rings along the fiber axis, having crystallite dimensions of a few nanometers. The size of the crystallites grows as the heat treatment temperature of the carbon fibers rises and also aligns better with the fiber axis. There seems to be no ABAB stacking continuum line, despite the layer planes being separated at 0.34 nm, which is identical to graphite. The structure is referred to as 'turbostratic,' and the fibers are carbon, not graphite. Transmission electron microscopy was used to analyze thin sections taken from carbon fibers utilizing a microtome, and the layer planes were defined. The layer

planes were aligned with the fiber direction in longitudinal sections, with marginally misoriented layer planes producing interconnecting fibrils that came together in the crystallites [51].

Although the layer planes in the crystallites are parallel to each other, cross-sections perpendicular to the fiber axis revealed that the crystallites are distributed at random throughout the section [52]. As a result, the fiber structure resembles that of multiple wrapped-up newspapers, as depicted in Figure 2.4. The crystallites expand in size as the heat treatment temperature rises, while greater disorganized areas of lower density appear amongst them. Therefore, carbon fibers resemble micro-composites.

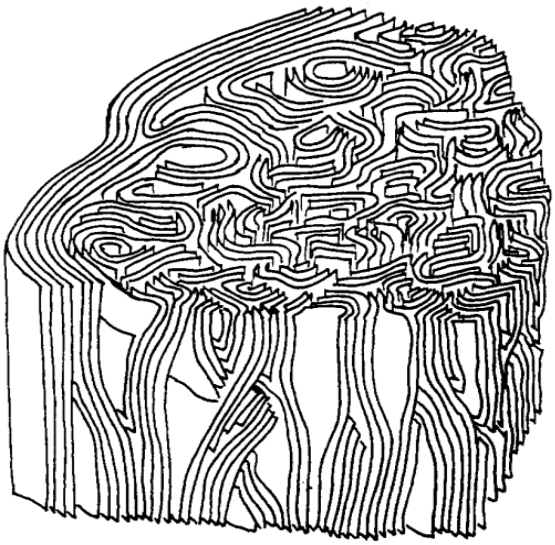

Figure 2.4 Schematic representation of carbon fiber structure [52].

2.3 Historical Development of Carbon Fiber

Carbon fibers were initially used on a large basis in electric light bulbs. The discovery of the dynamo-electrical concept by Werner von Siemens in 1866 was a prerequisite for this use. Electricity became available to everyone after the establishment of electrical networks. Thomas Alva Edison experimented with a variety of fibrous organic precursors obtained from across the world until he found a bamboo that provided adequate stability to the carbonized fiber. Edison utilized carbon fiber (testing materials) for the first time in his initial incandescent light bulb tests in 1879 [53]. When compared

to what humans had previously used, this carbon fiber, contained in an evacuated bulb and heated by an electric current, offered a steady, brilliant, and pleasant illumination.

Figure 2.5 Carbon fiber filament model of Edison's first electric lamp [53].

As a result, this light bulb became a commercial breakthrough. After the discovery of carbon fibers in 1880, he patented the use of carbon fibers as filament material in his electric light [53]. Emil Rathenau, a German entrepreneur, licensed Edison's patent in 1882 and began working with Werner von Siemens on the electrical illumination of Berlin [53]. The Allgemeine Elektrizitäts Gesellschaft (AEG) was formed by Rathenau in 1886 and operated until 1996.

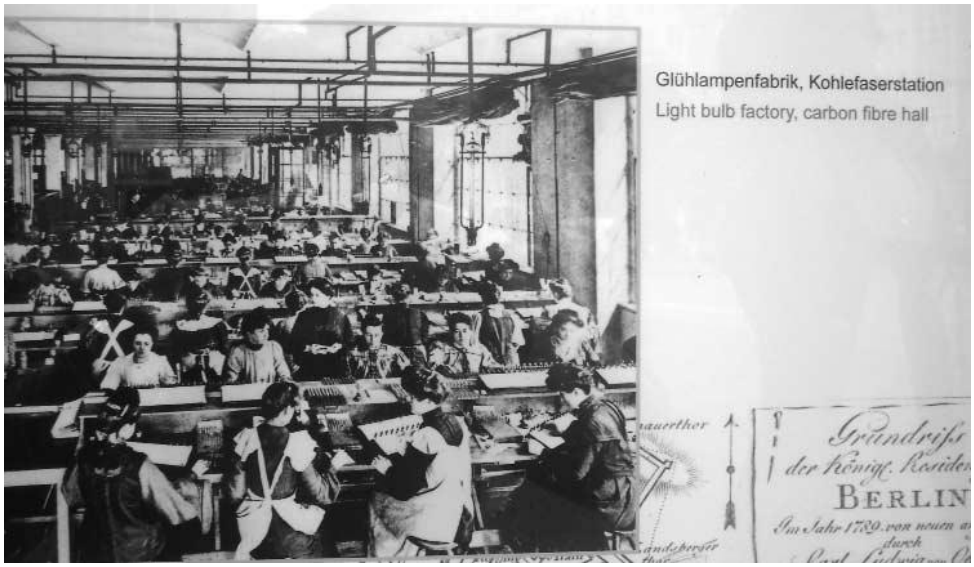

Figure 2.6 Light bulb factory, assembling station for the carbon fiber, Berlin around 1885 [54].

Edison might also be credited with developing the first commercial carbon fibers. Edison created fire-resistant carbon fibers from natural bamboo fibers or cotton fibers, which were perfect for his early illuminating filaments. Cotton and bamboo are mainly made up of cellulose, a natural linear polymer made up of glucose repeating units. Once heated in the absence of air in a hot gas burner, the filament carbonized and created a true carbon replica of the initial components with accurate sizes and forms [55].

Figure 2.7 Different forms of carbon [55].

Meanwhile, carbon filaments for electric lamps were only used for a short period before being replaced with tungsten wire. Carbon filaments, on the other hand, were used on US Navy ships as late as 1960 because they were more resistant to ship vibrations than tungsten. In the early development of the electric bulb, Edison used carbon fibers as a filament material, which set the path for the adoption of more efficient and enduring materials in the next few years. The fibrous feature, in particular, has been shown to be critical for structural improvements in the automobile and aerospace industries.

Carbon fibers were intended to replace glass fibers in a variety of applications, including transport, construction of buildings, maritime, thermal and electrical insulation, and industrial items. Since the 1960s, when it became obvious that carbon fibers, which served considerably to the strength and stiffness of structural goods, could

be produced for commercial purposes, such as reinforcements, viable commercial uses of carbon fibers have emerged [55].

During World War II, the Union Carbide Corporation (UCC) researched the fabrication of carbon fibers in the same way as rayon and polyacrylonitrile were investigated (PAN). Rayon, a semi-natural cellulose fiber, was the first precursor utilized in the manufacture of carbon fibers [56]. Rayon was replaced by polyacrylonitrile fiber a few years later, and PAN became the leading precursor fiber for the manufacture of carbon fibers [57].

In 1959 and 1962, two manufacturing techniques for carbon fibers comprising high-strength and high-modulus from rayon and PAN precursor fibers were invented concurrently. Pitch-based carbon fibers having high modulus features were first developed in 1963. Different precursor materials have been studied for producing carbon fibers, including polyesters, polyvinylidene, poly-p-phenylene, polyamides, polyvinyl alcohol, and phenolic resins [58–62]. Edison's discovery of carbon filaments opened the path for the oriented technique to make carbon fibers from synthetic fibers, which was developed almost a hundred years later.

2.4 Classification of Carbon Fiber

As mentioned in Table 2.1, carbon fiber can be categorized into three moduli (resistance to becoming deformed within elastic limit once force is exerted to a material) groups, including standard, intermediate, and high modulus. Typically, standard modulus carbon fiber accounts for 80–90% of the overall market. The cost of carbon fiber has a significant positive relationship with its modulus. Tensile strength, which is closely associated with modulus, is also used to classify carbon fiber. Because strength falls during the treatments necessary to produce high- and ultra-high modulus, high modulus carbon fiber can have lower tensile strength than intermediate modulus carbon fiber. Other significant carbon fiber physical features include light weight, excellent chemical inertness, electrical conductivity, fatigue resistance, and low coefficient of thermal expansion [63].

Table 2.1 Classifications of carbon fiber according to modulus [63].

Type	Modulus (GPa)	Strength (MPa)	Tow Size (K)	Application
Standard Modulus	230	3,500	12-50	Automobile, Aerospace
Intermediate Modulus	400	5,000	3-24	Aerospace, Wind Turbine Blades, Pressure Vessels
High Modulus	500	3,500	1-12	Aerospace

The phrase tow count represents the number of filaments per tow and is frequently represented using terminology like 24K, where K stands for 1,000. A carbon fiber tow with 24,000 filaments is referred to as 24K. Small tow is categorized as CF with less than 24,000 filaments. 1K, 3K, 6K, 12K, and 24K tows are the most popular small-tow product sizes. Large tows are defined as tows with more than 24K filaments, particularly 48K and 50K tows being the most frequent large-tow product types [63]. There are, however, tows with hundreds of thousands of filaments available. Small tow material characteristics, such as greater tensile strength and modulus whenever laid or woven into a composite, outperform big tow, and are thus preferred in areas like aerospace where superior performance is required. Small-tow filaments, on the other hand, are more expensive than high-tow filaments.

Another way to categorize carbon fiber is by precursor material, which is a multi-element initial material that has been heat-treated to remove almost all non-carbon atoms, keeping just carbon. PAN, pitch, and rayon are examples of precursor materials. Because of its cost-effectiveness and the quality of the fiber generated, the latter, PAN, dominates over 96% of the carbon fiber market [63].

2.5 Production Stages of Carbon Fiber

2.5.1 Stabilization/ Oxidation

Thermal stabilization is an essential and crucial step in the production of high-quality carbon fiber. Thermal stabilization likewise enables the precursor fiber to withstand the

high temperatures experienced in the carbonization phase, which range from 1000 to 1500 °C. Higher temperatures up to 400 °C [64–66] are also utilized to minimize the carbonization duration with increased heating rates of >100 °C min^{-1} in a single step to the carbonization and graphitization phases.

Thermal stabilization durations in the air might require up to several hours depending on the stabilization time, temperature, precursor diameter, and other precursor fiber properties [16, 67]. It is crucial to avoid contraction during the stabilization step by applying strain to the precursor fibers. In this approach, the precursor fiber's alignment can be retained in the stabilized structure. The alignment of the final carbon fiber is well established to be correlated to the alignment of the precursor fiber [68]. The elastic modulus of the resulting carbon fiber will be greater if the precursor fiber has a higher molecular orientation.

Figure 2.8 Thermal stabilization oven used for the oxidation process.

Thermal stabilization is generally performed in the air [69], ozone-contained air [70], pure oxygen environments [71], and inert atmospheres such nitrogen and argon [72]. It has been observed that cyclization and dehydrogenation proceed hand in hand for copolymer fibers stabilized in the air, while dehydrogenation happens before cyclization for homopolymer fibers. The ring sequence of fibers stabilized in oxygen is reported to be narrower than that of fibers stabilized in air or nitrogen [73]. The strong exothermic

action of oxygen on the polymer chains, which creates interruptions in the series of ring structures, is thought to be the source of this phenomenon. Thermal stabilization in ozone-enriched air [70] is observed to result in the development of skin-core structure, the intensification of chemical processes, and the reduction of the stabilization duration.

Thermal stabilization in an inert environment is reported to be quicker, and it is known to generate carbon fibers having poor tensile characteristics and a low carbon yield (30–40% in helium at 1000 °C) [74]. While stabilization in an oxygen-rich environment requires longer finishing the cyclization process, resulting in carbon fibers with superior tensile characteristics and a greater carbon yield (60% in helium at 1000 °C). The use of different stabilization environments has been reported to enhance the rate of thermal stabilization, including hydrochloric acid/oxygen (HCl/O_2), sulfur dioxide (SO_2) [75–77], bromine/oxygen (Br_2/O_2), ammonia/oxygen (NH_3/O_2) [78, 79] mixtures. Dehydrogenation and cyclization processes are accelerated in the acidic environment generated by these gases.

2.5.2 Carbonization

The stabilized precursor fibers, which are flame-resistant and non-meltable due to the stabilization process, are heated in an inert environment and transformed into carbon fibers through carbonization. In the low-temperature range, the cyclized polymer structure crosslinks, and further condensation processes occur up to T = 1600 °C, where a carbon phase known as "turbostratic" carbon forms. The graphite-type carbon layers are properly aligned in the fiber direction, although there are still numerous tetrahedral carbon-type crosslinks between them. This specified structure leads to form the characteristic high tensile strength carbon fiber [31].

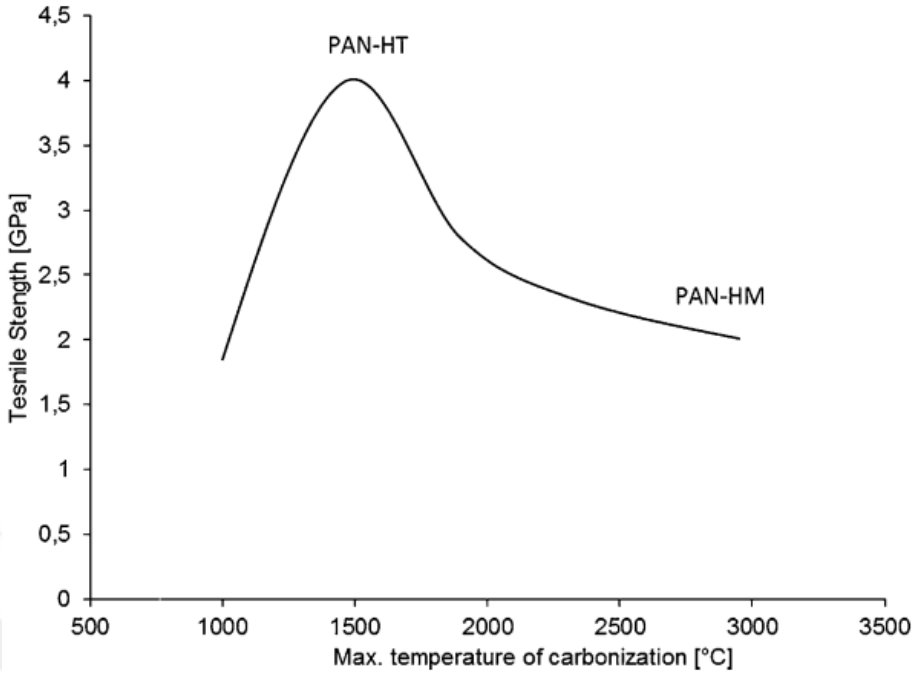

Figure 2.9 Typical growth of tensile strength (GPa) of PAN-based carbon fibers over maximum heat treatment temperature (°C) [31].

A very high carbonization rate causes flaws in the carbon fibers, whereas a very low carbonization rate results in substantial amounts of nitrogen being lost early in the carbonization process, which is usually preferable for high-strength carbon fibers. At T<700 °C, the whole carbonization process produces hazardous gases such as NH_3 and HCN [80]. Dehydrogenation and denitrification become increasingly significant above this temperature for the formation of carbon sheet-like layers from carbon-like ribbons.

2.5.3 Graphitization

The carbonized fibers were further graphitized employing a graphitization technique that involved elevated temperatures of up to 3000 °C, stretching the fibers to 50–100% extension. The stretching of the fibers enabled a chosen crystallographic alignment, resulting in a higher desired modulus than carbonized fibers. Crystalline distribution, crystallinity, molecular orientation, defect ratio, and carbon content were all factors in the attributes of the resulting carbon fibers. Finally, post-treatment operations such as epoxy sizing and surface modification of carbon fibers were carried out to improve their adherence to composite matrices [81–83].

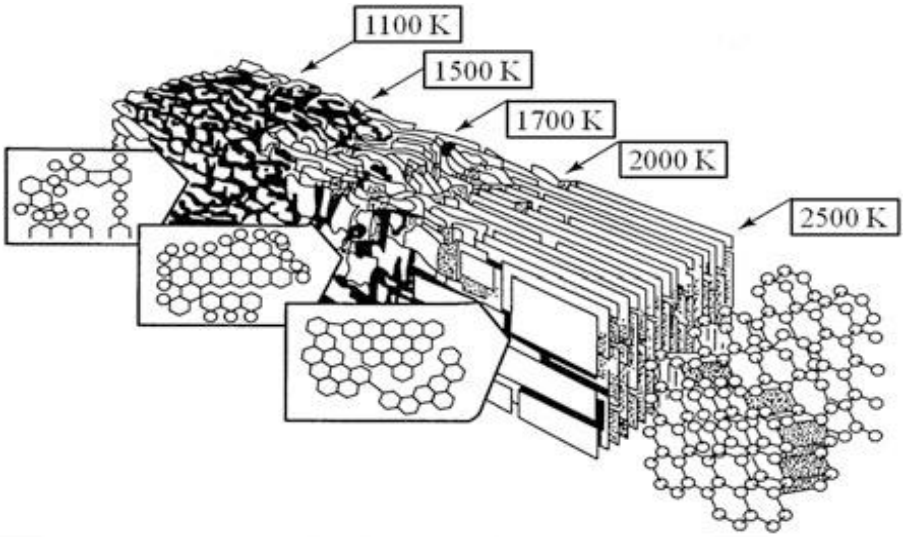

Figure 2.10 Structural model for carbon fiber in graphitization method [84].

2.6 Commercial Precursors for Carbon Fiber Manufacture

Promising precursors for carbon fiber manufacturing include polymeric compounds that generate a carbon residue while not melting in the pyrolysis process. Further physical properties of a good precursor of carbon fiber include low linear density, round cross-section, high tensile strength, high tensile modulus, and fewer imperfections in the polymer structure [85].

Table 2.2 Comparison of different carbon fiber precursors, their source, and average strength.

Precursors	Source	Average tensile strength (GPa)	Spinning method (preferred)	Carbon Yield (%)	Reference
PAN	Propylene from crude oil	6.6	Wet	>50	[86]
Rayon	Cellulose (wood pulp)	0.4	Wet	10	[74]
Pitch	Petroleum, coal tar	0.6	Melt	60-80	[87]
Mesophase pitch	Petroleum, coal tar	3.5	Melt	60-80	[88]
Sulfonated polyethylene	Natural gas, petroleum	2.5	Melt	60-80	[89]
Lignin	Cellulose (wood pulp)	1.2	Electro, Wet	10	[90]

Regardless of the precursor material, the carbon content of the carbon fiber needs to be more than 90% by weight. Carbon fibers have a fundamental structure comprising turbostratic layers of graphene aligned to confine the fiber axis. Turbostratic layers are graphene sheets layered without complete crystallographic sequence, having succeeding sheets in random rotational orientations around their normal, resulting in a spacing of 0.344 nm as compared to 0.335 nm for graphite crystals [91].

The cross-sectional morphology of the carbon fiber, as well as the orientation of the graphitic layers through the fiber axis, are absolutely vital for its modulus. These two microstructural properties of carbon fiber are developed mostly during precursor synthesis and are generally refined during carbonization. Figure 2.11 depicts the apparent cross-sectional microstructure shapes of carbon fibers. Lateral texture has been shown to influence graphitizability; fibers containing radial transverse structures are easier to graphitize than fibers with random transverse structures [92].

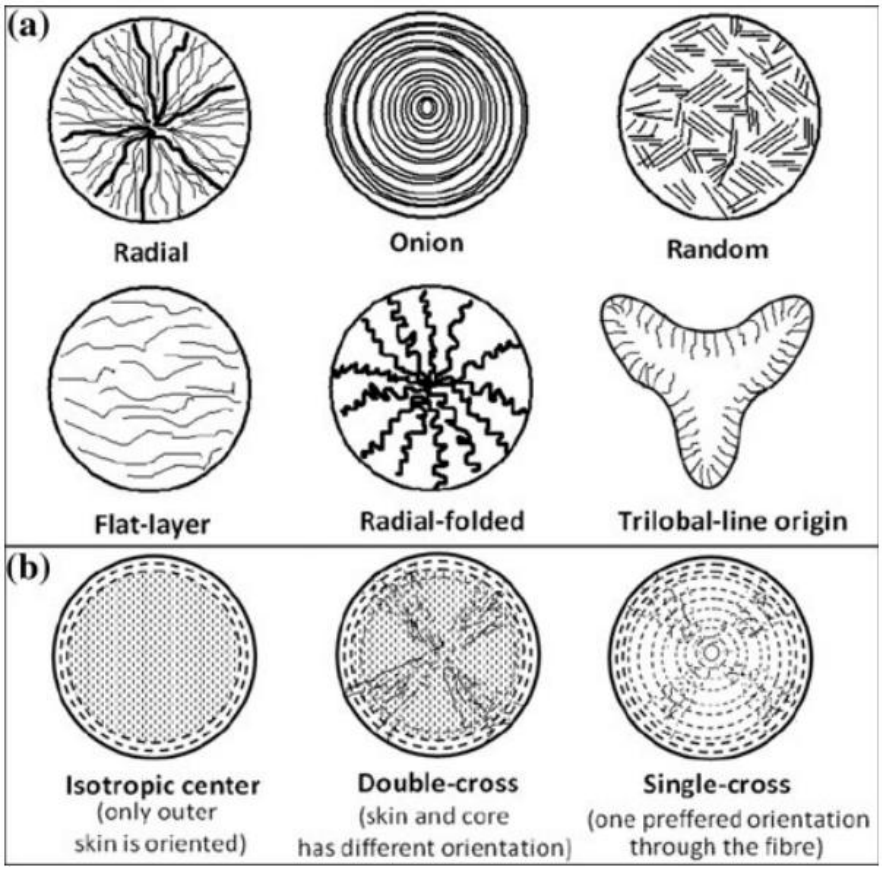

Figure 2.11 Cross-sectional microtextures of carbon fiber from various precursors are depicted schematically. a) Pitch-based carbon fiber, b) PAN-based carbon fiber [92].

Graphitizable carbon offers excellent planar orientation and graphene layer stacking. In contrast, non-graphitizable carbon does not exhibit a long-range parallel arrangement of graphene layers, as illustrated in Figure 2.12. It is important to be able to graphitize the precursor to attain excellent mechanical properties, particularly in terms of axial stiffness. Non-melting materials, like cellulose, are usually classified as non-graphitizable carbon [93]. Nevertheless, particular species of native cellulose, like tunicate-based and bacterial cellulose, have a far greater crystallinity than the most frequent sources of cellulosic carbon, which are those from higher plants, which might help to increase graphitization potential.

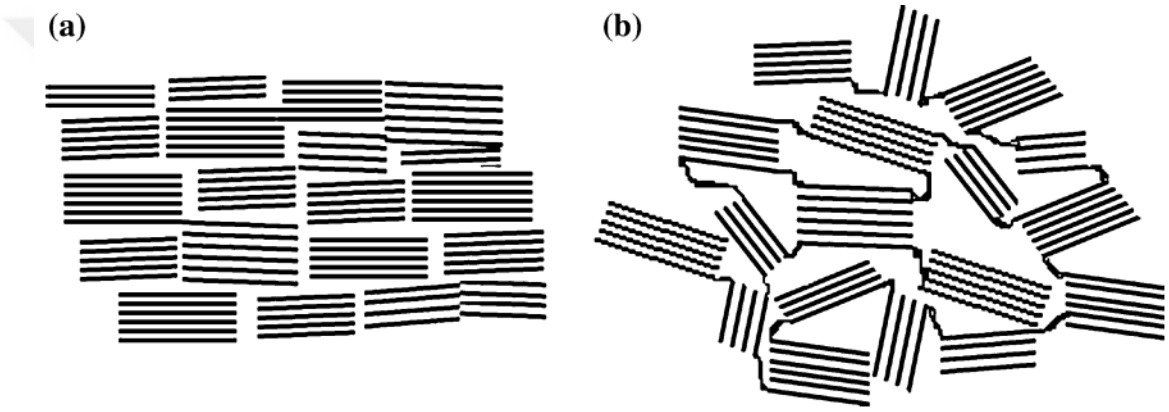

Figure 2.12 Graphitizable carbon structure (a) vs. non-graphitizable carbon structure (b).

PAN is the most common precursor on the market, although pitch is utilized for the majority of other carbon fiber variants. The precursor rayon, which has been commonly used earlier, is now obsolete. Carbon fiber processing from diverse precursors necessitates a variety of procedures in order to get high-quality final products. Although the processing techniques are identical, they are substantially different in terms of details [31].

2.6.1 PAN as a Precursor of Carbon Fiber

PAN fibers are now the most commonly utilized precursors for high-strength carbon fiber production [7, 94, 95]. Despite the presence of various precursors such as Rayon and Pitch, PAN fibers have dominated over 90% of the sector due to their ability to produce carbon fibers having high performance and high carbon yield [96]. Because of its capacity to develop into a well-tuned carbon network following carbonization, PAN

cements its position as the primary precursor for carbon fiber manufacturing. The chemical composition of the precursor and its thermal stability are the starting points for the evolution of carbon fiber morphology and, eventually, its physical characteristics [97, 98].

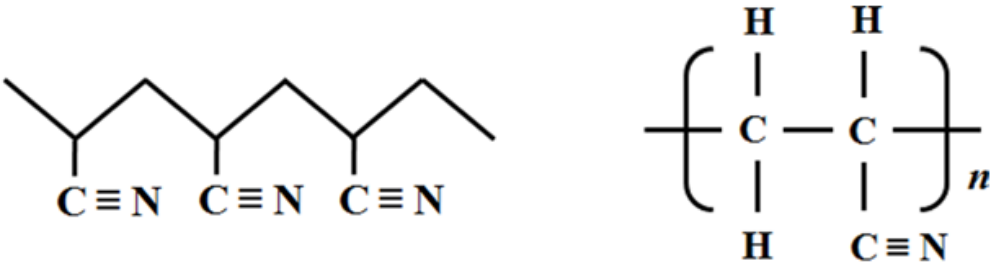

Figure 2.13 Molecular structure of polyacrylonitrile precursor.

The method was introduced to achieve the best mechanical characteristics possible. PAN precursors have a potential carbon yield of 67%. The PAN includes polar nitrile groups, which prevent the molecular chains from aligning while spinning. For carbon-fiber synthesis, a copolymer of PAN and additional monomers including acrylic acid, methacrylate, and methacrylic acid in the range of 2–15% are employed. Thermal oxidative stabilization (at temperatures from 200-300 °C in the air), carbonization (at temperatures from 1000-1700 °C in the inert atmosphere (usually up to 1600 °C in a nitrogen environment, and at higher temperatures in an argon environment)), and graphitization (at temperatures from 2500-3000 °C) are all steps in the manufacture of carbon fibers from PAN [7].

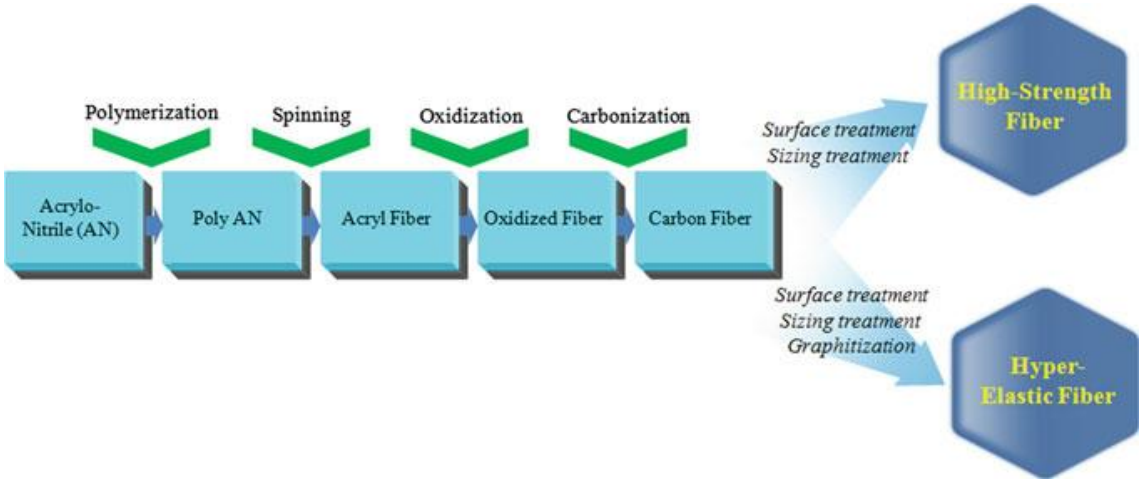

Figure 2.14 Production stages for PAN-based carbon fibers.

2.6.1.1 Production of PAN Precursor Fibers

PAN is a highly polar nitrile end group-containing atactic, linear polymer. Pristine PAN has a glass transition temperature of 120 °C and seems to disintegrate before melting due to its highly polar character. PAN precursor fibers need therefore be manufactured utilizing extremely polar solvents in either dry or wet spinning methods. PAN homopolymer is utilized only as a carbon fiber precursor only particular circumstances. Numerous different monomers, including methyl acrylate, acrylic acid, itaconic acid, methacrylic acid, vinyl bromide, and others, are usually found in commercialized PAN precursor fibers in the range of 6 to 9% [99, 100]. These compounds reduce the glass transition temperature and alter the polymer structure's reactivity. Each of these modifications might have a significant impact on succeeding stages.

The wet spinning process is applied to produce almost all precursor fibers utilized in commercial PAN-based carbon fiber procedures, despite the fact that PAN fibers may indeed be manufactured using either wet or dry spinning techniques. PAN or PAN copolymers dissolved in a polar solvent, such as dimethylacetamide, nitric acid, or sodium thiocyanate, is often employed in a wet-spinning process. This solution is filtered before being ejected into a coagulation bath through a spinnerette [101, 102]. Dimethylacetamide, dimethylformamide, water and sodium thiocyanate, or dimethylacetamide to ethylene glycol can all be used in the coagulation bath. The fiber production rate is regulated by controlling factors, including extrusion rate, drawdown rate, solution concentration, bath temperature, coagulation bath concentration, etc. [103].

In the wet-spinning method, mass transfer at the fiber-liquid contact is comparatively sluggish. The possible explanation for this is that the coagulation bath's solvent concentration is reasonably higher. As a result, the solvent can disperse radially across the solidifying fiber more quickly than it can disperse away from the surface of the fiber. For this reason, during solidification, the solvent density is comparatively consistent across the cross-section of the fiber. Therefore, the fiber contracts evenly in the radial direction, offering to give wet-spun PAN a circular cross-section. Nevertheless, if the spinning fluid density of the polymer is low, a reasonably stiff fiber skin might appear before the fiber's center solidifies, resulting in a dog bone-shaped fiber.

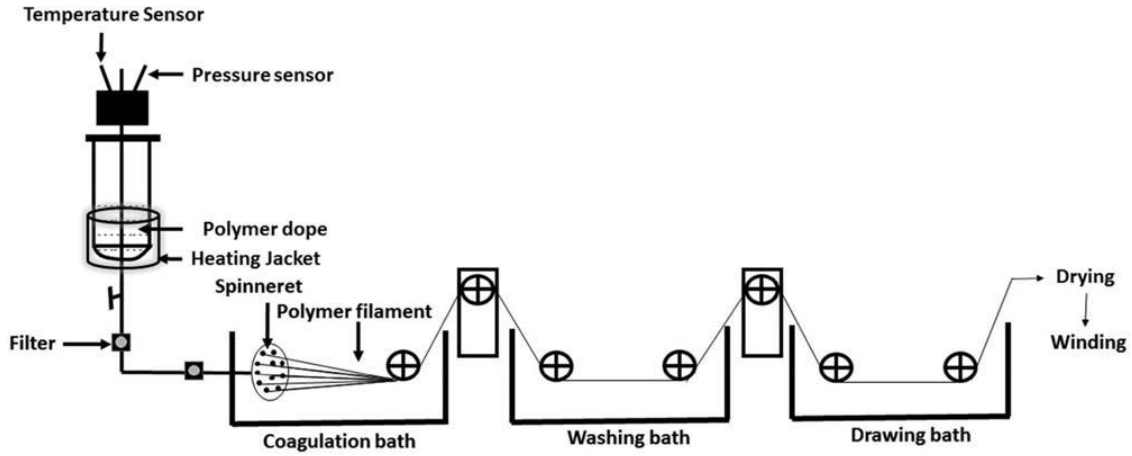

Figure 2.15 Wet spinning process in producing PAN precursor fiber [102].

The shear field seeks to align the hardening polymeric structure parallel to the flow direction when the PAN solution is pushed through the spinneret capillaries. Several studies have demonstrated that a solvent can reduce polymer tangling and improve alignment in the extrusion process [68]. PAN, like most other polymers, tends to crystallize into fibrils. The fibrillar structure and alignment inside the as-spun PAN fiber may be influenced by a variety of processing factors, including solvent concentration, coagulation bath temperature, and stretch [103]. To put it differently, wet-spinning produces a precursor fiber where the PAN molecules are arranged into fibrils that are aligned parallel to the fiber axis. As-spun fiber electron micrographs reveal that these fibrils are connected in a three-dimensional network [104]. Stretching improves the alignment of the PAN after it has been spun into fibers. Despite the fact that the highest degree of crystallinity inside the PAN fiber is only 50%, this process is critical for generating a finished carbon fiber with sufficient strength and modulus [68]. Stretching, like most polymeric fiber techniques, does not significantly improve crystallinity or molecular order inside the PAN, but it does improve the axial alignment of the PAN fibrils. In the graphene network, this fibrillar network seems to be a precursor that emerges after final thermal processing [68].

2.6.1.2 Stabilization of PAN Precursor Fibers

To become carbonizable, any precursor fiber must be ‘‘stabilized." The polymer chains are transformed to a hetero-aromatic structure during the stabilization, which is comparable in some ways to the following carbon phase. The phenomenon is known as

‘‘cyclization" [31]. The stabilization step's main goal is to crosslink this as-spun structure, ensuring that the molecular and fibrillar orientations are preserved throughout the ultimate thermal processing. To achieve this, either the PAN molecules' natural stiffness must be enhanced, or the molecules must be "linked" together to prevent or at least minimize chain breakage and relaxation during the final carbonization phase [105, 106]. The PAN fiber is stabilized in most commercial procedures by subjecting it to air at temperatures between 230 and 280 °C. To prevent the polymer structure from relaxing, tension must be introduced during this phase. Both cyclization and dehydrogenation might take place in the stabilization stage, according to most experts. Cyclization is very exothermic; however, when PAN copolymer precursors are used, the exotherm is decreased. The comonomer appears to be the catalyst for the stabilization process [3]. The copolymer content of the PAN fiber, the temperature, and also the imposed tension have all been found to influence the speed of oxidative stabilization in several investigations [107, 108]. Although the majority of studies conclude that a ladder polymer emerges during this process, the specific structure of the ladder polymer is yet unknown.

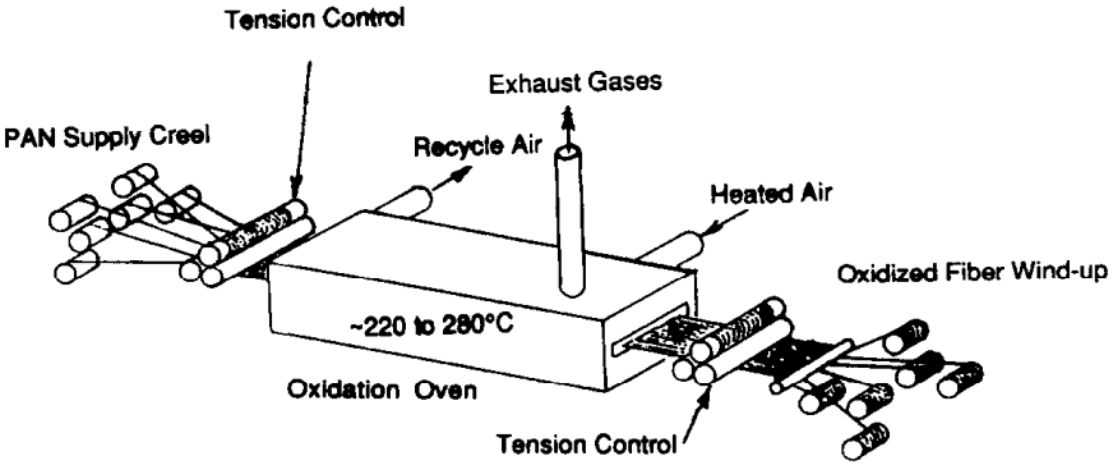

Figure 2.16 Schematic diagram of thermal stabilization process of PAN fiber [99].

2.6.1.2.1 Reactions Involved in Stabilization Process of PAN

2.6.1.2.1.1 Oxidation

The oxidation reaction aids in the development of aromatic and conjugated molecular structures, which improves the thermal stability of fibers [18]. Generally, the amount of

oxygen in a fully stabilized fiber ranges from 8 to 12.3% by weight [19, 109]. According to Fitzer et al. [110], oxygen may present in PAN structure in a variety of ways. According to their findings, PAN stabilized in the oxygenated environment had a greater frequency factor and activation energy compared to the fibers processed in the inert environment. Furthermore, fibers stabilized in an inert environment have reduced thermal stability as a result.

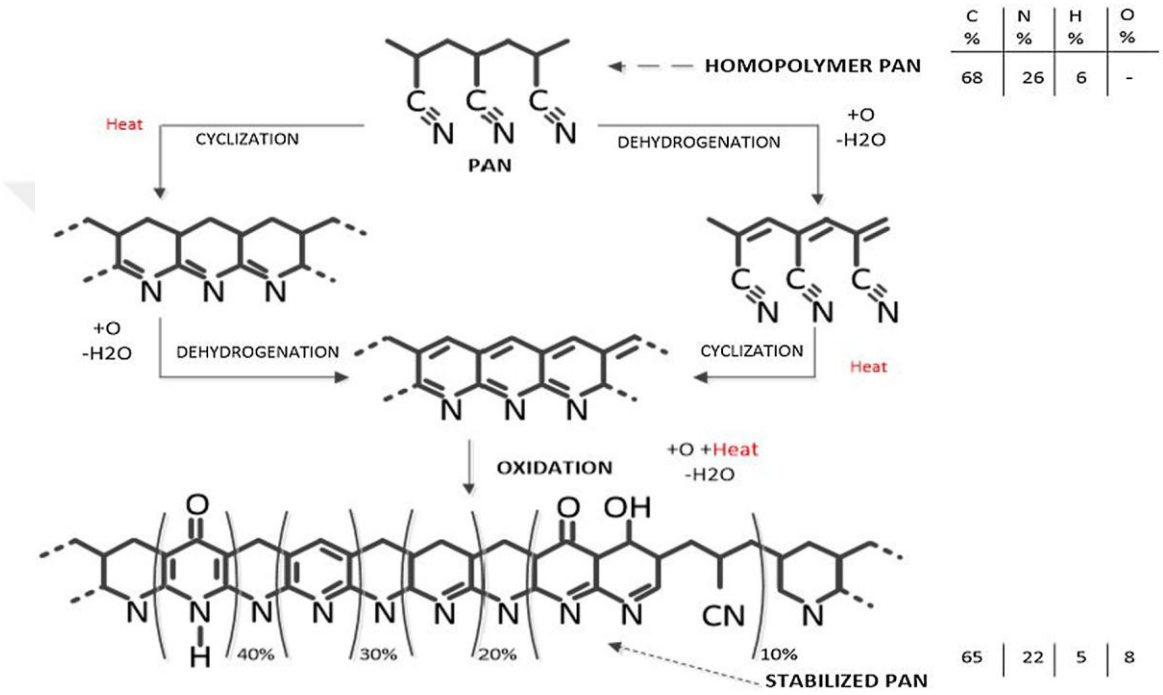

Figure 2.17 Proposed chemical reactions during thermal stabilization of PAN fiber [110].

Besides the cyclization and dehydrogenation processes, the oxidation reaction is the most complicated to comprehend since it may exist in various states in the polymer structure [18, 111, 112]. The following equation is a simplified representation of this reaction.

$$P + \frac{1}{2}O_2 \rightarrow P - O - R$$

P denotes a polymer segment that has not been oxidized, while the reaction's outcome denotes an oxidized section. In the ether functional group, R stands for either carbon or hydrogen [113].

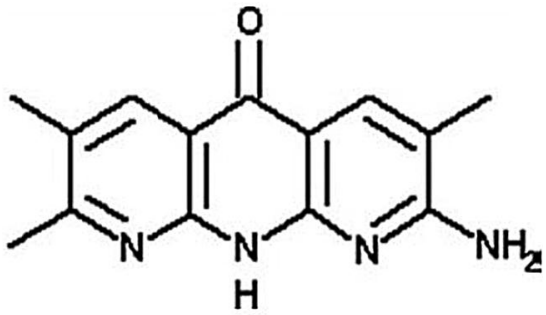

Figure 2.18 An oxidized portion of a stabilized fiber as an example [114].

2.6.1.2.1.2 Cyclization

In the stabilization process, cyclization is a fundamental reaction. The conversion of C≡N to C=N results in the formation of a double bond and, as a result, a cyclic structure. In contrast to dehydrogenation, cyclization could take place in an inert environment [97]. As a result, the thermal assessment of other stabilizing processes has been separated from cyclization. Therefore, the reaction is energy-dependent instead of mass-dependent. As a result, the cyclization process is governed by temperature and time to assure energy (heat) transmission into the polymer.

The incidence of cyclization reaction could be caused by a variety of factors. Polymer impurities, such as remnant polymerization intermediates, catalyst remnants, and inhibitors, can function as cyclization initiators [115]. It can also be launched by converting a nitrile to an axomethine [116] or in chain end groups [117]. Friedlander [118] suggested that cyclization start is caused by the production of a keto-nitrile during polymerization, while Peebles et al. [119] claimed that it is caused by the hydrolysis of nitriles to acids in polymerization. Cyclization is an exothermic process that, if carried out too quickly, could degrade fibers by causing severe shrinkage, mass loss, and even melting and fusing the fibers [120]. In contrast, if the stabilization process is so sluggish and the fibers are only partly stabilized, the unstabilized sections of the fibers will vaporize in the following carbonization and graphitization stages, causing significant damage to the end product [25].

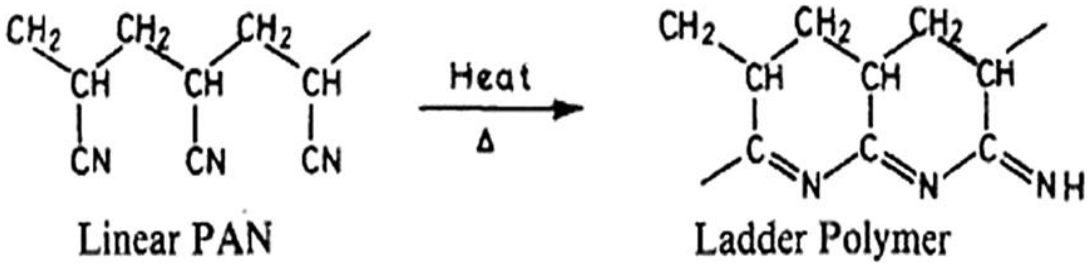

Figure 2.19 Cyclization reaction in PAN polymer [112].

The initiation can commence with either free radical or ionic processes, depending on the precursor fiber chemistry [121]. Whenever the precursor is a homopolymer, free radical processes occur. The C≡N bonds are broken by free radicals, resulting in C=N bonds [122], which initiate the cyclization process [123]. When free radical processes are the initiator, propagation is quite quick. If not treated properly, this causes an intense exothermic reaction that can damage, melt, or fuse the fibers.

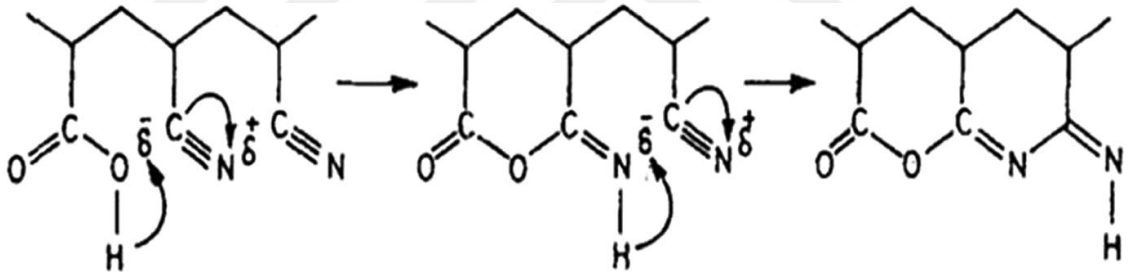

Figure 2.20 Cyclization reaction process of acidic comonomers [121].

Ionic processes occur in the precursor fibers once the precursor is a comonomer. In this instance, the cyclization is initiated by the fission of the ionic groups [121]. The ionic process, according to Bajaj and Roopanwal [121], is the most preferred mechanism for regulating reaction progress and distributing exothermic energy release across a larger temperature range [124]. The development of the cyclization process affects the other reaction processes underlying throughout the thermal stabilization in the synthesis of carbon fibers from PAN precursors [114].

2.6.1.2.1.3 Dehydrogenation

Dehydrogenation involves eliminating hydrogen with oxygen in the form of water and stabilizing the carbon chain by forming a double bond between two carbon atoms. Double bond synthesis in dehydrogenation causes thermal stability and a decrease in chain scission during carbonization [125]. The dehydrogenation process may occur before or after cyclization, as shown in Figure 2.21, according to a series of stabilization tests carried out by Fitzer et al. [110] in 1975 using Differential Thermal Analysis (DTA) and regulation of the air or nitrogen atmosphere.

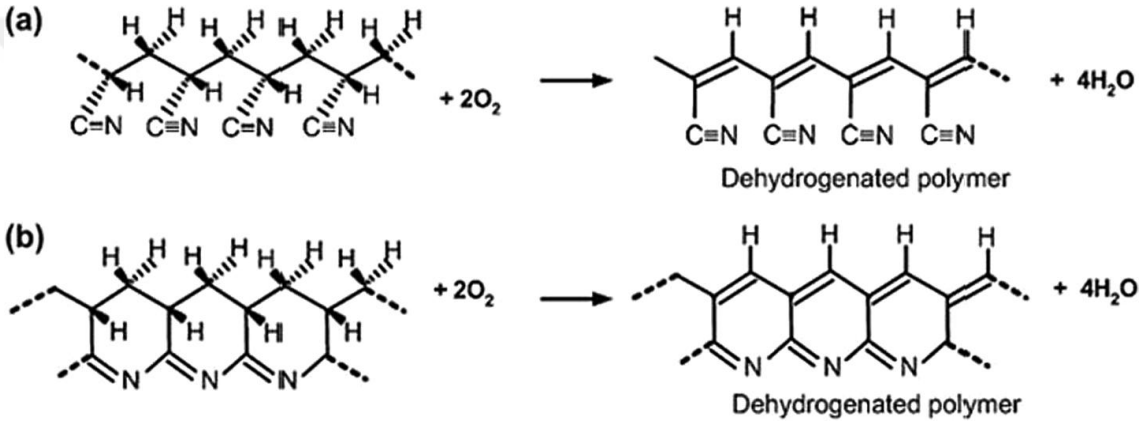

Figure 2.21 Dehydrogenation takes place before (a) or after (b) cyclization of PAN polymer [8].

Dehydrogenation is a slower process in stabilizing method that is best used on chains that have previously been cyclized. Dehydrogenation occurs literally simultaneously with oxidation, according to Liu et al. [126], comparative analysis of DSC and FTIR findings. The activation energies and frequency parameters were discovered in one case by stabilizing fiber in an inert environment, and the cyclization processes happened independently and in a quick and intensive way. When these fibers were further stabilized in air, it was shown that oxidation and dehydrogenation processes need considerably less activation energy and take much longer than cyclization reactions [114, 126]. These observations demonstrate that dehydrogenation is a stumbling block to fiber stabilization. Because the order of reactions is unclear, the bundle model considers dehydrogenation as a single reaction [112, 113]. The speed of dehydrogenation is determined by the concentrations of oxygen and fragments in the polymer structure, which are never engaged in the process.

2.6.1.3 Carbonization of Stabilized PAN Precursor Fibers

The PAN fiber is carbonized at temperatures between 1000 and 1500 °C in an inert environment once it has been stabilized [99, 106]. During this phase, the majority of the fiber's non-carbon components are released as hydrogen, water, methane, ammonia, hydrogen cyanide, carbon dioxide, carbon monoxide, and other gases [104, 127]. The weight of the fiber is reduced by 55 to 60% due to the formation of these components. Therefore, the diameter of the fiber decreases. As a result, the precursor fiber may start with an as-spun thickness of 35 μm and then be stretched to a diameter of 10.5 μm in a conventional PAN process. Eventually, after carbonization, shrinkage results in carbon fiber with a thickness of 7 μm. To put it another way, tiny carbon fiber diameters are an indication of PAN's rapid weight loss during processing. Despite the fact that the thickness of most PAN-based carbon fibers is lower than most other pitch-based carbon fibers, the precursor fiber's as-spun diameter is substantially higher. Rising the ultimate thermal processing temperature boosts tensile strength at first. Once thermal processing temperatures approach 1600 °C, however, tensile strength declines dramatically [128].

According to Fitzer, this drop is due to the release of nitrogen, and the strength loss can be reduced by applying tension in thermal treatment [129]. On the other hand, as the heat treatment temperature rises, the extent of preferred alignment inside the fiber and, therefore, the modulus of PAN-based carbon fibers constantly increases [128]. As a result, the different grades of PAN-based carbon fiber offered from a specific producer are often the result of temperature variations during the heat treatment process.

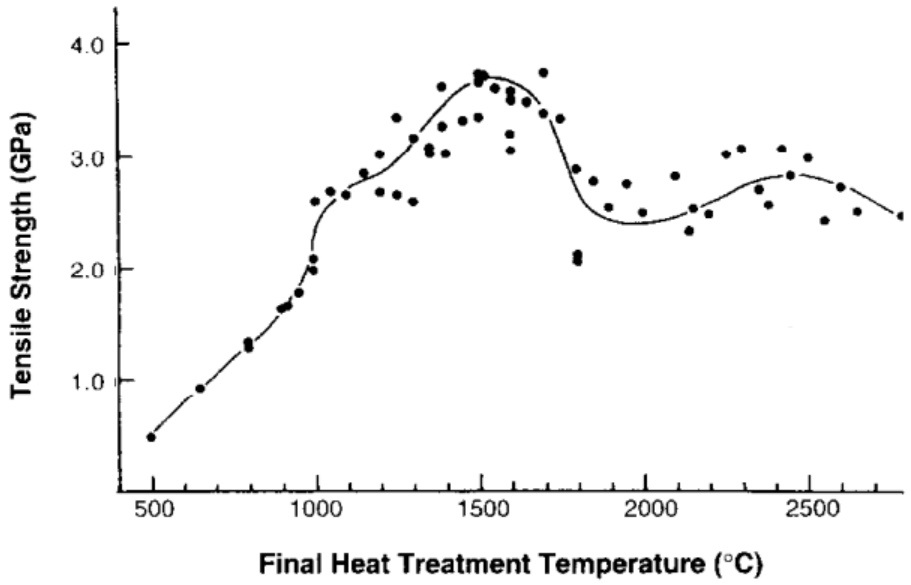

Figure 2.22 Tensile strength of PAN-based carbon fiber as a function of final heat treatment temperature [128].

Graphitization is a technique wherein fibers are treated to temperatures between 1600 and 3000 °C. The turbostratic carbon fixes its "deformities", and graphitic structures are formed at this temperature. In PAN-based carbon fibers, it results in greater moduli but reduced strength (Figure 2.22) [31]. Very high carbonization speeds cause flaws in the carbon fibers, but very low carbonization speeds cause substantial amounts of nitrogen to be lost early in the carbonization stage, which is actually desirable for high-strength carbon fibers. At T< 700 °C, the whole carbonization process generates hazardous gases, including NH_3 and HCN [80]. Dehydrogenation and de-nitrification are becoming increasingly essential for the formation of carbon sheet-like layers from carbon-like ribbons beyond this temperature (Figure 2.23).

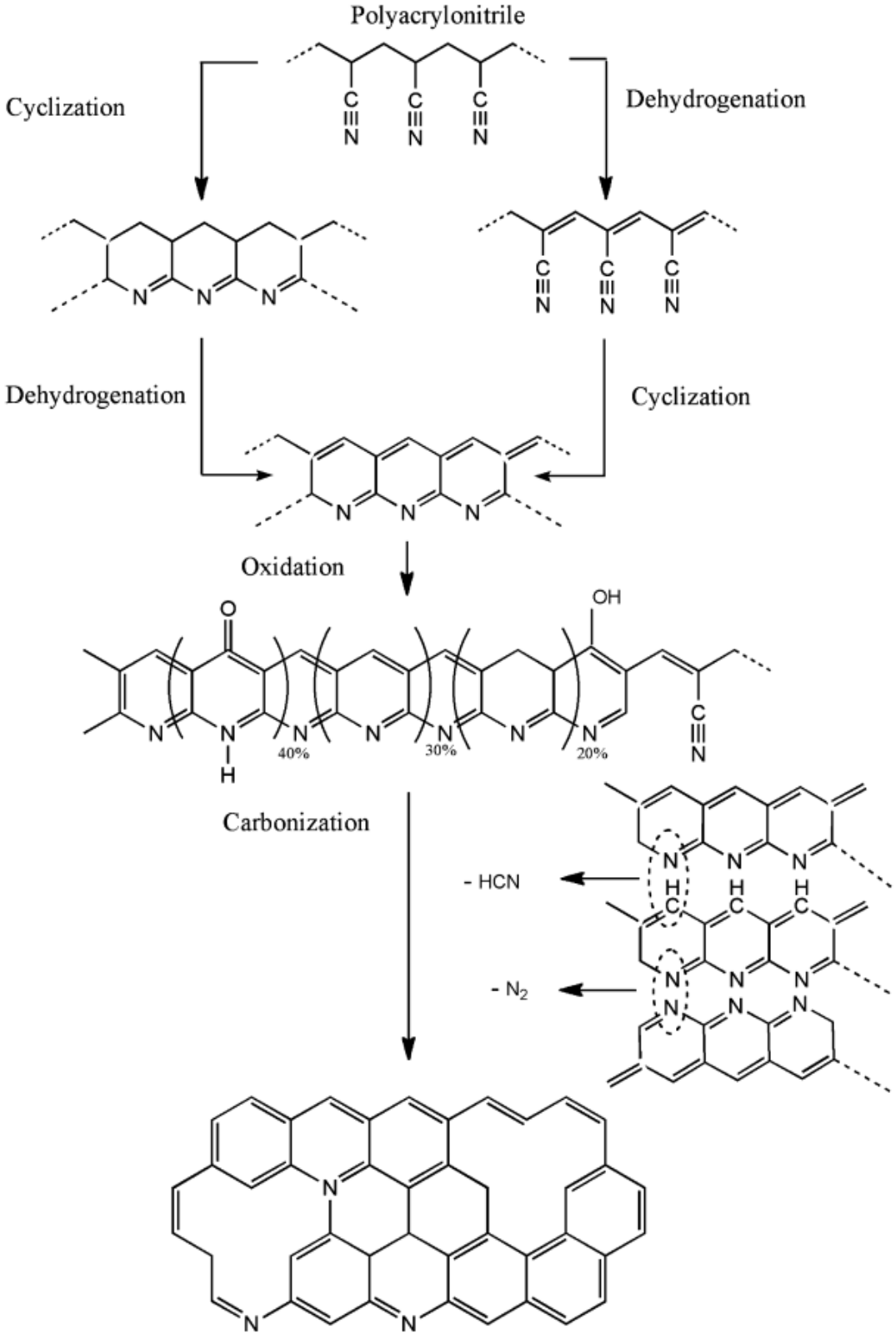

Figure 2.23 Model of overall reaction paths from PAN to carbon phase [31].

2.6.2 Pitch as a Precursor of Carbon Fiber

Pitch-based carbon fibers were established in the quest for low-cost, high carbon-containing (>80% carbon) raw materials. Pitch is often produced as a byproduct of coal or petroleum chemistry. Synthetic pitch can also be derived from synthetic polymers, like PVC. Because coal pitch is hard to clean from natural impurities like defect-sensitive particulates, petroleum pitch is preferred. In addition, the pitch is a low-molecular-weight substance, unlike PAN-based predecessors.

In order to eliminate volatile substances from pitch, it is cleaned in the vacuum firstly [130]. The pitch is then heated in an inert environment at temperatures between 350 and 5000 °C [131]. A mesophase is formed by the condensation of pitch oligomers in this thermal process. This is a complicated process to manage, and a thorough understanding of it is required (some temperature ranges are distinctive). The resultant mesophase, on the other hand, has the benefit of being able to be spun as fiber using a melt-spinning technique rather than a solution-based process. The precursor fiber undergoes a relatively high alignment of the aromatic layers during the melt spinning process, which is subsequently converted precisely into the ultimate carbon fiber. Yet, for melt spinning processes, both the molecular weight and the mesophase concentration must be adjusted.

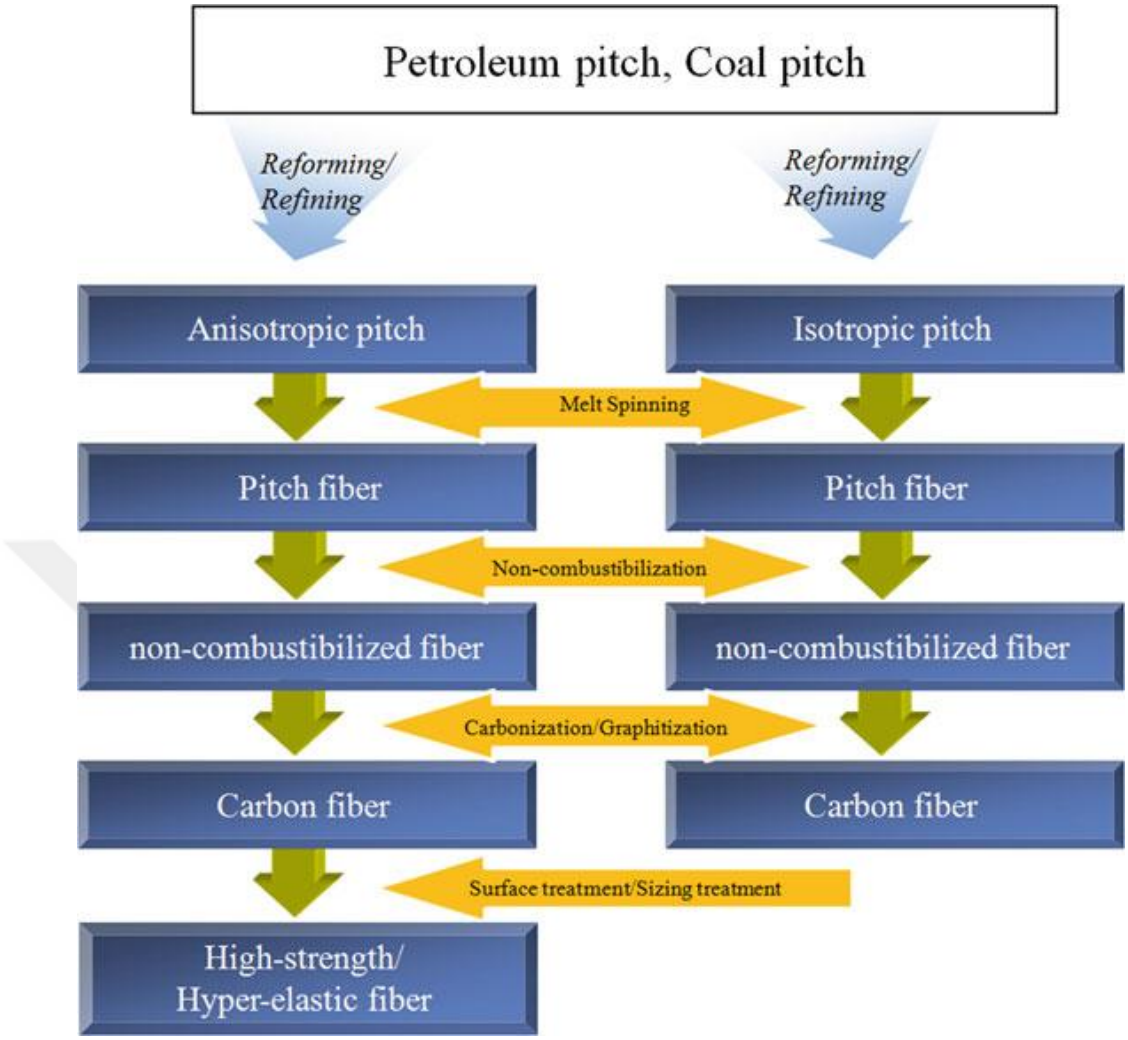

Figure 2.24 Manufacturing process for pitch-based carbon fibers.

Carbon fibers are made from isotropic and mesophase pitches. The planar aromatic molecules in a mesophase pitch have a preferential orientation in the liquid state, tending to lay parallel to one other, resulting in a discotic nematic liquid mesophase structure. Pitch produced from petroleum, or coal tar is composed of fused aromatic rings, and the potential yield for carbon fiber manufacturing is about 80%. Carbon fibers derived from these sources have a modulus nearly equivalent to that of a single crystal of graphite (~1050 GPa), which is substantially greater than high-modulus PAN-based carbon fibers [132]. Moreover, pitch-based carbon fibers outperform PAN-based fibers in terms of thermal and electrical characteristics [7]. Yet, there are numerous differences in pitch structure, including surface imperfections, internal voids, and other contaminations, which affect mechanical characteristics to be lowered [133].

2.6.2.1 Stabilization and Carbonization of Pitch-Based Carbon Fibers

Pitch-based precursor fibers are stabilized in the same approach that PAN-based precursor fibers are stabilized. After the formation of mesophase, the precursor fiber is crosslinked to a non-meltable fiber, which is fully prepared for carbonization by thermal treatment at 250–350 °C in air. The temperature and time required for stabilization are determined by the precursor's inner structure. To eliminate volatile components without leaving voids in the carbon fibers, the fibers need to be pre-carbonized at temperatures between 700 and 900 °C. End-temperatures of 1500–1800 °C are used to carbonize in obtaining carbon fiber. A graphitization stage of up to 3000 °C is used for ultra-high modulus (UHM) carbon fibers. UHM carbon fibers are highly costly and only used in some specific purposes, such as aviation [31].

2.6.3 Lignin-Based Carbon Fibers

Apart from PAN and pitch, biopolymers have recently resurfaced as potential carbon fiber precursors. Rayon was the typical precursor in the early days of carbon fiber research, but poor carbon yield and the high cost of production limited its availability. Biopolymers should, in general, have higher carbon content and lead to high carbon yield at a minimal cost. Lignin is a component of wood and is a prominent by-product of chemical pulping operations in the paper industry. Lignin seems to be the only biopolymer that has substantial amounts of aromatic or phenolic constituents in terms of structure. The Kraft process, which employs sulfides and alkali salts to break natural lignin into soluble oligomers in order to extract it from rayon, is the most widely used method for obtaining lignin. In comparison to Kraft lignin and other lignin methods, the so-called organosolve lignin is just commercially accessible in extremely small amounts [31].

Lignin was originally explored as a precursor for carbon fibers in the late 1960s [134]. Sudo et al. treated lignin with hydroxyl groups in the 1990s to produce carbon fibers with intermediate characteristics [90, 135]. Sano and co-workers used a melt-spinning technique to investigate pure organosolve lignin that is free of sulfur and other contaminants [136, 137]. They synthesized carbon fibers having tensile strengths as low as 0.3 GPa, compared to 3.5 GPa for a standard commercial PAN-based carbon fiber.

Kraft, organosolve lignin, and also lignin blends were studied by Kadla et al. [138]. Maximum tensile strength and modulus values were reported as 0.5 GPa and 60 GPa respectively for the melt-spun fibers stabilized at 250 °C carbonized at 1000 °C [138].

2.6.4 Fully Synthetic Precursor Based Carbon Fibers

Different synthetic polymers were studied in the past as alternatives to PAN and pitch precursor materials. Modified melt-spun polyacetylene filaments were thermally stabilized and carbonized at 1000 °C temperature, yielding carbon fibers with a tensile strength of 2.3 GPa and a modulus of 386 GPa [139]. Polyvinylacetylene was studied as a PAN substitute and cyclized in nitrogen with a 300 nm UV generator, then oxidized at 225 °C temperature in the air [140], although no characteristics of the final fibers have been reported yet. Horikiri et al. [141] explored and patented polyethylene (PE) as a low-cost synthetic polymer. Strong acids, like as sulfuric acid, oxidized and sulfonated PE fibers. The carbonized fiber had a carbon yield of 75%, a tensile strength of 2.5 GPa, and a modulus up to 139 GPa [141] after being heat-treated to 1200 °C. Newell and Edie [142] explored polybenzoxazole (PBO), which may be carbonized into carbon fibers without stabilization using a standard approach. The resultant carbon fibers have modest tensile features, including tensile strength of 1 GPa and modulus of 245 GPa. To sum up, a variety of different polymers have been studied; yet, polymers lacking aromatic groups or the ability to generate aromatic units quickly tend to have lower carbon yield and require costly thermal treatment [131].

2.7 Precursors of Activated Carbon Fibers

In the manufacture of activated carbon fibers, a number of natural and synthetic fibers were reported to employ including flax [143], hemp [144], sisal [145], viscose rayon [146], polyacrylonitrile [147], phenolic resin [148], polyvinyl alcohol [149], and aromatic polyamide fibers [150–154]. Due to the easy accessibility to considerable extents, natural fibers, as an alternative biomass-based, renewable, and cost-efficient precursor for activated carbon fiber manufacturing, have received significant attention in recent years [5, 138, 155, 156]. Increasing attention is noticed to applying lingo-cellulosic materials, such as banana, coconut, curaua, sisal, and jute fibers, as activated

carbon fiber precursors. The use of these natural fibers in carbon fiber manufacturing has numerous benefits like environmental friendliness, cost-effectiveness, recyclability, sustainability, and so on [38, 39, 157–161]. However, the bio-based natural fibers are restricted in fiber length and are not continuous, which results in comparatively lower tensile properties than the polyacrylonitrile or pitch-based activated carbon fibers.

2.8 Properties of Carbon Fibers from Different Precursors

In the past forty years, significant advances have been made in addressing the underlying material process interactions needed to generate high-performance carbon fibers using PAN and pitch-based precursor fibers. Nevertheless, the difficulties associated with these precursors, such as the creation of alkaline-free PAN and the manufacture of low thickness fibers, are likely to raise manufacturing costs, which are critical in the highly competitive high-performance materials industry. In obtaining the alkaline-free PAN fiber, melt-spinning has been introduced as a compatible solution of this issue [162]. Typical PAN copolymer precursors, on the other hand, thermally degrade under their melting point, rendering melt spinning challenging, though not unattainable. The inclusion of melt-spinnable PAN copolymers can overcome this problem. Even though the melt-spinnable copolymer may look appealing as a carbon fiber precursor, the integration of methyl acrylate co-monomer into the PAN polymer structure dramatically changes the carbonization processes [163].

As a result, further research and innovation will be required to improve this technology. Despite their relatively low theoretical carbon yield (44.4% for cellulose), much cheaper precursor materials, for example, cellulose and lignin are becoming the focus of increased interest in building an improved scientific basis from which to determine whether a further growth drive is justifiable. Table 2.3 presents a quick overview of the physical and tensile characteristics of carbon fibers derived from various precursors.

Table 2.3 Properties of different precursor based carbon fibers [5].

Carbon Fiber	Density (g/cm^3)	Diameter (µm)	Tensile strength (GPa)	Tensile modulus (GPa)	Extension at break (%)
PAN-based CF	1.70-1.80	5-10	3.5-6.3	200-500	0.8-2.2
Pitch-based CF	1.80-2.20	10-11	1.3-3.1	150-900	0.3-0.9
Rayon-based CF	1.40-1.50	5-10	0.5-1.2	40-100	-
Lyocell-based CF	-	8	0.9-1.1	90-100	1.0-1.1

2.9 Demand and Market of Carbon Fiber and Carbon Fiber Reinforced Polymer

Carbon fiber has received widespread attention in recent years as a potential material for high-performance applications due to its lightweight along with excellent tensile strength and stiffness [68, 164]. Global carbon fiber demand is expected to rise from 58,000 tons to 120,000 tons from 2015 to 2022, according to certain market forecast estimations. Carbon fiber composites have followed a similar upward trend (i.e., from 91,000 tons in 2015 to 191,000 tons in 2022) [165]. This is due to carbon fiber composites' potential to provide lightweight alternatives for optimized fuel consumption [165]. Based on contemporary standards, the early manufacturing of carbon fiber would not be regarded as challenging, especially before 1970, when the application of tension was not used [85]. Continuous expenditures in this field, on the other hand, showed that the importance of carbon fibers was understood early on. Furthermore, when carbon fiber production processes advanced, the mechanical characteristics of carbon fiber composites were significantly enhanced. The key production processes, intermediates, and estimated unit costs in the value chain that turn crude oil into carbon fiber and eventually carbon fiber reinforced polymers are depicted in Figure 2.25.

In the production of acrylonitrile, propylene produced from crude oil breakdown reacts with ammonia in an ammoxidation mechanism. Usually, carbon fiber producers start their supply chain with acrylonitrile purchases from distributors. In-house polymerization and precursor spinning technologies are available to all carbon fiber

producers in the market. As a result, the methods and formulas required to transform acrylonitrile into carbon fiber-grade PAN and afterward precursor are carefully maintained intellectual rights that the producers are unwilling to outsource. The original Japanese producers, who still lead the sector, have a strategic advantage as a result of this. Different comonomers are found in precursor fibers with PAN only in minuscule amounts (about 5% by precursor weight). These comonomers, like acrylonitrile, are usually acquired from different vendors. Carbon fiber is commonly accessible for acquisition in the marketplace, but precursors are not. Carbon fiber can be acquired directly from carbon fiber producers or through various distributors on the market. On the other hand, no precursor of carbon fiber-grade is accessible for purchase since carbon fiber producers keep all such precursors in-house for their own intra-company operations [63].

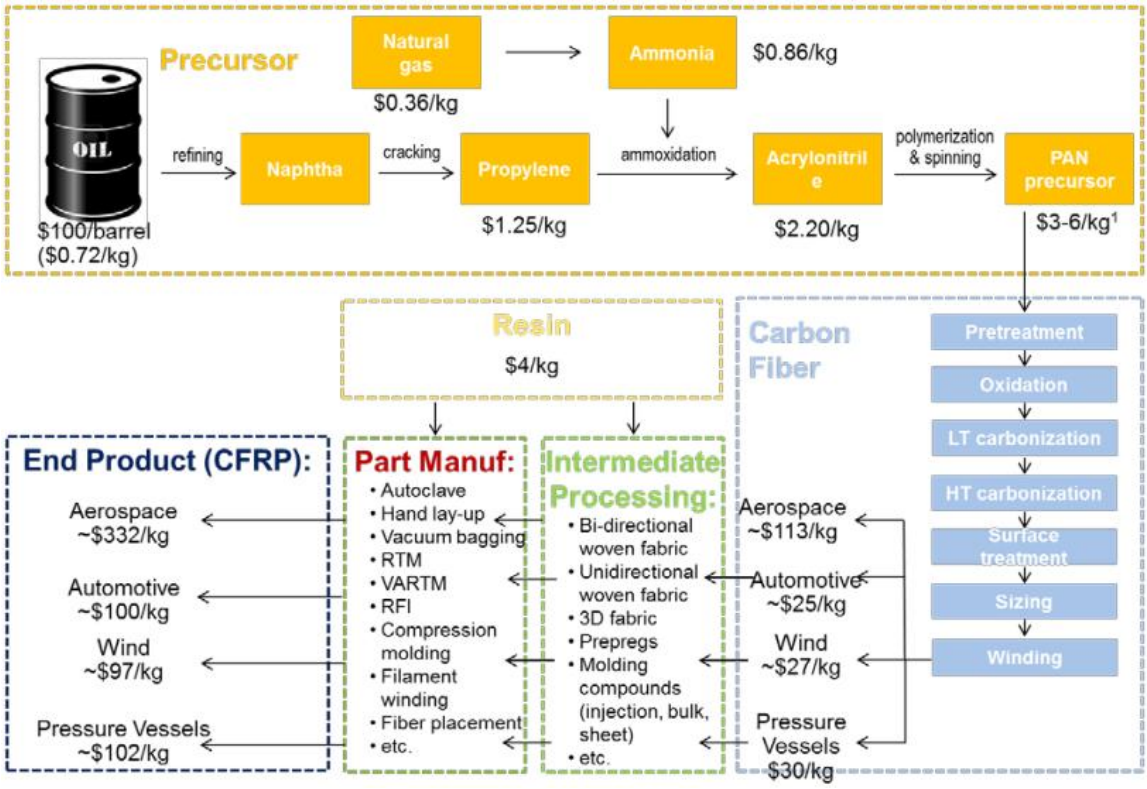

Figure 2.25 Carbon fiber and CFRP value chain [63].

[RTM= Resin transfer molding, VARTM = Vacuum-assisted resin transfer molding, HT = High temperature, LT = Low temperature]

Despite the fact that the basics of PAN-based carbon fibers were established in the United Kingdom, commercialization and additional development was undertaken in the United States and Japan. In 2008, the overall capacity of PAN-based carbon fiber nameplates was 68000 t [54]. Around 60% of these industries have their headquarters in Asia, mostly Japan (Figure 2.26). Home-based manufacturers in the United States, such as Hexel, Zoltek, and Cytec, are in second place. The Carbon Company, a subsidiary of SGL Group, is the sole manufacturer with its home base in Europe [54].

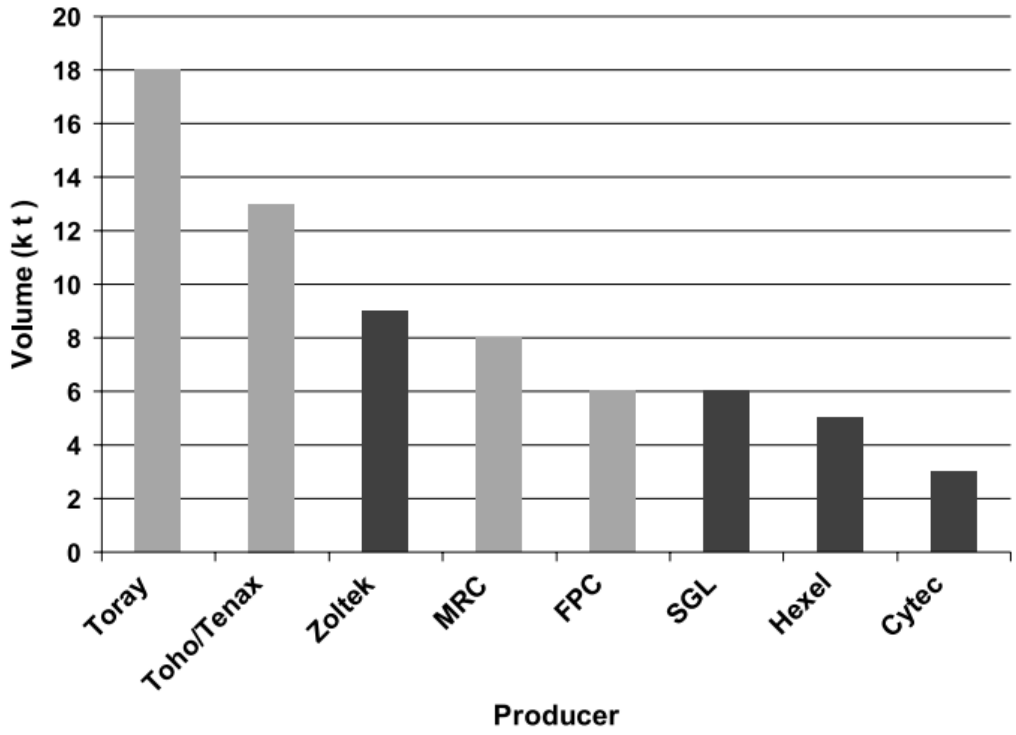

Figure 2.26 Nameplate capacities of major carbon fiber manufacturers [54]

Most leading Japanese carbon fiber companies have operations in Europe and the United States. Manufacturing capacity in the United States and abroad is sufficient to meet the demands of the North American market. The Asian market's capacity is greater than its own requirement. The European market has just a limited amount of domestic capacity, and indeed the foreign capacity operating in Europe is insufficient to meet demand. Imports from Asia and the United States must fill the gap (Figure 2.27). Despite being the largest consumer of carbon fibers, Europe has failed to manage its own domestic source [54].

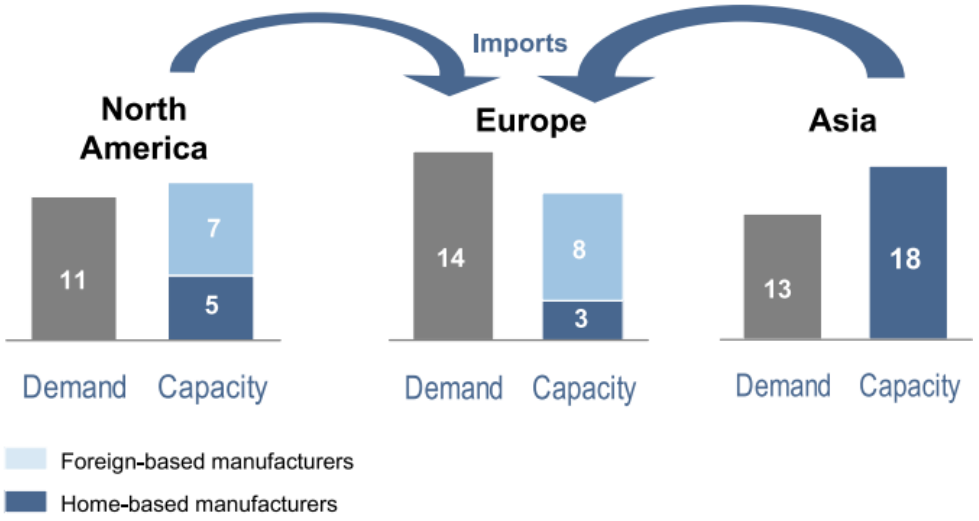

Figure 2.27 Effective demand and capacity balance of carbon fiber.

The accessibility of a sufficient PAN precursor material is most important for the synthesis of carbon fibers. Only in its fundamentals does the manufacture of this unique precursor resemble that of a textile PAN fiber. Furthermore, the chemical contents, pureness, spinning procedure, coagulation method, and textile manufacturing characteristics of this precursor need special consideration. This information belongs to each manufacturer as proprietary and is not available to the general public. As a result, each prominent carbon fiber company developed its specific precursor expertise and manufacturing skills. When viewed on a worldwide scale, the satellization of the United States and Europe from Japan or Asia may be regarded as remarkable (Figure 2.28) [54].

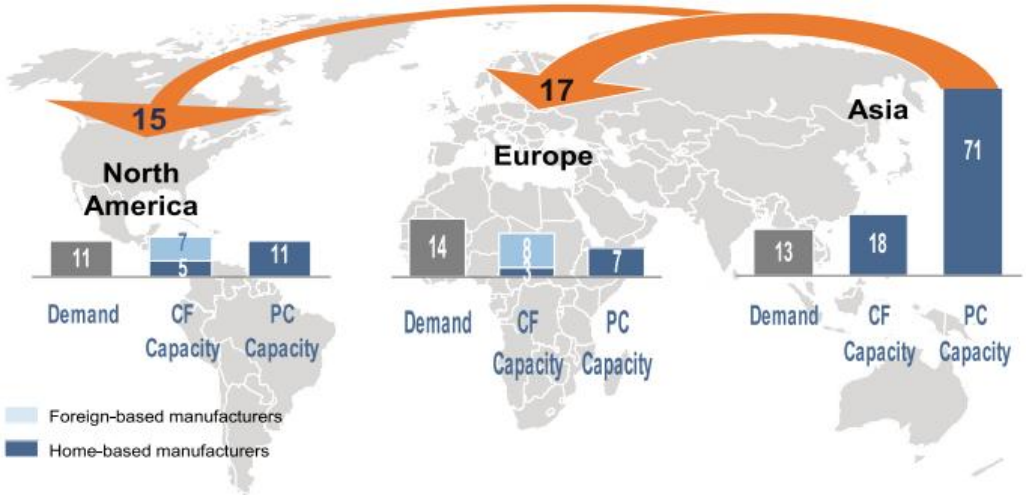

Figure 2.28 Supply of carbon fiber precursor.

The manufacturing of carbon fiber reinforced composites has a significant cost-cutting potential. When compared to low filament tows, using high filament tows keeps costs down. This, of course, necessitates the development and implementation of innovative textile production processes. Highly automated textile methods will boost production while maintaining high component quality repeatability, lowering in-process monitoring costs, and increasing carbon fiber and resin usage rates. Figure 2.29 is an illustration of a contemporary, highly automated manufacturing facility. The atomized wrapping of carbon fiber strips on a mold forms the cockpit and nose part of Boeing's Dreamliner [166].

Figure 2.29 Production of nose and cockpit section of Boeing's 787 Dreamliner [167].

The aviation sector has boosted the amount of CFRP composites in aircraft to over 50%, owing to innovative textile technology (Figure 2.30). Since CFRP is quite important in contemporary aircraft applications, Boing and Airbus have engaged in major supply agreements with carbon fiber producers. In 2006, Boing and Toray agreed on a 3 to 6 billion dollar supply deal for the Boing Dreamliner. Hexcel and Airbus Industries negotiated on a procurement volume of 4 to 5 billion dollars for the Airbus 350-XWB two years later, in 2008 [54].

Figure 2.30 Rise of CFRP usage in civil aircraft manufacture.

2.10 Application Areas of Carbon Fiber

Military applications were the early drivers of the carbon fiber sector, followed by demand from space programs. Carbon fibers were subsequently adopted by the sporting goods sector. High fiber pricing and labor-intensive manufacturing hampered widespread adoption in mass markets like the automobile sector. This scenario has been going on for more than 30 years. The energy was inexpensive, and the oil supply was thought to be virtually limitless. However, this scenario has drastically changed. In 2008, the oil price had hit 140 dollars per barrel, and the concept of peak oil had become general acceptance [54]. CO_2 and the generation of energy from fossil fuels have been criticized due to the climate change issue. Alternative energies, energy conservation, and energy efficiency have all become megatrends in recent years. In the long to medium term, combustion engine-powered transportation will have to contend with electromobility. All of this creates an excellent potential for carbon fibers to reach mainstream markets such as civil engineering, civil aviation, automobiles, wind energy generation, and so on (Figure 2.31).

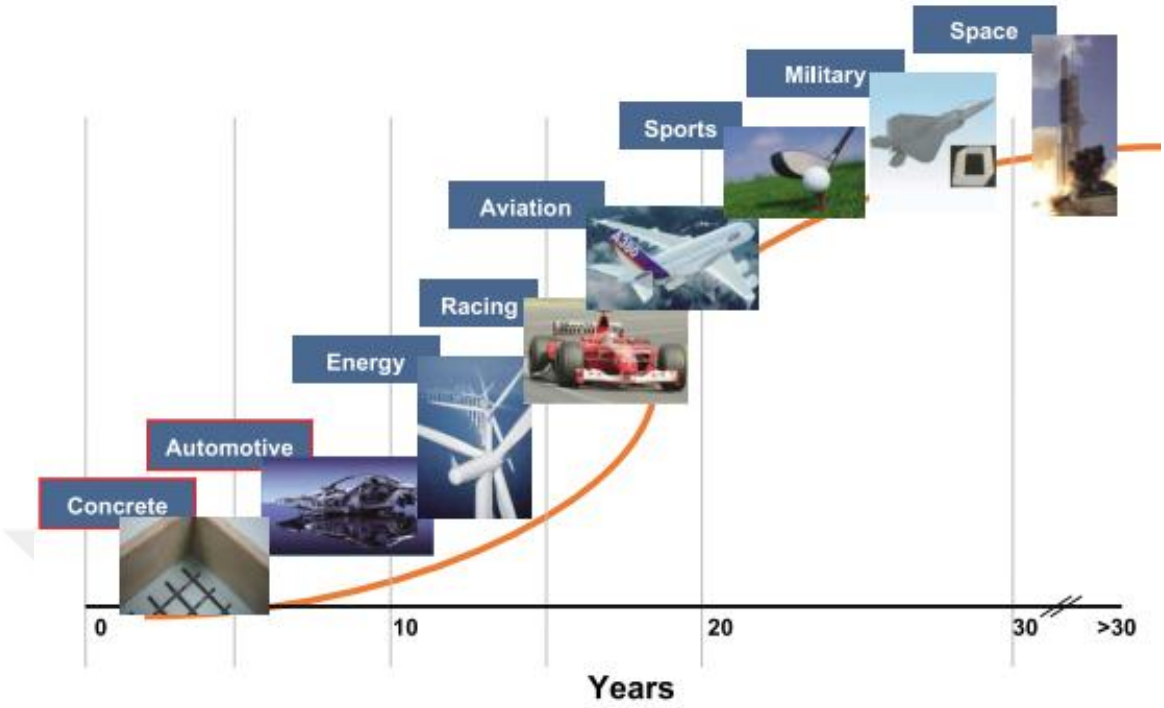

Figure 2.31 Maturity of different markets of carbon fiber [54].

2.10.1 Automotive Application

A significant reduction in automotive pollutant emissions, particularly CO_2, must accompany an increase in the sustainable relief of future vehicle systems. The introduction of competitive and innovative technologies combined with a substantial reduction in moving masses can make a significant contribution to meeting the needs of the future motor vehicle sector. One approach to solving the issue is to develop lightweight design through the implementation of both structural and material lightweight strategies. Hence, in new developments, traditional materials such as steel and lightweight materials such as aluminum and magnesium alloys are employed. In recent times, greater progress has been made on the employment of fiber-reinforced plastics in automobiles [168].

Due to extreme competitiveness, automobile manufacturers in the present time are forced to seek new technologies and innovations in the production of vehicles. Customers now expect automobiles to have all of the amenities they want at a low price. As a result, composite materials are being used to produce auto components, including

the chassis, interiors, hoods, body, and electrical systems. The composite materials have the required characteristics to meet the demands of the automobile industry. As a result, composites are more important in the automotive industry now and will continue to be in the future. The usage of carbon-fiber-reinforced plastics (CFRP) with different thermosets of thermoplastic composites has been made possible by recent advancements in the field of advanced composites in the automobile production sector [169].

Figure 2.32 Automotive parts made from carbon-fiber-reinforced plastic.

CFRP enables a significant decrease in vehicle weight, which improves fuel economy and efficiency while also lowering CO_2 emissions. It has been observed that substituting steel with CFRP reduces vehicle weight by 60%, improves fuel efficiency by 30%, and reduces CO_2 emissions by 20% [170]. In brief, a decrease of 100 kg in vehicle weight is expected to lower fuel consumption by around 0.3-0.4 liters per 100 kilometers. Furthermore, lowering the weight of the vehicle's body structure can result in secondary

weight reductions in other major components like the chassis, brakes, and gears [171]. Additionally, any ‘super cars' capable of exceeding 322 kilometers per hour (kph) and accelerating from 0 to 100 kph in four seconds may be achieved by using CFRP in the framework [170].

Figure 2.33 CNG cylinders manufactured using fiber-reinforced composites [172].

Compressed natural gas (CNG) has become a popular alternative energy source for vehicles and public transport in recent times. CNG decreases CO_2 and nitrogen oxides emissions compared to the employment of carbon fiber-reinforced composites, which has contributed to desirable lightweight alternatives [172].

2.10.2 Aerospace Application

Fiber-reinforced composites were mentioned to employ in aircraft for the very first time, named F-14 for the US Navy and F-15 for the US Air Force around three decades ago, where boron/epoxy skins were used in their empennages [173–175]. As a result of its impressive performance, carbon fiber-reinforced composites were increasingly used in military and transport aircraft. Secondary components, including body panels, side

doors, and control surfaces, were among the first uses of carbon fiber-reinforced composites for aircraft structures. The employment of carbon-fiber-reinforced composites for main components like wings and fuselages expanded with technological advancements [145]. Table 2.4 shows the present aircraft's applications as well as the typical usage of composite materials in each aircraft.

Table 2.4 Application of carbon-fiber-reinforced composites in aerospace [172].

Fighter aircraft	(US) F-14, F-16, F-18, F-22, YF-23, UCAV, JSF (Europe) Rafael, Mirage 2000, Lavi, Typhoon, Gripen JAS-39, Eurofighter DASA Makoc (Russia) MiG-29, Su series
Transport aircraft	(US) C-17, KC-135 (US-Commercial) B-767, B-777, MD-11 (Airbus, European) A-320, A-340, A380, ATR42, Tu-204, A300-600 ST, Falcon 900
General aviation	Premier 1, Starship, Piaggio
Rotary aircraft	Comanche RAH-66, EH101, Eurocopter Tiger, V-22, S-92, Bell/Agusta BA-609, Super Lynx 300

Carbon fiber-reinforced composites are used by the aerospace industry not just to save weight but also for their corrosion and fatigue resistance properties. However, the high cost of these materials in comparison to traditional metals has been a limiting factor in their broad usage. Figure 2.34 demonstrates the growth in the employment of fiber-reinforced composites in fighter jets. The initial proportion by weight of composite materials employed for F-15E was minor, at 2%, but it has since increased to over 25% for the F-22, which is the intended successor for the F-15E. The F-22 has shown the practicality and usefulness of using techniques like resin transfer molding (RTM) to make composite materials more affordable in combat aircraft applications [172].

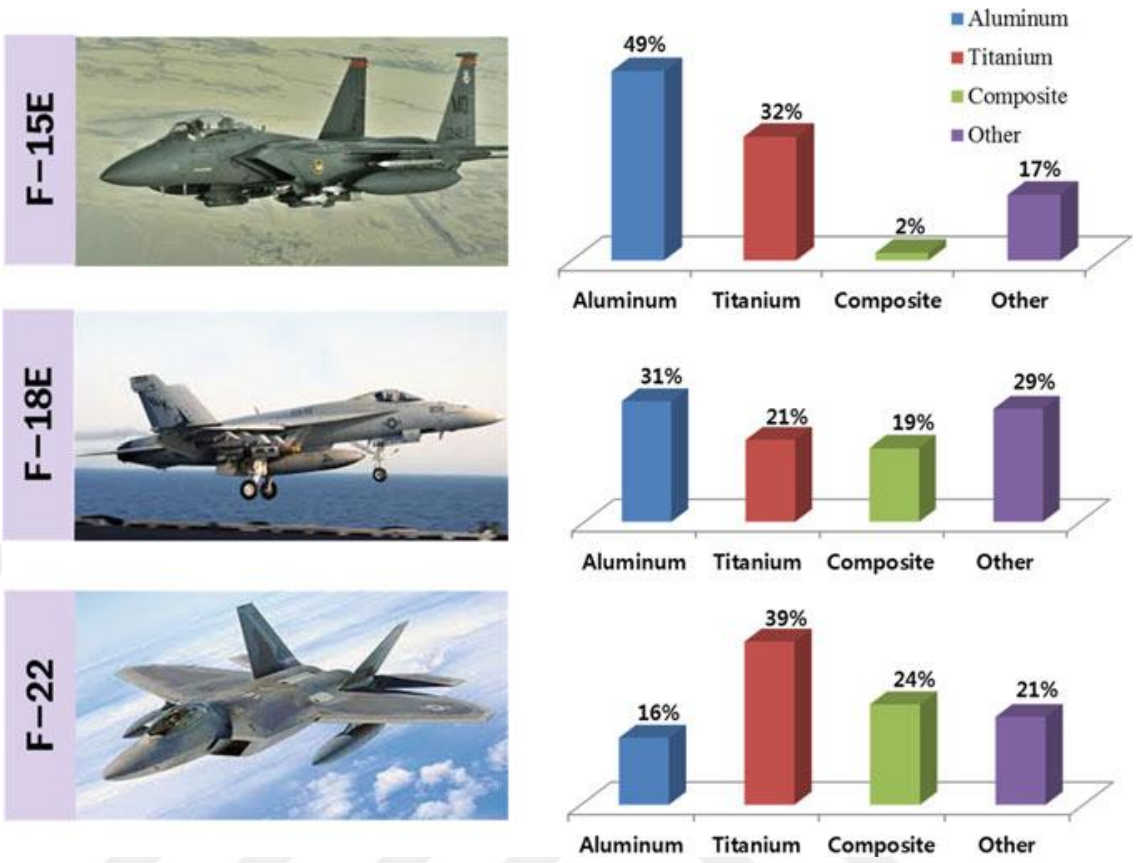

Figure 2.34 Trend of fiber-reinforced composite application in fighter jets [172].

Carbon fiber-reinforced composites account for about 20% of the structural weight in flight crucial components of the US Navy's F/A-18E/F. The necessity to reduce weight while improving strength, efficiency, and maintenance in an aircraft carrier context led the use of composite materials in the F/A-18E/F. The F/A-18E/center F's aft fuselage skins, as well as various auxiliary components like dorsal coverings and speed brakes, are all made of carbon/toughened epoxy. The wing and tail skins are usually made of carbon fibers with enhanced strength and stiffness features, such as Hexcel's IM7. Since composite materials are delicate to impact damage in nature, toughened materials like Fiberite's 977-3 toughened epoxy system, which is utilized in the F/A-18E/F, have effectively handled this issue in combat. The AV-8B's airframe is made up of almost 25% composite materials by weight [176].

The Airbus A300 airplane, which first operated in 1972, was built using advanced composites. Fin leading edges and other glass fiber shielding components were made

with the composite material. After the Airbus A300's in-service assessment in 1979, composite parts such as CFRP spoilers, air brakes, landing-gear doors, rudders were added to the aircraft. The Airbus A310 airplane used composites from 1980 to 1985, and the Airbus A320 aircraft in 1987. Glass fiber frameworks were utilized exclusively on the Airbus A300B2/B4 aircraft. In the Airbus A310-200 airplane, AFRP and CFRP constructions were utilized. The composite structures of the Airbus A320 and Airbus A330/340 airplanes are made of AFRP, CFRP, and GFRP. Since the launch of the Airbus A300, the usage of composites in the Airbus series of airplanes has increased steadily.

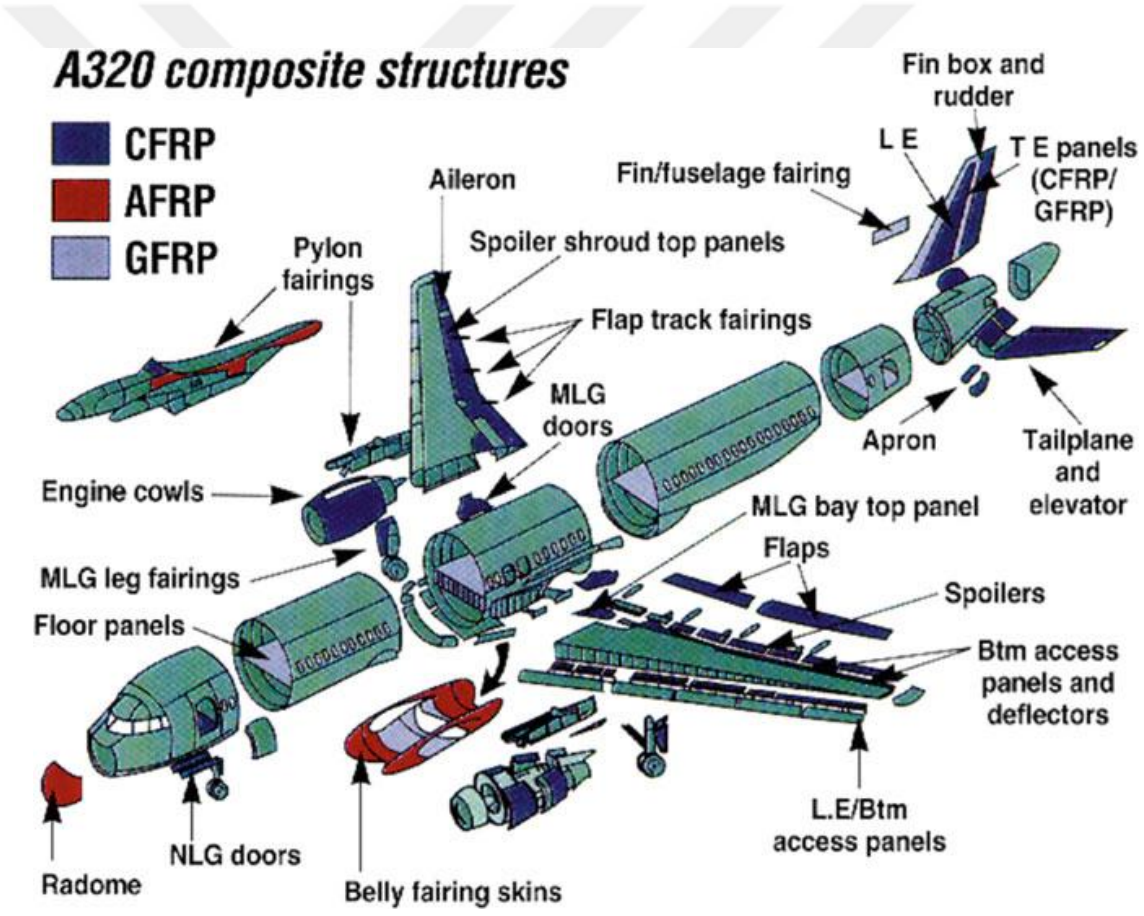

Figure 2.35 Carbon fiber-reinforced composite structures in Airbus A320 [176].

The Airbus A320 airplane's composites make up around 15% of its construction. Despite the fact that the overall weight of composite structures in the Airbus A330/A340 airplane is significantly larger, the proportion of weight in comparison to

the overall weight of the airplane is approximately 12%. Figure 2.35 depicts the usage of composite materials on the Airbus A320 [176]. Modern helicopters, made of about 50% composites by weight, also employ important structural composite components. The formability of composites has been utilized to minimize the number of structural parts and, as a result, costs in helicopter production [177].

2.10.3 Sports Application

For carbon fibers, sports serve as a testing ground. Carbon fibers are increasingly used in sports items with technological advances in both production and application. Carbon fibers have been utilized to manufacture hockey sticks, golf clubs, and bicycle supports over the years. Baseball, softballs, snowboards, tent poles, backpacks, rackets, windsurfing masts, fishing rods, marine hulls, and bats are now available as carbon fiber products [172].

The comparative significance of racket construction's main parts, the shaft, and head-string system, vary with sports. Where the ball motion is greater (tennis), the head-string arrangement is more dominating, and shaft action seems to be essential, as in badminton. The kinetic energy of the ball was absorbed in the racket at impact (zero ball velocity) and distributed in the ratio of 1/10 in both shaft strain energy and head-string energy, according to a high-speed photographic assessment of a ball striking a squash racket. This proportion varies with distinct shafts, reducing with more flexible shafts, but it always showed that the shaft played a lesser role in the energy transfer. The head and shaft of various racket types must be properly fitted. The head frame's main purpose is to produce a solid structural shape that can counteract string strain without causing deformation. Because the stresses would be predominantly compressive, high stiffness and strength will be critical, and therefore, CFRP is expected to be useful in this area, particularly in badminton, where a minimum weight is essential to maintain. The main challenge in fiber design is keeping the strings in place without drilling holes in the CFRP, which may be accomplished in a variety of methods, such as the use of material sandwich structures. Torsion parameters at the shaft-head transition must also be considered [178].

Figure 2.36 Carbon fiber-reinforced plastics in badminton racket making.

The utilization of carbon fibers enhances the overall quality and playing performance significantly in both badminton and tennis rackets. The most recent design improvements in each of these examples have utilized all-metal tubular construction in an effort to achieve a technically efficient design. Modification of wood structures using CFRP in tennis rackets will strengthen and provide lighter designs. Figure 2.37 depicts a tennis racket made of carbon-fiber-reinforced plastic.

Figure 2.37 Application of carbon-fiber-reinforced plastics in tennis racket manufacturing.

In the case of golf shafts, it is commonly recognized that minimum-weight shafts with adequate stiffness, strength, and impact resistance to perform the basic shaft purpose of speeding and placing the club-head are preferred. The large weight savings (50% is easily attainable) are conceivable with CFRP shafts, resulting in a measurable hitting benefit, although the attraction of CFRP as a shaft material is more likely to be in its great design prospects with a relatively modest weight cut.

Figure 2.38 Golf shaft manufactured from carbon-fiber-reinforced plastics.

CFRP shafts of different structures, utilizing both low-modulus and high-modulus carbon fibers, have successfully met these fundamental requirements, resulting in significant weight reduction. The CFRP shafts have fulfilled minimum playing criteria, indicating that CFRP usage is practical and likely to be beneficial. Since particular material formulations may modify the static and vibrational properties of shafts, design refinement is feasible, including exact head-to-shaft alignment and limited variation within sets. For example, the balance of torsional and flexural rigidity is a design parameter [179].

2.10.4 Marine Application

Due to showing high resilience to the maritime environment, carbon fiber-reinforced composites have recently attracted much attention in the marine industry [180]. CFRP

boats were developed as a result of complex configurations together with the features of seamless hulls. For high-performance craft and driver safety, racing powerboats use sophisticated and hybrid composite materials. Composite materials have been used in fishing boats, navy vessels, high-speed boats, barges, sail boats, high-capacity trawlers, and other ship equipment for the last few decades. Carbon fiber-reinforced epoxy was the most popular composite material in the maritime sector. Advanced composite materials in ships have the potential to significantly decrease manufacturing and maintenance expenditures while also improving styling, reducing overall weight, and increasing dependability [181, 182].

Figure 2.39 Carbon-fiber-reinforced plastics in marine applications.

2.10.5 Wind Turbine Blades

The blades of a wind turbine transform the mechanical energy generated by the wind into electric power. They are utilized in the equipment that directs and concentrates energy from the wind into a cable that links the turbine generator to the transmission

line [183]. Energy costs are reliant on modern and cost-effective technologies for fabricating massive structural components like wind blades. The composites are a low-cost option for large-diameter turbines, and they offer the necessary strength and toughness in the frameworks [184].

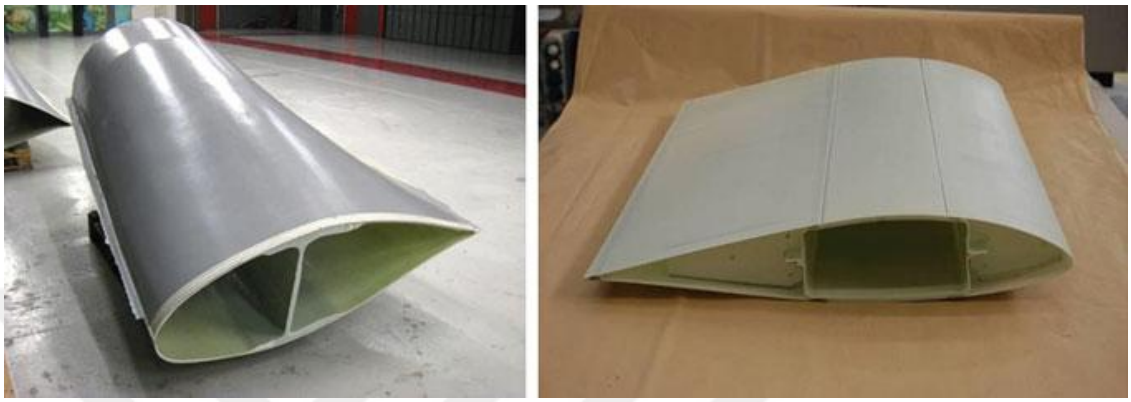

Figure 2.40 Turbine blades made of carbon-fiber-reinforced plastics.

Wind turbine blades should be light, stiff, and fatigue resistant over the course of a minimum 10-year life span. Advanced composite materials are an excellent alternative for such applications. An outer layer reinforced by a primary spar is the standard of a wind turbine blade. E-glass reinforcing fibers bonded in an unsaturated polymer resin matrix were utilized in conventional materials for the spar. As a matrix resin, epoxy provides greater tensile strength and flexural strength, whereas carbon fibers offer a very high stiffness-to-density ratio, enabling lengthier and lightweight turbine blades. Hence, carbon fiber-reinforced composites have been used to produce high-quality wind turbine blades [185].

2.10.6 Construction Application

In the construction sector, reinforcement is one of the most common applications of carbon fibers nowadays. The core principle is to bind textiles or laminates to a structure's external surface to improve strength and stiffness. When the cost of destruction or rebuilding is significantly higher than the cost of repair, this form of exterior strengthening is employed to ensure the safe use of distinctive, costly, and

historically significant structures. Reinforcement of concrete buildings is the most typical application of carbon strips.

Carbon fibers are currently being used in concrete casting; even though this is a relatively new field, it is rapidly growing. In 2003, carbon fibers began to appear in mass-produced cast concrete. Carbon fiber grids are utilized as a mechanical connection between the exterior and interior portions of a concrete wall and as an alternative for woven steel fabric strengthening. The non-corrosive carbon fiber pattern on the exterior of the wall panel allows for the installation of a lower quantity of concrete, reducing the mass and material consumption. Wall panels strengthened with a carbon fiber matrix can be up to 40% lighter than traditional cast panels [186].

The prospect of carbon fiber applications is also mentionable in the construction of bridges. Since 1992, a number of pedestrian bridges have been built mostly from composite materials comprising carbon fibers. The Fredikstat bridge in Norway has a length of 56 meters, the Leida pedestrian bridge in Spain has a length of 38 meters, and the Fiberline bridge in Denmark has a length of 40 meters [186]. The primary reason for using plastic reinforced materials featuring carbon fibers was to minimize the weight and expenditure of bridge-opening equipment.

Figure 2.41 Fredikstat Balance Bridge for pedestrians, Norway [186]

CHAPTER 3
MATERIALS AND METHODS

3.1 Materials

3.1.1 Polyacrylonitrile (PAN) Multifilament

PAN is an influential engineering polymer with great commercial significance because of its exclusive thermal characteristics and high solvent resistance [187]. It is a multipurpose polymeric material utilized in a variety of applications, including household textiles (wall hangings, carpeting, furniture coverings, textile wall covering, drapery materials, etc.), water treatment filters, and most importantly, carbon fiber manufacturing [188].

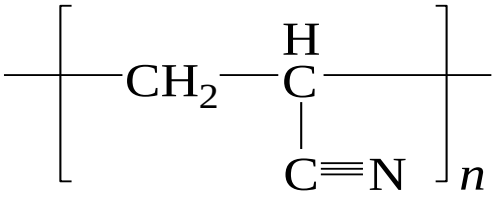

Figure 3.1 Chemical structure of PAN multifilament.

PAN is the preferred precursor used for the production of carbon fibers, dominating the market with a share of approximately 90%. It provides fibers with exceptional mechanical properties and high production yields [19].

Figure 3.2 The PAN multifilament package used in this study.

PAN fibers employed as carbon fiber precursors are composed of copolymers having more than 90% acrylonitrile. Genuine PAN has a melting temperature of 326 °C or marginally lesser, however copolymer PAN has melting temperatures that are relatively low [189]. PAN fiber can be stabilized easily due to its higher melting point. The PAN multifilament employed in this research has a linear density of 539 denier per 180 filaments, with 3 dpf each.

3.1.2 Polyamide 66 (PA66) Multifilament

Polyamide 66 (PA66) or Nylon 66 is one of the most crucial engineering thermoplastics and a fiber-forming semicrystalline polymer. Melting point of polyamide 66 is 255 °C. Due to its outstanding qualities such as chemical resistance, high tensile strength, wear, and abrasion resistance, PA66 is extensively utilized in various applications, including airbags, conveyer belts, tire cords, rope, bearing, gear, and so on.

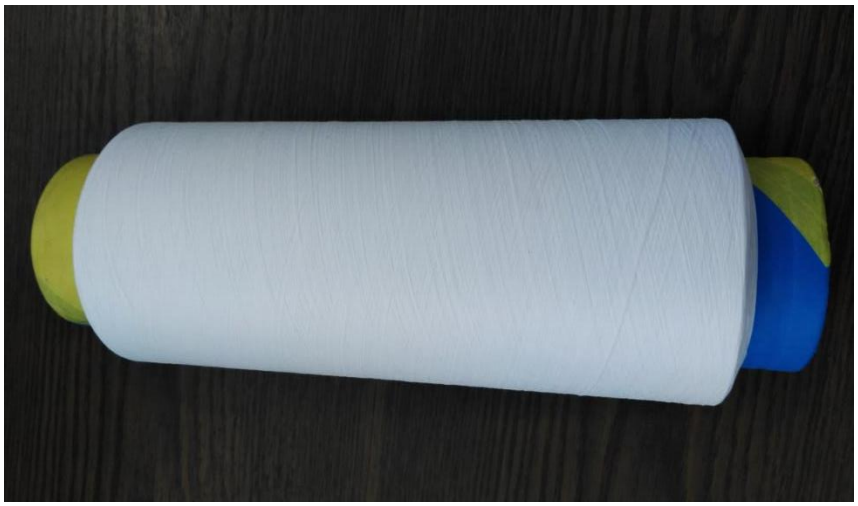

Figure 3.3 The polyamide 66 multifilament package used in this study.

PA66 is synthesized by polycondensation reaction of hexamethylenediamine and adipic acid (two monomers, each containing six carbon atoms) [190]. PA66 fibers are generally produced by the melt spinning process.

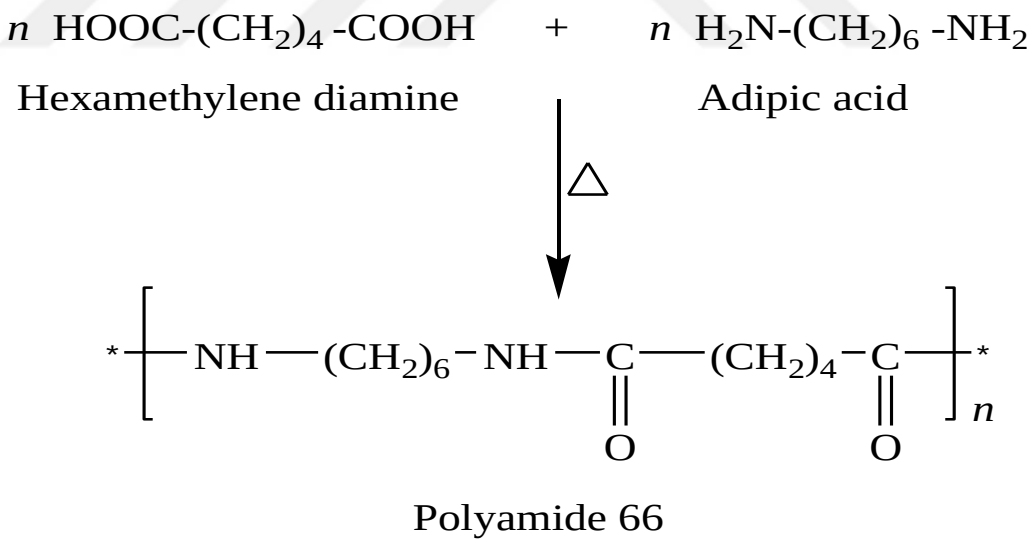

Figure 3.4 Polycondensation reaction in forming polyamide 66.

Polyamide 66 multifilament with a linear density of 16.28 tex per 69 filaments, produced for textile applications, was utilized during the course of this study. The PA66 single filament cross-sectional shape is circular, as confirmed by the yarn manufacturer (POLYTEKS AŞ, Turkey).

3.1.3 Jute Fiber

Jute fiber is one of the most common natural biodegradable vegetable fibers, obtained from the stems of *Corchorus capsularis* L. and *Corchorus olitorius* L., and occupies the second position by means of total cellulosic fibers production [191, 192]. Jute fiber is predominantly cultivated in Bangladesh, China, India, Thailand, and Nepal. These countries generate nearly all of the world's jute fibers together, accounting for over 95% of total production [193].

Figure 3.5 The jute yarn package used in this study.

Jute is a multicellular and multiconstituent fiber, which is composed of cellulose (59-63%), hemicellulose (21-23%), lignin (13-14%), fats and waxes (1.92%), protein (2%), and water solubles (1.88%) [191, 194, 195]. Cellulose is considered to be the major portion of jute molecular structure, and it provides strength, stiffness, and structural stability properties. The cellulose structure consists of crystalline and amorphous phases. In the case of hemicellulose and lignin, the molecular structures are completely amorphous in character [196]. Crystalline regions of cellulose structure are characterized by strong hydrogen-bonded OH-groups. Strong hydrogen bonding prevents the accessibility of chemical compounds into the crystalline regions. In the

case of amorphous cellulose structure, the hydroxyl functional groups are relatively free to be attached to the jute fiber structure. These OH groups are easy to react with other chamicals. The presence of OH-groups in the amorphous regions of cellulose, hemicellulose and lignin find themselves in a more favourable position to react with water molecules and facilitate the access of water to penetrate the fiber surface. This makes the jute fiber strongly hydrophilic in nature.

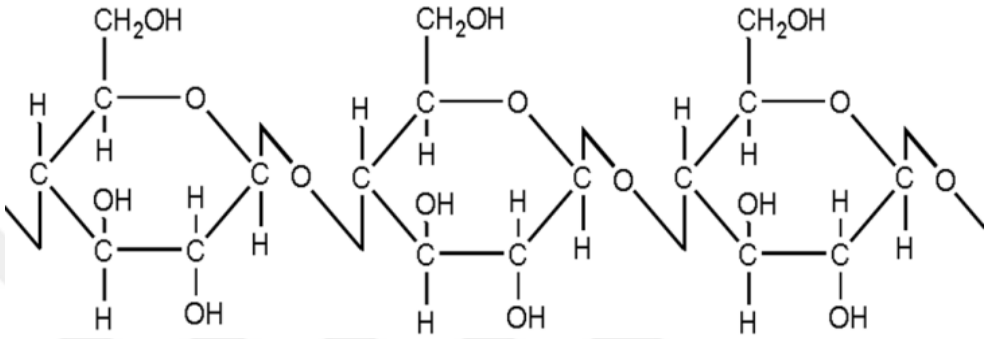

Figure 3.6 Structure of cellulose.

Jute fiber contains comparatively higher lignin and cellulose contents, both of them are essential elements for activated carbon fiber manufacturing [90, 195]. Lignin contains a high amount of carbon content approximately (60−65%), indicates greater yield after activated carbon fibers manufacturing, offering it a potential substitute for petroleum-based polyacrylonitrile precursor [197].

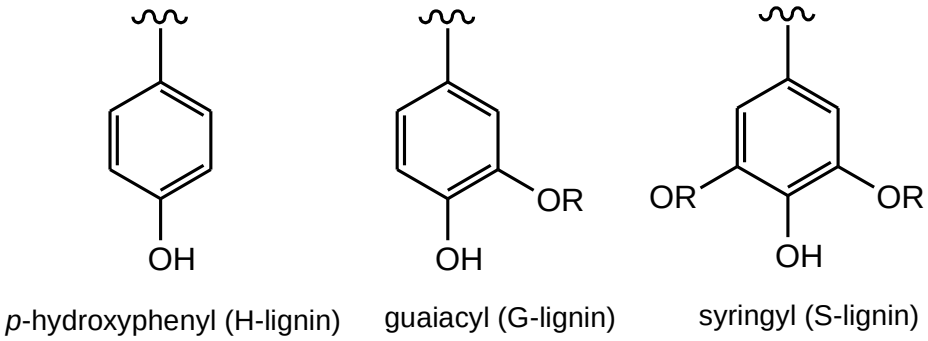

Figure 3.7 Structural units of lignin [198, 199].

Jute yarns were employed as the precursor of activated carbon fiber in this study, brought from the Bangladesh Jute Research Institute (BJRI). The yarn has a linear density of 332.28 tex, and the average fiber length was 65 to 75 mm. The chemicals including sodium hydroxide (NaOH), sodium metasilicate pentahydrate, and urea

employed in this study were analytical-grade manufactured and supplied by TEKKIM chemical industries limited, Turkey.

3.1.4 Bamboo Fiber

Bamboo is a non-wood forest resource as well as a naturally occurring composite material found in most tropical nations. Because of its numerous benefits like biodegradability, regeneration, low cost, and plentiful use, bamboo is now being used as a type of swiftly growing and fast harvested vegetable product [200]. Bamboo fibers have long attracted the attention of scientists and researchers to be used as reinforcing materials in composites, not just confined in conventional sectors such as pulp, constructions, and artworks [201, 202]. Viscous fibers made of bamboo pulp have been produced for industrial uses in certain Asian nations, like China and Japan. Furthermore, the synthesis of textile fibers from bamboo pulp has emerged as a new research area.

Figure 3.8 The bamboo yarn package used in this study.

The three primary chemical components of bamboo are cellulose (60-70%), hemicelluloses (14-25%), and lignin (20-30%), which are intimately linked in a complex structure [203]. These components account for around 90% of the overall bamboo content. Protein, pectin, pigments, fat, resin, tannins, inorganic salts, waxes, and ash are minor components. These components are present in the cell cavity or

specific organelles of bamboo and keep a crucial role in its physiological function [204]. Bamboo fibers are a type of ecologically friendly regenerated fiber made from bamboo, which is recyclable, fast-growing, biodegradable, and does not take up additional farmland. Moreover, especially in hilly locations, the exploitation of plentiful bamboo resources can provide a considerable economic advantage. Bamboo fiber may compensate for the shortage of natural textile fibers and may partially replace the requirement for synthetic fibers.

3.1.5 Flax Fiber

Flax fiber (*Linum usitatissimum L.*) is one of the strongest natural bast fibers that contain cellulose (70.5%), hemicellulose (16.5%), lignin (2.5%), and pectin (0.9%). The structure of flax fibers is highly complex, and it could be compared with a composite structure. Flax fibers are made up of a number of polyhedron-shaped primary fibers that are overlapped across a wide area and kept together by an interphase made up mostly of pectin and hemicellulose. Every fundamental fiber has a very thin primary cell wall, a secondary cell wall (which dominates the cross-section), and a lumen, which is an open channel in the fiber core.

Figure 3.9 The flax yarn package used in this study.

Because of having some attractive features like biodegradability, low cost, easy availability, convenient chemical and mechanical modification, renewable nature, and

improved performance, flax fiber is now broadly used in textiles and technical applications, including insulating material, composites, specialty papers, and so on [205, 206]. Fiber eco-friendly extraction processes such as retting, scouring, and bleaching were emphasized in textiles to enhance fiber diversity in color, fineness, and strength within the same variant.

3.2 Methods

3.2.1 Chemical Pretreatment and Thermal Stabilization

3.2.1.1 PAN Multifilament: Aqueous Solution of 15% Ammonium Persulfate

Ammonium persulfate [$(NH_4)_2S_2O_8$] was utilized for pretreatment under aqueous conditions before the stabilization step of PAN precursor fiber. Once followed by the optimum experimental conditions, ammonium persulfate has the ability to speed up the stabilizing process of PAN fiber. Ammonium persulfate is thought to demonstrate this acceleration potential in thermal stabilization due to the existence of free radical ions SO_4^- and H_2O_2 [207, 208].

The spin-finish oil was removed from the original PAN fiber by soaking it in a solution of isopropyl alcohol and perchloroethylene for 60 minutes at room temperature. To complete the surface cleaning process, the PAN sample was rinsed under running water for around 30 minutes before being air-dried.

Figure 3.10 PAN samples for chemical impregnation.

Chemical impregnation of the PAN multifilaments was accomplished by dipping the samples in a 15 percent aqueous $(NH_4)_2S_2O_8$ solution for 24 hours at room temperature. The pH of the solution was 2.5 at 20 °C. On a dry basis, the pretreated PAN comprised 10.68 percent (w/w) $(NH_4)_2S_2O_8$. The specimens were exposed to a multi-step stabilization procedure after being cleaned of surface contaminants and chemically impregnated. In an air circulation oven, the thermal stabilization procedure was carried out. The $(NH_4)_2S_2O_8$ pretreated yarns were wrapped onto rectangular-shaped stainless steel frames to limit the length of the samples and maintain physical shrinkage and molecular orientation [209, 210]. During the heating trials, the temperature rising rate was controlled at 2 °C/min to approach 200 °C from room temperature, after which 1 °C/min in each step to approach 250 °C, with the cooling rate set at 2 °C/min. The stabilization periods used in the thermal studies were 5 minutes, 15 minutes, 30 minutes, 45 minutes, and 60 minutes. Figure 3.11 shows a multi-step stabilization strategy used to stabilize the $(NH_4)_2S_2O_8$ pretreated PAN sample in the air environment.

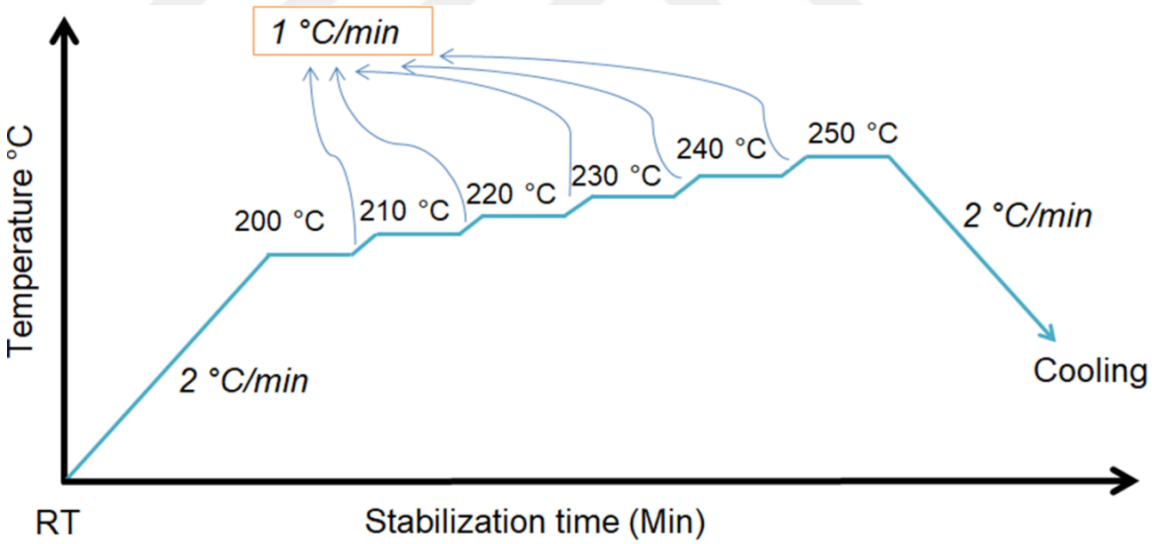

Figure 3.11 A multi-step stabilization approach was employed in this study. Stabilization times of 5, 15, 30, 45, and 60 minutes were utilized separately in every stage at temperatures between 200 and 250 °C.

3.2.1.2 PA66 Multifilament: Ethanol Solution of 3% Phosphoric Acid, 3% Boric Acid, and 3% Urea

The original polyamide 66 yarn was pretreated by a 10% (v/v) ethanol-water solution at 50 °C for 50 min to get rid of the surface impurities of the fibers. Following the removal of surface impurities, the sample was left to dry overnight at 25 °C, and afterward, dried again in an air oven at 80 °C for 4 hours until constant weight.

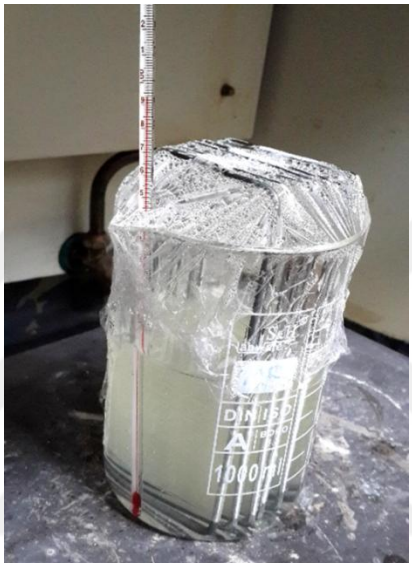

Figure 3.12 Chemical pretreatment of the precursor fibers.

Chemical incorporation was executed by soaking the PA66 yarn in a solution of 3% phosphoric acid, 3% boric acid, and 3% urea with ethanol at 25 °C for 24 hours. The chemical solution displayed a pH value of 2.46 at 19.3 °C. Following the chemical pretreatment, the samples were removed from the bath and dehydrated at 80 °C for 4 hours. The impregnated PA66 yarn was loaded with 8.1% (w/w) PBU on a dry basis. The TOS process was then executed in an air atmosphere at 245 °C for 30, 60, 90, 120, and 150 min stabilization times separately, while the temperature was raised from room temperature to 170 °C following a 1 °C/min rate and then without waiting, the temperature reached to 245 °C at a 0.3 °C/min rate.

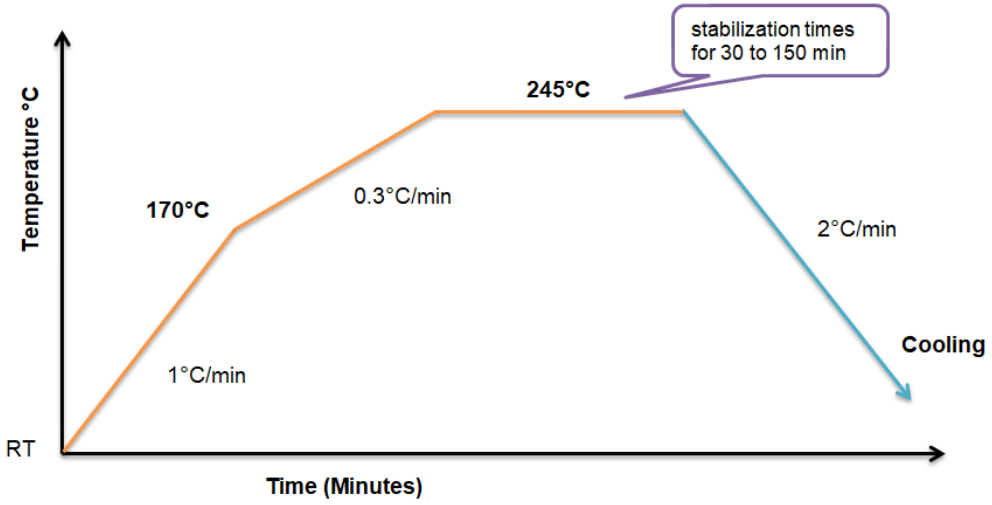

Figure 3.13 A two-step thermal stabilization approach applied for PA66 multifilaments in achieving thermal stability.

3.2.1.3 Jute Fiber: Aqueous Solution of 5% Sodium Metasilicate Pentahydrate and 6% Urea

The original jute yarns were mercerized by 18% NaOH-water solution for 60 min at room temperature to get rid of the surface impurities of the fibers. Following the removal of surface impurities, the sample was left to dry overnight at 25 °C and afterward dried again at 80 °C for 4 hours in the air.

Figure 3.14 Chemical impregnated jute fiber samples.

Chemical incorporation was executed by soaking the jute yarns in a water solution of 5% sodium metasilicate pentahydrate ($Na_2SiO_3.5H_2O$) and 6% urea (NH_2-CO-NH_2) at 90 °C for 60 min employing 1 °C/min heating rate. The chemical solution had a pH value of 12.39 at 20.17 °C. After the chemical impregnation, the jute samples were dehydrated at 80 °C for 4 hours. A multistep oxidation process was executed in the air at different temperatures including 150, 175, 200, 225, and 245 °C for different oxidation periods between 25 and 125 min separately, employing a common heating rate of 2 °C/min rate. Stainless steel frames were utilized to wrap the jute samples to obtain even chemical integration with the fibers and to avoid any physical shrinkage or molecular orientation loss.

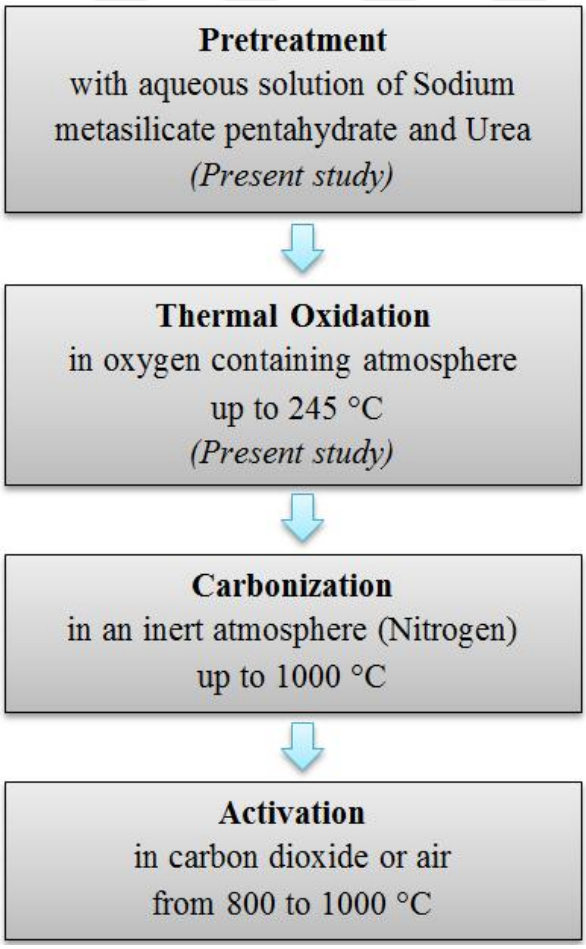

Figure 3.15 Production flow chart of jute-based activated carbon fiber.

3.2.1.4 Bamboo Fiber: Aqueous Solution of 3% DAP, 0.5% Sodium Metasilicate, and 3% Urea

To remove surface contaminants from the bamboo yarn, it was processed with an aqueous solution of 10% isopropyl alcohol at 40 °C for 60 minutes. After removing surface contaminants, the sample was allowed to dry at room temperature for 12 hours before being dried again in an air circulating oven at 70 °C for 2 hours.

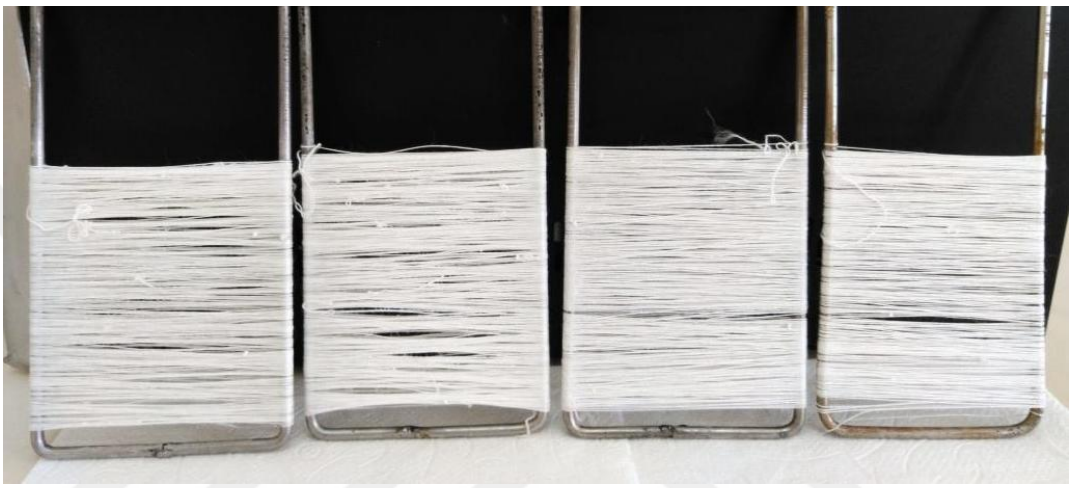

Figure 3.16 Chemical impregnated bamboo fiber samples.

The bamboo yarn samples were treated in an aqueous solution of 3% di-ammonium phosphate or DAP ($(NH_4)_2HPO_4$), 0.5% sodium metasilicate (Na_2SiO_3), and 3% urea (NH_2-CO-NH_2) for 24 hours at 25 °C. The solution had a pH value of 8.28 at 25.3 °C. The samples were taken from the bath after chemical pretreatment and dehydrated for 5 hours at 80 °C. On a dry basis, the impregnated bamboo yarn contained 4.2% (w/w) DAP-SMSU. The thermal oxidative stabilization step was then carried out in an air environment up to 245 °C, using a multistep strategy for stabilization periods of 40, 60, 80, 100, and 120 minutes. The multistep oxidation process includes rising temperature from room temperature to 155 °C, then 170 °C, 185 °C, 200 °C, 215 °C, 230 °C, and 245 °C for variable oxidation durations.

3.2.1.5 Flax Fiber: Aqueous Solution of 3% DAP, 3% Boric Acid, and 3% Urea

To remove surface contaminants from the fibers, the raw flax yarns were mercerized for 60 minutes at room temperature in an 18% NaOH aqueous solution. After removing surface contaminants, the sample was dried in the air for 4 hours at 80 °C after being allowed to dry overnight at 25 °C.

Figure 3.17 Chemical impregnated flax fiber samples.

The flax yarns were pretreated in a water solution of 3% di-ammonium phosphate or DAP ($(NH_4)_2HPO_4$), 3% boric acid (H_3BO_3), and 3% urea (NH_2-CO-NH_2) for 12 hours at room temperature. The pH value of the solution was 7.05 at 26.1°C. The flax specimens were dried at 70 °C for 5 hours after performing chemical integration. For the oxidation process, a multistep approach was utilized at temperatures 160, 180, 200, 220, and 245 °C. Oxidation durations were 25, 50, 75, 100, and 125 minutes, which were employed in different stabilization stages individually.

3.2.2 Thermal and Structural Characterization

3.2.2.1 Differential Scanning Calorimetry (DSC)

A Perkin Elmer Diamond DSC apparatus was used to conduct differential scanning calorimetry (DSC) measurements. The sample weights utilized were typically about 5 mg. A heating rate of 10 °C/min was specified, with a maximum temperature range of

450 °C. For heat flow assessment, indium (m.p. 156.6 °C and ΔH = 28.45 J/g) was employed. Temperature calibration was performed with indium and zinc (m.p. 419.51 °C) standards. The samples were examined at a flow rate of 50 mL/min of nitrogen.

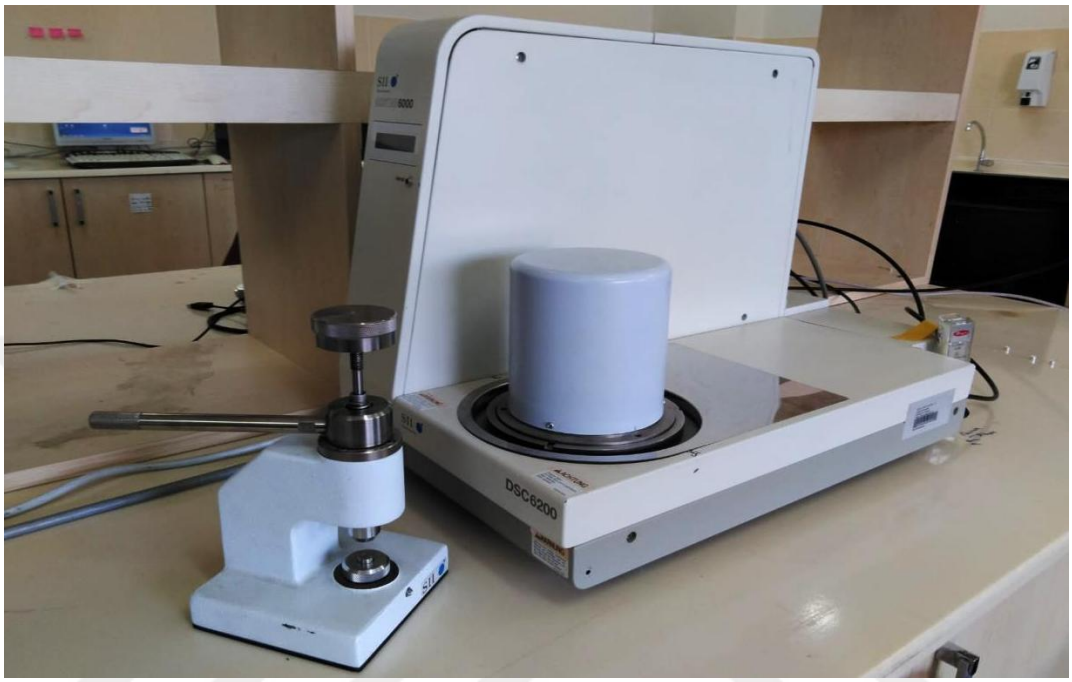

Figure 3.18 The differential scanning calorimeter used in this study.

3.2.2.2 Thermogravimetric Analysis (TGA)

The TGA thermograms of the untreated and stabilized samples were gathered employing a Perkin Elmer thermogravimetric analyzer. The heating rate in the TGA measurements was 10 °C/min, with the highest temperature of 1000 °C and a sample weight of 5-6 mg. The temperature adjustment of TGA was accomplished using the melting point standards of gold (1064.3 °C), tin (231.7 °C), indium (156.8 °C), and aluminum (660.1 °C). Throughout the trials, a constant flow of nitrogen gas (200 ml/min) was maintained. Carbon yield (%) and weight loss (%) for the pristine and thermally stabilized samples was determined using the TGA data set.

Figure 3.19 The thermogravimetric analyzer (TGA) used in this study.

3.2.2.3 Fourier Transform Infrared (FT-IR) Spectroscopy

Infrared analysis was carried out in absorbance mode using a Perkin Elmer® FT-IR spectrometer. The average value was calculated of 50 interferograms by employing a Norton-Beer apodization algorithm. Every single sample spectrum was ratioed by retaining unchanging device modifications in comparison to a conforming number of background scans. Lastly, all of the bands were investigated, where applicable, utilizing curve-fitting techniques and the SPECTRUM software [211, 212].

Figure 3.20 The Fourier transform infrared (FTIR) spectroscopy used in this study.

3.2.2.4 X-Ray Diffractometer (XRD)

To get wide-angle X-ray diffraction profiles, a Bruker® AXS D8 X-ray diffractometer employing nickel filtered CuK_{α} radiation (λ= 0.15406 nm) was employed [209, 213, 214]. The X-ray diffraction profiles of the original and oxidized samples were achieved in the 10-40º 2θ scattering range, respectively. In addition, Lorentz and polarization corrections were executed for the obtained X-ray diffraction profiles [215].

Figure 3.21 The X-ray diffractometer (XRD) used in this study.

3.2.2.5 Elemental Analysis

Elemental analysis was performed utilizing a LECO®TruSpec Micro Elemental Analyzer. A high-temperature combustion process was employed for the thermally stabilized samples to obtain the elemental percentage in the samples. The overall combustion process was performed in an oxygen-rich environment.

3.2.2.6 Scanning Electron Microscope (SEM)

The surface morphology of the samples was examined using a LEO 440 Scanning Electron Microscope. The spacing between the specimens and the detector was maintained between 8 and 12 mm, and a 10 kV working voltage was employed for most specimens. A gold coating was added to the surface of the samples to prevent electrostatic charging and enhance conductivity.

Figure 3.22 The scanning electron microscope (SEM) used in this study.

3.2.3 Physical and Mechanical Characterization

3.2.3.1 Optical Microscopy

For the measurement of fiber thickness of the samples, a polarizing microscope (Nikon ME600L, Japan) comprising a calibrated eyepiece was employed. An average of twenty thickness measurements from randomly chosen five fiber samples were taken for each sample type.

Figure 3.23 The optical microscope used in this study.

3.2.3.2 Volume Density Measurement

The volume density of the samples was determined by utilizing solutions of variable densities prepared by using isopropyl alcohol (ρ = 0.79 g/cm^3**)** and perchloroethylene (ρ = 1.612 g/cm^3). The amount of the ingredients were added to prepare the solution of predefined density according to the following formula:

$$\rho = \frac{\rho_1 v_1 + \rho_2 v_2}{v_1 + v_2}$$

The solution tubes were then kept in a centrifugal machine with the required density marking for a minimum of 30 minutes at 3000-3500 rpm to make the solutions fully uniform for using in density measurement.

Figure 3.24 The centrifugal machine used for control solution preparation in volume density measurement.

The measurement of densities of the original and thermally stabilized samples was performed by immersing the samples in the prepared solutions of variable densities. The samples were kept in the solution tubes for 24 hours for taking a stable position. Once a

sample takes its position in the middle of the solution, then the solution density also indicates the density of the sample.

Figure 3.25 Volume density measurement of the specimens.

3.2.3.3 Linear Density Measurement

The value of linear density was evaluated by taking the weight of the samples in grams per unit length. In this work, the unit "tex" is considered for linear density measurement, which can be expressed by the ratio of the weight of yarn (in gm) per 1000 meters [216–218]. The linear density values were evaluated by taking the mean value of five measurements. From the linear density values, stabilization yield was also assessed, which is the ratio of linear densities of pristine to thermally stabilized samples.

3.2.3.4 Flame Test

Thermally stabilized samples were tested with a match flame to see the flame resistance property of the samples for different stabilization periods. Once the samples show the non-burning property, it is assumed that the samples are completely stabilized. The observed findings were labeled pass or fail based on the samples' burning behavior in an ordinary match flame.

3.2.3.5 Tensile Properties Testing

The tensile strength values of the pristine and thermally stabilized samples were obtained by employing a PROWHITE tensile strength tester at room temperature. These values were collected in N/tex unit by utilizing 20 mm gauge lengths and 5 mm/min speed [213, 219].

Figure 3.26 The tensile strength tester used in this study.

The tensile strength of the sample was measured at the breaking point, and the average results were taken for 20 breaks for each instance. Afterward, by multiplying the individual volume densities (g/cm^3) and 1000 with the originally obtained N/Tex values, the tensile strength values of the jute yarns were obtained in MPa unit [220]. The initial slope of the tensile strength curve was used to determine tensile modulus values in GPa.

3.2.4 Data Analysis

3.2.4.1 X-ray Data Curve-Fitting

All traces of X-ray diffraction for the pristine and stabilized samples were fitted using the curve-fitting approach described by Hindeleh et al. [221] for the separation of

overlapping peaks. The Gaussian and Cauchy functions are both assumed to be present in each profile. When the patterns of experimental and estimated intensity accumulate in the most suitable parameters, computer programming offers some specific values for peaks as peak location (2θ), profile function (f), peak height in electron unit, and peak width at half height.

3.2.4.2 Assessment of IR-Conversion Index

To assess the overall amount of cross-linked ladder polymer in the stabilized sample in the oxidation step, the IR-conversion index is commonly employed, and was evaluated by Equation (1) [222].

$$IR\ -\ Conversion\ Index\ (\%)\ = \frac{I_0}{I_0 + I_N} \times\ 100\% \tag{1}$$

where I_o is conjugated spectrum intensity at about 1590 cm^{-1}, and I_N is nitrile spectrum intensity at about 2242 cm^{-1}, each above the baseline.

3.2.4.3 Assessment of X-ray Stabilization Index

To calculate the X-ray stabilization index, Equation (2) [223] was utilized in this study.

$$X-ray\ stabilization\ index\ (\%)\ = \frac{I_0 - I}{I_0} \times\ 100\% \tag{2}$$

where I_o is the (100) reflection intensity at 2θ = 17° of the raw sample, while I is the (100) reflection intensity at 2θ = 17° of the stabilized sample. The intensity values were collected by applying the curve-fitting procedure.

3.2.4.4 Assessment of Apparent X-ray Crystallinity

The proportion of integrated intensity under the resolved peaks to the integrated intensity of the cumulative scatter under the observational trace is regarded as apparent

X-ray crystallinity (χ_c) [224]. In most cases, it is expressed as in Equation (3). The assessment was carried out in the 2θ range, between 5º and 35º.

$$\chi_c = \frac{\int_0^{\infty} I_{cr}(2\theta)\, d(2\theta)}{\int_0^{\infty} I_{tot}(2\theta)\, d(2\theta)} \tag{3}$$

3.2.4.5 Assessment of Apparent Lateral Crystallite Size

The peak widths at half height were adjusted using Stoke's deconvolution technique [225]. The apparent lateral crystallite size was calculated using Scherrer Equation (4) for the specific reflection of oxidized samples.

$$L_{(hkl)} = \frac{K.\lambda}{\beta.\cos(\theta)} \tag{4}$$

where $L_{(hkl)}$ is the average crystallite length perpendicular to the hkl planes, λ is the radiation wavelength (λ = 0.154 nm), K is a Scherrer parameter, β is breadth at half-maximum intensity, and θ is the Bragg's angle for the reflection concerned.

CHAPTER 4
RESULTS AND DISCUSSION

4.1 Polyacrylonitrile (PAN) Multifilament

4.1.1 Characterization of Original PAN Multifilament

The PAN multifilament employed in this study had a linear density of 59.95 tex. The total number of filaments in the yarn was 180, each of them having 19.68±0.46 μm in diameter. The volume density of the PAN filament sample was 1.179 g/cm^3. Tensile properties of the PAN sample were measured by means of tensile strength (273.49±27.63 MPa), tensile modulus (12.99±2.19 GPa), and extension at break percentage (9.08±2.43).

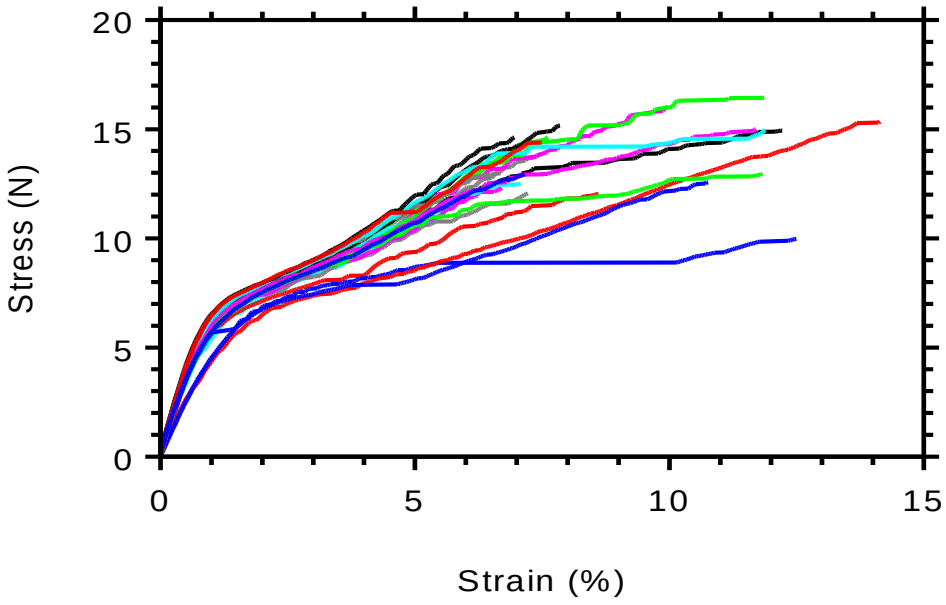

Figure 4.1 Stress-strain curve of original PAN multifilament.

4.1.2 Physical and Mechanical Characterization of Original and Thermally Stabilized PAN Filament Impregnated with 15% APS

Thermal stabilization is an essential step in the carbon fiber production process that takes place in an air environment and allows the precursor fiber to tolerate a high temperature in the carbonization phase. Due to the chemical reactions throughout the TOS process, various structural changes occur in the pendant nitrile (C≡N) groups in the polymer structure, and a ladder-like structure develops. Dehydrogenation also happens during the further transformation process, which results in conjugated structures with C=C when the carboxylic acid groups from a vinyl acetate comonomer are removed. A carbon atom from a nitrile group bonds with a nitrogen atom from a nearby nitrile group in the polymer chain. It undergoes a nitrilo (C=N) conjugation, resulting in the formation of a six-membered ring. A heterocyclic structure is usually produced by structural transformations. Carbonyl (C=O), C=C double bonds, nitrilo (C=N) groups, and the additional –C–H groups make up this structure. Combinedly, the oxidation and dehydrogenation processes result in conjugated double bonds with a cross-linked structure.

The thermal stabilization phase for ammonium persulfate treated PAN samples was carried out in a circulating air environment. This phase was accomplished using a multi-step annealing strategy up to 250 °C for various treatment durations ranging from 5 to 60 minutes. During the thermal stabilization process, the color of the precursor fiber changes from white to shades of brown and dark brown in the early stages to a blackish and black color in the latter stages. The thermally stabilized PAN filament is considered to have a strongly cross-linked aromatized structure, as indicated by the change in color. Changing into dark colors in the advanced phases authenticates the PAN filament's thermally stable structure.

The ammonium persulfate treated PAN specimens passed the crucial flame test by demonstrating non-burning characteristics when put in an ordinary match flame after 45 minutes of the multi-step stabilization process. As a result, under the multi-step method, the specimen with a 45 minutes stabilization period is predicted to be fully stabilized to withstand high carbonization temperatures. During thermal stabilization, the external surface of the precursor fiber is subjected to a rapid oxidation process, which inhibits

elemental oxygen diffusion into the inner region. As a result, certain differences arise between the outer and inner regions of stabilized fibers, leading to color variations. To achieve an adequately stable structure, both the outer and inner portions of the sample must undergo a comparable degree of thermal stabilization. The variance of the outer-inner zone may be avoided by picking compatible precursor characteristics, such as cross-sectional shape and fiber diameter [226], and ensuring proper temperature [227] and timing throughout the stabilization process [228, 229]. It has been documented that when the stabilization temperature and duration increase, the outer-inner zone heterogeneity gradually disappears [230]. The color variations across the cross-section of the PAN specimen are caused by inner-outer zone heterogeneity. The dark color in the external surface is due to the proper stabilization and accumulation of oxygen-based functional groups on the polymer chain backbone, such as carbonyl, hydroxyl, and carboxylic groups. However, the light color of the inner region of the precursor fiber may not endure higher temperatures in the carbonization stage due to insufficient stabilization [231].

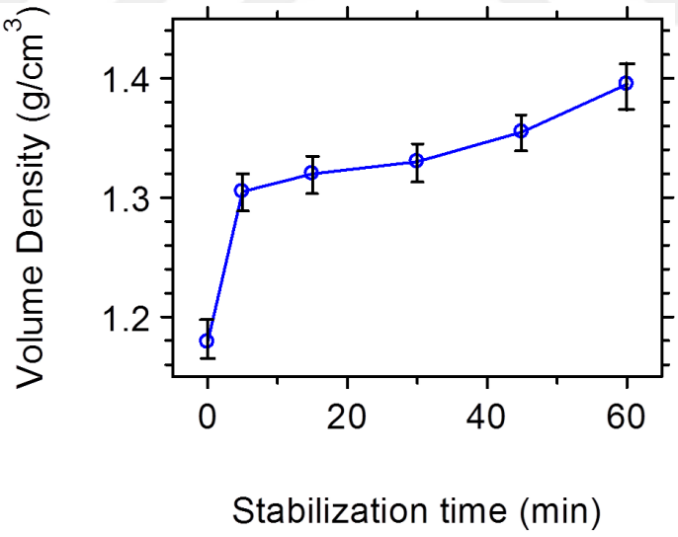

Figure 4.2 Volume density of untreated and stabilized PAN multifilaments.

Figure 4.2 presents the volume density results of the untreated and stabilized PAN samples integrated with 15% APS aqueous solution. The volume density increased continuously from 5 to 60 minutes. For the raw PAN sample, the volume density was 1.179 g/cm^3 and reached 1.395 g/cm^3 for the thermally stable PAN. The development of a ladder-like structure in the polymer was associated with the growth in volume

densities, which were incorporated by the close packing of the polymer chains due to the cyclization of the nitrile groups [121].

The current investigation shows a continuous increase in volume density values with the increase in stabilization duration. The increasing density values of elevated stabilization temperatures were reported by Takaku et al. [232]. They demonstrated that a lower stabilization period is enough at high temperatures to attain a given volume density. They further showed that the precursor fiber attained a constant density of 1.58 g/cm^3 over the prolonged stabilization time, regardless of the stabilizing temperature.

Results published in the literature show that the rise in the volume density of stabilized fiber reduces the carbon fiber's volume density value [232]. This reveals the considerable number of micro-level voids formations in the carbon fibers. These formations are acquired from high-density, thermally stabilized fibers. It also indicates that heat stabilized fibers with an optimal density must achieve desired carbon fiber tensile characteristics. The volume density of the stabilized fibers should need to be within 1.34 to 1.39 g/cm^3 and the oxygen concentration between 5 and 9% for manufacturing high-strength carbon fiber [232]. The increasing volume density values facilitate the growth of significant cross-linkage in stabilized fiber, which causes lateral compaction in the entire fiber structure.

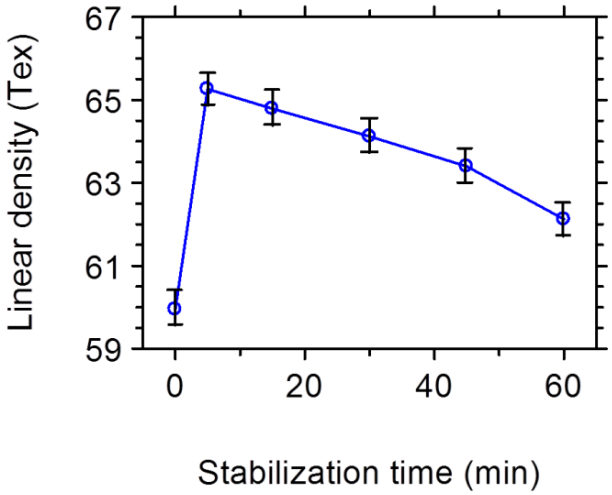

Figure 4.3 Linear density of untreated and stabilized PAN multifilaments.

The linear density of the original PAN was raised by 10.68% after APS impregnation and thermal stabilization, and reached 66.35 tex. The linear density value decreases by

1.6% compared to the APS impregnated PAN samples after 5 minutes of stabilization, and exhibits a steady decrease as the stabilization duration increases. The reduction of linear density continued until 60 minutes of stabilization time. In the 60 minutes stabilized samples, a linear density loss of 6.38% to the APS impregnated PAN sample was observed. The stabilization yield was assessed and shown to decline by 95.02% in the 60 minutes stabilized specimen. The reduction of linear density values as the stabilization duration increases is likely driven by the removal of the functional group elements, including carbon, oxygen, nitrogen, and hydrogen.

Stabilized PAN fiber thickness has declined from 19.68 to 17.22 μm for a stabilization time of 60 minutes. After 15 minutes of thermal treatment, fiber thickness dropped rapidly to 6.2%, and additional declines occurred during the subsequent stabilization periods. After 60 minutes of multistep heating, a maximum reduction was observed with a loss of fiber thickness of around 12.5% compared to the untreated PAN samples. The weight loss of the sample in achieving thermal stability is the key factor for the reduction of the fiber thickness.

The variation of tensile strength findings of original and APS incorporated-stabilized PAN samples are illustrated in Figure 4.4. Tensile strength of 5 minutes stabilized samples presents a rapid decrease of around 40.7% and reaches 162.2 MPa from 273.5 MPa of the original PAN specimens. Later, it shows a steady diminution until 45 minutes of thermal stabilization and reaches 152.4 MPa. The tensile strength values present a sudden drop by nearly 52.1% of the 60 minutes stabilized PAN. In the TOS procedure carried out in the air environment, the intermolecular cross-linking reaction transforms nitrile (C≡N) links into nitrile (C=N) bonds. This transition substantially affects cohesive energy loss within the polymer structures and is the prime cause of tensile strength reduction. The degree of the transition of nitrile bonds into nitrilo bonds influences the loss of tensile strength during the TOS process [233].

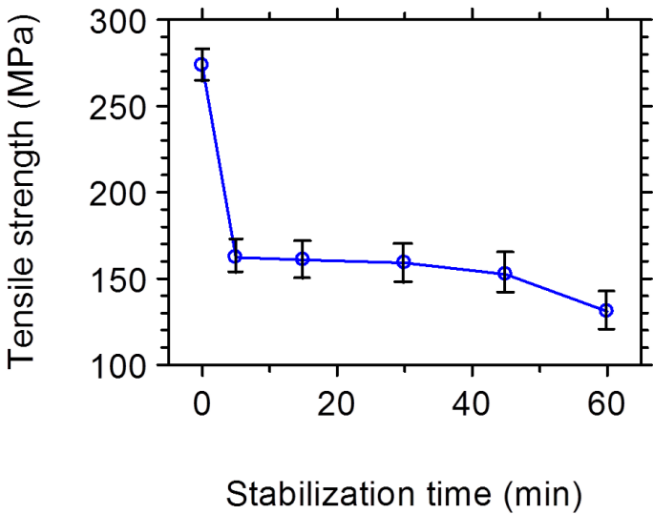

Figure 4.4 Tensile strength of untreated and stabilized PAN multifilaments.

The original PAN sample demonstrated the maximum elongation at break of around 9.08%. In the whole stabilization process, there was a tendency of decreasing values. The trend initiates with a rapid decrease in the 5 minutes multistep stabilization by 3.77%, and finally reached 1.44% for the 60 minutes stabilization period.

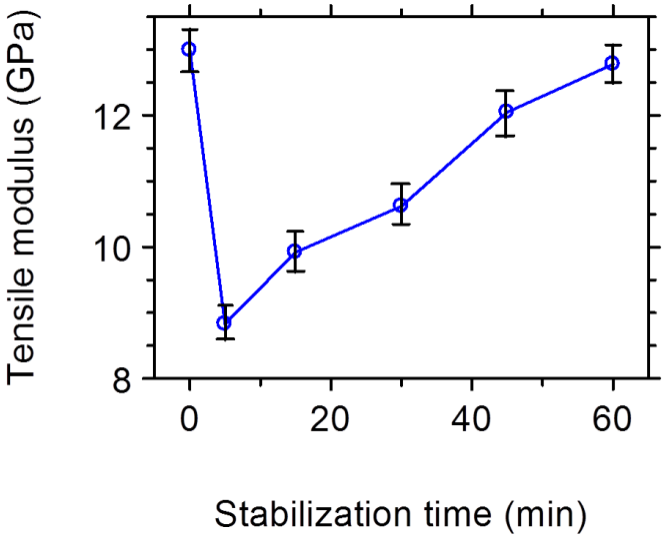

Figure 4.5 Tensile modulus of untreated and stabilized PAN multifilaments.

Tensile modulus results are illustrated in Figure 4.5 for the original and stabilized PAN specimens. The tensile modulus of the original PAN was 12.99 GPa, which decreased quickly at approximately 32% just after 5 minutes of the sample treated with APS.

Afterward, it showed a gradual increase up to the 60 minutes stabilization duration and reached 12.78 GPa.

4.1.3 Thermal and Structural Characterization of Original and Thermally Stabilized PAN Filament Impregnated with 15% APS

4.1.3.1 Assessment of Thermogravimetric Analysis (TGA)

TGA thermogram assessment is usually utilized to achieve carbon yield, which is considered an essential measure for thermally stabilized samples. Thermally stabilized PAN lose their weight by removing the organic elements as pyrolysis byproducts in the carbonization phase. Normally the temperature of the carbonization stage ranges from 200 to 600 °C and above, and most elements with the exception of carbon be eliminated in this phase from the PAN specimen. Hydrogen is usually eliminated as a component of the water vapor in the dehydrogenation process. Though nitrogen is removed as nitrogen (N_2) gas or hydrogen cyanide (HCN), and oxygen is removed in the form of oxygen (O_2) gas, water (H_2O) vapor, carbon monoxide (CO), or carbon dioxide (CO_2).

TGA thermograms for original and stabilized PAN are presented in Figure 4.6. TGA thermograms demonstrate a weight loss reduction as the treatment duration increases, suggesting an increase in carbon yield as the cross-linking density increases. Due to the development of more cross-linked ladder structures, stabilized PAN loses weight over a wider range of temperatures. Yet, the original PAN loses weight across a narrower temperature range.

An extreme thermal decomposition was detected in 5 minutes (by multistep approach) stabilized PAN samples between 300 and 450 °C with a weight loss of 63.5% at 500 °C and 56.6% at 1000 °C. The weight loss steadily decreased between 50 and 450 °C as the stabilization time increased (Figure 4.6). Weight loss of the 60 minutes thermally stabilized PAN became 75.9% at 500 °C and 69.2% at 1000 °C.

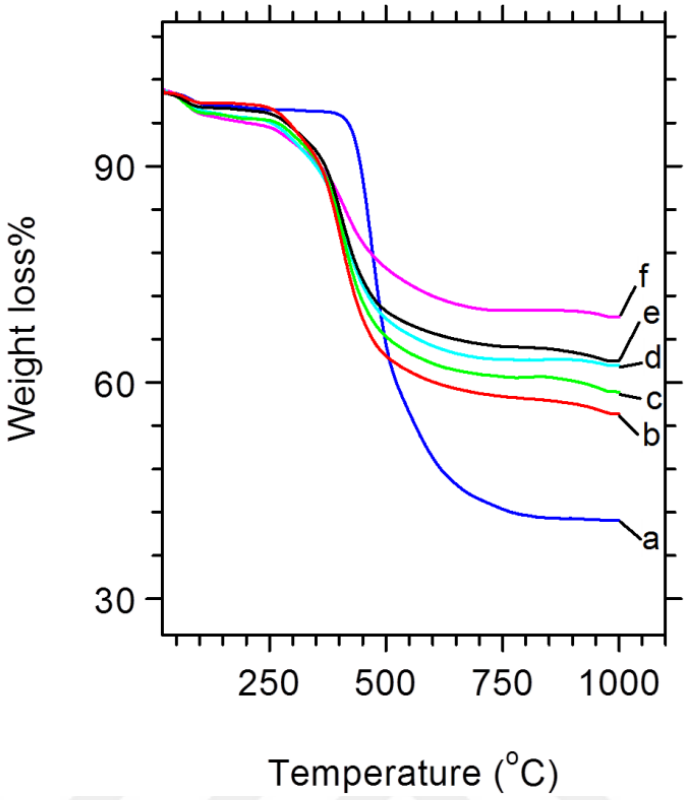

Figure 4.6 TGA thermograms of original (a) and stabilized PAN multifilaments for different stabilization durations. (b) 5 min, (c) 15 min, (d) 30 min, (e) 45 min, (f) 60 min.

An assessment of the carbon yields of the original and APS incorporated-stabilized PAN samples at temperatures between 500 and 1000 °C is illustrated in Figure 4.7. The TGA study indicates that the cross-linking reactions resulted in the thermally stabilized PAN to acquire higher thermal stability. The findings show that the carbon yield rises with the growing stabilization duration. The carbon yield of the 5 minutes stabilized PAN was 63.7% at 500 °C and 55% at 1000 ºC. APS impregnated and 60 minutes stabilized PAN shows the highest carbon yield of 75.9% at 500 °C and 69.1% at 1,000 °C (Figure 4.7).

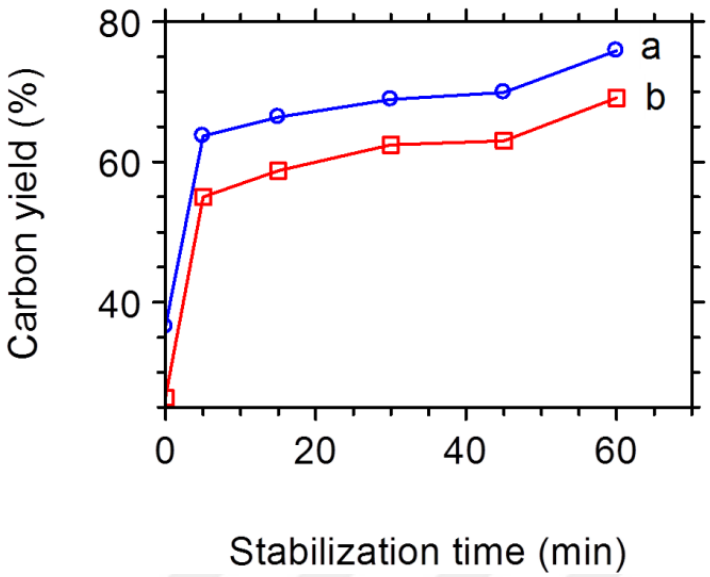

Figure 4.7 Comparison of carbon yield values at temperatures (a) 500 °C, and (b) 1000 °C of the original and stabilized PAN multifilaments.

Figure 4.8 demonstrates differential TGA (dTGA) traces of the TGA thermograms. The original PAN dTGA pattern exhibits exothermic peaks at 300 and 467 °C. The dTGA peak of the stabilized specimens move to 406 °C following the thermal stabilization process, and a new peak emerges at 300 °C. These peaks are thought to be responsible for the aromatization and cyclization reactions of PAN with releasing different gaseous compounds, such as acetylene, acrylonitrile, acetonitrile, adiponitrile, ammonia, benzonitrile, benzene, crotonitrile, dicyanobenzene, dicyanobutene, ethane, ethylene, methane, propene, propane, 1, 3 butadiene, ethyl nitrile, HCN, naphthalene, pyridine, and vinyl acetonitrile [234]. The peak positioned about 100 °C is owing to the vaporization of water existing in the specimens.

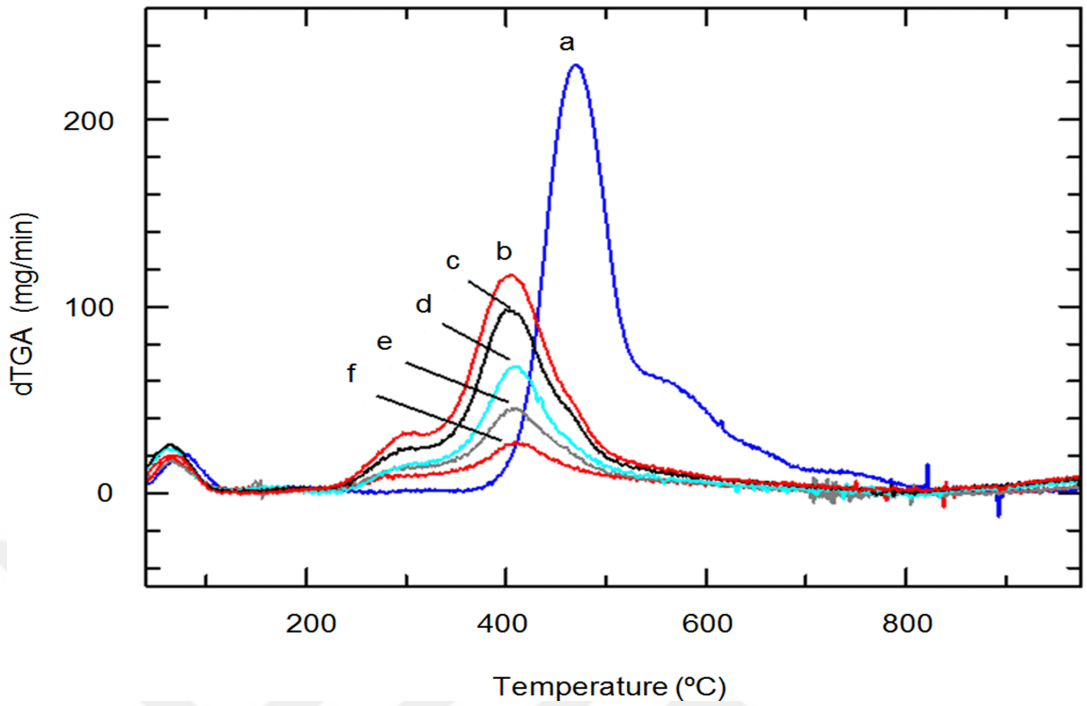

Figure 4.8 dTGA thermograms of original (a) and thermally stabilized PAN multifilaments for different stabilization durations. (b) 5 min, (c) 15 min, (d) 30 min, (e) 45 min, (f) 60 min.

4.1.3.2 Assessment of Infrared Spectroscopy Analysis (FT-IR)

Infrared spectroscopy was regarded as an incredibly efficient approach for the assessment of the structural and chemical alterations occurring in the thermal stabilization phase. APS pretreatment with PAN reveals distinctive changes in the infrared bands of the stabilized PAN samples. The polymer structure of the PAN sample contained about 90% acrylonitrile and 10% vinyl acetate monomers. Therefore, certain infrared vibrations of vinyl acetate comonomers were detected in the PAN spectra. Figure 4.9 shows the comparison between the infrared bands of the PAN sample and the vinyl acetate monomer in the range between 1850 and 850 cm^{-1}. It has been noticed that the IR vibrations at 1452 (CH_2 bending) and 1070 cm^{-1} are present owing to the presence of acrylonitrile units only. Yet, the existence of vinyl acetate monomers was confirmed by 1736 (C=O stretch), 1368, 1233, 1114, and 1022 cm^{-1} bands. The insignificant contribution of vinyl acetate in the IR spectrum positioned at 1452 cm^{-1} is presented in Figure 4.9.

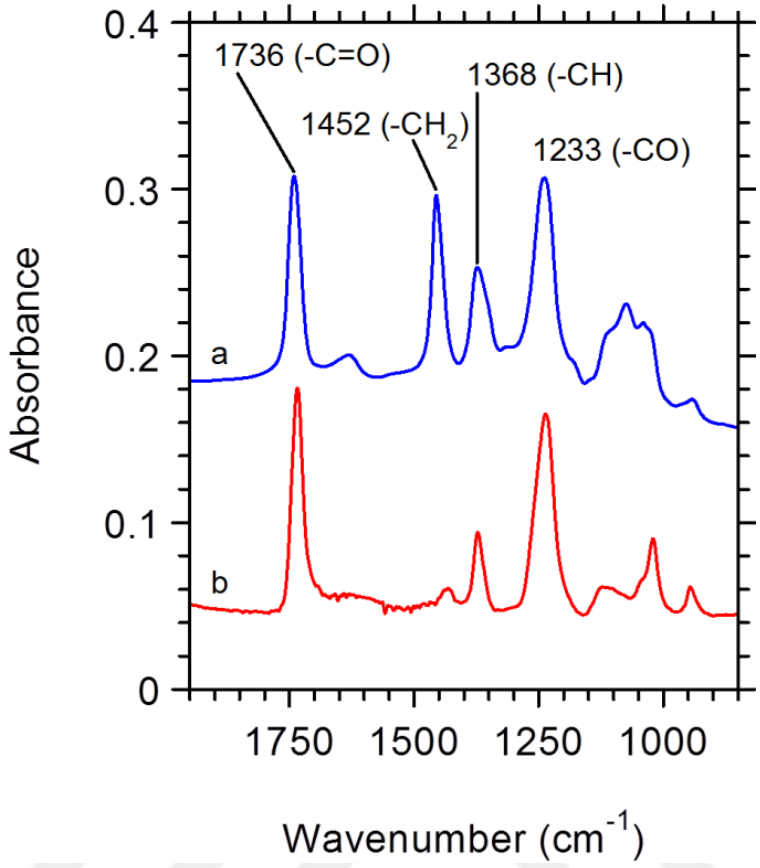

Figure 4.9 Investigation of IR spectra of PAN and vinyl acetate in 1950–850 cm^{-1} (a) PAN, (b) vinyl acetate monomer.

As a result of the aliphatic ketone stretching vibration of vinyl acetate monomer, a distinctive spectrum at 1736 cm^{-1} was noticed of the raw PAN. The IR bands at 1452 cm^{-1} and 1368 cm^{-1} are assigned to methylene (CH_2) and methine (CH), respectively [235, 236]. The CH_2 twisting mode of CH_2 groups is allotted for the spectrum at 1233 cm^{-1} [237]. The overlapping spectra of the IR band between 1154 and 980 cm^{-1} show combined skeletal modes of C–C stretching, C–H bending, C–H rocking, C–H wagging, CH_2 rocking, and C–C–CN bending at 1116, 1074, and 1035 cm^{-1}, correspondingly [235, 236]. Table 4.1 presents the assignments of the IR absorption bands in the region between 4000 and 800 cm^{-1}.

Table 4.1 Assignment of PAN infrared absorption spectra between 4000 and 800 cm^{-1}.

Frequency cm^{-1}	**Intensity**	**Polarization**	**Assignment** [235, 236, 238]
+3626	medium	//	-OH asymmetric stretch
3543	medium	⊥	-OH symmetric stretch
2939	strong	⊥	$-CH_2$ asymmetric stretch
2920	shoulder	⊥	-CH stretch symmetric stretch
2873	medium	⊥	$-CH_2$ symmetric stretch
2245	v. strong	⊥	-C≡N stretch
1736	v. strong	⊥	-C=O stretch (PVA)
1629	medium	⊥	PVA
1452	v. strong	⊥	$-CH_2$ bending
1368	strong	⊥	-CH bending
1233	v. strong	-	-C-O stretch (PVA)
1070	strong	⊥	$-CH_2$ stretching
1035	strong	-	-
1028	shoulder	-	-C-O stretch (PVA)
941	medium	-	-
785	medium	⊥	-CH bending

The IR bands of stabilized PAN present several key intensity deviations owing to different stabilization durations. The assessment of IR bands between 2000 and 450 cm^{-1} of original and stabilized PAN for different stabilization periods is shown in Figure 4.10. Considerable structural alterations were observed in the bands compared to the original PAN vibration. After 5 minutes of stabilization of PAN, the carbonyl (C=O) stretching band of the aliphatic ketone group at 1736 cm^{-1} lost maximum intensity, and moves to a lower frequency with growing stabilization durations till it was noticed as a shoulder on the foremost conjugation absorption (Figure 4.10). This property was reported as an apparent indication of becoming a conjugated structure fragment of the carbonyl groups [239].

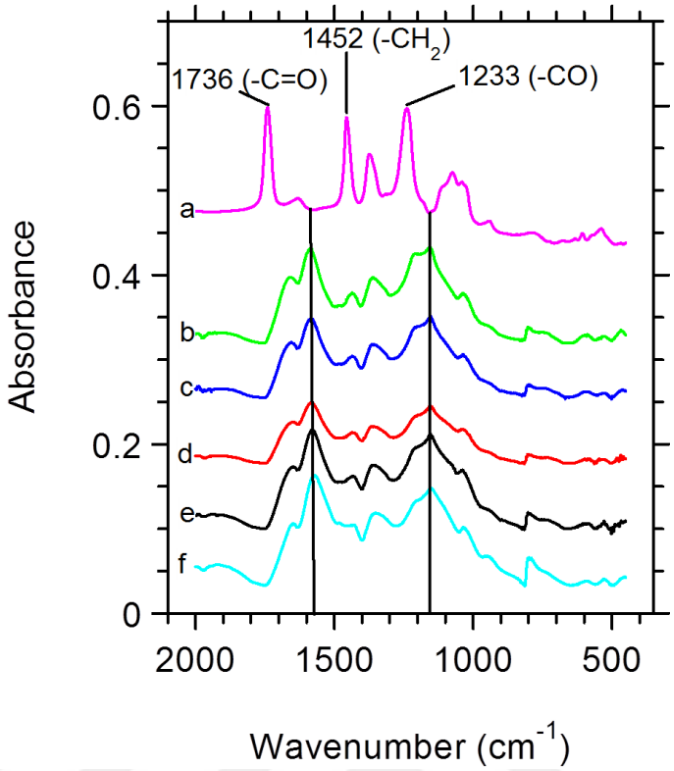

Figure 4.10 IR spectra in 2000–450 cm^{-1} of original (a) and stabilized PAN multifilaments for (b) 5 min, (c) 15 min, (d) 30 min, (e) 45 min, (f) 60 min.

It is understandable in Figure 4.10 that by the IR spectra at 1655, 1583, 1154, and 806 $cm^{-1,}$ the attendance of APS is confirmed. A new band at 1583 cm^{-1} was observed in the APS impregnated and stabilized PAN spectra due to the structural changes in the thermal stabilization procedure. The band was gradually expanding with the increasing stabilization duration. The intramolecular reactions and the conversion of the nitrile (C≡N) into nitrilo group (C=N) was thought to be responsible for the spectrum at 1583 cm^{-1}. In the published literature, various assignments have been stated for this spectrum. It was allotted to conjugated nitrilo (C=N) groups attained from cyclization in some studies [239–241]. Clarke and Bailey mentioned this spectrum that was allocated as C=C and C=N groups [18]. This spectrum was further allocated for the C=C and C=N band combinations [64, 242]. For the stabilized PAN, the combination of C=C, C=N stretching, and N–H in-plane bending bands is another assignment [243].

The formation of the IR vibrations at 1583 cm^{-1} and 1655 cm^{-1} are thought to be created by oxygen uptake processes [244]. The incidence of a continuous oxygen uptake

reaction is represented by oxygen-containing functional groups such as aliphatic ketone, hydroxyl, and conjugated ketone in the thermal stabilization procedure. This indicates that the oxidation process was accompanied by dehydrogenation and cyclization reactions. A single bonded C–C was transformed into a double-bonded C=C species during the thermal stability process, which forms five and six cyclic ring structures in which oxygen was thought to play an essential role by supporting the dehydrogenation process [244]. The development of a new peak at 1154 cm^{-1} indicates the creation of a C–O group in α, β-unsaturated esters, and carboxylic acids and is also thought to be as a result of oxygen uptake processes [245]. Development of the oxygen-containing functional groups like carbonyl (–C=O), carboxyl (–COOH), and hydroxyl (–OH) is considered the secondary role of oxygen, which is crucial in producing intermolecular cross-linking in polymer structures. The structural development categorized by high-thermal stability is supposed because of the oxygen-containing functional group formation [8]. This sort of attribute carries higher significance prior to executing the carbonization procedure for the stabilized specimen.

With growing stabilization duration, the CH_2 vibration at 1452 cm^{-1} and –C–O stretch (PVA) at 1233 cm^{-1} lose their intensity (Figure 4.10) and increasingly turn less dominant due to the occurrence of dehydrogenation and formation of C=C bonds. The IR bands in the region of 1600-1300 cm^{-1} are categorized by the extensive broadening and intensity rise by forming a new band at 806 cm^{-1}, which is assigned to a conjugated C–H (C=C–H) band [246]. Only a few C=C double-bonded groups are generated in the initial stages of the stabilization procedure and indicated as the limitation of that spectrum. The chained hydrocarbon structure gets sufficiently developed in the higher stabilization duration, which is shown by increased band intensity in the subsequent stabilization phases.

Two noticeable vibrations at 2920 and 2852 cm^{-1} are located in the range of 3000-2800 cm^{-1}, where the methylene (CH_2) and the nitrile (C≡N) bands are positioned, respectively (Figure 4.11). With growing treatment duration, the intensity difference of the nitrile groups of the acrylonitrile monomer is also illustrated in Figure 4.11. A nitrile band is located at approximately 2242 cm^{-1}. The methylene (CH_2) spectra lose their maximum intensity in 5 minutes of the stabilization time (multistep approach), which specifies hydrogen atom removal by the dehydrogenation processes that occurred in the

polymer chain and the cross-linked structure. The dehydrogenation process is thought to integrate oxygen partly with the specimens in the stabilization time.

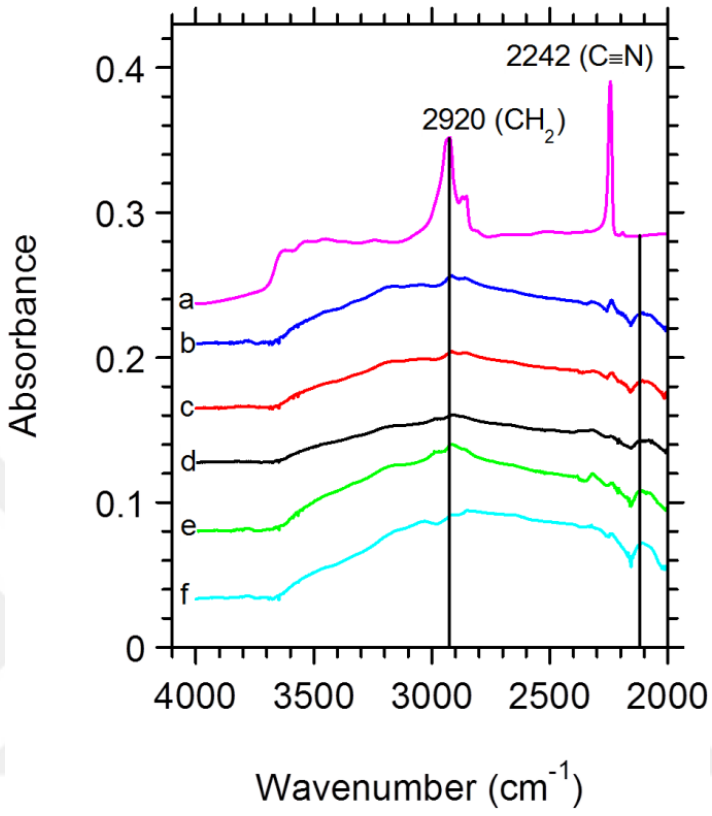

Figure 4.11 IR spectra in 4000–2000 cm^{-1} of original (a) and stabilized PAN multifilaments for (b) 5 min, (c) 15 min, (d) 30 min, (e) 45 min, (f) 60 min.

A rapid intensity loss is detected of the nitrile absorption band at 2242 cm^{-1} in Figure 4.11. Yet, a new peak appears linked with thiocyanate (S=C=N) stretching at 2120 cm^{-1} [245]. Another freshly appearing peak at 2200 cm^{-1} is assigned to nitrilo (C=N) conjugation, and accredited to the ionic structures [239]. This band is thought of as the consequence of the α,β-unsaturated, and β-imino nitrile groups produced from the dehydrogenation process or from the tautomerization and isomerization of the ladder structure [123, 247]. This spectrum is also allied with baminonitrile groups [242, 248]. Stabilized PAN samples represent a greater intensity loss ratio of nitrile groups in the oxygen-rich air atmosphere than at higher temperatures [18].

The bands in the 3700 to 2300 cm^{-1} comprise a common foremost peak at 2920 cm^{-1}, which remains in the spectrum of 60 minutes stabilized sample. The dehydrogenation

process occurs in the polymer chain backbones and the cross-linked polymer structures due to the hydrogen atom loss, which is designated by the constant intensity loss of the methylene band at 2920 cm^{-1}. For the growing stabilization duration, the intensity variation of the nitrile (C≡N) groups of acrylonitrile monomer is shown in Figure 4.11. Gradual intensity loss of the nitrile band indicates the incidence of the cyclization reaction in the thermal stabilization process. With the rise of stabilization duration, the intensity of the methylene in-plane bending at 1452 cm^{-1} and the aliphatic methylene (CH_2) stretching at 2920 cm^{-1} fades progressively, along with the improved conjugation of =C-H spectrum at 806 cm^{-1}. It specifies conjugated backbone polymer structure development. IR curve-fitting of the spectra between 1850 and 850 cm^{-1} was employed to attain the specific peak height in absorbance mode to evaluate the dehydrogenation index (A_{1432}/A_{1366}) (Figure 4.12).

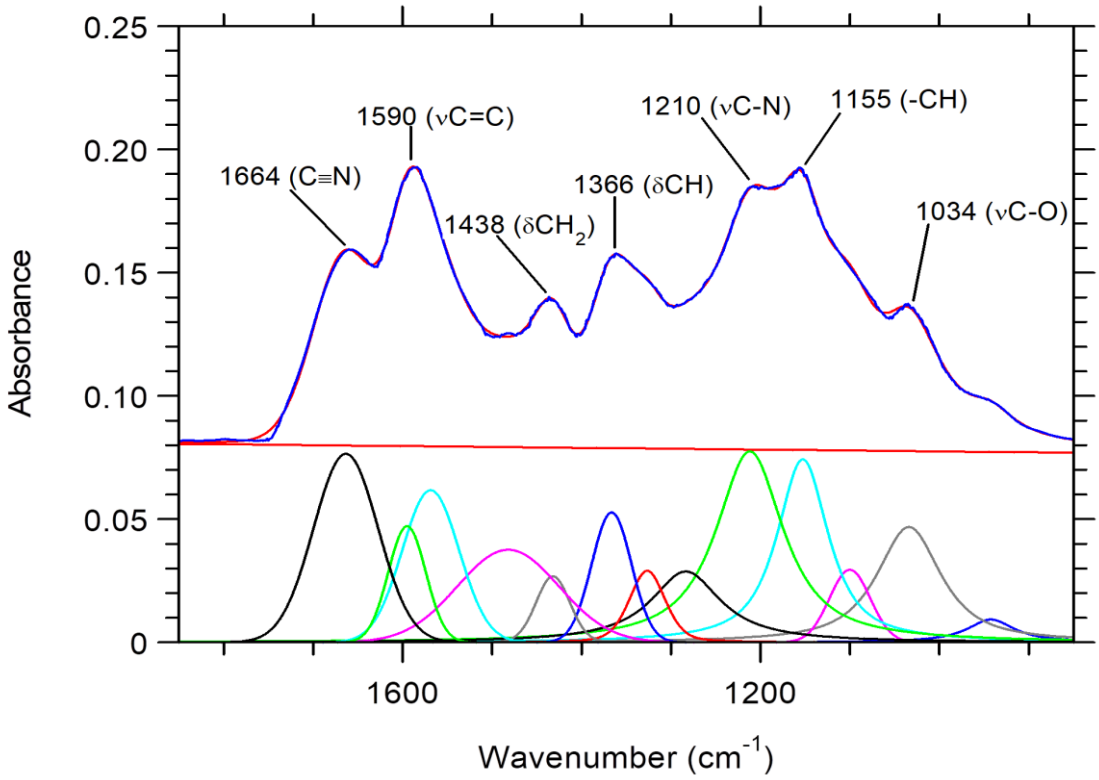

Figure 4.12 Curve-fitting of IR bands in 1850-850 cm^{-1} of the stabilized PAN samples.

The IR-conversion index was calculated using Equation 1 to investigate the structural transformation to a greatly cyclized and cross-linked structure by the conjugated structure band at 1583 cm^{-1} and the nitrile band at 2242 cm^{-1}. APS impregnation with

PAN shows the quicker alteration of pristine PAN structure to the cross-linked and cyclized structure (Figure 4.13). The IR-conversion index is usually utilized to analyze the formation of the ladder structure of the polymer, which is quicker in the early stages. Though, it becomes slower with increasing stabilization period. The IR-conversion index increases rapidly in the first 5 minutes of the multistep stabilization and reaches 92%. However, it slows down step by step and reaches 96% for the 60 minutes stabilization duration. The findings of the IR analysis show that the conversion of the PAN structure into a cross-linked and cyclized ladder-like structure occurred in the 5 minutes stabilization of the PAN.

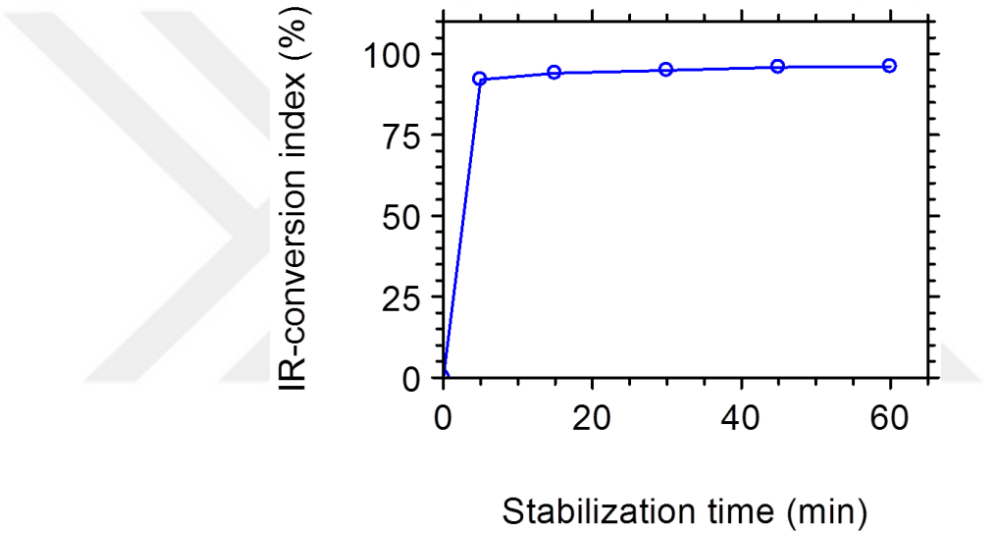

Figure 4.13 IR-conversion index of original and stabilized PAN samples.

Owing to the incidence of dehydrogenation reactions, the dehydrogenation index specifies the steady hydrogen atom loss, which was evaluated by utilizing the absorbance ratios of A_{1452}/A_{1368} and A_{2920}/A_{1368} (Figure 4.14). The findings also indicate a quicker dehydrogenation process. Hence, it is clear that the reduction of the dehydrogenation index causes to decrease in hydrogen content. APS impregnation with PAN accelerates the dehydrogenation process leading to transforming the C-C bond into the C=C bond of the polymer chain.

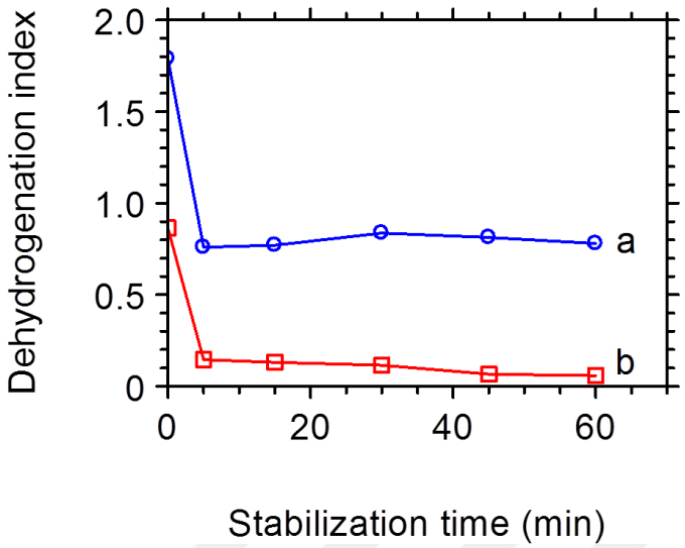

Figure 4.14 Dehydrogenation index of original and stabilized PAN samples. (a) A_{1452}/A_{1368}, (b) A_{2920}/A_{1368}.

4.1.3.3 Assessment of X-ray Diffraction Analysis (XRD)

Equatorial X-ray diffraction traces of pristine and APS incorporated and stabilized PAN multifilaments for the stabilization duration between 5 and 60 minutes are illustrated in Figure 4.15. Evaluation of the XRD profile of the pristine PAN sample represented in Figure 4.15 shows two ordered peaks with d-spacing of 0.308 and 0.539 nm, which are allocated to a hexagonal unit cell [209, 210, 233]. The findings reveal that the ordered peaks (PE1 and PE3) can be allotted to the (100) and (110) peaks of a hexagonal unit cell with the basal plane of a = b = 0.6 nm [233]. The outcomes listed in Table 4.3 indicate that d-spacing of (110) peak showed a lattice expansion of 0.68% for the stabilization duration between 5 and 60 minutes. No such remark was presented in the case of the (100) peak. An additional but less ordered and broad peak (PE2) with d-spacing of 0.345 nm (at about 25.5° 2θ) is also present in the diffraction pattern (Figure 4.16). This peak can be assigned to the unoriented and disordered phase. The d-spacing of this peak is attributed to (002) reflection of the pre-graphitic structure (such as ladder/aromatic) [233]. The intensity of this peak above the baseline is used to determine the X-ray stabilization index presented in Equation 2.

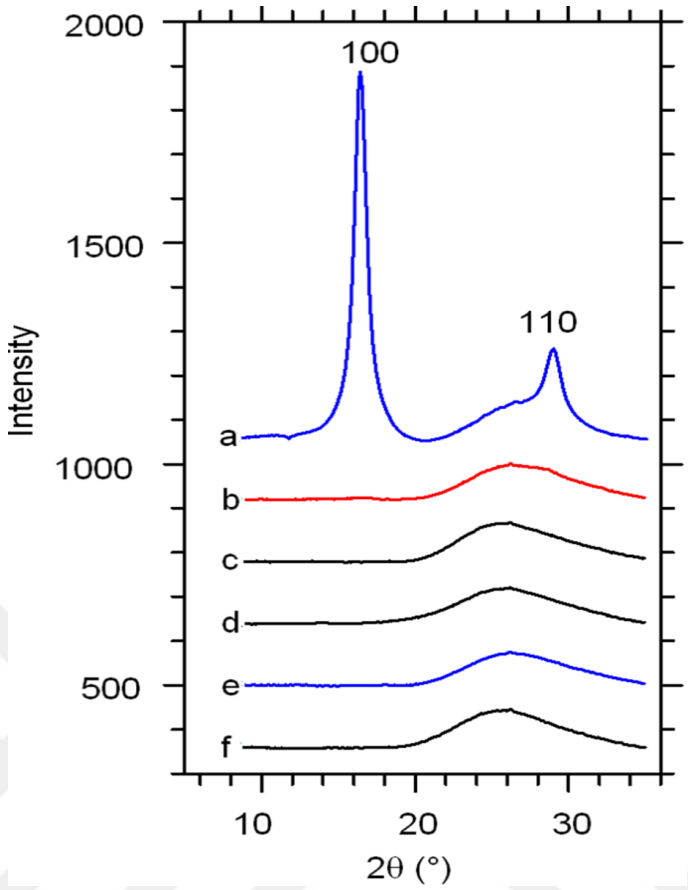

Figure 4.15 Equatorial X-ray diffraction profiles of original (a) and stabilized PAN samples for variable stabilization durations. (b) 5 min; (c) 15 min; (d) 30 min; (e) 45 min; (f) 60 min.

The TOS process considerably affects crystal structure by means of the degree of crystallinity and crystallite size for the laterally ordered structure. A curve-fitting technique was utilized to obtain detailed peak parameters by means of peak position, peak height, and half-height width [209, 210, 233]. Curve-fitted XRD traces of pristine and stabilized PAN specimens are illustrated in Figure 4.15 and Figure 4.16. The assessment of Figure 4.15 shows a quick loss of laterally ordered structure allocated to the hexagonal crystal phase with the progress of the stabilization process [209, 210, 233]. The (100) peak retains its attendance in the 5 minutes stabilized sample but vanishes entirely in the 15 minutes and more stabilized samples (Figure 4.15). An equivalent remark was made for the (110) peak, which allows its attendance in trivial amounts during the stabilization process up to 60 minutes thermal stabilization (Figure

4.17). The XRD traces illustrated in Figure 4.16 shows the existence of the (110) peak as an extensive peak due to the decrystallization processes.

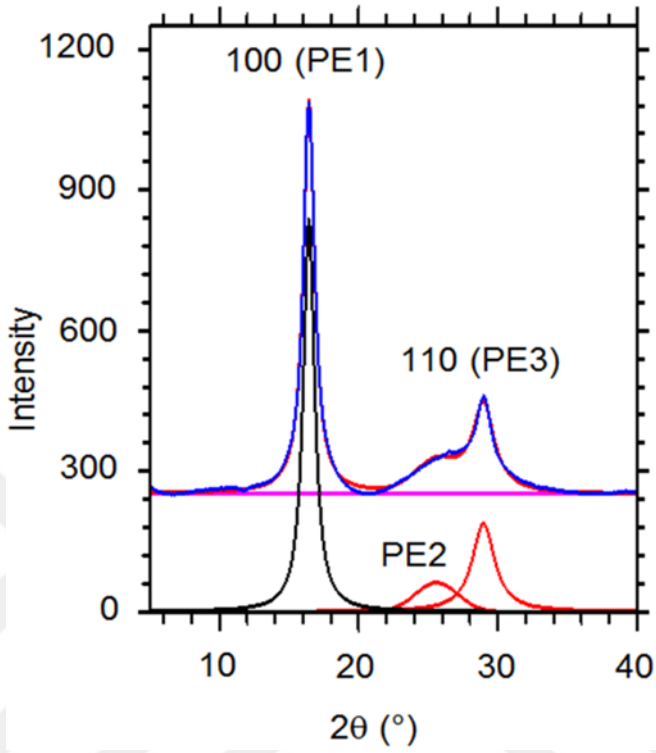

Figure 4.16 Curve-fitting of the X-ray diffraction profile of the original PAN sample.

The apparent X-ray crystallinity was considered as a measure of lateral order. This is because of employing XRD traces following the curve-fitting technique. Therefore, the term ‘apparent crystallinity’ should be used instead of ‘crystallinity’ that recommends absolute crystallinity [233]. The apparent crystallinity values were calculated in this study by employing Equation 3. Curve-fitting of the XRD traces resulted in the effective assessment of apparent X-ray crystallinity and amorphous fraction values illustrated in Figure 4.18. The curve-fitting technique was further used to attain detailed peak parameters, principally the peak heights above baseline, to assess X-ray stabilization index values [233] using Equation 2. The X-ray stabilization index values were noticed to increase with progressing stabilization duration (Figure 4.18) and could be considered as a reliable way to evaluate the amount of aromatic structure formation in the stabilization process [233].

The findings illustrated in Figure 4.18 present that the apparent X-ray crystallinity showed a downward and increasing trend, as was noticed in the amorphous fraction results. The apparent X-ray crystallinity presented a decreasing trend ranging from 19 to 12.7%. Conversely, the amorphous fraction values showed an opposite propensity, increased from 81 to 87% with growing stabilization duration (Figure 4.18). The findings indicate that the X-ray stabilization index increased promptly with increasing stabilization time.

Considering no impact of crystal perfection, the assessment of lateral crystallite size was executed after correcting instrumental broadening effects related to the ordered PE1 and PE3 peaks (100 and 110 ordered reflections) utilizing the Scherrer Equation 4 of the pristine and stabilized PAN samples [233]. The curve-fitting technique was used to obtain specific peak parameters of the XRD profiles in evaluating lateral crystallite sizes related to the (100) and (110) ordered peaks as presented in Table 4.2 and Table 4.3.

Table 4.2 Evaluation of X-ray diffraction outcomes of the original and stabilized PAN samples for (100) reflection.

Stabilization time (min)	Peak height	Peak Position 2θ (deg).	d-spacing (nm)	Corrected half-height width 2θ (deg).	Corrected crystallite size (nm)	No. of Chains
0	842.2	16.43	0.539	0.92	9.66	18
5	5.2	16.50	0.537	1.97	4.42	8
15	-	-	-	-	-	-
30	-	-	-	-	-	-
45	-	-	-	-	-	-
60	-	-	-	-	-	-

Table 4.3 Evaluation of X-ray diffraction outcomes of the original and stabilized PAN samples for (110) reflection.

Stabilization time (min)	Peak height	Peak Position 2θ (deg).	d-spacing (nm)	d-spacing enlargement (%)	Corrected half-height width 2θ (deg).	Corrected crystallite size (nm)	No. of Chains
0	189.5	30.31	0.294	0.00	1.89	4.82	16
5	33.3	30.33	0.294	0.00	5.88	1.56	5
15	32.9	30.25	0.295	0.34	6.18	1.48	5
30	31.7	30.25	0.295	0.34	6.25	1.46	5
45	25.9	30.20	0.296	0.68	6.37	1.44	5
60	22.3	30.20	0.296	0.68	6.59	1.39	5

The corrected, half-height widths of the ordered peaks (PE1 and PE3) were employed to evaluate apparent crystallite sizes. The findings listed in Table 4.2 show that the lateral dimension of the (100) peak was reduced from 9.66 to 4.42 nm. The number of chains in the hexagonal crystal structure normal to the (100) planes responsible for the lateral crystallite sizes is also listed in Table 4.2. Yet, the pristine sample size relates to 18 chains, whereas the lateral crystallite size was reduced to 8 chains for the 5 minutes stabilization duration.

The outcomes listed in Table 4.3 represent that the lateral size of the (110) peak was decreased from 4.82 to 1.39 nm. The number of chains in the hexagonal crystal structure normal to the (110) planes responsible for the lateral crystallite sizes is also enlisted in Table 4.3. Though the pristine specimen size corresponds to 16 chains, the lateral crystallite size was evaluated as five chains for 5 minutes stabilization duration. The number of chains responsible for the lateral crystallite size for the other samples stabilized for 15 to 60 minutes did not alter significantly. The lateral dimensions (such as crystallite size) for the disordered peak (PE2), which experienced stabilization duration between 15 and 60 minutes was noticed to fluctuate in the range of 2.54 to 1.3 nm. It was seen that the speedy thermal stabilization causes reduced apparent crystallinity and reduced lateral crystallite size due to the fast stabilization reactions.

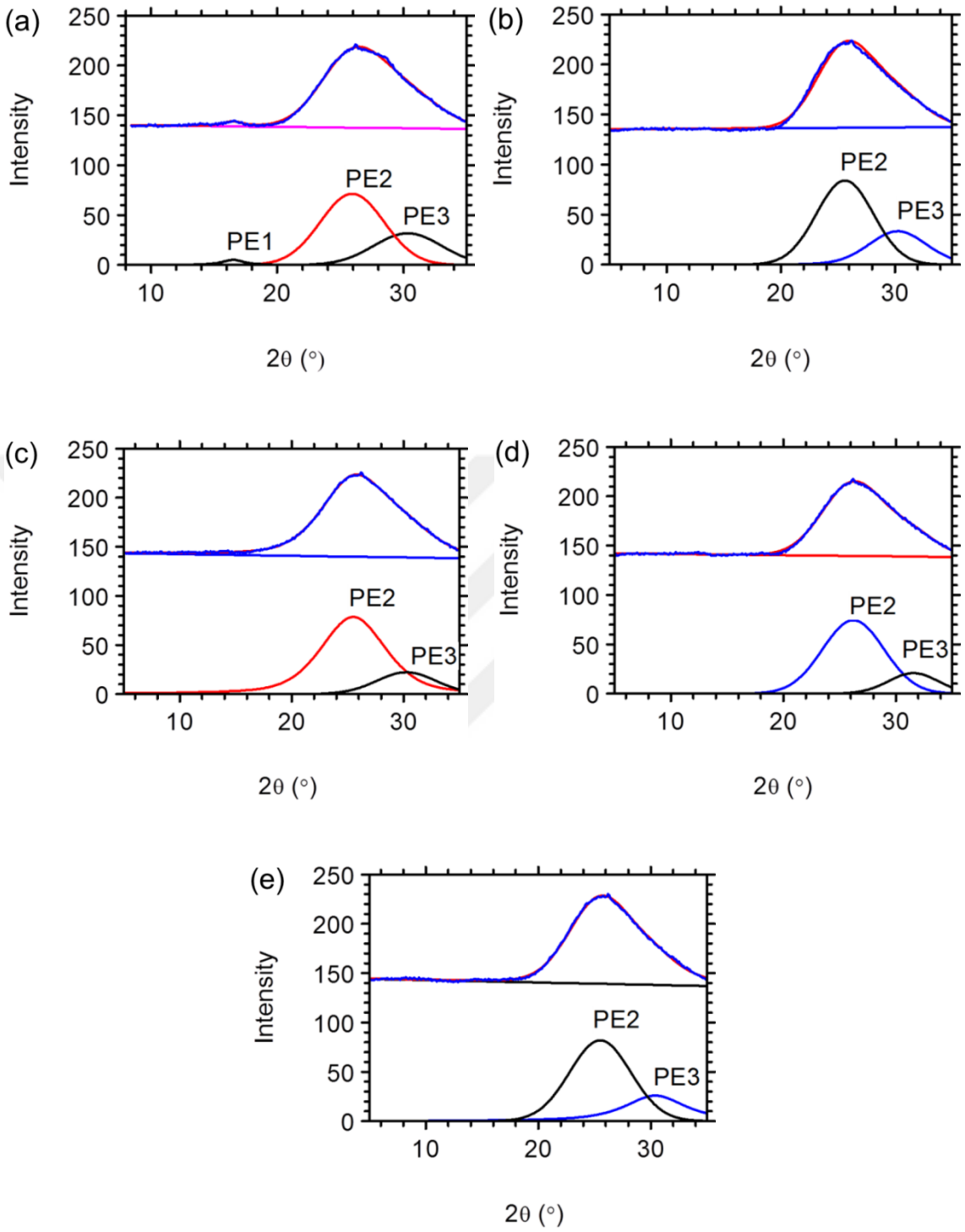

Figure 4.17 Curve-fitting of the X-ray diffraction profiles of stabilized PAN samples for variable stabilization durations. (a) 5 min; (b) 15 min; (c) 30 min; (d) 45 min; (e) 60 min.

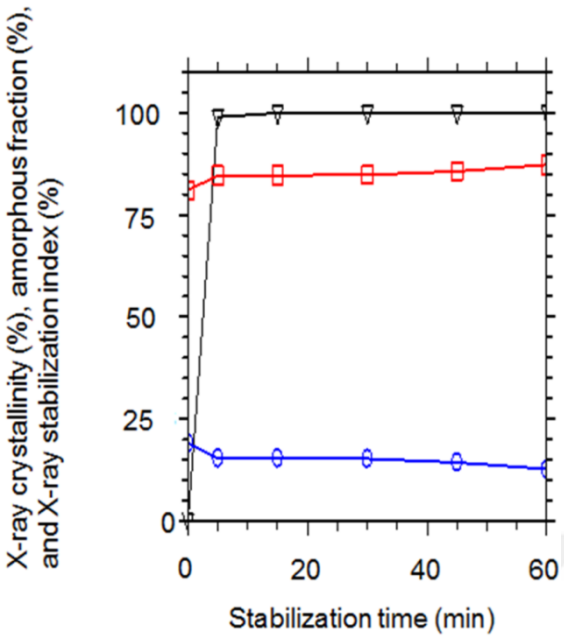

Figure 4.18 Changes of X-ray crystallinity, amorphous fraction, and X-ray stabilization index for variable stabilization durations.. (O) X-ray crystallinity (%), (□) Amorphous fraction (%), and (∇) X-ray stabilization index (%).

4.1.3.4 Assessment of Scanning Electron Microscopy (SEM)

Scanning electron microscopy (SEM) was used to examine the surface characteristics of original, and APS integrated-stabilized PAN samples. Due to the filament extrusion in the wet spinning process, grove-like patterns and uneven superficial topographies were detected over the longitudinal direction of the samples (Figure 4.19).

Figure 4.19 Longitudinal SEM image of original PAN multifilament.

These surface topographies are thought to be generated by liberating solvents from the filaments in the coagulation pan. The discharge of solvents also results the formation of the kidney-like cross-sectional pattern of the PAN filaments (Figure 4.20).

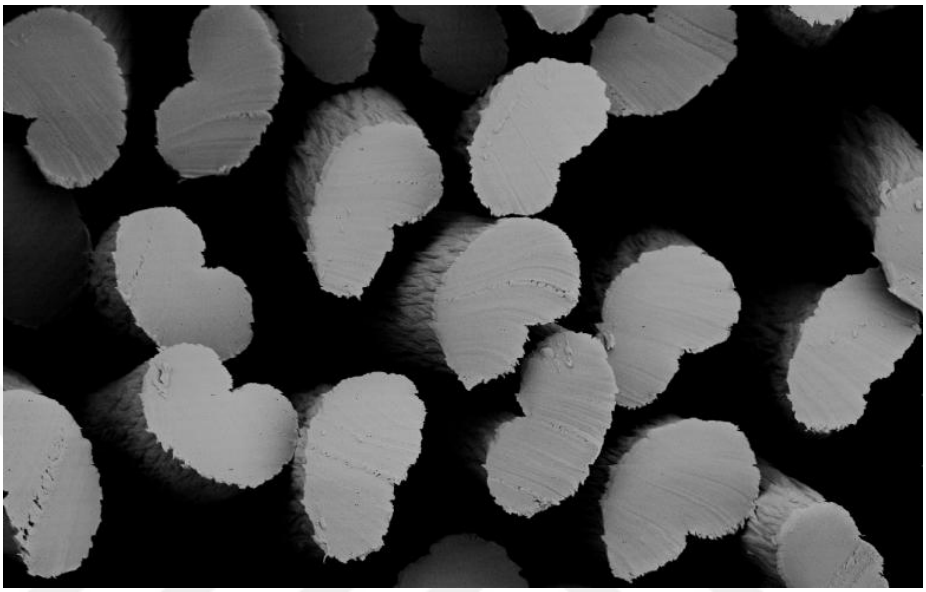

Figure 4.20 Cross-sectional SEM image of original PAN multifilament.

Figure 4.21 represents the surface images of APS treated and stabilized PAN samples. The SEM study showed that the surface features do not represent major deviations of the stabilized PAN filaments for different stabilization duration (Figure 4.21). The formation of central areas of the stabilized PAN samples was reported by Layden [249]. In that investigation, it was observed that the surface temperature was lesser than the inner temperature of the PAN fiber. For this reason, the transmitted heat in the stabilization step is thought to influence the cyclization process and to generate a disoriented (i.e., amorphous) ladder-like structure in the central zone of the stabilized PAN filament. Hence, the disoriented central zone is expected to lessen the oxygen dispersion from the external surface area [250].

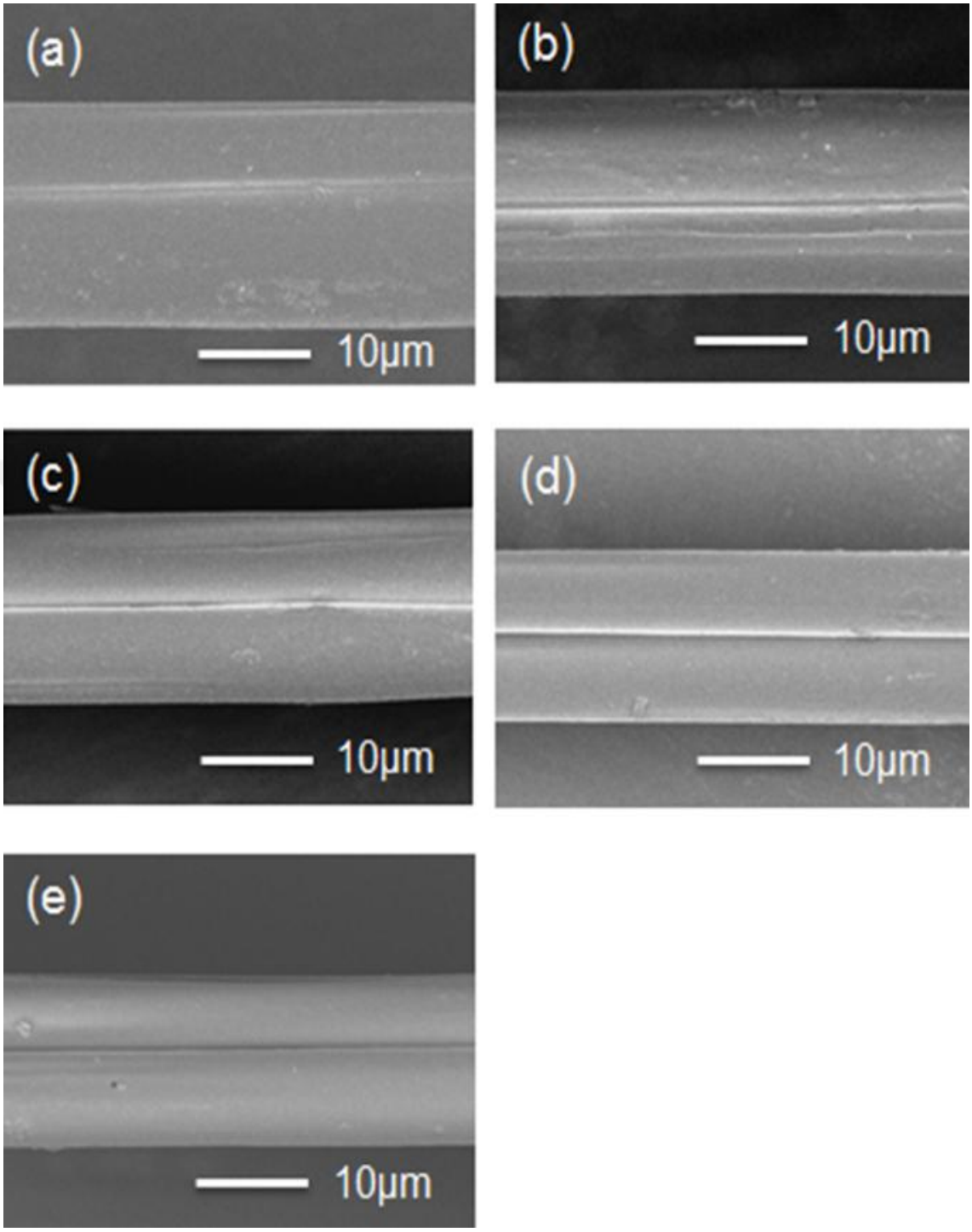

Figure 4.21 SEM images of stabilized PAN samples for variable stabilization durations. (a) 5 min, (b) 15 min, (c) 30 min, (d) 45 min, (e) 60 min.

4.1.4 Impact of Heating Rate Variation on Mechanical Properties of Thermally Stabilized PAN Filament Impregnated with 15% APS

First of all, de-oiling for PAN filaments was done by using isopropyl alcohol and perchloroethylene solution. After that, the samples were washed in running water and rinsed in distilled water for 1 hour each case. Later on, impregnation with 15% ammonium persulfate was performed at room temperature (25 °C) for 24 hours. Afterward, impregnated PAN sample was dried for 24 hours at 25 °C. At this stage, the sample was ready for annealing, and the process was performed up to 250 °C by a stepped annealing approach (Figure 3.11) for 45 minutes in each stage separately. The heating rate was kept different for each experiment to evaluate the impact of the heating rate on the PAN multifilament sample. Utilizing different heating rates in the thermal stabilization process offers variable physical and mechanical properties. From the findings of this experiment, it is clearly observable that the maximum tensile strength as 152.38 ± 14.3 MPa was obtained for the heating rate of (2 °C/min – 1 °C/min) set in the stepped thermal stabilization process (Figure 3.11) of 15% APS impregnated PAN multifilaments.

Table 4.4 Impact of heating rate on 15% APS impregnated and stabilized PAN multifilaments in the air atmosphere up to 250 °C by stepped annealing approach for 45 minutes.

Heating Rate (°C/min)	Flame Test	Linear Density (Tex)	Volume Density (g/cm^3)	Extension at break (%)	Tensile Strength (MPa)	Tensile Modulus (GPa)
1 °C/min – 1 °C/min	Flameproof	62.21	1.375	1.38 ± 0.29	119.02 ± 24.6	12.63 ± 2.3
1 °C/min – 2 °C/min	Flameproof	63.88	1.375	1.33 ± 0.32	107.62 ± 8.2	12.37 ± 2.2
2 °C/min – 1 °C/min	Flameproof	63.40	1.355	2.49 ± 0.63	152.38 ± 14.3	12.02 ± 2.7
2 °C/min – 2 °C/min	Flameproof	64.53	1.37	1.98 ± 0.73	120.89 ± 7.8	13.04 ± 1.3
3 °C/min – 1 °C/min	Flameproof	64.91	1.36	1.79 ± 0.18	143.69 ± 8.4	13.87 ± 0.8
3 °C/min – 2 °C/min	Flameproof	65.26	1.36	1.74 ± 0.49	136.79 ± 19.2	14.39 ± 2.2
3 °C/min – 3 °C/min	Flameproof	66.64	1.37	1.63 ± 0.45	119.05 ± 15.4	13.60 ± 1.7

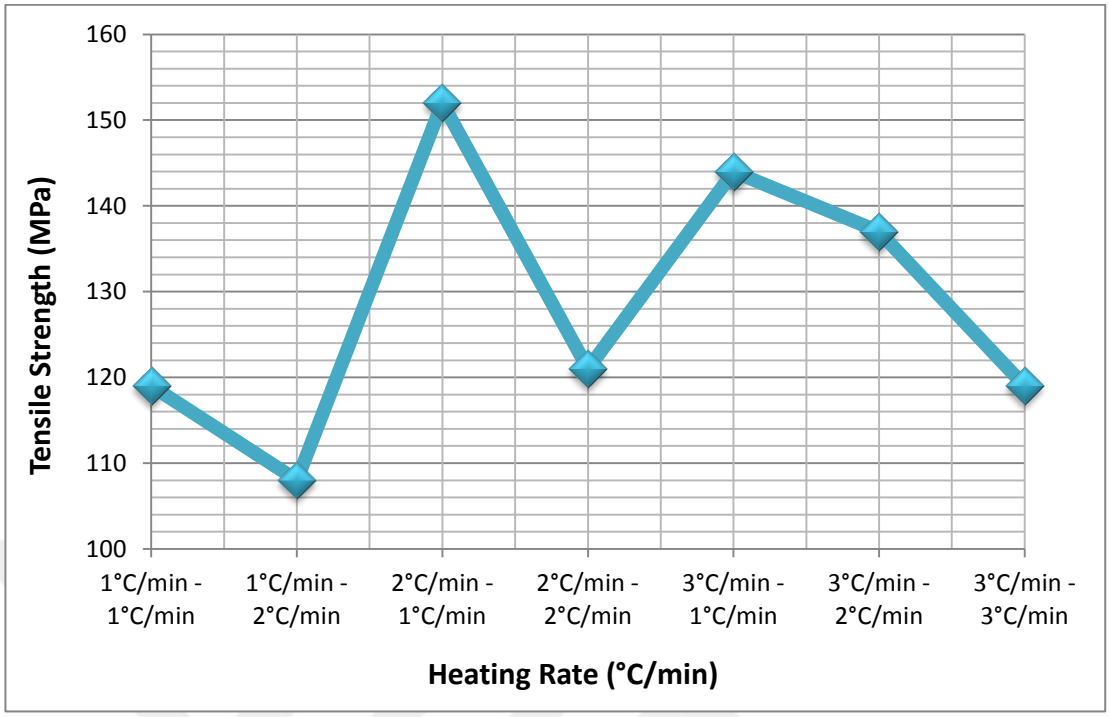

Figure 4.22 Impact of heating rate on tensile strength of 15% APS impregnated PAN filament.

4.1.5 Tensile Stretching / Load Application Experiments During Stabilization Process of 15% APS Pretreated PAN

Tensile stretching by applying variable load during oxidative thermal stabilization process was executed of 15% ammonium persulfate impregnated PAN multifilaments. The stabilization process was accomplished employing a multistep annealing approach as illustrated in Figure 3.11 for variable stabilization durations. Afterward, physical and mechanical properties were characterized of the obtained samples.

Figure 4.23 Tensile stretching experiments during stabilization of PAN multifilament.

4.1.5.1 Fiber Diameter Variation of PAN Multifilament for Tensile Stretching in Thermal Stabilization Process

Due to applying load during oxidative thermal stabilization process of 15% ammonium persulfate impregnated PAN multifilaments, fiber diameter decreases continuously with increasing stabilization periods. It is also noticeable that with increasing applied load, the values of fiber diameter decreases due to occurring higher stretching of the samples during the stabilization process.

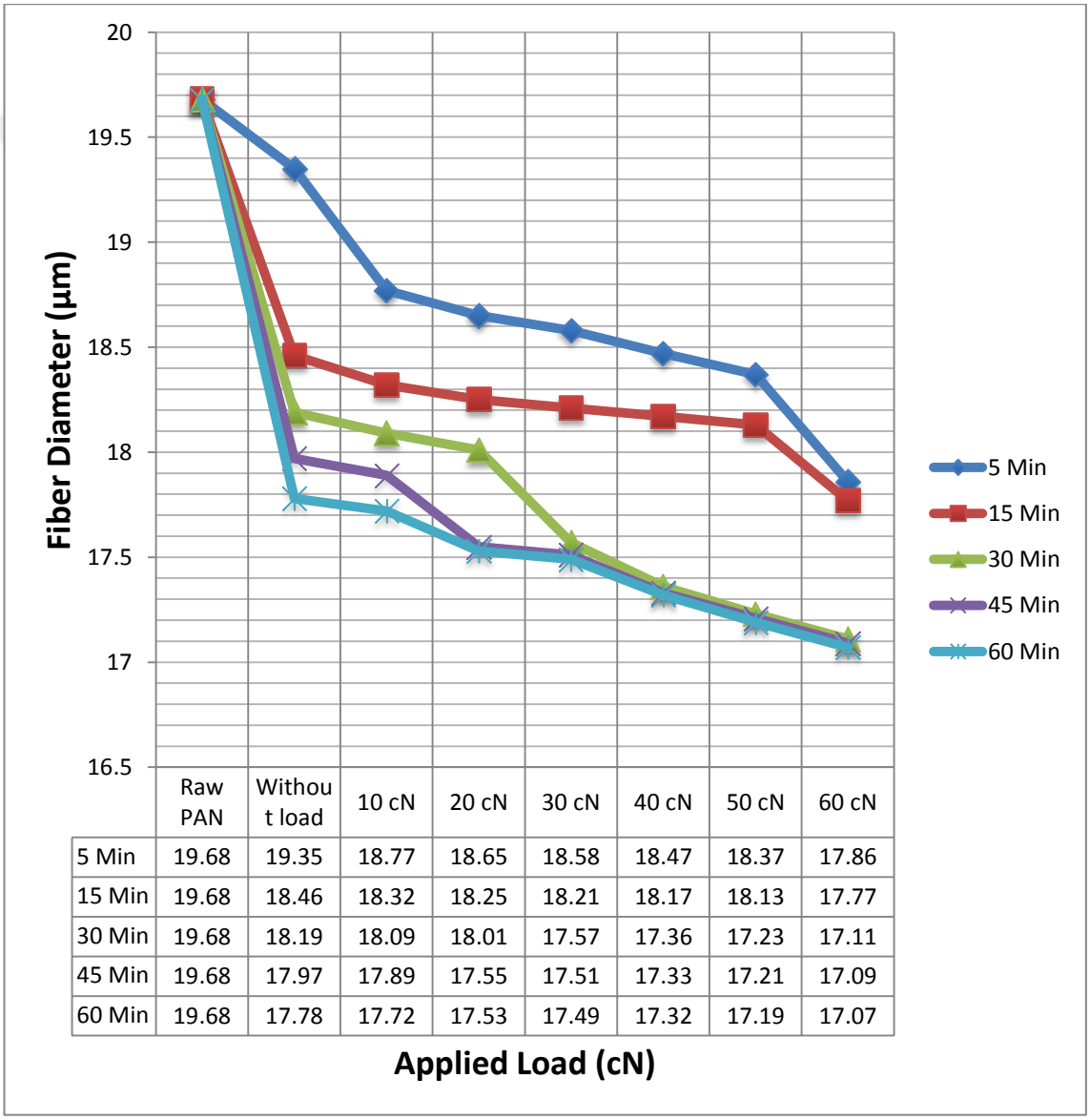

	Raw PAN	Without load	10 cN	20 cN	30 cN	40 cN	50 cN	60 cN
5 Min	19.68	19.35	18.77	18.65	18.58	18.47	18.37	17.86
15 Min	19.68	18.46	18.32	18.25	18.21	18.17	18.13	17.77
30 Min	19.68	18.19	18.09	18.01	17.57	17.36	17.23	17.11
45 Min	19.68	17.97	17.89	17.55	17.51	17.33	17.21	17.09
60 Min	19.68	17.78	17.72	17.53	17.49	17.32	17.19	17.07

Figure 4.24 Fiber diameter variation of original and 15% APS impregnated and stabilized PAN multifilament by applying variable load for different stabilization periods.

4.1.5.2 Tensile Strength Variation of PAN Multifilament for Tensile Stretching in Thermal Stabilization Process

Tensile strength of 15% APS impregnated PAN multifilaments showed a sudden decline once stabilized without applying any load. However, after applying variable loads, higher tensile strength values were obtained. The maximum tensile strength value was 212.73 MPa for 30 minutes stabilized samples when 20 cN load was applied. For the same load application, 45 and 60 minutes stabilized samples had the highest tensile strength of 209.06 and 208.02 MPa, respectively.

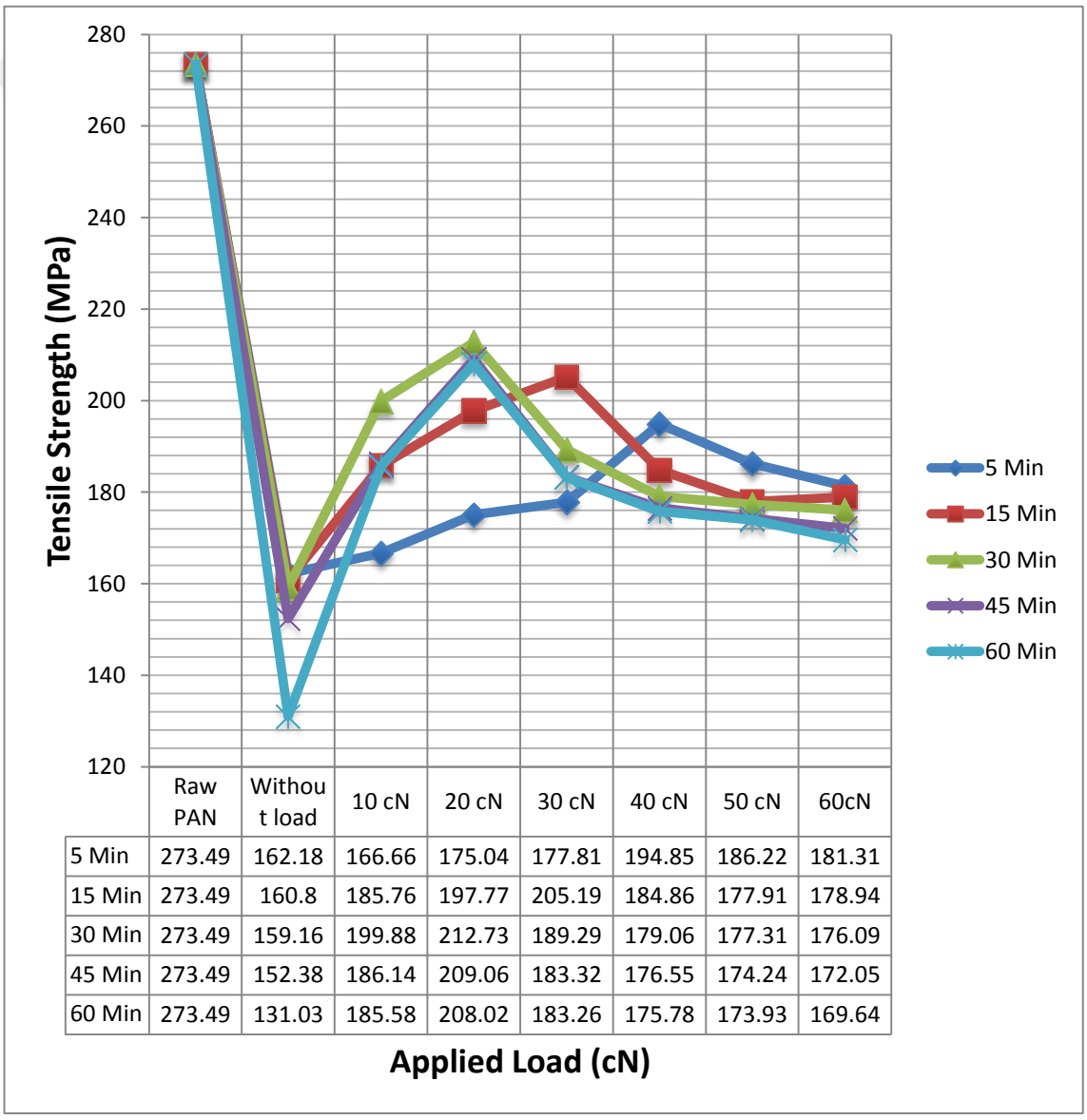

	Raw PAN	Without load	10 cN	20 cN	30 cN	40 cN	50 cN	60cN
5 Min	273.49	162.18	166.66	175.04	177.81	194.85	186.22	181.31
15 Min	273.49	160.8	185.76	197.77	205.19	184.86	177.91	178.94
30 Min	273.49	159.16	199.88	212.73	189.29	179.06	177.31	176.09
45 Min	273.49	152.38	186.14	209.06	183.32	176.55	174.24	172.05
60 Min	273.49	131.03	185.58	208.02	183.26	175.78	173.93	169.64

Figure 4.25 Tensile strength variation of original and 15% APS impregnated and stabilized PAN multifilament by applying variable load for different stabilization periods.

4.1.5.3 Tensile Modulus Variation of PAN Multifilament for Tensile Stretching in Thermal Stabilization Process

In the case of thermal stabilization of 15% APS incorporated PAN samples, tensile modulus values demonstrated a sharp fall for variable stabilization times without applying any load. However, the tensile modulus values grew steadily when variable loads were applied throughout the stabilization process.

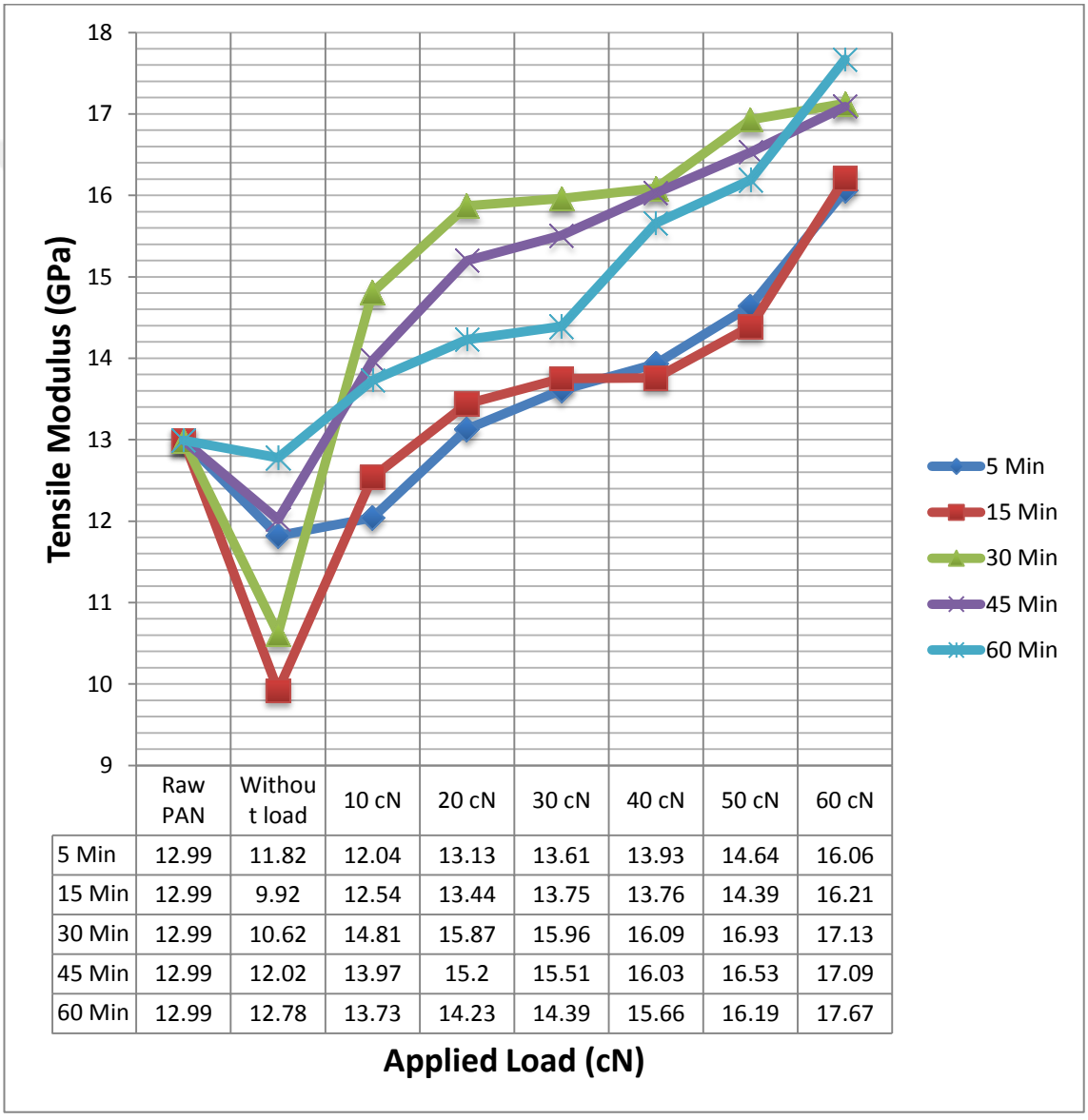

	Raw PAN	Without load	10 cN	20 cN	30 cN	40 cN	50 cN	60 cN
5 Min	12.99	11.82	12.04	13.13	13.61	13.93	14.64	16.06
15 Min	12.99	9.92	12.54	13.44	13.75	13.76	14.39	16.21
30 Min	12.99	10.62	14.81	15.87	15.96	16.09	16.93	17.13
45 Min	12.99	12.02	13.97	15.2	15.51	16.03	16.53	17.09
60 Min	12.99	12.78	13.73	14.23	14.39	15.66	16.19	17.67

Figure 4.26 Tensile modulus variation of original and 15% APS impregnated and stabilized PAN multifilament by applying variable load for different stabilization periods.

4.1.5.4 Extension at Break (%) Variation of PAN Multifilament for Tensile Stretching in Thermal Stabilization Process

Tensile stretching during thermal stabilization helps to improve extension at break percentage values up to a certain amount of load application. For 45 and 60 minutes of stabilization, APS impregnated PAN samples showed maximum values of 6.35% and 4.96% once 20 cN load was applied. However, the highest value of extension at break (6.61%) was noticed for 15 minutes stabilized samples when 30 cN was applied.

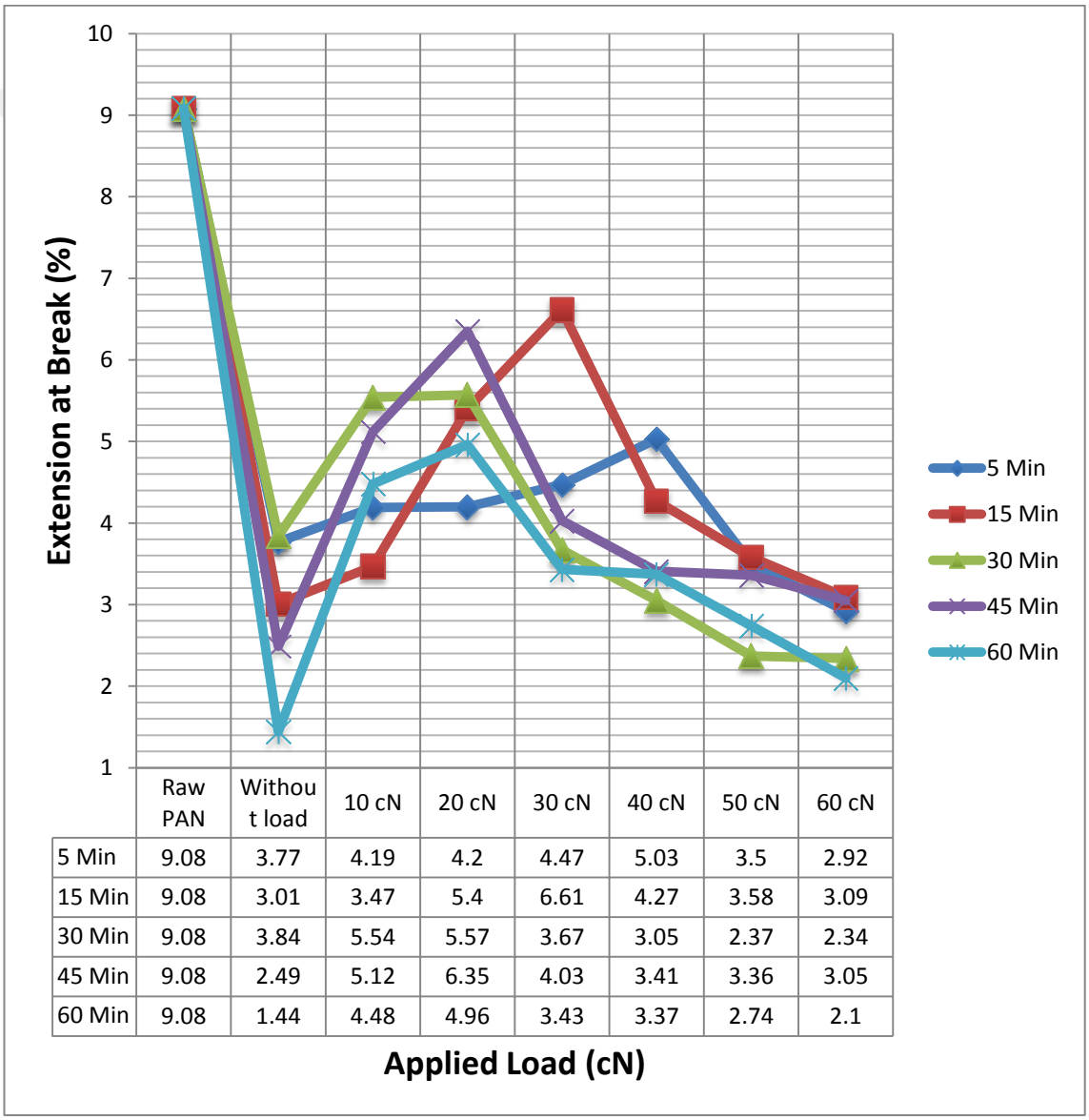

	Raw PAN	Without load	10 cN	20 cN	30 cN	40 cN	50 cN	60 cN
5 Min	9.08	3.77	4.19	4.2	4.47	5.03	3.5	2.92
15 Min	9.08	3.01	3.47	5.4	6.61	4.27	3.58	3.09
30 Min	9.08	3.84	5.54	5.57	3.67	3.05	2.37	2.34
45 Min	9.08	2.49	5.12	6.35	4.03	3.41	3.36	3.05
60 Min	9.08	1.44	4.48	4.96	3.43	3.37	2.74	2.1

Figure 4.27 Extension at break (%) variation of original and 15% APS impregnated and stabilized PAN multifilament by applying variable load for different stabilization periods.

4.2 Polyamide 66 Multifilament

4.2.1 Characterization of Original PA 66 Multifilament

During the course of this investigation, a polyamide 66 multifilament precursor yarn with a linear density of 16.28 tex per 69 filaments was utilized.

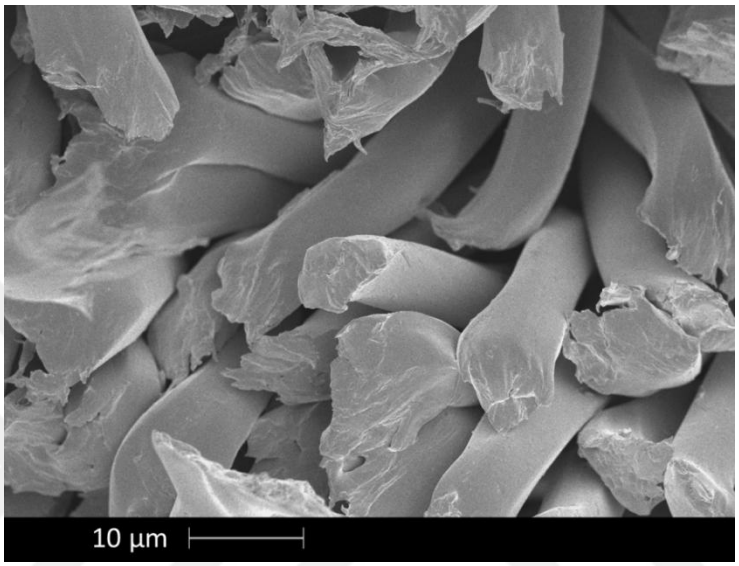

Figure 4.28 Representative surface morphologies of original PA66 fibers.

The filament thickness and the volume density of the polyamide 66 samples were 11.32 ± 0.31 µm and 1.160 g/cm^3, respectively. The findings of mechanical properties measurement of the PA66 samples were 285.27±11.61 MPa tensile strength, 15.93±3.43 GPa tensile modulus, and 28.98±3.81 extension at break percentage.

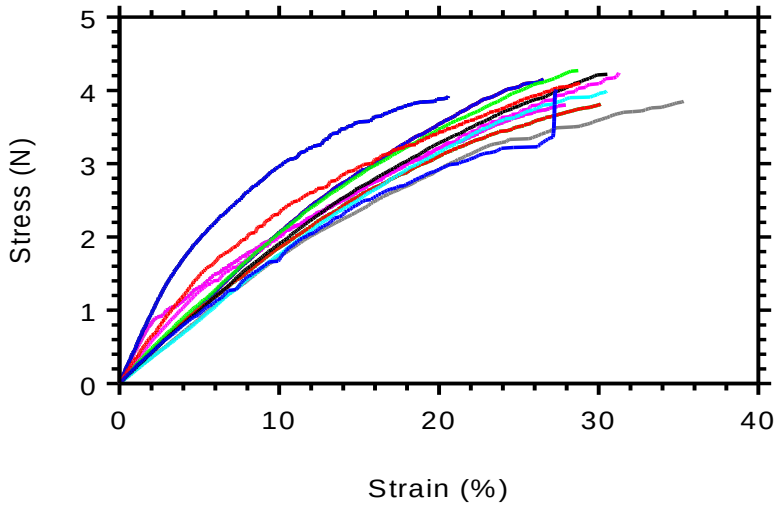

Figure 4.29 Stress-strain curve of original PA66 multifilament.

4.2.2 Physical and Mechanical Characterization of Original and Thermally Stabilized PA66 Filament Impregnated with PBU

Different chemical compositions were trialed to impregnate PA66 multifilament prior to the thermal stabilization process. Ethanol solution of 3% phosphoric acid, 3% boric acid, and 3% urea was found as the best option for the chemical impregnation of PA66 multifilament. The original polyamide 66 yarn was pretreated by a 10% (v/v) ethanol-water solution at 50 °C for 50 minutes to get rid of the surface impurities of the fibers. Following the removal of surface impurities, the sample was left to dry overnight at 25 °C, and afterward, dried again in an air oven at 80 °C for 4 hours until constant weight. Chemical incorporation was executed by soaking the PA66 yarn in a solution of 3% phosphoric acid, 3% boric acid, and 3% urea with ethanol at 25 °C for 24 hours. The chemical solution displayed a pH value of 2.46 at 19.3 °C. Following the chemical pretreatment, the samples were removed from the bath and dehydrated at 80 °C for 4 hours. The impregnated PA66 yarn was loaded with 8.1% (w/w) PBU on a dry basis. The TOS process was then executed in an air atmosphere at 245 °C for 30, 60, 90, 120, and 150 minutes stabilization times separately, while the temperature was raised from room temperature to 170 °C following a 1 °C/min rate and then without waiting, the temperature reached to 245 °C at a 0.3 °C/min rate. Stainless steel frames were employed to wind the PA66 samples to avoid any physical shrinkage or molecular orientation loss.

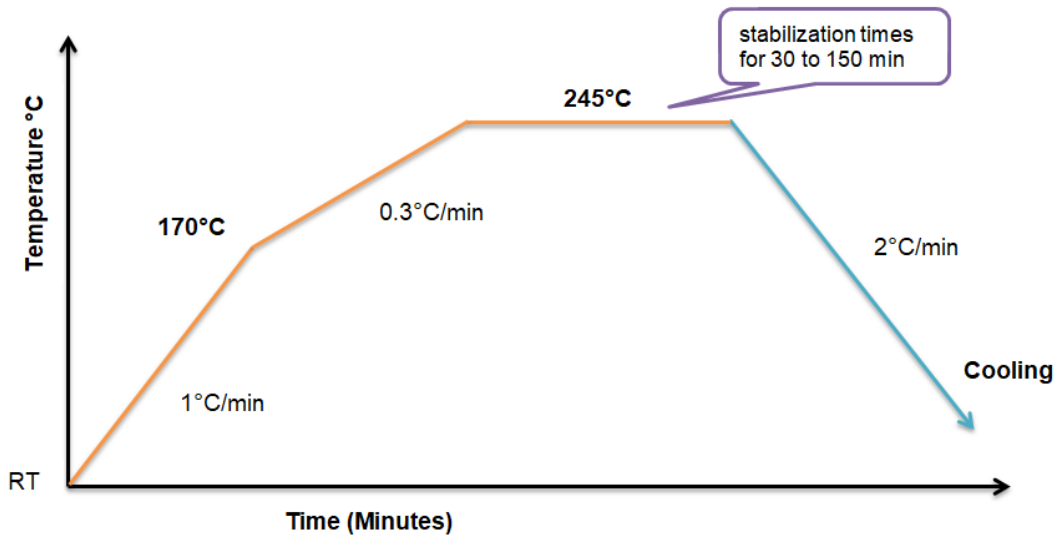

Figure 4.30 Annealing stages of PA66 multifilament

In the process of manufacturing carbon fibers from PA66 precursors, TOS is a very important stage prior to the carbonization phase that allows the precursor fibers to endure higher temperatures in the carbonization process. The main aim of this study was to show the impacts of PBU pretreatment on PA66 multifilaments followed by the TOS process. Thermal stabilization in the air environment has altered the color of the PA66 multifilaments from white to black for a 150 minutes oxidation period at a temperature of 245 °C, through shades of brown in the middle stages. It is believed to have a highly cross-linked aromatized structure in the thermally stabilized PA66 sample, which is specified by the changing color. In the subsequent steps, converting into dark colors confirms the existence of a thermally stabilized structure of the samples. It is supposed to generate a dark color because of performing adequate stabilization and the complexation of the oxygen-based functional groups into the PA66 structure by means of carbonyl (-C=O), hydroxyl (-OH), and carboxylic (-COOH) groups [73]. After 150 minutes TOS process, the PBU incorporated PA66 specimens passed the important flame test by presenting the flame retardant property. Hence, the specimen with a stabilization period of 150 minutes is supposed as entirely stabilized to tolerate higher carbonization temperatures.

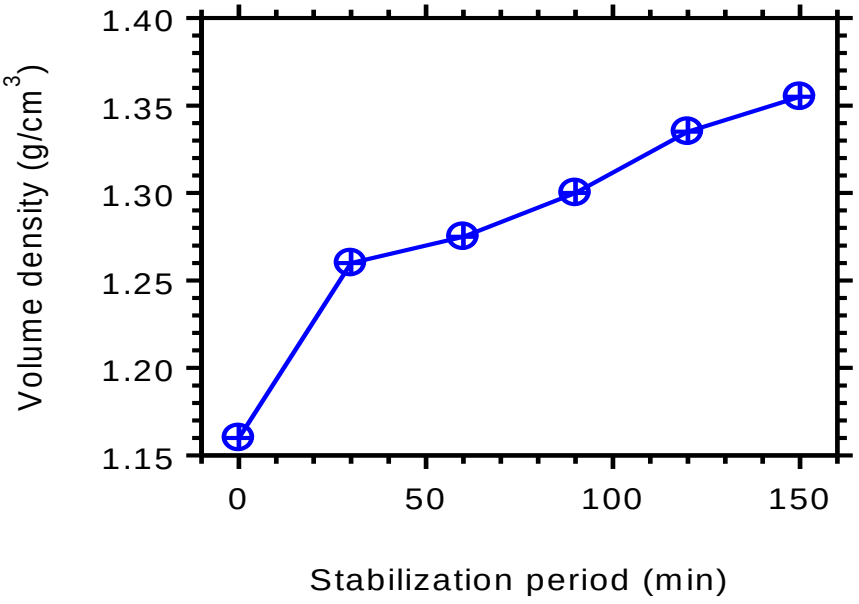

Figure 4.31 Volume density of pristine and PBU incorporated-oxidized PA66 multifilament.

Figure 4.31 shows the volume density values of the pristine and oxidized PA66 samples, which were incorporated with PBU and stabilized for variable times ranging from 30 to 150 minutes. A continuous rise of density values is observed between 30 and 150 minutes of stabilization times. Density values start from 1.145 g/cm^3 for the untreated PA66 and reach 1.355 g/cm^3 for the 150 minutes oxidized PA66 multifilaments. The faster growth of the density values of PBU incorporated-oxidized PA66 multifilaments is ascribed to the development of cyclized and cross-linked ring structures along with the closer packing of the polymer structures ensuing from the cyclization and intra-molecular cross-linking reactions [232].

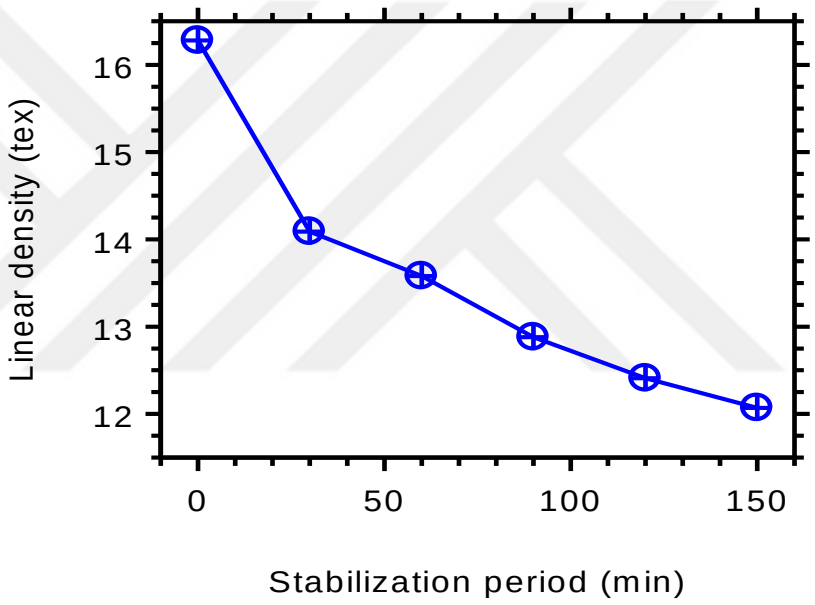

Figure 4.32 Linear density of pristine and PBU incorporated-oxidized PA66 multifilament.

For different TOS periods, the deviation in the linear density of PBU incorporated and stabilized PA66 multifilaments are presented in Figure 4.32. The linear density value was 16.28 tex of the original sample. After 30 minutes of stabilization, the linear density value reduced by 13.45%, and showed a continuous reduction with increasing stabilization period. By 150 minutes oxidative stabilization at 245 °C, the linear density value reached 12.07 tex, which presents the maximum loss of 25.84%. This high level of linear density loss is attributed to water loss by dehydration reactions in the TOS phase.

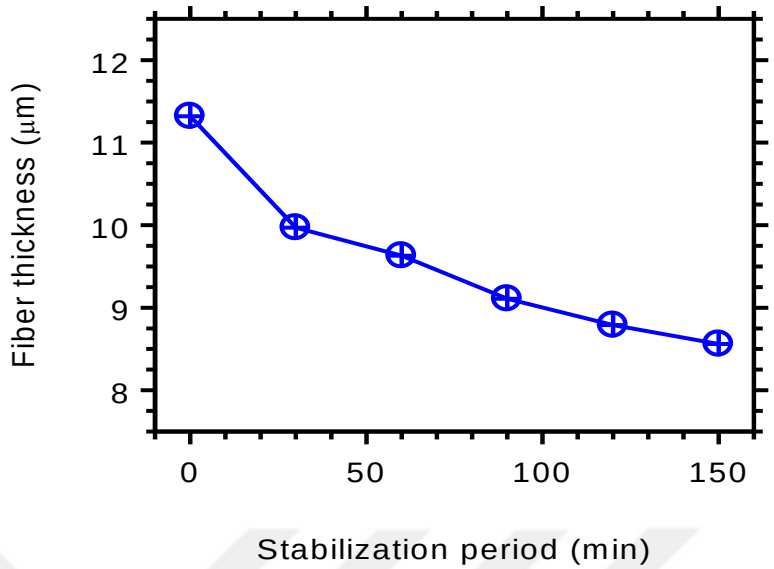

Figure 4.33 Fiber thickness of pristine and PBU incorporated-oxidized PA66 multifilament.

Variations of fiber thickness of the stabilized PA66 fibers are illustrated in Figure 4.33 for the variable stabilization durations. Fiber thickness of the stabilized PA66 was diminished from 11.32 to 8.56 μm with stabilization duration of 150 minutes annealing. The fiber thickness declined continuously with the rise of the stabilization period. The highest drop in fiber thickness was noticed after 150 minutes stabilization with around 24.38% loss in comparison to the original PA66 sample. The primary reason for decreased fiber thickness is the loss of weight of the thermally stabilized sample.

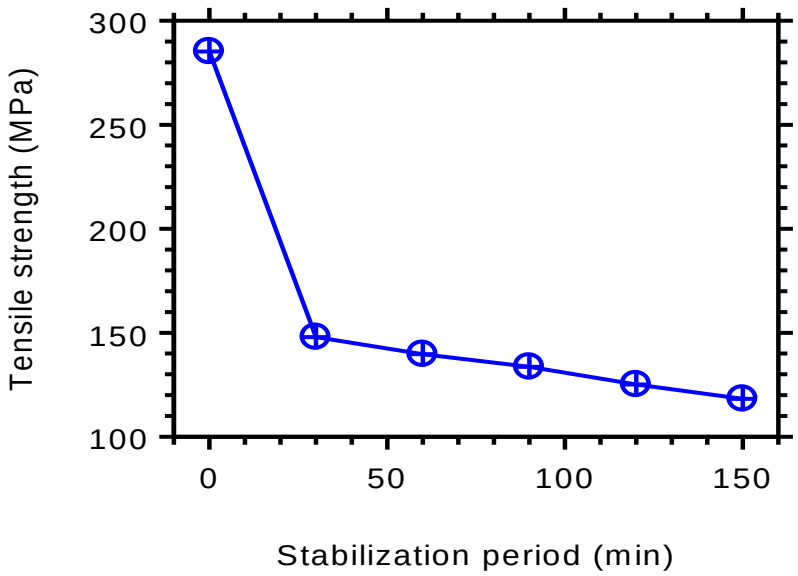

Figure 4.34 Tensile strength of pristine and PBU incorporated-oxidized PA66 multifilament.

The deviations of tensile strength of the pristine and stabilized PA66 multifilaments are illustrated in Figure 4.34. Tensile strength of 30 minutes stabilized PA66 demonstrates a quick decline of around 48.15% from 285.27 MPa of the original PA66 sample. After that, it shows a steady drop until 150 minutes thermal stabilization with 58.54% loss. However, the value of the extension at break of the PBU incorporated-stabilized PA66 sample declines sharply from 28.98% to 3.38%, just after experiencing 30 minutes thermal stabilization at 245 °C. Afterward, this value dropped continuously and reached 1.46% for the 150 minutes thermal stabilization. The reason behind this is the development of the cyclized and cross-linked ring structure along with the closer packing of the polymer structures ensuing from the cyclization and intra-molecular cross-linking reactions that occurred in the TOS process.

The values of linear density, fiber thickness, and tensile strength decrease with increasing stabilization period. This is because of the probable loss of elementary carbon, hydrogen, oxygen, and nitrogen-containing functional groups during the thermal stabilization. However, the components from the PBU impregnation are not estimated to disappear in the TOS process because of their high melting and volatilization temperature.

4.2.3 Thermal and Structural Characterization of Original and Thermally Stabilized PA66 Filament Impregnated with PBU

4.2.3.1 Evaluation of Infrared Spectroscopy Analysis (FT-IR)

The outcomes of IR spectroscopy were examined carefully to observe the pattern of the chemical alterations that occurred in the TOS process. The infrared bands of the original and oxidized PA66 multifilaments in the 4000–2000 cm^{-1} wavenumber zone are illustrated in Figure 4.35 for different TOS temperatures. In the 3500 to 3100 cm^{-1} zone, the spectrum is ascribed for the N–H stretching spectra. Intermolecular hydrogen bonds (H-bonds) are formed within the amide groups in the neighboring polymer chains of the original PA66. The results (Figure 4.35) reveal that the original PA66 multifilament comprises approximately 100% H-bonded chains owing to the absence of spectra beyond 3300 cm^{-1} [251]. The N-H stretching is a combined spectrum that consists of lower frequency '*cis*-conformation' along with higher frequency '*trans*-conformation'

[252]. Because of the transformation of the PA66 structure from '*cis*' to '*trans*', the unbalanced characteristics of the N-H vibration with a lower frequency shoulder and the following modifications can be clarified [252]. It is observable from Figure 4.35 that the original PA66 structure is progressive in 'trans' conformation as at wavenumber 3297 cm^{-1}, where the peak is balanced and sharp. It recommends that there is some type of chemical shrinkage that occurs in the stabilization reactions. Chemical shrinkage is anticipated to cause some chains to change conformation from '*trans*' to '*cis*'. It is also estimated that there is a loss of hydrogen bonds because the interaction between the PBU and the amide groups may cause such transformations. The $GaCl_3$ impregnated PA66 structure was mentioned to show a major intensification of N-H vibration [253].

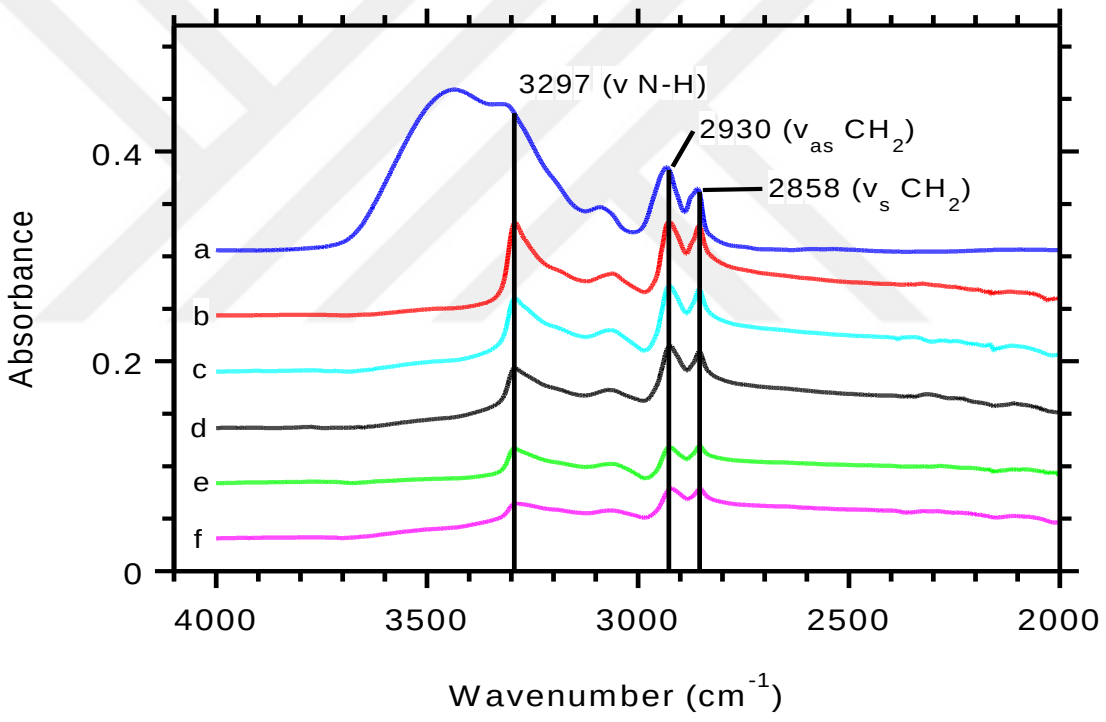

Figure 4.35 IR spectra between 4000–2000 cm^{-1} zone of pristine (a), and stabilized PA66 multifilaments for different stabilization periods (b) 30 min, (c) 60 min, (d) 90 min, (e) 120 min, (f) 150 min.

After the PBU impregnation and TOS process in the air environment, the infrared vibrations of PA66 multifilaments exhibited characteristic intensity deviations, particularly in the vibrations related to CH_2 and N-H stretching at the wavenumber range of 3400 to 2800 cm^{-1}. The development of a wide 'free N-H' spectrum across the wavenumber between 3600 and 3400 cm^{-1} is observable for the oxidized PA66

multifilaments. The addition of PBU combination with the oxygen molecule of amide groups results in the existence of free N-H spectra (Figure 4.35). As soon as the PBU generates coordination bonding with the oxygen molecule of amide groups, H-bonds from the polymer structures become separated and liberate the N-H spectra [253]. Because of the unchanged peak position with the alteration of crystalline phases, the N-H spectra were noticed to be conformationally insensitive [254]. The vibrations at 3297 and 1630 cm^{-1} are accredited to C=O and N-H stretching bands, which intensely rely on the interactions of the H-bonds within the PA66 structure [253].

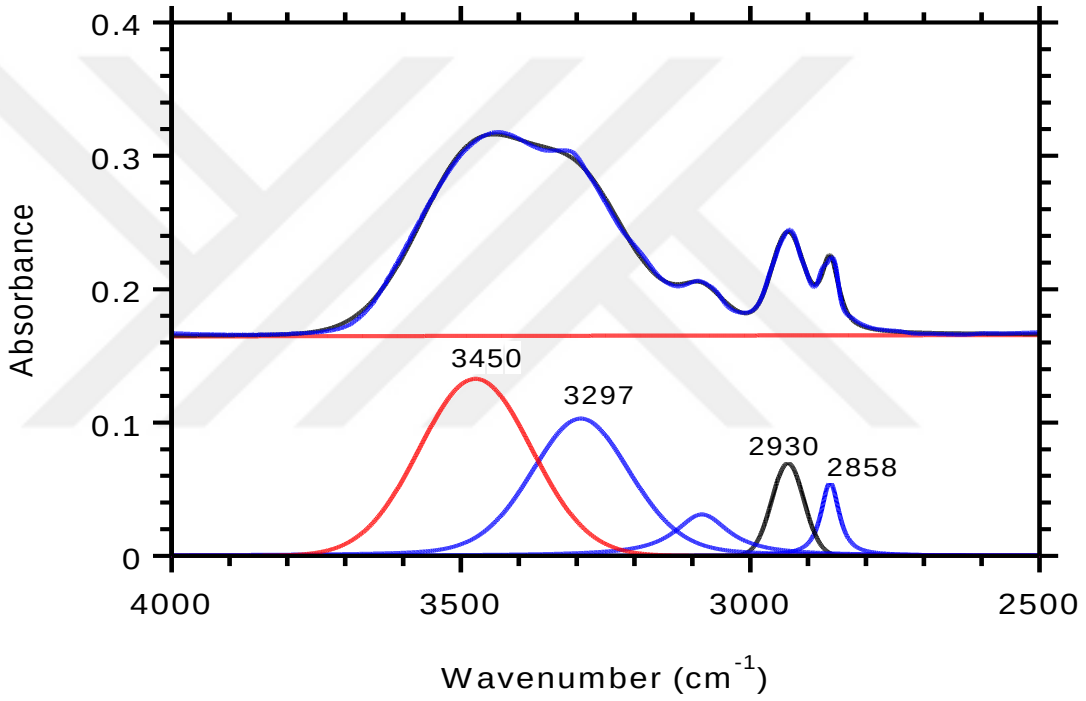

Figure 4.36 Curve fitting of original PA66 multifilaments in the 4000-2500 cm^{-1} wavenumber zone.

With an increased stabilization period, the intensity of the CH_2 and N-H bands at 3297, 2930, and 2858 cm^{-1} declined steadily instead of disappearing entirely. The bandwidths of the CH_2 and N-H vibrations were noticed to extend with the increase of the stabilization period. As the stabilization period progressed, most of the intensities of the CH_2 spectra at 2930 and 2858 cm^{-1} were gradually lost. However, a small amount of intensity persisted, which indicates that few of the hydrogen atoms did not participate in the dehydrogenation process. Table 4.5 presents the band assignments of the infrared absorption spectra of polyamide 66 fiber.

Table 4.5 The band assignments of the IR absorption spectra of polyamide 66 fiber.

Band position, cm^{-1}	**Band Assignment**
3450 (sh)	'Free' N-H stretching [251]
3298 (s)	Hydrogen bonded N-H stretching [251]
3190 (sh)	N-H stretch + amide (I + II) overtone [255]
3075 (m)	N-H stretching + amide II overtone [255]
2930 (s)	CH_2 asymmetric stretching [251]
2860 (s)	CH_2 symmetric stretching [251]
1743 (w)	Carbonyl (C=O) stretching [251]
1634 (s)	Amide I (mainly C=O stretching) [251]
1530 (s)	Amide II, N-H in-plane bending+C-N stretch+C-C stretching [251]
1475 (m)	CH_2 scissoring vibration next to N-H group, trans conformation [255]
1465 (m)	CH scissoring not adjacent to the amide group [255]
1417 (m)	CH_2 scissoring vibration next to C=O group, trans conformation [255]
1370 (m)	Amide III, C-N stretching + in-plane N-H deformation [256]
1328 (w)	CH_2 wagging or twist + Amide III (NHCO) stretching mode [255]
1270 (m)	Amide III coupled with hydrocarbon skeleton [257]
1224 (w)	CH_2 wagging or twisting + NHCO stretching mode, 'fold' band [255]
1197 (m)	Amide III coupled with hydrocarbon skeleton, 'Crystalline' [256]
1180 (m)	CH_2-NH (amorphous) [258]
1147 (m)	C-CH symmetric bending + CH_2 twisting Gauche confirmation [251]
1140 (m)	C=O twisting (amorphous) [259]
1063-1066 (w)	Skeletal C-C stretching [259]
1033-1043 (w)	Skeletal C-C stretching [259]
1014-1019 (sh)	Skeletal C-C stretching [259]
988 (w)	NH rocking mode [259]
934 (m)	Amide stretching mode (C-C=O), '*trans* conformation' [259]
906 (m)	Amide stretching mode (C-C=O) [259]
728 (w)	Amide IV (N-H rocking) [258]
684 (m)	Amide V [258]
578 (m)	Amide VI [258]
533 (w)	Skeletal bending (O=C-N) [258]

The occurrence of dehydrogenation reactions in the TOS process is confirmed by the intensity loss of CH_2 vibration. The intensity of the hydrogen-bonded N-H band for the sample stabilized at 245 °C for 150 minutes disappeared completely, indicating the complete loss of H-bonds from the amide groups of polymer structure. This also confirms the full participation of hydrogen-bonded N-H groups in the complexation with PBU. Due to the integration of PBU with the PA66 chains, the status of the CH_2 spectra was noticed to be unchanged. In the wavenumber range of 3000 to 2800 cm^{-1}, the C-H stretching spectra are not anticipated to be influenced by the chemical incorporation. Likewise, these bands do not have any prime contribution to H-bond development [253].

In the wavenumber zone between 3700 and 2800 cm^{-1}, the intensity values of CH and NH declined continuously; however, they never vanished entirely with an increased stabilization period (Figure 4.35). Because of the loss of intermolecular H-bonding, the NH vibrations of the stabilized PA66 multifilaments primarily displayed certain sharpening; however, they lost the maximum intensities with increased time. Because of the influence of dehydration occurred by the interaction of boron phosphate (BPO_4) with NH groups in the primary stages of the TOS process, the intensity values of 3215 and 3176 cm^{-1} vibrations accredited for the gradual decrease of intermolecular NH groups with the progress of the stabilization time (Figure 4.35). This specifies the incidence of interruption in the intermolecular H-bonding within the PA66 polymer structures. Certain intensity loss was observed in the wavenumber zone comprising 3537, 3442, and 3297 cm^{-1} vibrations accredited to intra-molecular NH groups; however, complete intensity loss was never observed for the rise in stabilization time (Figure 4.35).

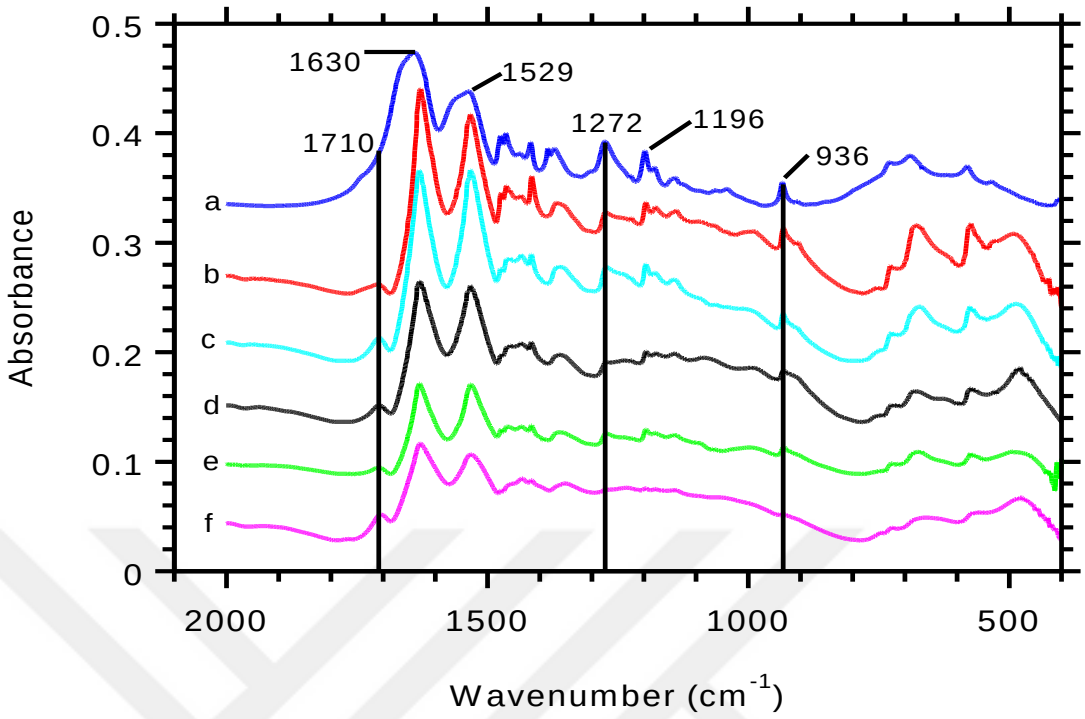

Figure 4.37 IR spectra between 2000–400 cm^{-1} zone of pristine (a), and stabilized PA66 multifilaments for different stabilization periods (b) 30 min, (c) 60 min, (d) 90 min, (e) 120 min, (f) 150 min.

In Figure 4.37, the infrared spectra of original and oxidized PA66 multifilaments are illustrated for different stabilization periods in the range of 2000 to 400 cm^{-1}. This range comprises a number of vibrations of amide I, amide II, amide III, amide IV, amide V, and amide VI bands alongside some amorphous and crystalline spectra [256, 258, 259]. For the oxidative cross-linking reactions, the infrared bands of the oxidized PA66 multifilaments revealed the existence and development of a new shoulder at a wavenumber of 1710 cm^{-1} that is accredited to C=O stretching. As the stabilization period increased, the band intensity of this shoulder steadily strengthened. At 1630 and 1529 cm^{-1}, the peaks of amide I and amide II are the strongest vibrations in the spectra. At 1630 cm^{-1}, the amide I vibration is recognized to be controlled by the C=O stretching spectrum [255]. At 1272, 1196, and 936 cm^{-1}, the infrared spectra conforming to the crystalline phase have lost their maximum intensities with the increase of the oxidation period because of the loss of H-bonds present in the polymer structure initiates the apparent de-crystallization reactions.

The IR spectra of the samples with stabilization times between 30 and 120 minutes show the shifting of the frequency of the amide I vibration at 1635 cm^{-1} to a lower frequency at 1630 cm^{-1}, specifying the interaction of PBU with the carbonyl oxygen atoms. Whereas the amide II vibration at 1529 cm^{-1} did not change during the stabilization reactions. The intensities of most of the bands were lost once the TOS period of 150 minutes was reached because the onset of de-crystallization reactions occurred for the integration of PBU with the PA66 sample.

In particular, the IR spectrum positioned at 936 cm^{-1} is reported to be a crystalline band [251]. The IR band positioned at 1630 cm^{-1} is allotted to amide-I vibrations mostly due to the (C=O) carbonyl group being used as an internal reference band to follow the structural changes occurring during the thermal stabilization reactions for different stabilization periods [251]. The absorbance ratio of 936 cm^{-1}/1630 cm^{-1} for different stabilization periods is illustrated in Figure 4.38.

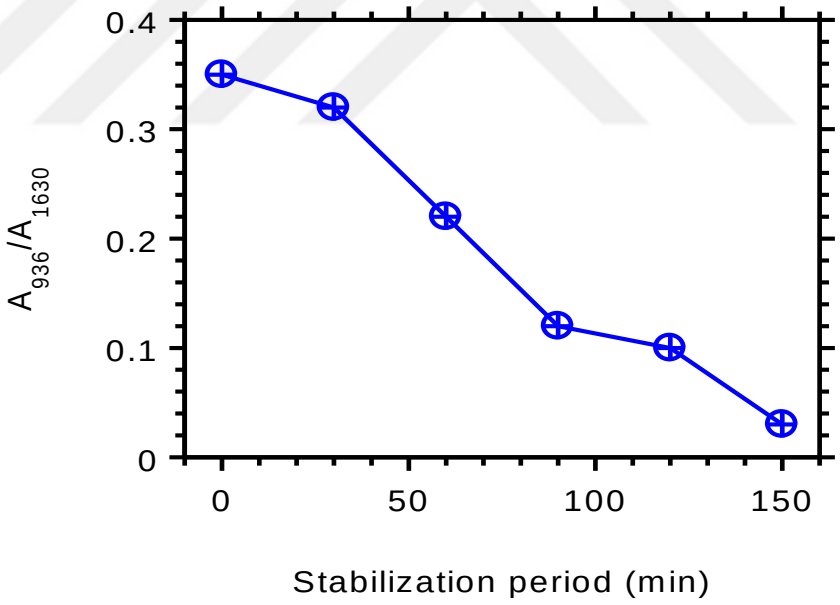

Figure 4.38 Normalized absorbance ratio (A_{936}/A_{1630}) of pristine and PBU incorporated-oxidized PA66 multifilament.

The outcomes illustrated in Figure 4.38 indicate that the degree of crystallinity of the PA66 multifilaments under consideration decreases because de-crystallization reactions occur in the thermal stabilization reactions with the stabilization period progress.

IR bands located at 2930 and 2858 cm^{-1} are allotted to methylene (CH_2) asymmetrical and symmetrical stretching vibrations [259]. As mentioned before, the IR spectrum at 1630 cm^{-1} allotted to carbonyl (C=O) vibration is used as a reference band to normalize the absorbance values. With progressing stabilization reactions, dehydrogenations occur to produce a thermally stabilized structure.

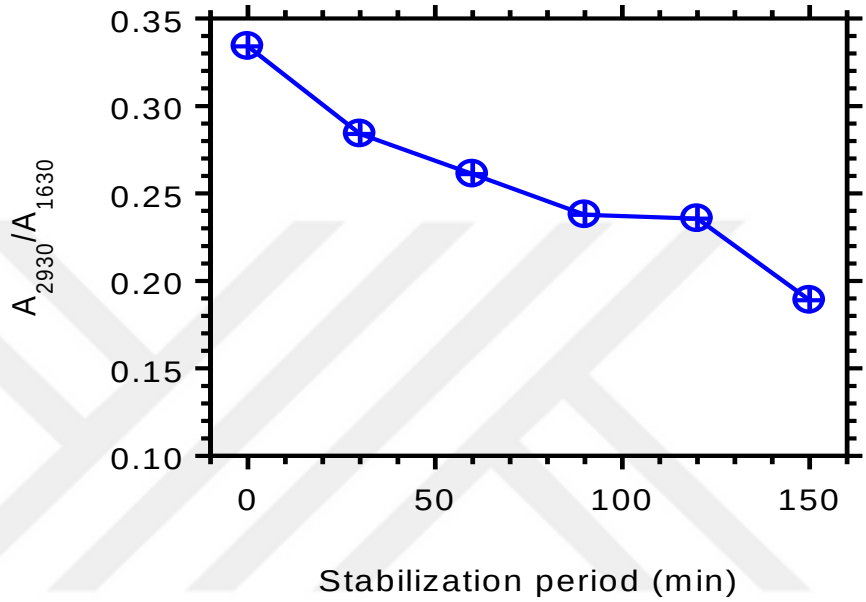

Figure 4.39 Variation of dehydrogenation index (A_{2930}/A_{1630}) for different stabilization periods.

We have also considered the definition of dehydrogenation index. The absorbance ratio of A_{2930}/A_{1630} is used to describe dehydrogenation index values. Variations of dehydrogenation index values for different stabilization periods are presented in Figure 4.39. The results suggest progressing dehydrogenation reactions with the stabilization period increases. In the TOS reactions, dehydrogenation of methylene groups results in thermally stabilized structures in the development of cyclized structures comprising (C=C) double-bonded carbon-carbon groups.

The IR bands of the PA66 multifilaments stabilized at 245 °C for 150 minutes demonstrated the existence of a spectrum at 1415 cm^{-1} because of the asymmetric B–O stretching of the BO_3 group. Another band is also present at 1161 cm^{-1}, which is ascribed to B–O–H bending [260]. The existence of unaffected H_3BO_3 in the PA66 multifilaments is directed by the 1415 and 1161 cm^{-1} vibrations. A spectrum, ascribing the borate group (O–B–O, BO_4), was observed at 1124 cm^{-1} for all the stabilized PA66

multifilaments [261]. The shoulder at 1066 cm^{-1} is ascribed to the P–O symmetrical spectrum in the phosphate groups (O–P–O) for the PA66 multifilaments [262]. In polyphosphates, the asymmetrical stretching of P–O–P was indicated by the 990 cm^{-1} spectrum [262]. In the PBU impregnated-stabilized PA66 multifilaments, the attendance and development of phosphate groups are affirmed by the existence of P–O–P and P–O bands. The existence of O–P–O in the PBU impregnated PA66 samples stabilized at 245 °C for 150 minutes is specified by the 552 cm^{-1} spectrum [263].

From the IR analysis, the obtained outcomes revealed that the incorporation of PBU with PA66 multifilaments stimulated the dehydration process. At reduced temperatures, the cross-linking and dehydration reactions were improved by the development of boron phosphate. By hindering the primary hydroxyl groups, BPO_4 also stopped the development of volatile substances

4.2.3.2 Evaluation of Thermogravimetric Analysis (TGA)

The thermogravimetric analysis technique was employed to characterize the thermal stability of the original and the PBU impregnated-stabilized PA66 multifilament samples. Experience demonstrates that comparatively sharper and contracted temperature range associated with declining weight results in a quicker decomposition process and results in significant weight losses and in poorer carbon yield percentages.

The TGA thermogram of the original PA66 (Figure 4.40a) is characterized by a single-step decomposition at 430 °C in a nitrogen environment. For the PBU impregnated and oxidized PA66 samples (Figure 4.40b-f), the TGA thermograms exhibit a two-step decomposition at 430 and 360 °C under nitrogen atmosphere. At temperatures from 50 to 350 °C, the raw PA66 multifilaments persist as thermally stable without showing any indication of weight loss. Figure 4.40a shows a single-step decomposition above 400 °C. This region of thermal stability is followed by a comparatively quicker rate of decomposition up to 470 °C. At about 1000 °C, the overall weight loss was 99.5%, and the resultant char yield was 0.6%. In Figure 4.40b-f, a loss of absorbed water from the samples was observed up to 104 °C and afterward, at temperatures of 330 to 470 °C, a

sudden massive weight loss was noticed because of the catalytic influence of PBU in the degradation reactions.

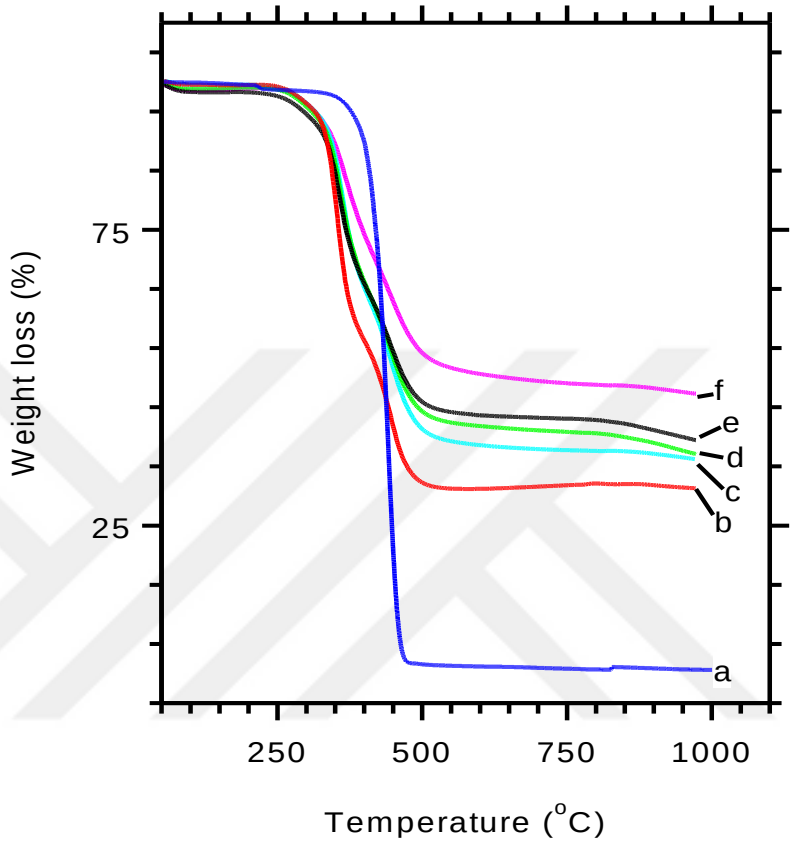

Figure 4.40 TGA thermograms of pristine (a) and PBU incorporated-stabilized PA66 multifilaments for different stabilization periods. (b) 30 min; (c) 60 min; (d) 90 min; (e) 120 min; (f) 150 min.

For different stabilization periods, TGA thermograms of PBU incorporated and oxidized PA66 multifilaments are illustrated in Figure 4.40. TGA thermograms show the decline of weight loss with an increase of stabilization periods, which confirms the enhancement of carbon yield for the cross-linking reactions within PA66 molecular structure. Because of the development of a ladder-like structure with improved cross-linking, PBU impregnated and oxidized PA66 samples present their weight loss through a wider temperature range. In contrast, the weight loss of the pristine PA66 sample is observed within a narrow temperature range.

For the pristine and PBU incorporated-oxidized PA66 multifilaments, an assessment of the carbon yield values at temperatures of 500 and 1000 °C is presented in Figure 4.41. The outcomes reveal the continuous increase of carbon yield percentage by the intensification of the stabilization period. At 500 °C, the value of carbon yield is noticed to be greater than that of 1000 °C, ranging from 31% and 47%. The results show the highest carbon yield value of PBU impregnated 150 minutes stabilized PA66 multifilaments by 47% at 1000 °C.

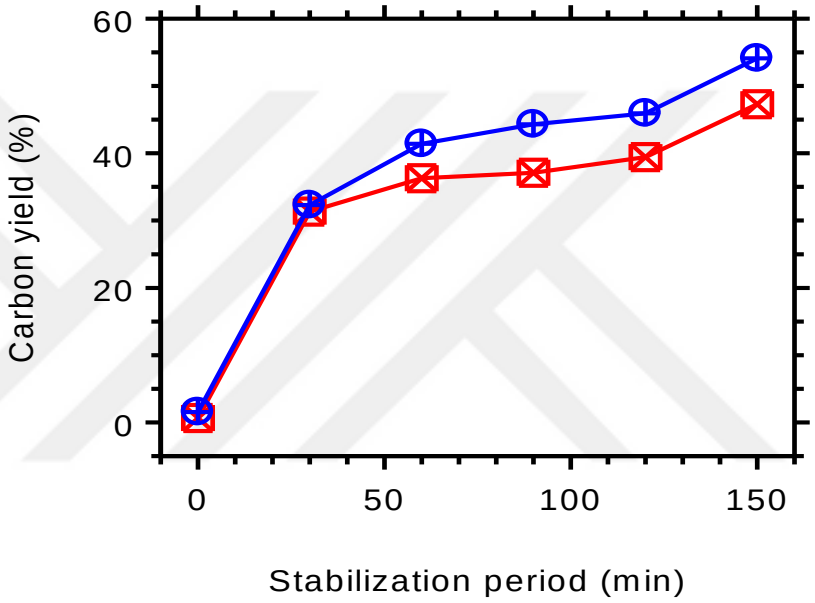

Figure 4.41 Deviation of carbon yield (%) of pristine and PBU incorporated-oxidized PA66 multifilament at temperatures of (O) 500 °C and (□) 1000 °C.

The outcomes acquired from the TGA analysis revealed that enhanced thermal stability is more noticeable in the PBU incorporated-oxidized PA66 multifilaments than in the pristine sample due to vast cross-linking within the PA66 molecular structure. PBU incorporation seems to stimulate very influential oxidation and carbonization (in the imitated carbonization of TGA performed in nitrogen environment) process because of the intermolecular and intramolecular cross-linking reactions and cyclization reactions. PBU integration with PA66 multifilaments helped greatly to result in the occurrence of dehydrogenation and cyclization processes. The unsaturated sites, formed in the dehydrogenation reactions, are advanced by the development of intermolecular cross-links, which result in greater carbon yield percentage in the samples.

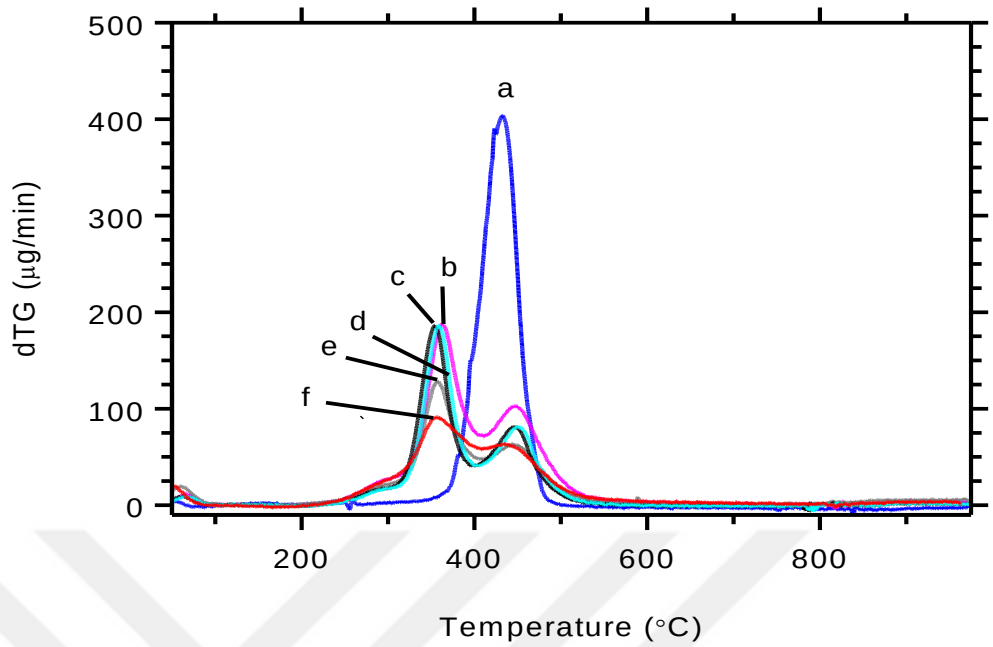

Figure 4.42 dTG thermograms of original (a) and thermally stabilized PA66 multifilament for different residence periods. (b) 30 min (c) 60 min (d) 90 min (e) 120 min (f) 150 min.

The dTG profile of the pristine PA66 ample represents two major exothermic peaks positioned at around 430 and 403 °C (Figure 4.42). After the thermal stabilization process, the dTG peak for the stabilized samples moves to 360 °C, and a new peak appears at 445 °C. The exothermic peak located at 360 °C is large in intensity in comparison with the peak at 445 °C. These peaks are assigned to cyclization and aromatization reactions of the polyamide 66 multifilament with the discharge of different gaseous byproducts, such as NH_3, HCN, H_2O, CO, CO_2, amines, and low molecular weight organic species [217, 264–266].

Table 4.6 dTG results due to the original and PBU impregnated and thermally stabilized PA66 multifilament

Residence time (min)	1st peak temperature (°C)	1st peak temperature height	2nd peak temperature (°C)	2nd peak height
0	430.0	403.0	-	-
30	359.0	187.0	446.0	102.0
60	359.0	186.0	445.0	98.0
90	356.0	180.0	446.0	81.0
120	356.0	128.0	446.0	62.0
150	356.0	91.0	444.0	63.0

The peak noticed at 100 °C is assigned to the presence of water. From the results obtained, it can be seen that aromatization reactions occur because of the development of C=C (C=N) bonds resulting in the creation of aromatic structures [264]. At the end of the residence time (150 min), a significant exothermic reaction in thermally stabilized PA66 samples was not observed. During TOS reactions, stabilized PA66 multifilaments are involved in intramolecular aromatization reactions, ensuing in a continuous decrease of the exothermic peak zone with the increase of residence period.

Table 4.6 and Figure 4.42 show that the exothermic heat steadily decreases with the increase of the stabilization period and results in the reduction of the heights of the peaks. The steady reduction of exothermic heat due to aromatization reactions with increasing stabilization time is observed in Figure 4.42. Gradual weakening of exothermic peaks may be involved with the formation of aromatic structures that occurred in the course of TOS reactions. Detailed analysis of TGA thermograms strongly suggests that PBU incorporation improves thermal stability for different stabilization periods.

4.2.3.3 Evaluation of X-ray Diffraction Analysis (XRD)

The extents of X-ray diffraction mentioned by Bunn and Garner [267] specified the presence of α and β crystalline forms coexisting in the PA66 multifilaments. The α-phase structure was originally recommended [267] as the main phase in the PA66 multifilaments. Only a small fraction of the β-phase was observed at $2\theta=12°$ associated to the 010 reflection. Each of these crystalline patterns are known to have a triclinic unit cell, whereas the α-phase was mentioned to have the unit cell parameters as follows [267]: a = 0.49 nm, b = 0.54 nm, c = 1.72 nm, $\alpha = 48.5°$, $\beta = 77°$, $\gamma = 63.5°$.

In the (010) plane, the α-phase is identified to hold the H-bonded chain contained planar sheets. In this stage, the polymer chains are connected to each other by H-bonds within the amide groups to generate sheets. These H-bonded sheets are moved in the upward direction by 0.36 nm. In the (010) plane, hydrogen-bonded sheets are also present for the β-phase. Along the c-axis, the comparative positions of the following H-bonded sheets are the only dissimilarity between the two crystalline phases. In the β-phase, the

subsequent H-bonded sheet is moved in the upward direction as regards the first one, and the third sheet comes back to a similar stage as the first sheet [267], for the pristine and PBU incorporated-oxidized PA66 multifilaments stabilized at 245 °C by different stabilization periods. The equatorial X-ray diffraction profiles are illustrated in Figure 4.43.

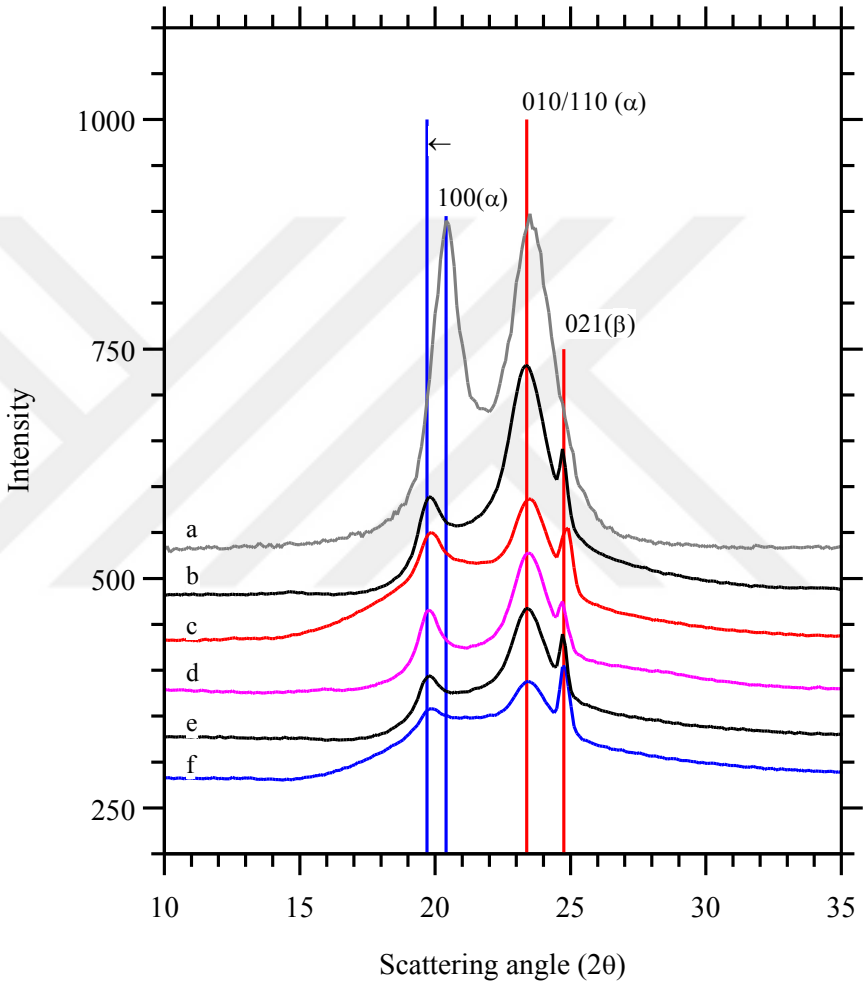

Figure 4.43 Equatorial X-ray diffraction profiles of pristine (a) and 3% PBU incorporated-oxidized PA66 multifilament for different stabilization periods (b) 30 min; (c) 60 min; (d) 90 min; (e) 120 min; (f) 150 min.

Table 4.7 Peak parameters of the equatorial X-ray diffraction profile of pristine PA66 multifilament acquired by the curve-fitting technique.

Peak ref.	f	A (Height)	W (Width)	Position (2θ)	d-obs spacing (nm)	d-calc spacing (Å)
100 (α)	0.9	245.9	1.28	20.38	0.434	0.436
Amorph.	0.8	145.7	6.00	22.20	0.400	-
010/110 (α)	1.0	234.7	1.89	23.65	0.376	0.369
021 (β)	1.0	36.7	0.5	25.35	0.351	0.350

In the Equatorial X-ray diffraction profile, the co-existence of a polymorphic structure comprising α- and β-crystalline forms accompanied by an amorphous phase is revealed for the pristine PA66 multifilament (Figure 4.44). With the curve-fitting technique, the acquired peak parameters of pristine PA66 multifilament are mentioned in Table 4.7 along with the contrast of the calculated and observed d-spacing values.

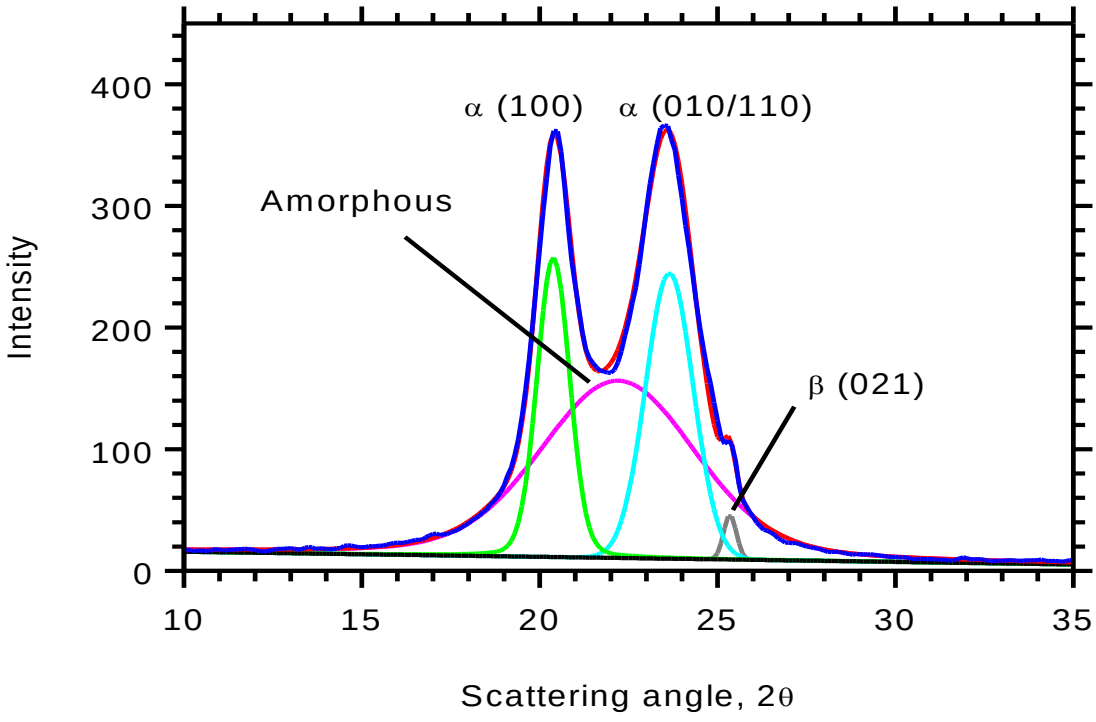

Figure 4.44 Curve-fitting of the equatorial X-ray diffraction profile of pristine PA66 sample.

Table 4.8 Peak parameters of pristine PA66 acquired by the curve fitting technique.

Peak	Profile function parameter (f)	Peak height (A)	Peak width (2θ°)	Peak position (2θ°)	Peak area
100 (α)	0.77	291.5	1.16	20.40	482.5
010/110 (α)	0.44	280.5	1.77	23.61	627.5
Amorphous	0.0	79.3	4.72	22.26	398.3
021 (β)	0.94	45.3	0.22	25.34	15.5

A thorough analysis of the equatorial X-ray diffraction profile of pristine PA66 multifilament (Table 4.8, Figure 4.43a) demonstrates two major reflections at 2θ=20.40° and 23.61°, mentioned as a (100) and (010/110) α-phase peak [267], which was superimposed on a wide amorphous corona. In Figure 4.44, the resolved X-ray diffraction profile also reveals the existence of a peak positioned at 2θ=25.36° as a shoulder, cited as the (021) β-phase peak.

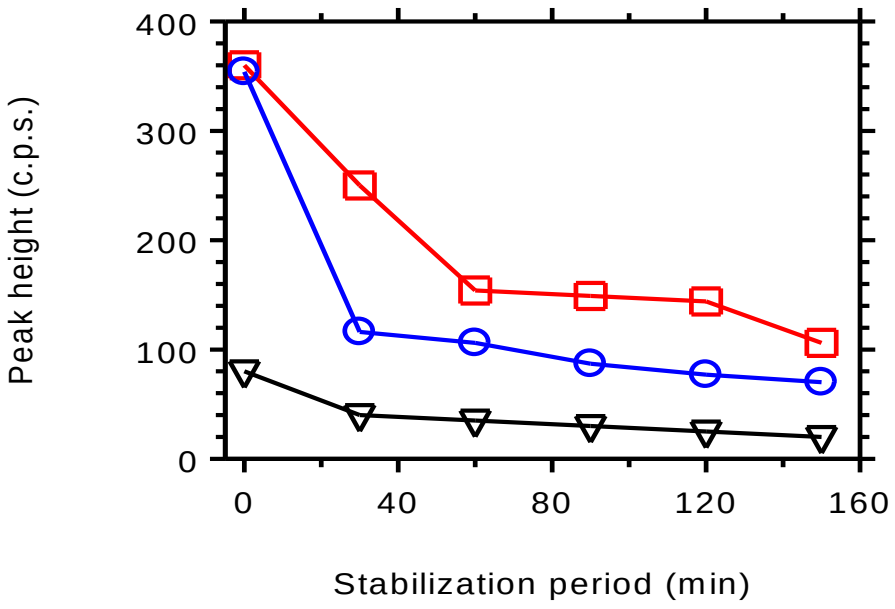

Figure 4.45 Comparison of resolved peak heights of the original and PBU incorporated-oxidized PA66 multifilament for different stabilization periods. (□) (010/110) α-phase peak; (O) (100) α-phase peak; (∇) Amorphous peak at 22.5° 2θ.

A comprehensive analysis of the equatorial X-ray diffraction profiles of the pristine and PBU incorporated-oxidized PA66 multifilaments shows a continuous crystalline structure loss by progressing stabilization period (Figure 4.43). By employing curve fitting technique, the obtained intensity of the 100 and 010/110 α-phase peaks constantly dropped (Figure 4.44 and Figure 4.45). It seems that the intensity of (010)/110) peaks is persistently higher than the (100) α-phase peak (Figure 4.45).

From this characteristic, it is clearly understandable that certain amorphization reactions take place in the TOS process. In the equatorial X-ray diffraction profile, the existence of the (100) and (010/110) α-phase peaks seem to weaken considerably but survived the stabilization reactions followed by the 150 minutes TOS period (Figure 4.45). In any case, the intensity of the (010/110) reflection appears to be continuously greater than the (100) α-phase peak. Within (010) planes, the H-bonded layers of the α- and β-phases take place, as illustrated in Figure 4.45. With the increase of the stabilization period, a great loss of H-bonding is observed within the amide groups of the PA66 structure, which is directed by the intensity loss of the (010) α-phase peak structure.

Because of the loss of the H-bonding between the PA66 structures, the values of d-spacing of the (100) and (010/110) α-phase peaks seem to demonstrate deviations by the TOS reactions. The value of d-spacing of the (100) α-phase peak declined from 0.434 nm for the original PA66 multifilament to 0.430 nm, owing to the PBU incorporation and TOS process in the sample. This clearly demonstrates that the internal gap between the H-bonded layers drops gradually, and the layers come closer separately (Figure 4.44). The value of d-spacing of the (010/110) α-phase peak increased from 0.376 nm for the original PA66 to 0.382 nm for the PBU incorporated-stabilized PA66 samples. This demonstrates that the H-bonded layers go away individually because of the displacement of the H-bonds within the PA66 structure.

By means of the curve fitting technique, the obtained peak parameters can be employed to obtain the degree of apparent crystallinity and the crystalline phases. By employing Equation 3, the phase fractions were assessed by employing resolved peak areas. The entire peak areas of both the (100) and (010/110) peaks were used to evaluate the α-phase, while only the peak area of the (021) reflection was used to evaluate the β-phase fraction.

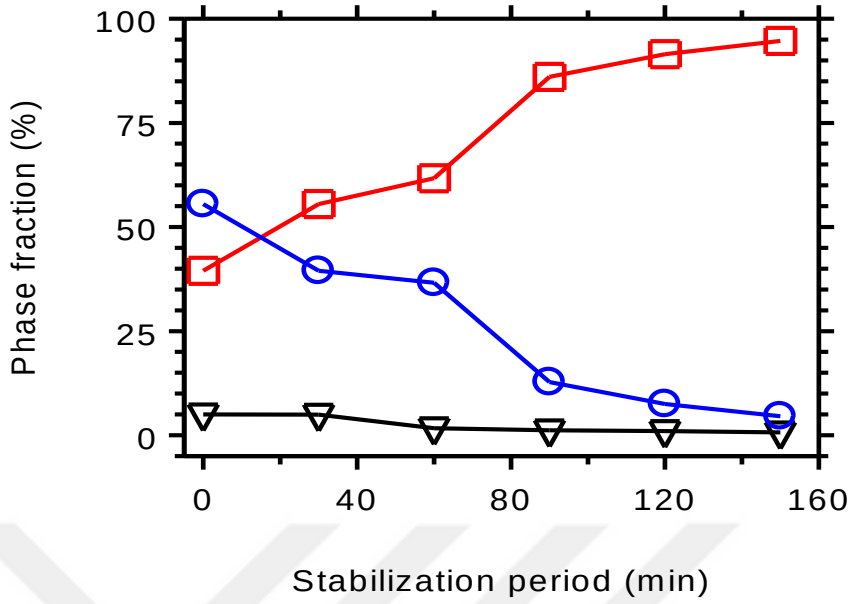

Figure 4.46 Changes of phase fractions for the PBU treated and oxidized PA66 multifilament for different stabilization periods. (O) α–phase; (∇) β– phase; (□) Amorphous phase.

For different stabilization periods, the changes of the phase fractions are demonstrated in Figure 4.46 by means of α-, β-, and amorphous phases. From Figure 4.46, it is clear that the α-phase fraction is persistently greater than the β-phase, and in both cases, the fraction value falls with the progression of the stabilization period. In contrast, the fraction of the amorphous phase constantly intensified by increasing time because of the onset and advancement of the de-crystallization reaction occurrence in the TOS process. After the 150 minutes TOS period, the value of α-phase declines from 56% to 5%, while the β-phase declines from 5% to 1%. In contrast, the fraction value of the amorphous phase increases from 40% to 95% after the 150 minutes TOS process.

The X-ray stabilization index was evaluated by employing a novel approach employing the intensity values of the (100) and (010/110) α-phase peaks acquired by the curve-fitting technique by means of Equation 2. The outcomes shown in Figure 4.47 reveal the growing X-ray stabilization index values by the growing stabilization period, which can be a dependable way to measure the percentage of ladder structure developed in the TOS stage. The outcomes illustrated in Figure 4.47 reveal prompt stabilization within 30 minutes of the TOS period, attaining about 50%. The PA66 multifilament stabilized at 245 °C for 150 minutes, showed an X-ray stabilization index value of 75%.

Integration of PBU combination with the PA66 fiber structure is supposed to help in forming ladder-like structures, which contribute to increasing the X-ray stabilization index value with the increasing stabilization period.

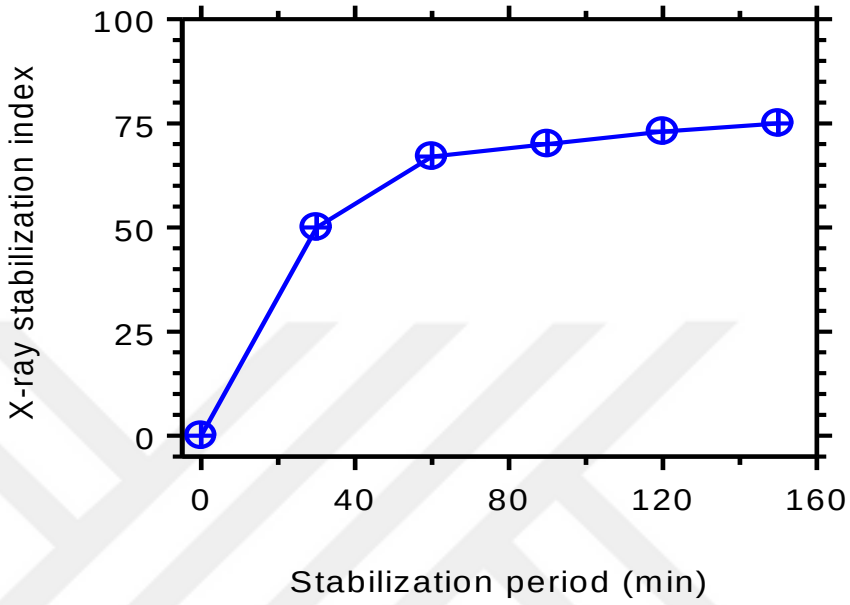

Figure 4.47 Changes of X-ray stabilization indices for the PBU incorporated-stabilized PA66 multifilament for different stabilization periods.

4.2.3.4 Elemental Analysis

Figure 4.48 shows the findings of elemental analysis of PBU incorporated and stabilized PA66 multifilaments for different stabilization periods. The outcomes represent a steady decrease of carbon and nitrogen content while a constant increase of oxygen content over the TOS period. In the TOS process, the integration of oxygen and the subsequent loss of hydrogen are intimately linked to the declining amounts of carbon and nitrogen content [268]. After impregnating phosphoric acid, boric acid, and urea solution and stabilizing for 30 min, the phosphorus and boron content in the PA66 samples were 3.43% and 0.04%, respectively. However, with the progress of stabilization duration, these values decreased steadily.

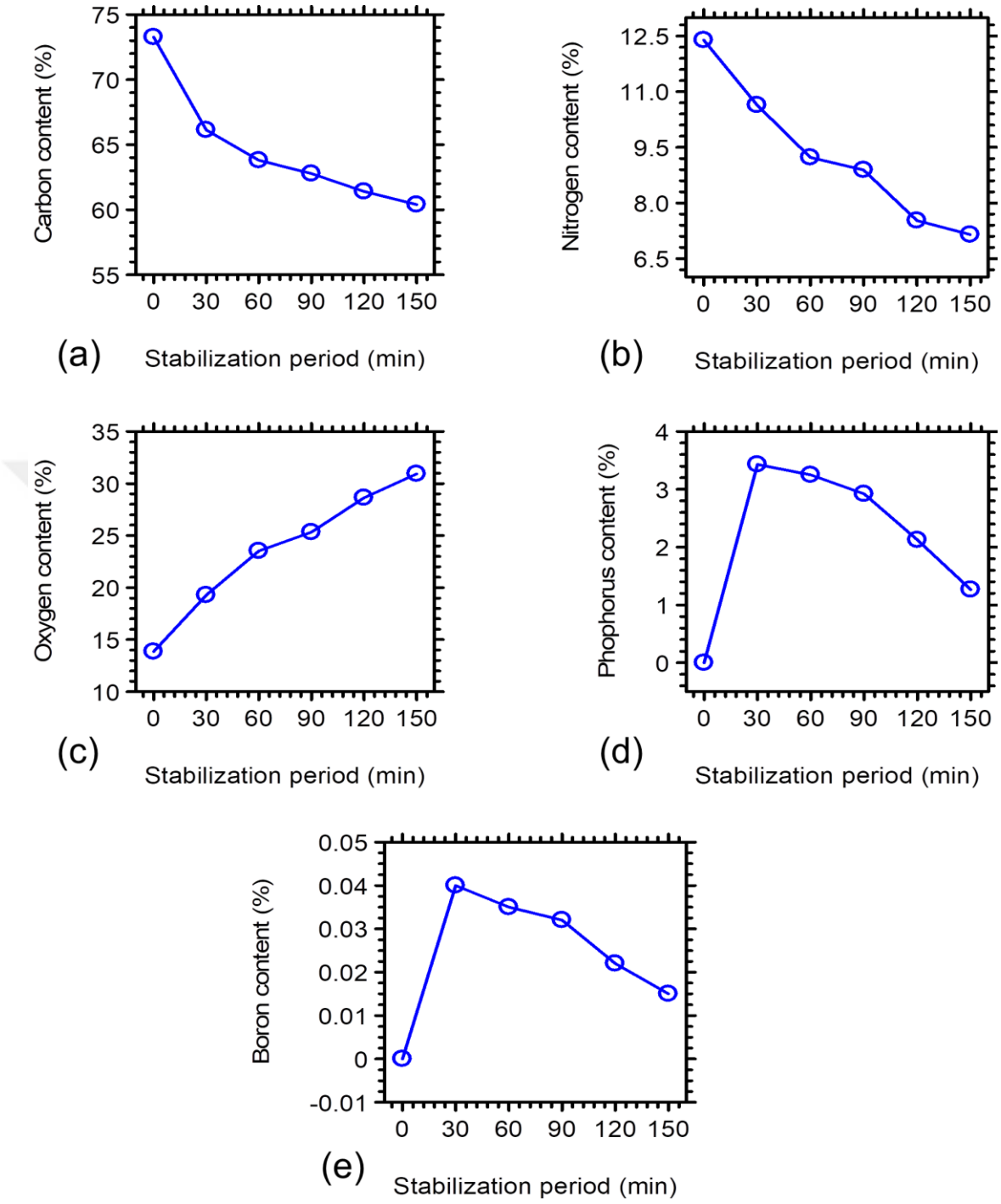

Figure 4.48 Elemental analysis of pristine and PBU incorporated-stabilized PA66 multifilaments for different stabilization periods. (a) carbon (wt%), (b) nitrogen (wt%), (c) oxygen (wt%), (d) phosphorus (wt%), and (e) boron (wt%).

4.2.3.5 Scanning Electron Microscopy (SEM)

Scanning electron microscopy was employed to assess the surface properties of the PBU incorporated and stabilized PA66 samples as represented in Figure 4.49. The SEM study revealed that the surface characteristics do not signify severe changes of the stabilized PA66 specimens for variable stabilization periods.

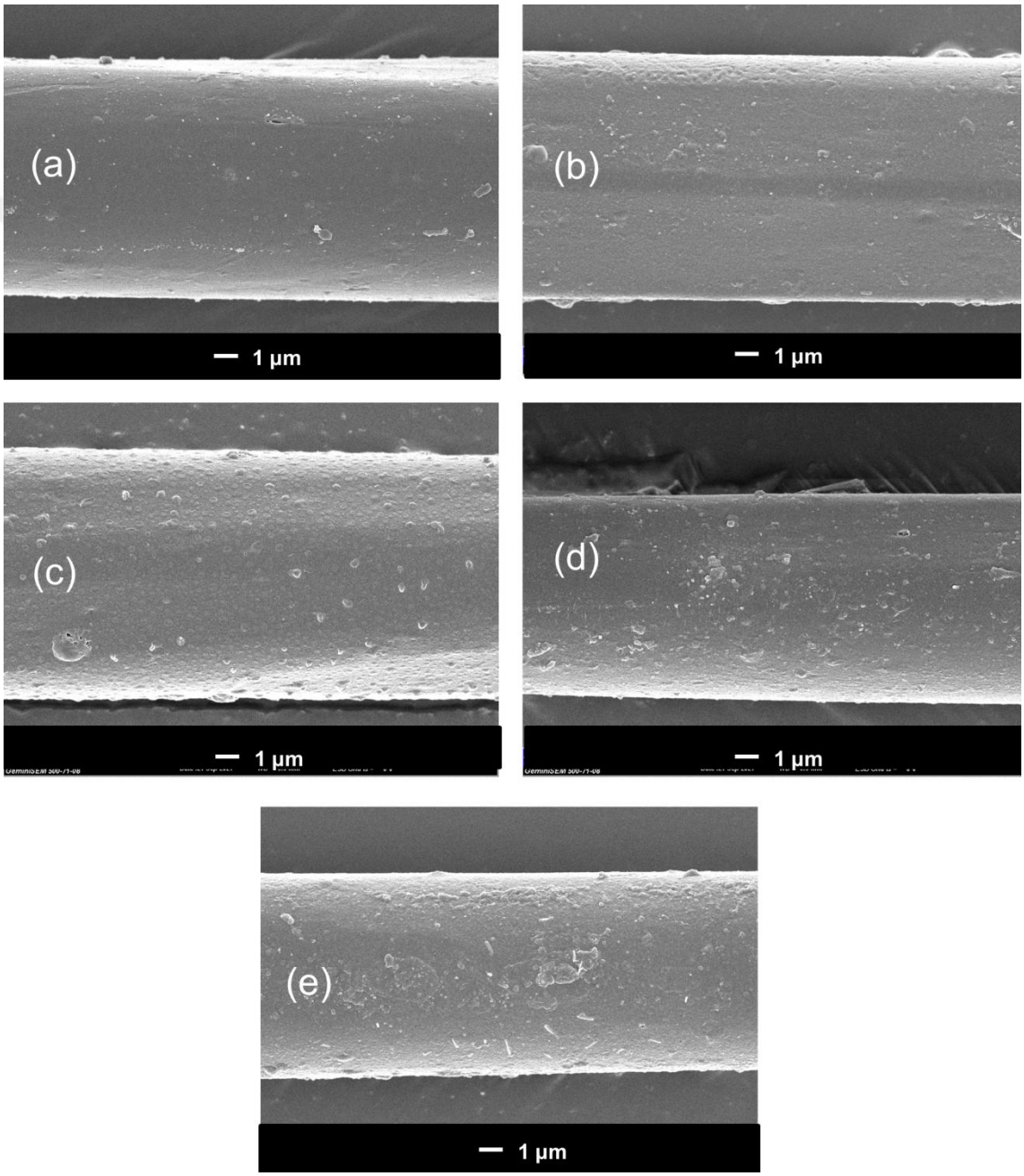

Figure 4.49 SEM images of PBU incorporated-stabilized PA66 multifilaments for different stabilization periods. (a) 30 min, (b) 60 min, (c) 90 min, (d) 120 min, (e) 150 min.

4.3 Jute Fiber

4.3.1 Characterization of Original Jute Fiber

As a natural originated precursor, jute yarn was used in this study with having a linear density of 332.28 tex, fiber thickness of 50.33±0.84 μm, and volume density of 1.37 g/cm^3. Tensile properties were measured of the jute samples through the tensile strength (182.87±22.41 MPa), tensile modulus (11.36±1.72 GPa), and extension at break percentage (1.83±0.30).

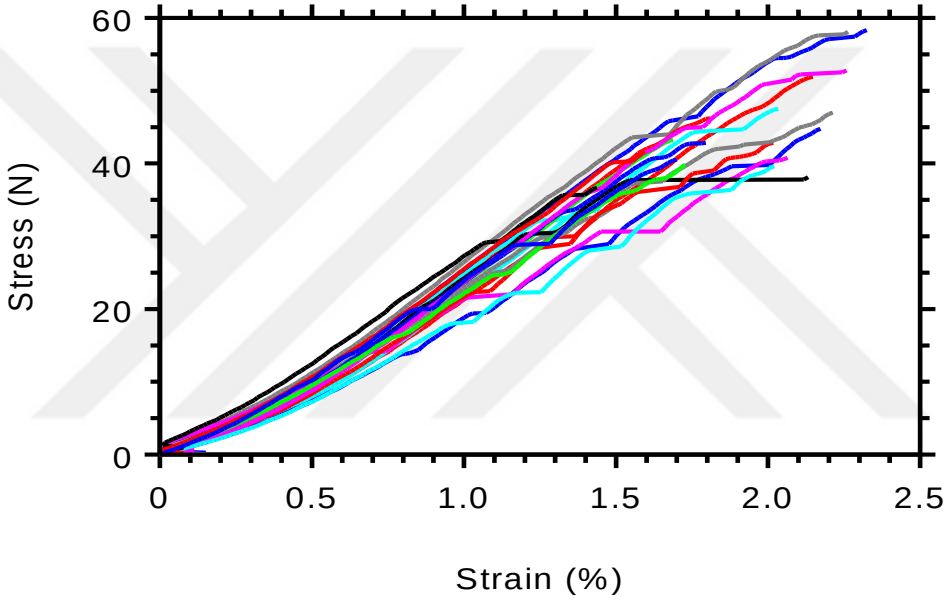

Figure 4.50 Stress-strain curve of original jute fiber.

4.3.2 Physical and Mechanical Characterization of Original and Thermally Stabilized Jute Fiber Impregnated with SMSPH-U

The color of the jute fibers changed dramatically as a result of thermal oxidation, from light brown to dark brown in the initial phases to black in the advanced oxidation phases. The dehydration of SMSPH-U impregnation is thought to be partly responsible for causing color deviations in the thermal oxidation of jute fibers. The presence of a thermally stable structure can be confirmed from the color change to complete black in the samples [218]. The flame test also revealed that the samples passed after 175 minutes of oxidation, indicating that SMSPH-U integration followed by thermal

oxidation produced jute fibers with a non-burning feature when exposed to match flame. As a result, the 175 minutes oxidized jute sample is thought to be fully oxidized, allowing it to withstand high carbonization and activation temperatures.

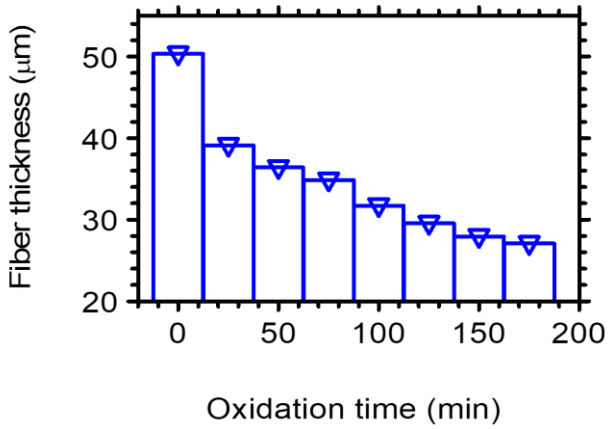

Figure 4.51 Fiber thickness of pristine and oxidized jute fiber.

With a 175 minutes multistep annealing, the fiber thickness of the oxidized jute was reduced from 50.33 to 27.08 μm. With the increase of the stabilization period, the fiber thickness decreased. After 25 minutes of annealing, a significant decrease in fiber thickness was observed, with a loss of approximately 22.23% compared to the original jute fiber. The main cause of decreased fiber thickness is thought to be the weight loss of the jute sample because of dehydration of the cellulose structure in the thermal oxidation process.

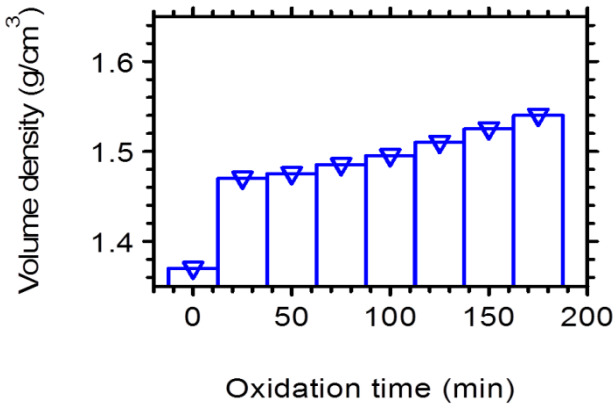

Figure 4.52 Volume density of pristine and oxidized jute fiber.

Figure 4.52 shows the volume density results for pristine and oxidized jute fibers impregnated with SMSPH-U and stabilized for 25 to 175 minutes. The pristine sample

has a volume density of 1.37 g/cm^3, while the 175 minutes oxidized jute fiber has a volume density of 1.54 g/cm^3. The growth of cyclized and cross-linked ring structures is attributed to the faster growth of the volume density values of SMSPH-U incorporated-oxidized jute fibers [232].

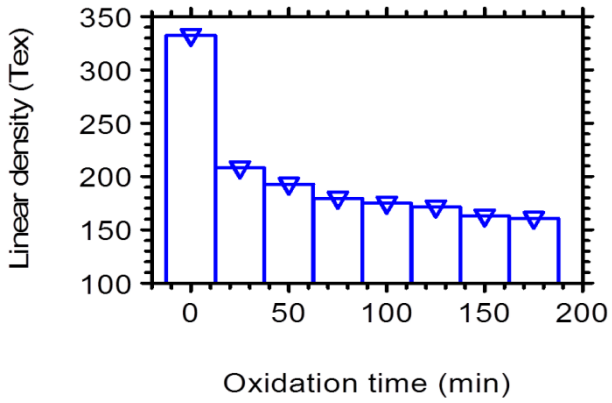

Figure 4.53 Linear density of pristine and oxidized jute fiber.

The original jute sample had a linear density of 332.28 tex. The linear density value dropped sharply by 37.39% after 25 minutes of oxidation, and the reduction continued as the oxidation time increased. The linear density value of jute samples reached 160.85 tex after 175 minutes of oxidative stabilization at 245°C, which represents the maximum loss. Water loss through the dehydration process in the oxidation phase is responsible for the high linear density loss.

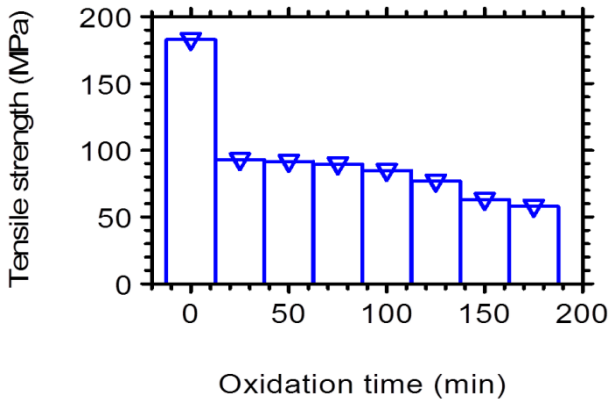

Figure 4.54 Tensile strength of pristine and oxidized jute fiber.

The tensile strength of 25 minutes thermally oxidized jute fiber declined by 49.22% from 182.87 MPa in the raw jute sample. Afterward, it decreased gradually until 175

minutes of thermal oxidation and reached 57.94 MPa. The development of the cyclized and cross-linked ring structure along with the closer packing of the polymer structures causing by the cyclization and intra-molecular cross-linking reactions that occur in the oxidation process are the reasons for the continuous loss of tensile strength.

4.3.3 Thermal and Structural Characterization of Original and Thermally Stabilized Jute Fiber Impregnated with SMSPH-U

4.3.3.1 Evaluation of Thermogravimetric Analysis (TGA)

The TGA method continuously measures the weight loss of samples for increasing time or temperature at a linear rate. The various steps in the TGA trace provide valuable information on thermal stability, original sample composition, the thermal stability of intermediates formed, and kinetic data. Essentially, the TGA method is dynamic and offers quantitative information about the thermal stability of the samples under investigation.

In the case of jute fibers, the weight loss occurring during TGA scanning is caused by the decomposition of cellulose, hemicellulose, and lignin structural elements. Usually, higher decomposition temperatures result in higher thermal stability [196]. In cellulosic fibers, there is no glass transition or melting transitions. The only transition is that of decomposition around 365-370 °C at 10 °C/min heating rate. It should be emphasized that the exact positions of these transitions are heavily dependent on the rate of heating and the impurities present in the material. According to the published literature [269], the heating rate is an important factor for differentiating the relative merits of good quality fibers. When the heating rate is increased from 5 °C/min to 150 °C/min, the decomposition maxima of cellulose is increased from 321 °C to 394 °C for water-retted lignocellulosic flax fibers [269]. According to Archibald [269], the transition temperatures of 256 °C for pectin, 290 °C for hemicellulose, 364 °C for cellulose, and 429 °C for lignin were observed in a typical TGA scan of lignocellulosic flax fibers at 10 °C/min heating rate.

For the thermal characterization, TGA of the original and oxidized jute fibers was utilized to quantify the influence of SMSPH-U incorporation on the pyrolysis behavior.

In the development of jute-based ACFs, quicker pyrolysis is not desirable. It is believed to form volatile carbon-containing elements and lower carbon yield by intensifying side reactions [146]. The formation of volatile byproducts, including organic acids, aldehydes, and carbon dioxide in the accelerated pyrolysis leads to lower carbon yields. To obtain higher carbon yields, the existence of oxygen in the air also plays a significant role.

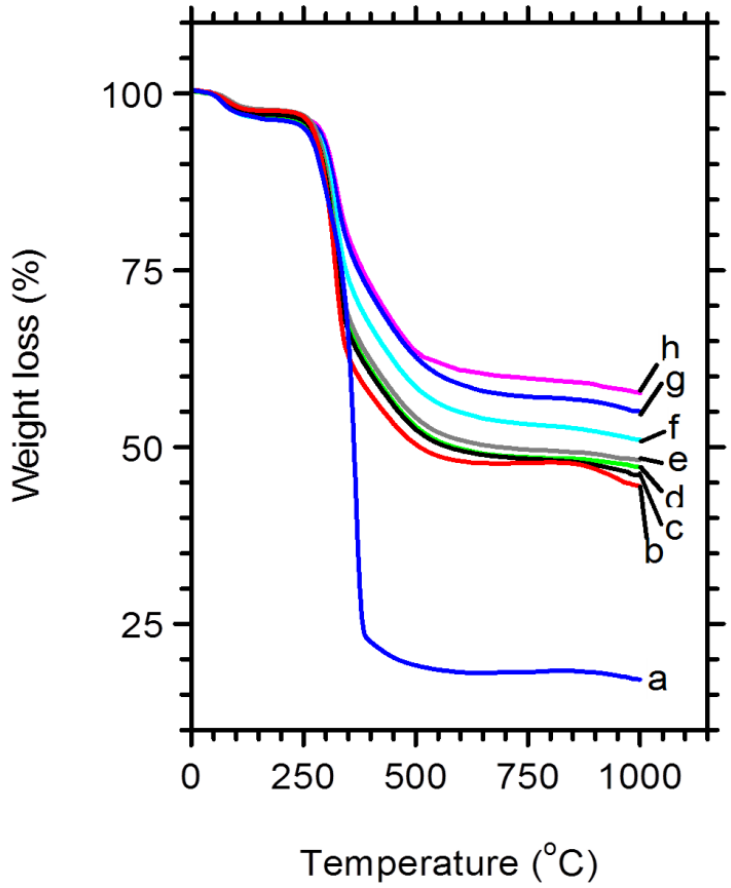

Figure 4.55 TGA thermograms of pristine (a) and SMSPH-U incorporated-stabilized jute fibers for different oxidation periods. (b) 25 min; (c) 50 min; (d) 75 min; (e) 100 min; (f) 125 min; (g) 150 min; (h) 175 min.

For different oxidation periods, the TGA thermograms of original and oxidized jute fibers are illustrated in Figure 4.55. TGA thermograms revealed the loss of weights at 100 °C, indicating moisture evaporation due to bonded water of fibers. Afterward, no significant weight loss of the untreated jute sample was observed up to 300 °C [Figure 4.55(a)]. Between 290 and 390 °C, the rate of weight loss rose dramatically, followed by moderate weight loss up to 1000 °C. However, the thermal behavior of SMSPH-U

incorporated-oxidized jute fibers was noteworthy [Figure 4.55(b–h)]. With increasing oxidation temperatures, the TGA traces of the oxidized jute fibers revealed lesser weight loss. It indicates that higher carbon yields lead to increased cross-linking and aromatization reactions within the cellulose structures. Due to the ladder-like structure formation by these reactions, oxidized jute fibers lost weight through a wide temperature range, although the pristine jute lost weight through a limited temperature range.

A comparison of the carbon yield values at temperatures of 500 and 1000 °C for the raw and SMSPH-U integrated-oxidized jute fibers is presented in Figure 4.56. The outcomes reveal the constant growth of carbon yield percentage by the increase of the oxidation period. At 500 °C, the carbon yield is noticed to be higher than that of 1000 °C. The outcomes reveal the highest carbon yield value of SMSPH-U integrated 175 minutes oxidized jute fibers by 57.65% at 1000 °C.

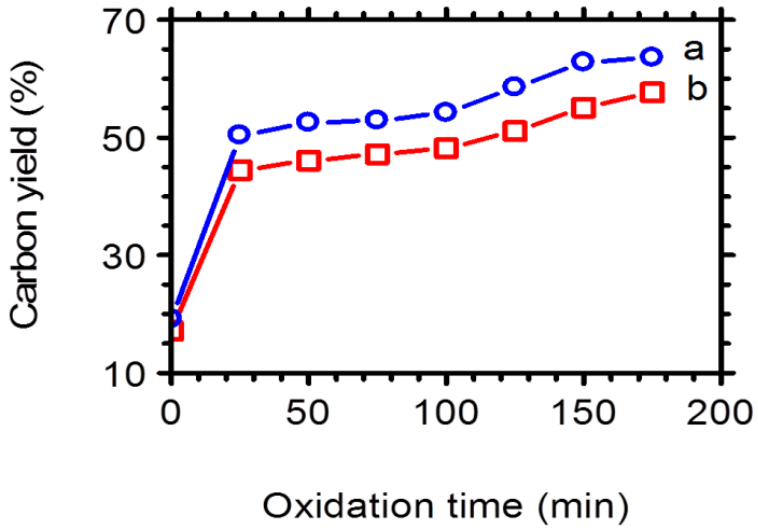

Figure 4.56 Comparison of carbon yields at scanning temperatures (a) 500 °C and (b) 1000 °C of the pristine and oxidized jute fibers impregnated with SMSPH-U.

The findings from the TGA analysis shown that greater thermal stability is more noticeable in the SMSPH-U impregnated-oxidized jute fibers than in the raw jute due to higher cross-linking within the jute molecular structure. SMSPH-U impregnation seems to stimulate very influential oxidation and carbonization (imitated carbonization of

TGA executed in nitrogen) process because of the intermolecular and intramolecular cross-linking reactions and cyclization reactions. SMSPH-U impregnation with jute fibers helped greatly to result in the occurrence of dehydrogenation and cyclization processes. The unsaturated sites, formed in the dehydrogenation reactions, are advanced by the development of intermolecular cross-links, resulting in greater carbon yield percentage in the jute fibers.

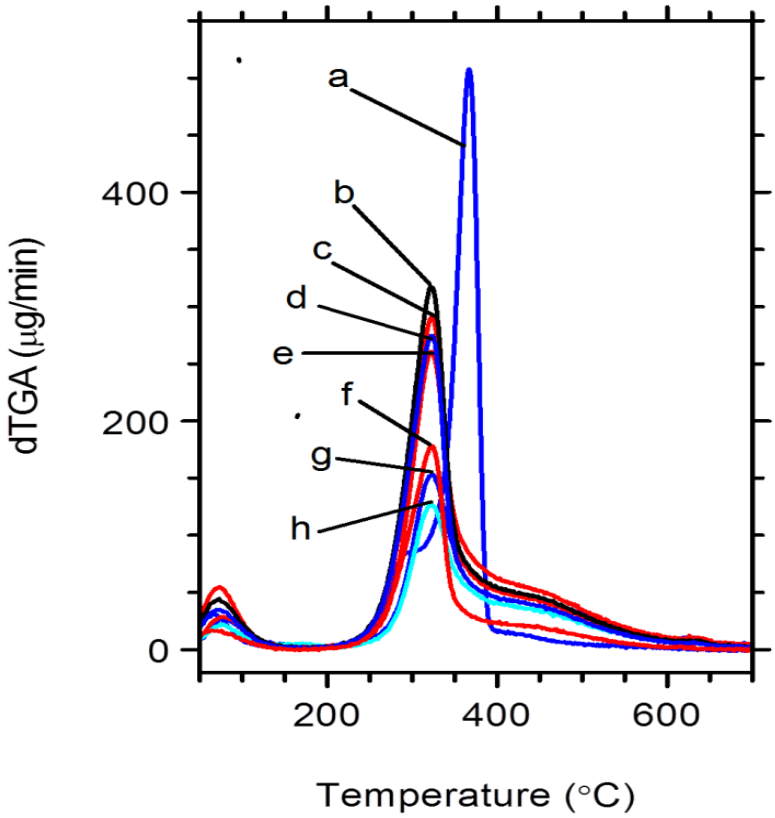

Figure 4.57 dTGA thermograms of pristine (a) and oxidized jute fibers for different oxidation periods. (b) 25 min; (c) 50 min; (d) 75 min; (e) 100 min; (f) 125 min; (g) 150 min; (h) 175 min.

The dTGA curves of TGA thermograms are illustrated in Figure 4.57. The dTGA curve of the raw jute fibers (Figure 4.57a) exhibits two exothermic peaks located at 290 and 365 °C assigned to the decomposition of hemicellulose and cellulose. Lignin decomposition peak appeared at 430 °C, but it is weak in intensity. Following the oxidation reactions, the dTGA peak for the oxidized samples shifts from 365 °C assigned to decomposition cellulose to 322 °C. In original jute fibers, there was no clear pectin peak at 256 °C, although gradual weight loss started around 250 °C.

Hemicellulose decomposition peak was located at 290 °C but disappeared in the oxidized samples. The lignin decomposition peak, located around 430 °C, became broader in the oxidized samples. The appearance of these new peaks indicates the presence of oxidation and aromatization reactions of jute fibers resulting in the production of various reaction products in terms of H_2O, CO, CO_2, and CH_4 [270]. The peak positioned at around 100 °C is due to the presence of water vapor on the samples.

The area under the main exothermic peak positioned at 365 °C is noticed to decrease due to the reactions between Silanol (Si-OH) and the primary hydroxyl group of cellulose rings (–CH_2–OH) as well as the main OH-groups of hemicellulose and lignin components of jute fiber. These reactions eventually eliminate hydroxyl (-OH) groups and hydrogen atoms from the water (H_2O) molecules formed, and by dehydration reactions, the development of functional groups (mostly C=O and C=C) occurs. In dehydration reactions, the cellulose structure is retained, the development of volatile byproducts is minimized, and the weight loss is restricted only to the water loss [5].

4.3.3.2 Evaluation of X-ray Diffraction Analysis (XRD)

Native cellulose (Cellulose I) is found in all higher plants as a structural material in the cell walls and can exist in several crystallographic forms as characterized by their distinctive X-ray diffraction patterns and their infrared spectra. The cellulose chains form crystalline microfibrils. Native cellulose may be converted to cellulose II by regeneration and mercerization techniques. As the most abundant natural polymer, considerable effort has been directed towards determining its physical structure. Crystallographic study of cellulose dates back to the work of Meyer and Misch [271], who determined the unit cell dimensions of native cellulose (cellulose I) from ramie fibers to be a= 0.835 nm, b= 1.03 nm (fiber axis), c= 0.79 nm, and β = 84°. The calculated crystalline density from this unit cell is 1.5823 g/cm^3. We have been able to tentatively fit the d-spacings obtained from the equatorial X-ray diffraction profile of pristine jute fiber to a monoclinic unit cell parameters of cellulose I structure suggested by Meyer and Misch [271]. The corresponding crystalline structure contains two chains per unit cell.

Cellulose I may be derived from cotton, flax, jute, and certain marine algae bacteria and contains two chains in the unit cell. More recently, refined crystal structures of cellulose I have been reported [272, 273]. The dimensions of these unit cells and their corresponding crystalline densities are presented in Table 4.9. However, Blackwell et al. [272] doubled the a and b-axes of Meyer and Misch unit cell and refined a unit cell containing eight chains arguing that the three weak reflections found in the Valonia pattern necessitated this doubling. They further acknowledged that the bands with odd h and k are too faint to be noticed, indicating that the variation between Meyer and Misch cells is very minor. The directions of the cellobiose units are parallel to the b-axis of the unit cell, while the planes of the glucose molecules are in the ab plane.

Table 4.9 Unit cell dimensions of Cellulose I.

	a (nm)	b (nm)	c (nm)	β (°)	Space group	Crystalline density (g/cm^3)
Meyer and Misch	0.835	1.030	0.790	84.0	$P2_1$	1.582
Sarko and Muggli	0.814	1.034	0.785	83.4	$P2_1$	1.629
Blackwell and Gardner						
Valonia (2-chain)	0.818	1.034	0.786	83.0	$P2_1$	1.620
Valonia (8-chain)	1.634	1.038	1.572	83.0	$P2_1$	1.616

Equatorial X-ray diffraction traces of pristine and SMSPH-U integrated and oxidized jute fibers are illustrated in Figure 4.58. Assessment of the equatorial X-ray diffraction trace of pristine jute fibers presented in Figure 4.58(a) demonstrates the presence of four well-defined crystalline peaks as the most prominent feature.

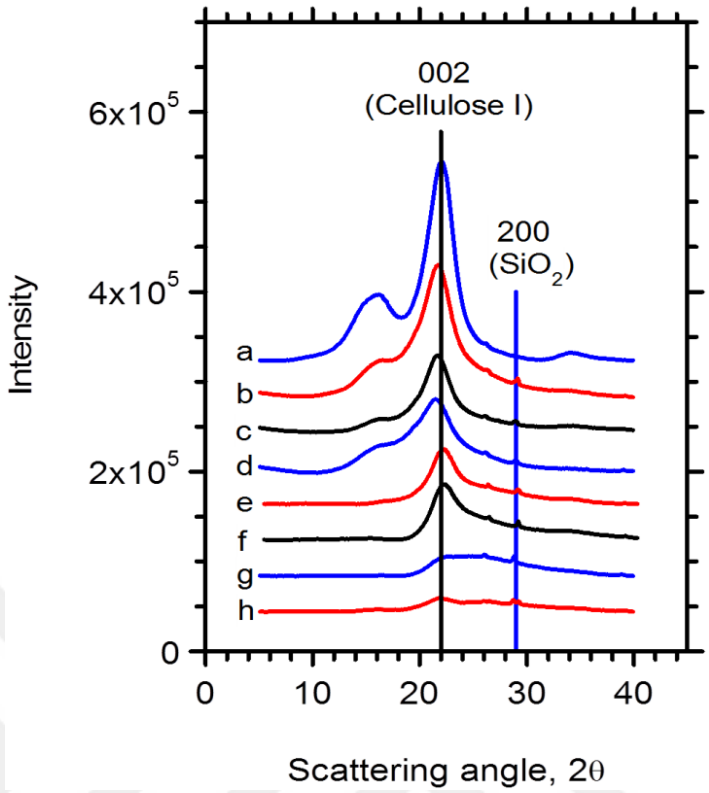

Figure 4.58 Equatorial X-ray diffraction profiles of pristine (a) and oxidized jute fibers for different oxidation times. (b) 25 min; (c) 50 min; (d) 75 min; (e) 100 min; (f) 125 min; (g) 150 min; (h) 175 min.

A curve-fitting technique was utilized for the equatorial X-ray diffraction profiles to get precise peak parameters. Peak resolution was used to obtain apparent X-ray crystallinity, amorphous ratio, crystal size, and X-ray oxidation index for different oxidation times. The equatorial X-ray diffraction profile of pristine jute fibers illustrated in Figure 4.59 can be resolved into four crystalline peaks of cellulose I structure located at about 14.8±0.2, 16.4±0.3, 22.4±0.2 and 34.8±0.3 attributed to (101), ($10\bar{1}$), (002) and (040) reflections. These reflections correspond to a monoclinic unit cell. It is obvious that the 002 peak intensity is the strongest compared to the intensities of the (101), ($10\bar{1}$), and (040) reflections. An additional peak positioned at 18.2° (d-spacing of 0.488 nm) was used to improve the peak resolution in the tail areas of the adjacent reflections. In terms of peak parameters, the additional reflection used at 18.2° is a broad peak in terms of half-height width and demonstrates a characteristic amorphous structure. The peak parameters obtained from the peak resolution of pristine jute fibers are presented in Table 4.10 and compared to the calculated and observed d-spacings.

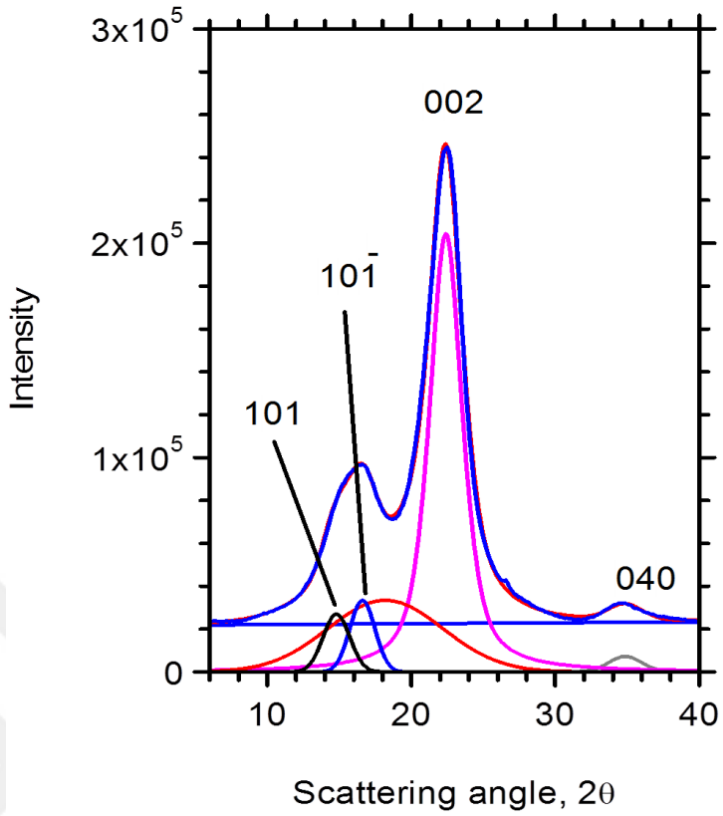

Figure 4.59 Curve fitting of equatorial X-ray diffraction trace of original jute fibers.

Table 4.10 Resolved peak parameters of curve fitted equatorial X-ray diffraction profile of pristine jute fiber.

Peak ref.	f	A (height)	W (width)	Position (2θ)	d_{obs} (nm)	d_{calc} (nm)
(101)	0.0	27032	2.2	14.8	0.602	0.603
($10\bar{1}$)	0.0	33431	2.0	16.4	0.540	0.543
Amorph.	0.0	33446	9.4	18.2	0.488	-
(002)	0.6	204434	2.7	22.4	0.396	0.392
(040)	0.0	7248.0	2.8	34.8	0.259	0.258

SMSPH-U impregnation followed by oxidation in an air atmosphere at a temperature of 245°C and oxidation times ranging from 25 to 175 minutes indicated a considerable influence on the crystalline structure of jute samples relating to the degree of apparent crystallinity of the cellulose I structure. A close investigation of the X-ray diffraction

profiles presented in Figure 4.58 exhibited a continuing loss of crystal structure with growing oxidation time. The loss of the intensity of the X-ray diffraction profiles indicates the development of amorphization (i.e., decrystallization) reactions with progressing oxidation time.

Table 4.11 The presence and absence of X-ray diffraction reflections of the jute fibers.

Reflection				
Oxidation time (min)	101	$10\bar{1}$	002	040
0	+	+	+	+
25	+	+	+	+
50	+	+	+	+
75	+	+	+	+
100	-	-	+	+
125	-	-	+	+
150	-	-	+	-
175	-	-	+	-

Key: + : Reflection is present

- : Reflection is absent

The results presented in Table 4.11 show that some of the crystalline peaks seem to disappear with progressing oxidation reactions as a result of the ongoing decrystallization process. It seems that (101) and ($10\bar{1}$) reflections disappear after the oxidation time of 100 minutes, whereas (040) reflection disappears after the oxidation time of 150 minutes. On the other hand, the (002) reflection appears to survive the oxidation reactions through the oxidation time from 25 to 175 minutes.

Peak resolution of equatorial X-ray diffraction profile of oxidized jute sample at an oxidation time of 25 minutes is presented in Figure 4.60. In addition to cellulose I reflections, two addition reflections appeared at 26.7 and 29.5° 2θ. These additional reflections correspond to silica (SiO_2) crystals containing monoclinic unit cell with cell dimensions of a=b= 0.717 nm, c=1.238 nm, $\alpha=\beta=90°$ and $\gamma=120°$ [274]. It seems that the oxidized samples do possess silica (SiO_2) layers on the surface of the fibers.

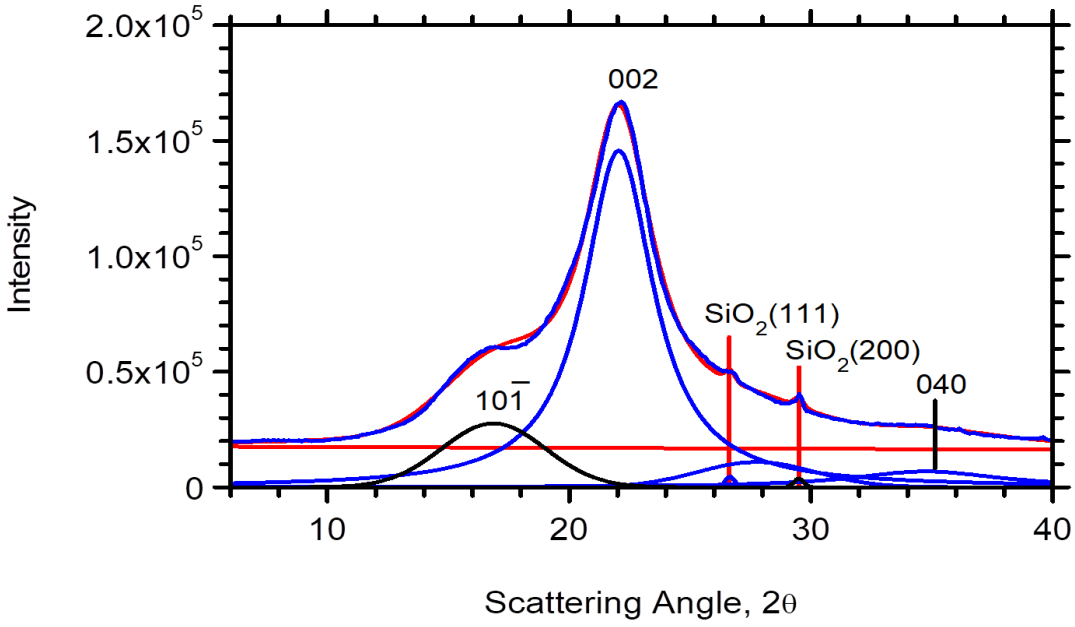

Figure 4.60 Curve fitting of equatorial X-ray diffraction profile of 25 min thermally stabilized jute fibers.

Peak extents attained from the curve-fitting of equatorial X-ray diffraction profiles plotted in Figure 4.58 were utilized to assess the ratios of crystalline (i.e., cellulose I) and amorphous structures utilizing Equation 3. The outcomes illustrated in Figure 4.61 indicate the X-ray crystallinity was reduced from 58 to 3% after an oxidation period of 175 minutes, whereas the amorphous fraction improved from 42 to 97% in this period.

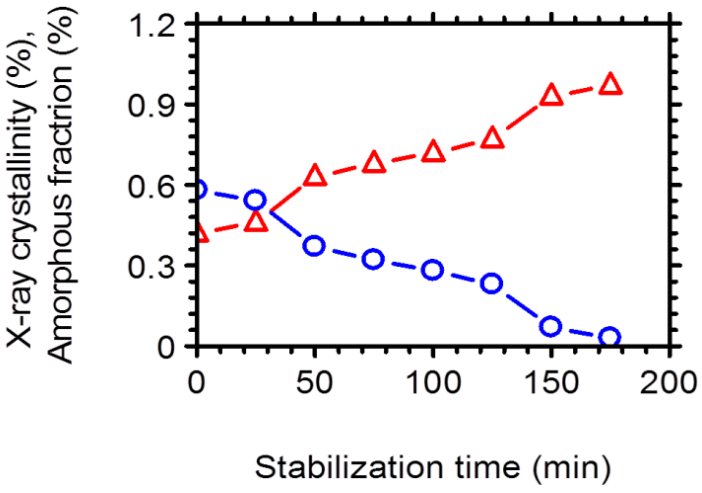

Figure 4.61 Comparison of phase ratios of pristine and oxidized jute fibers for different oxidation times. (o) X-ray crystallinity (%), and (Δ) Amorphous fraction (%).

Equation 2 was employed for assessing the X-ray stabilization index employing the intensity of the (002) as a prominent reflection [225]. The outcomes illustrated in Figure 4.62 represent the X-ray stabilization index values for the oxidized jute samples for different oxidation times. When the oxidation time was raised from 25 to 175 minutes, the X-ray stabilization index grew from 29 to 96 percent. The X-ray stabilization indices increased by the rise of oxidation time. It can be considered a dependable method to assess the aromatic and cross-linked structure formed in the oxidation reactions [275]. The experimental outcomes point out that SMSPH-U impregnated and oxidized jute fibers resulted in the disappearance of cellulose I crystal structure and a rise in the disordered fraction along with an enhancement in the ratio of aromatic structure possessing cross-linked ladder-like structural species.

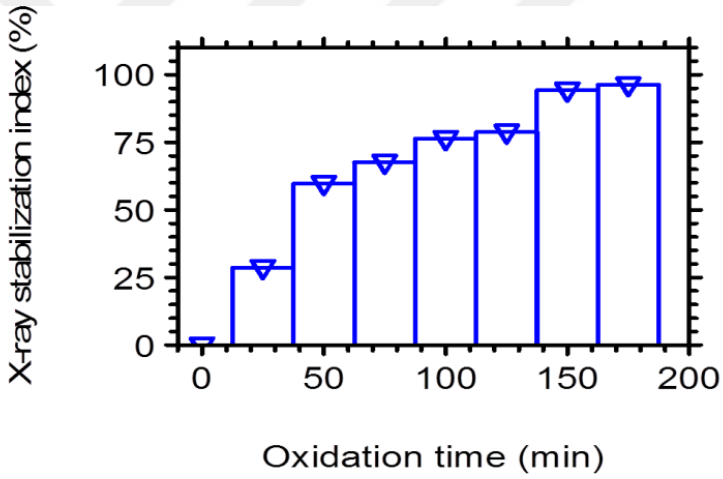

Figure 4.62 Comparison of X-ray stabilization index for different oxidation times.

During the oxidation reactions, 101, $10\bar{1}$ and 040 reflections disappeared as a result of ongoing oxidation reactions. The most prominent (002) peak kept its presence during the oxidations reactions. The half-height widths of the reflections widened with growing oxidation times, indicating a progressive reduction in the crystal dimensions. This result is believed to be due to the collapsing structure as part of the amorphization reactions [275]. The gradual loss of the 101, $10\bar{1}$ and 040 peaks are likely to be caused by the collapsing cellulose I crystal structure as part of the ongoing amorphization procedure.

Since the (002) reflection kept its presence during the oxidation process, it was used for the evaluation of crystal size during the oxidation process. Evaluation of crystal sizes due to pristine and oxidized jute fibers was evaluated using Equation 4. Figure 4.63

shows the variation of crystal size corresponding to prominent (002) peak for different oxidation times. Crystal size for (002) reflection was lowered from 4.2 to 2.6 nm by the rise of the oxidation period due to ongoing decrystallization reactions.

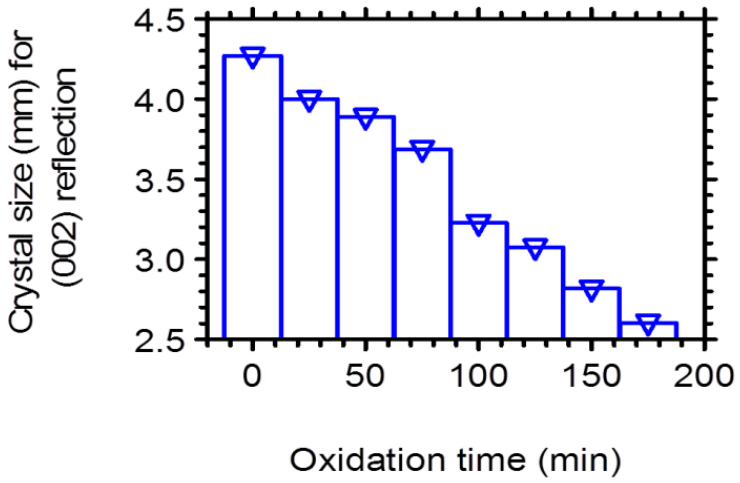

Figure 4.63 Comparison of the crystal size for (002) planes calculated for pristine and oxidized jute fibers for different oxidation times.

4.3.3.3 Evaluation of Infrared Spectroscopy Analysis (FT-IR)

In the present investigation, vibrational spectroscopy was extensively utilized to investigate structural changes occurring during the oxidation reactions. Structural changes happening during the oxidation process were monitored and followed as a function of oxidation time. Information from vibrational spectroscopy is one of the most useful methods for understanding of the structure of cellulose, mainly for recognizing the network of H-bonds in cellulose crystals. The IR vibrations of pristine and oxidized jute fibers are presented in Figure 4.64 for different oxidation times between the 4000 and 2000 cm^{-1} region.

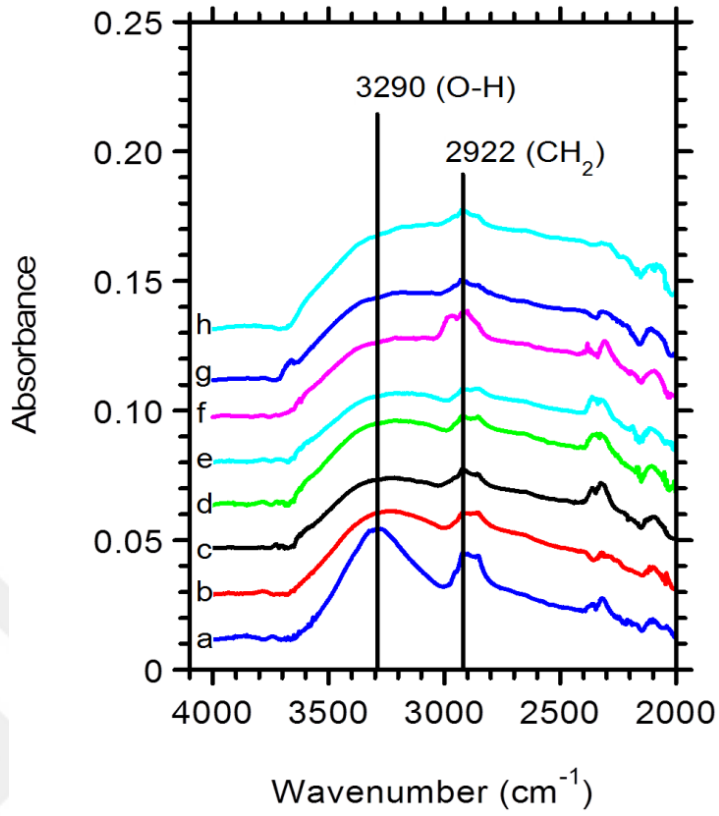

Figure 4.64 Infrared spectra in the 4000–2000 cm^{-1} region of pristine (a) and SMSPH-U incorporated-oxidized jute fibers for different oxidation times. (b) 25 min; (c) 50 min; (d) 75 min; (e) 100 min; (f) 125 min; (g) 150 min; (h) 175 min.

The IR region between 4000 and 3000 cm^{-1} is considered to be due to intermolecular and intramolecular hydrogen-bonded OH group spectra. The OH groups available in the molecular structure of cellulose readily form inter and intramolecular H-bonds results in the creation of crystalline regions [5, 276–278]. In the infrared spectrum of cellulose, the 3000-2000 cm^{-1} region is assigned to the methine (C-H) and methylene (CH_2) stretching vibrations. The IR spectrum of pristine jute fiber contains vibrations due to cellulose, hemicellulose, and lignin [276]. Band assignments of the range between 4000-500 cm^{-1} of the IR spectrum of jute fiber are listed in Table 4.12, which are based on references [279–281]. Following SMSPH-U pretreatment and oxidation in an air atmosphere, noticeable changes in relative intensity values were observed in terms of hydrogen-bonded and CH stretching vibrations spanning from 4000 to 3000 cm^{-1} region. The IR range from 4000-3000 cm^{-1} is ascribed to bands of free intermolecular and intramolecular vibrations.

Table 4.12 Band assignments of the range between 4000-500 cm^{-1} of the IR spectrum of jute fiber [279–282].

Wavenumber (cm^{-1})	**Assignment**
3580	Free OH vibrations
3520	OH stretching intramolecular hydrogen bonding
3450	OH stretching intramolecular hydrogen bonding
3405	OH stretching intramolecular hydrogen bonding
3350	OH stretching intramolecular hydrogen bonding
3300	OH stretching intermolecular hydrogen bonding
3260	OH stretching intermolecular hydrogen bonding
3120	OH stretching intermolecular hydrogen bonding
2922	CH_2 asymmetrical stretching
2900	CH and CH_2 stretching
2860	CH stretching
1730	C=O stretch (before annealing)
1705	C=O stretch in unconjugated ketones, carbonyls, and ester groups of hemicellulose structure (after annealing)
1635	Adsorbed H_2O (shoulder)
1588	Lignin (aromatic skeletal vibrations, C=C stretch + C=O stretch)
1508	Lignin (aromatic skeletal vibrations)
1455	CH-deformation and CH_2 bending
1424	CH_2 symmetric bending
1368	CH_2 bending (crystalline)
1317	CH_2 wagging
1235	C–O stretching in acetyl group
1205	OH in-plane bending
1200 (broad)	Si-O-cellulose (after annealing)
1160	Asymmetrical in-phase ring stretching (crystalline)
1102	Asymmetrical in-phase ring stretching (crystalline)
1007	CO stretching
895	Asymmetrical out of phase ring stretching (C-O-C)
800	Ring breathing
760-780	Si-O-Si (symmetric stretch)
663	OH out of plane bending

The IR spectrum of pristine jute fiber covering 3700 and 3000 cm^{-1} regions illustrated in Figure 4.65 was analyzed and fitted with eight peaks using a curve-fitting procedure. The curve-fitting procedure was performed using band positions located at 3580, 3530, 3450, 3350, 3305, 3260, 3178, and 3120 cm^{-1}. The infrared peak located at 3580 cm^{-1} is attributed to free OH vibrations (Table 4.12). In contrast, the IR vibrations positioned at 3520, 3450, 3405, and 3350 cm^{-1} are attributed to OH vibration of the intramolecular H-bonds (Table 4.12). Intermolecular H-bonded bands are positioned at 3300, 3260, and 3120 cm^{-1}. Intermolecular H-bonding appears to be more sensitive to temperature variations than intramolecular H-bonding [283]. OH, CH, and CH_2 bands positioned in the wavenumber zone starting from 3700 to 3000 cm^{-1} lost their intensities steadily, yet never totally gone.

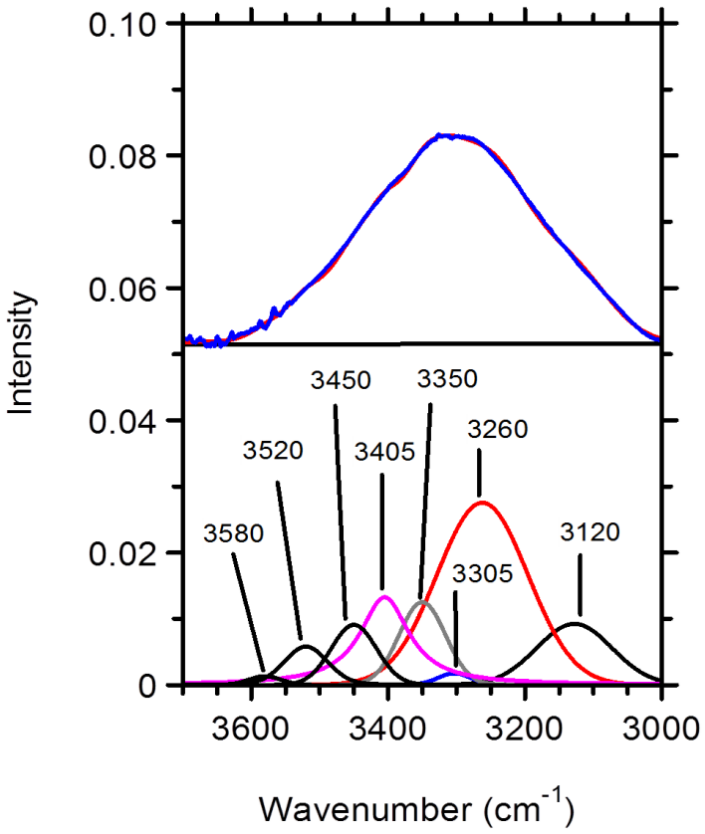

Figure 4.65 Curve fitting of the infrared band of pristine jute fibers in the 3700-3000 cm^{-1} range.

OH bands attributed to oxidized jute fibers originally exhibited broadening. However, by the increase of oxidation time, most of their intensity was lost. Because of the influence of dehydration reactions that occurred by the interaction between SMSPH-U

and the OH groups in the initial phases of oxidation reactions, the intensities of the bands located at 3305, 3260, 3120 cm^{-1} involved in the intermolecular H-bonded OH groups gradually weakened with increasing oxidation time. This behavior indicated an interruption in intermolecular H-bonding. The IR vibrations located at 3520, 3450, 3405, and 3350 cm^{-1} attributed to intramolecular H-bonded OH groups also lost their intensity, although never vanished entirely. This outcome suggests that the majority of oxidation reactions occurred between OH-groups of cellulose, hemicellulose, and lignin with SMSPH-U functional groups. The interruption of the intermolecular H-bonding network in the oxidation process is thought as the main cause for the continuous loss of crystallinity and development of the amorphous phase due to oxidation reactions.

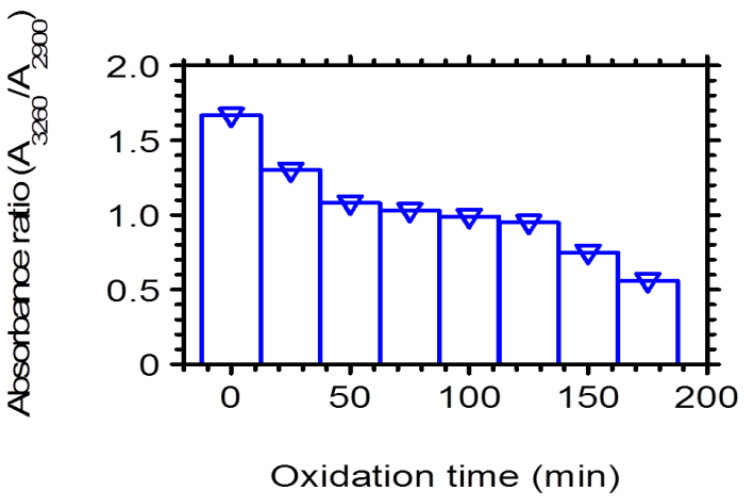

Figure 4.66 Changing of absorbance ratio (A_{3260}/A_{2900}) for different oxidation times. The absorbance value of 2900 cm^{-1} is taken as an internal standard.

The methine (CH) and methylene (CH_2) vibrations located at 2922, 2900, and 2860 cm^{-1} also lost most of their intensities, but a minor amount still remained due to the rise of oxidation time, demonstrating that not all hydrogen species are involved in dehydrogenation and dehydration processes. The continuing loss of the hydrogen from the CH groups and H-bonded OH groups clearly indicates that dehydrogenation and dehydration reactions occurred in the stabilization process. Gradual reduction of intermolecular hydrogen bonding between OH groups of jute fibers occurring for different oxidation times is presented quantitatively in Figure 4.66. The infrared spectrum located at 2900 cm^{-1} was taken as an internal standard for normalization purposes [158]. The vibration located at 2900 cm^{-1} is clearly well-defined and prominent

vibration in the pristine jute fiber. The use of internal standard vibration makes it easy to make comparisons between different samples for different oxidation times. The infrared vibrations in the 2000-500 cm^{-1} region of pristine and SMSPH-U incorporated-stabilized jute fibers for different oxidation periods are presented in Figure 4.67.

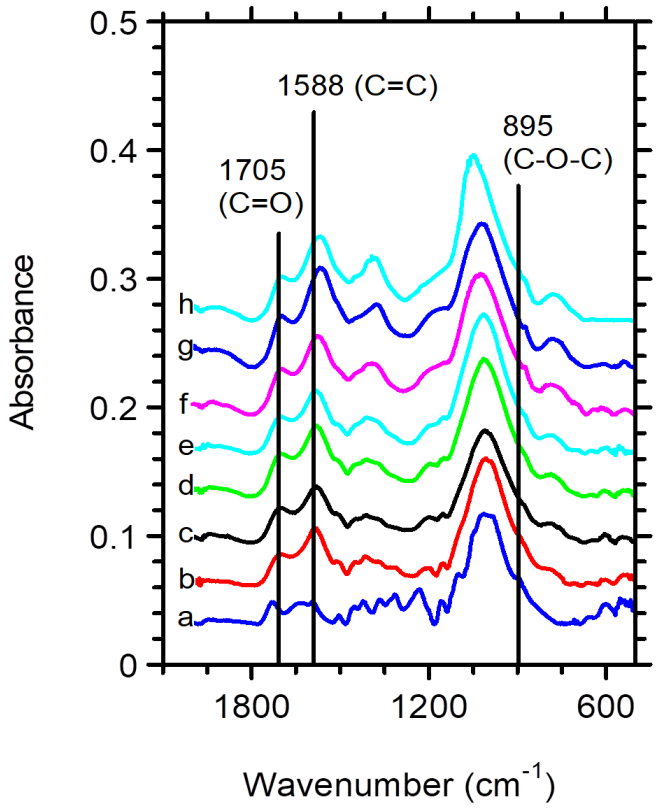

Figure 4.67 Infrared spectra in the 2000–500 cm^{-1} region of pristine (a) and SMSPH-U incorporated-oxidized jute fibers for different oxidation periods. (b) 25 min; (c) 50 min; (d) 75 min; (e) 100 min; (f) 125 min; (g) 150 min; (h) 175 min.

From quantitative and qualitative viewpoints, the wavenumber range of 2000-500 cm^{-1} of the cellulose infrared band is the most valuable portion. The 1500-1200 cm^{-1} region is assigned to CH_2 bending vibrations. The vibrations at 1422, 1162, 1102, and 895 cm^{-1} are recognized as crystallinity spectra. Infrared spectra of pristine and oxidized jute fibers in the presence of SMSPH-U impregnation in the wavenumber between 2000 and 500 cm^{-1} for 25 minutes oxidation time are presented in Figure 4.68.

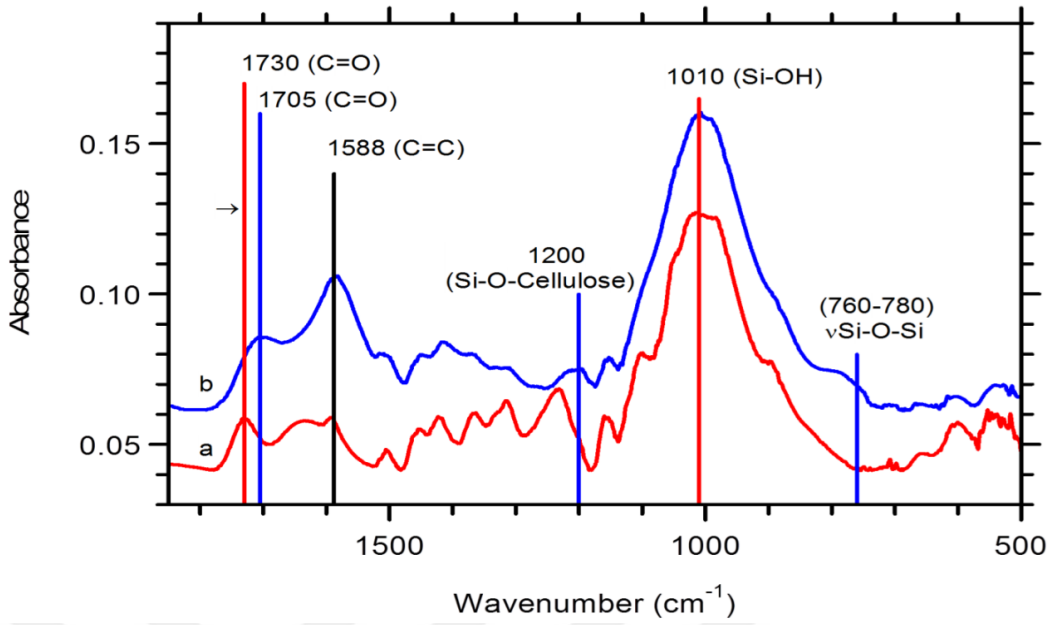

Figure 4.68 FT-Infrared spectra of pristine (a) and thermally oxidized jute fibers (b) in the presence of SMSPH-U impregnation in the 1850-500 cm^{-1} region for 25 min.

Carbonyl stretching vibration located at 1730 cm^{-1} allotted to C=O stretching band is moved to 1705 cm^{-1} indicating strong interaction with OH groups in forming H-bonds [282]. IR spectra in Figure 4.67 indicate that the carbonyl (C=O) intensity grows with increasing oxidation time. This outcome suggests that oxygen-containing functional species are produced during the thermal treatment. The ratio of the absorbance value of the carbonyl (C=O) vibration to 2900 cm^{-1} is defined as an oxidation index for comparison purposes. The results presented in Figure 4.69 suggest that the oxidation index increases with increasing oxidation time suggesting increased oxygen content.

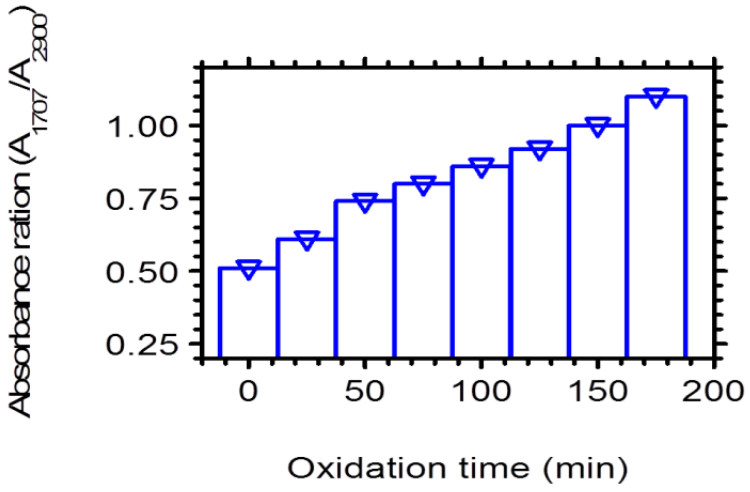

Figure 4.69 Changing of absorbance ratio (A_{1707}/A_{2900}) as a function of oxidation time.

A completely new band placed approximately 1588 cm^{-1} appeared as a strong vibration assigned to C=C stretching became major in the samples stabilized at oxidation times of 25 minutes and higher suggesting the formation of the highly aromatic structure during the oxidation process (Figure 4.70). The crystalline bands located at 1422, 1162, 1102, and 895 cm^{-1} gradually lost maximum intensities, specifying the steady loss of crystallinity with increasing oxidation time. The ratio of the absorbance value of the C=C stretching vibration to 2900 cm^{-1} is defined as an aromatization index for comparison purposes. The results presented in Figure 4.70 suggest increasing aromatization index values with increasing oxidation time due to the formation of highly aromatic structures.

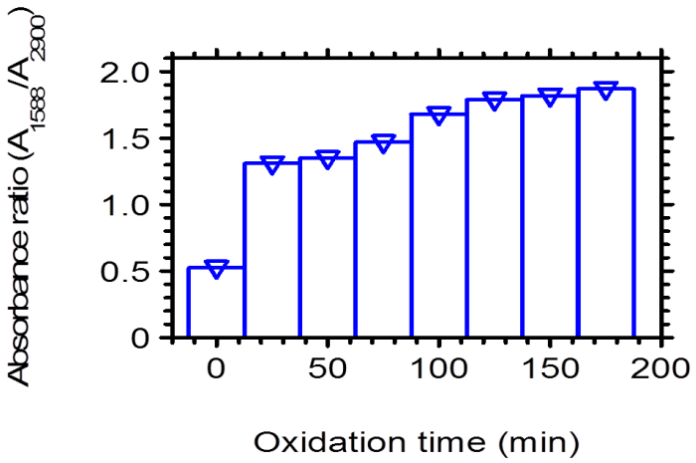

Figure 4.70 Changing of absorbance ratio (A_{1588}/ A_{2900}) as a function of oxidation time.

Following SMSPH-U impregnation, new bands appeared at 1200, 1010, and 760-780 cm^{-1} allotted to Si-O-cellulose, Si-OH, and symmetric stretching Si-O-Si vibrations, respectively [282, 284]. The broad IR spectrum at 1200 cm^{-1} is allotted to Si-O band, suggesting the binding of silica (SiO_2) groups onto the cellulose structure through cellulose OH groups. The IR vibration located around 760-780 cm^{-1} is allotted to the symmetrical stretching band of Si-O-Si, indicating intermolecular condensation between neighboring Si-OH groups suggesting strong intermolecular reactions. This indicates the formation of Si-O-Si coating on the jute fiber surface.

The vibration at 895 cm^{-1} allotted to asymmetrical out of phase cellulose ring stretching (C-O-C) lost its intensity by the progress of oxidation reactions with increasing

oxidation time, indicating the replacement of hydrogen atoms from the cellulose ring structures by functional groups or due to the creation of ring structures [279]. The results suggest that SMSPH-U impregnation seems to have catalyzed the dehydrogenation and dehydration reactions occurring in the oxidation reactions leading to the development of highly aromatic structures. SMSPH-U also restricted the production of tar and other volatile compounds typically observed in cellulosic fibers, leading to higher carbon yield [150].

4.4 Bamboo Fiber

4.4.1 Characterization of Original Bamboo Fiber

The bamboo yarn with a linear density of 29.892 tex was utilized in achieving thermal stabilization in this study. The sample had a volume density of 1.41 g/cm^3 and fiber thickness of 13.66±0.32 μm. The tensile strength of the bamboo yarn was 291.37±25.72 MPa.

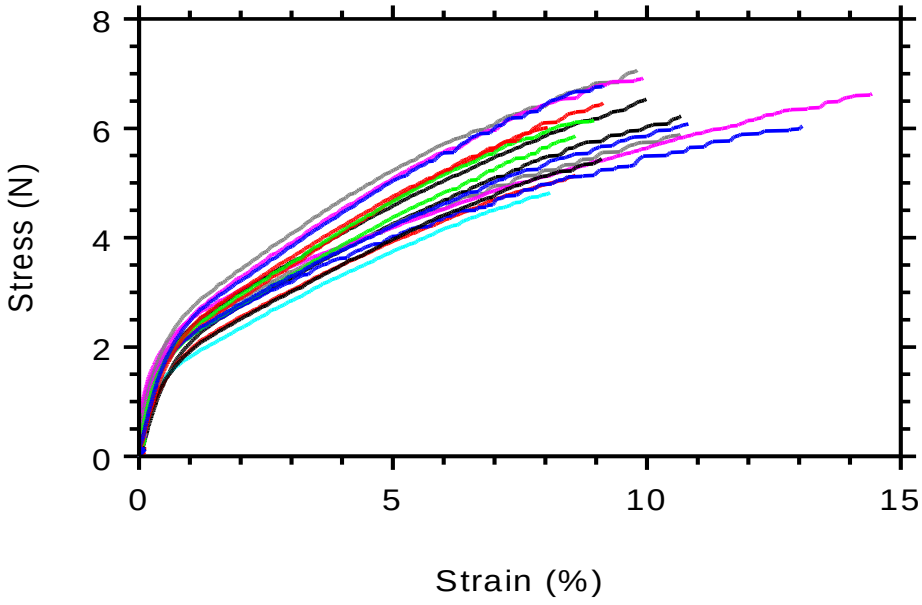

Figure 4.71 Stress-strain curve of original bamboo fiber.

4.4.2 Physical and Mechanical Characterization of Original and Thermally Stabilized Bamboo Fiber Impregnated with DAP-SMSU

With the progress of oxidation time, volume density values increased gradually from 1.41 g/cm^3 for untreated bamboo fiber to 1.56 g/cm^3 for the DAP-SMSU impregnated and 120 minutes oxidized samples. However, a sharp rise in volume density was observed within just 40 minutes of thermal stabilization and reached 1.505 g/cm^3.

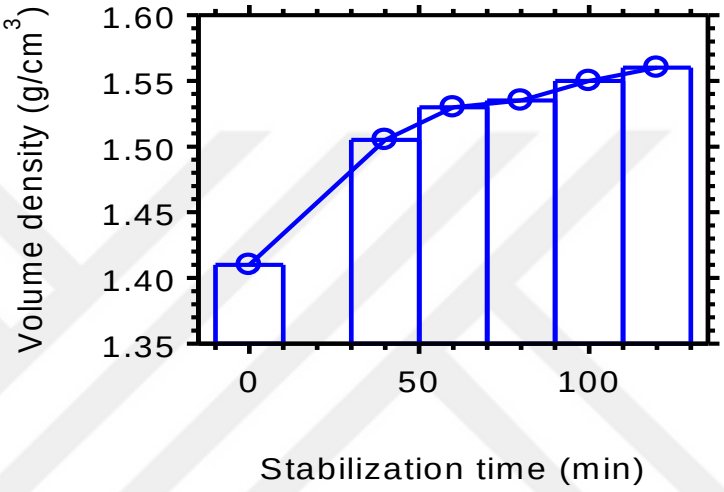

Figure 4.72 Volume density of the untreated and oxidized bamboo fiber.

Linear density values presented a downward trend throughout the whole oxidation period. The linear density value of untreated bamboo yarns was 29.89 tex. In the 40 minutes oxidized samples, this was lost by 17.80%, and reached 24.57 tex. For the 120 minutes oxidized bamboo samples, the linear density was 19.83 tex.

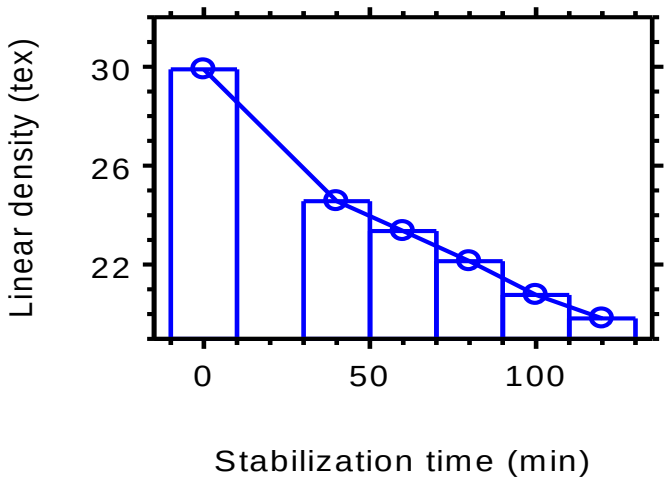

Figure 4.73 Linear density of the untreated and oxidized bamboo fiber.

The raw bamboo sample had a fiber thickness of 13.66 μm. The fiber thickness value plummeted sharply by 18.37% after 40 minutes of oxidation, and the reduction continued with growing oxidation time. The fiber thickness of bamboo samples reached 8.89 μm after 120 minutes of oxidation at 245°C, representing the highest loss.

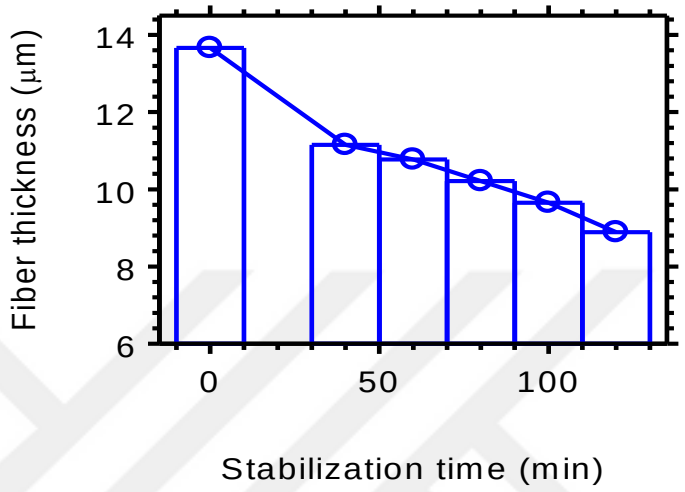

Figure 4.74 Fiber thickness of the untreated and oxidized bamboo fiber.

The tensile strength of the untreated bamboo sample was 291.37 MPa. For 40 minutes of oxidative thermal stabilization, the tensile strength value declined sharply to 142.51 MPa. Afterward, the reduction followed a trend of gradual loss with growing oxidation duration.

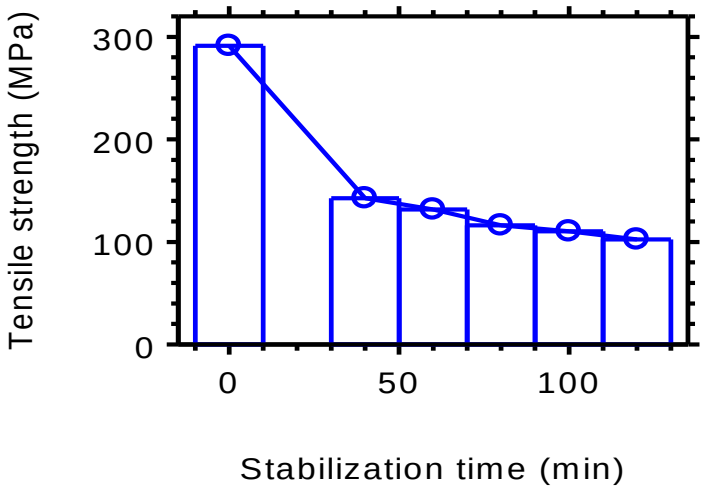

Figure 4.75 Tensile strength of the untreated and oxidized bamboo fiber.

4.4.3 Thermal and Structural Characterization of Original and Thermally Stabilized Bamboo Fiber Impregnated with DAP-SMSU

4.4.3.1 Evaluation of X-ray Diffraction Analysis (XRD)

Equatorial X-ray diffraction profiles of pristine, DAP-SMSU integrated and thermally stabilized bamboo fibers are illustrated in Figure 4.76. Inspection of the equatorial X-ray diffraction trace of pristine bamboo fibers demonstrates the presence of four well-defined crystalline peaks as the most prominent feature.

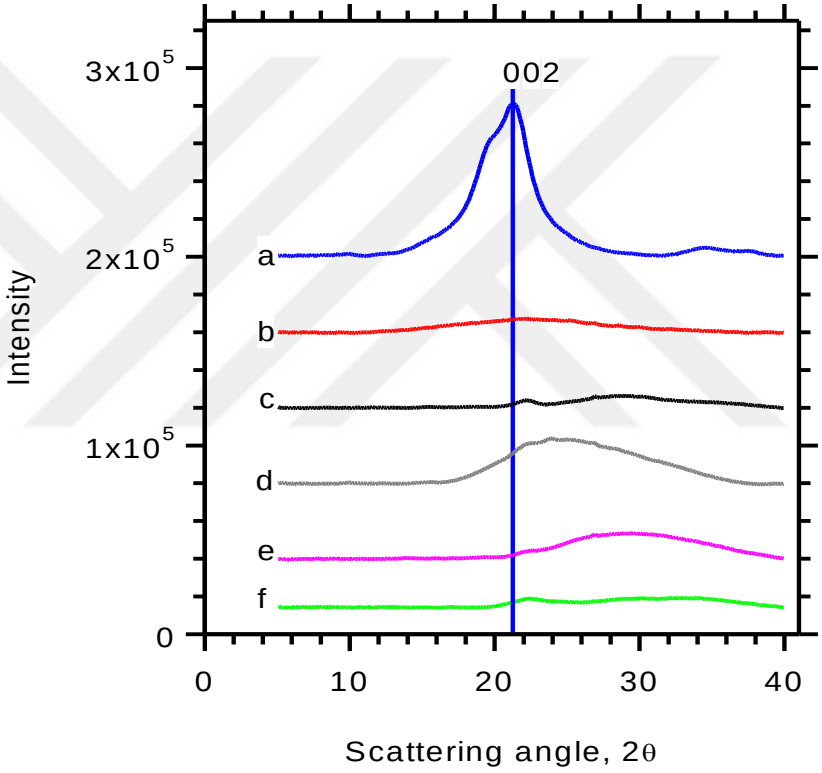

Figure 4.76 Equatorial X-ray diffraction profiles of pristine (a), and DAP-SMSU incorporated-oxidized bamboo fibers for different oxidation times. (b) 40 min; (c) 60 min; (d) 80 min; (e) 100 min; (f) 120 min.

A curve-fitting method was utilized for the equatorial X-ray diffraction profiles to acquire precise peak parameters by means of apparent X-ray stabilization index, X-ray crystallinity, crystal size, and amorphous ratio for different oxidation periods. The equatorial X-ray diffraction profile of pristine bamboo fibers can be resolved into four crystalline peaks of cellulose I structure located at about 16.4±0.3, 19.7±0.2, 22.4±0.2 and 34.8±0.3 attributed to $(10\bar{1})$, (120), (002) and (040) reflections (Figure 4.77).

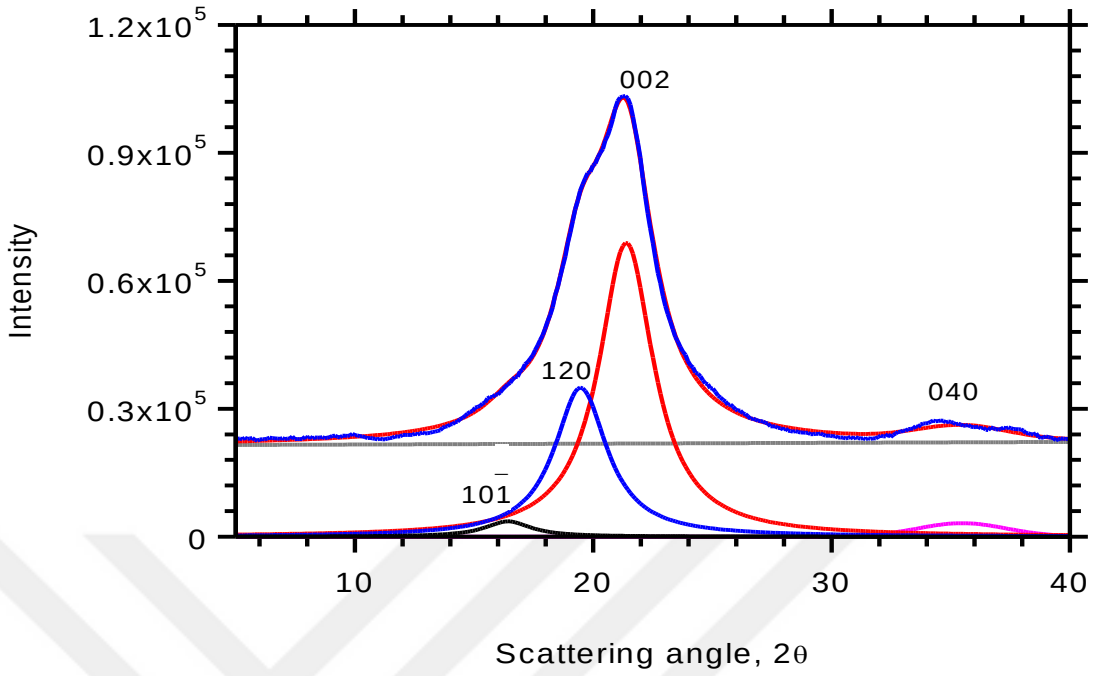

Figure 4.77 Curve fitting of equatorial X-ray diffraction trace of original bamboo fiber.

A monoclinic unit cell is truly represented by these reflections. When compared to the intensities of the ($10\bar{1}$), (120), and (040) reflections, it is apparent that the 002 peak has the highest intensity. To strengthen peak sharpness in the tail portions of adjacent peaks, an extra peak positioned at 29° (d-spacing of 0.488 nm) was utilized. The additional reflection used at 29° is a broad half-height width peak, representing a typical amorphous behavior. A comparative assessment of the calculated and observed d-spacing values, and the peak parameters obtained from the curve-fitting method of pristine bamboo fibers are presented in Table 4.13.

Table 4.13 Resolved peak parameters of curve-fitted equatorial X-ray diffraction profile of pristine bamboo fibers.

Peak ref.	f	A (height)	W (width)	Position (2θ)	d_{obs} (nm)	d_{calc} (nm)
($10\bar{1}$)	0.1	7266	3.73	16.4	0.540	0.543
(120)	0.43	34944	2.59	19.7	0.450	-
(002)	0.95	69112	2.66	22.4	0.396	0.392
(040)	0.41	3176	3.02	34.8	0.259	0.258

DAP-SMSU impregnation followed by oxidation in the air atmosphere at temperatures up to 245 °C and oxidation times ranging from 40 to 120 minutes showed a remarkable effect on the crystalline structure of bamboo fibers as the degree of apparent crystallinity of the cellulose I structure. A close observation of the X-ray diffraction profiles illustrated in Figure 4.76 indicated a steady disappearance of the crystalline structure by increasing oxidation time. The loss of the intensity of the X-ray diffraction traces indicates the development of amorphization (i.e., decrystallization) reactions with progressing oxidation time. The results presented in Table 4.14 show that some of the crystalline peaks seem to disappear with progressing oxidation reactions as a result of the ongoing decrystallization process. It seems that (101) reflection did not exist, whereas an amorphous carbon peak appeared after the oxidation time of 60 minutes. On the other hand, the (002) and (040) reflections appeared to survive the oxidation reactions through the oxidation time from 40 to 120 minutes.

Table 4.14 The presence and absence of X-ray diffraction reflections of the bamboo samples under investigation.

Stabilization time (min)	Reflection				
	101	$10\bar{1}$	002	040	Amorphous carbon
0	-	+	+	+	-
40	-	+	+	+	-
60	-	-	+	+	+
80	-	-	+	+	+
100	-	-	+	+	+
120	-	-	+	+	+

Key: + : Reflection is present

- : Reflection is absent

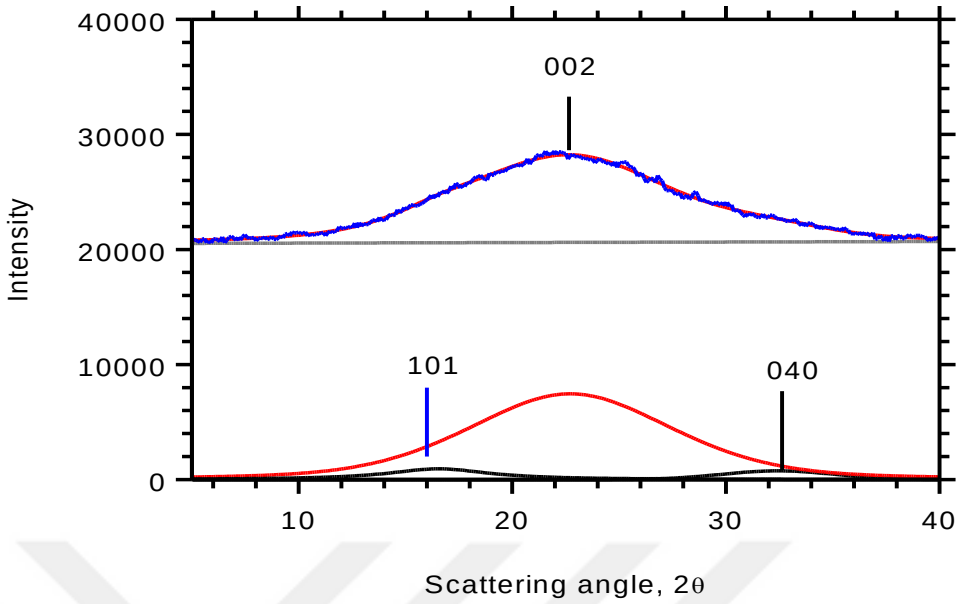

Figure 4.78 Curve fitting of equatorial X-ray diffraction trace of thermally stabilized bamboo fibers (40 min stabilization time).

Curve-fitting of X-ray diffraction profile of oxidized bamboo sample at stabilization duration of 40 minutes is presented in Figure 4.78. Equation 3 was used to calculate the ratios of amorphous and crystalline (i.e., cellulose I) structures based on peak areas derived from curve-fitting of X-ray diffraction patterns shown in Figure 4.76. The findings illustrated in Figure 4.79 indicate the X-ray crystallinity was reduced from 36 to 3% after the oxidation time of 120 minutes. In contrast, the amorphous fraction rose from 64 to 97.6% after 120 minutes of oxidation.

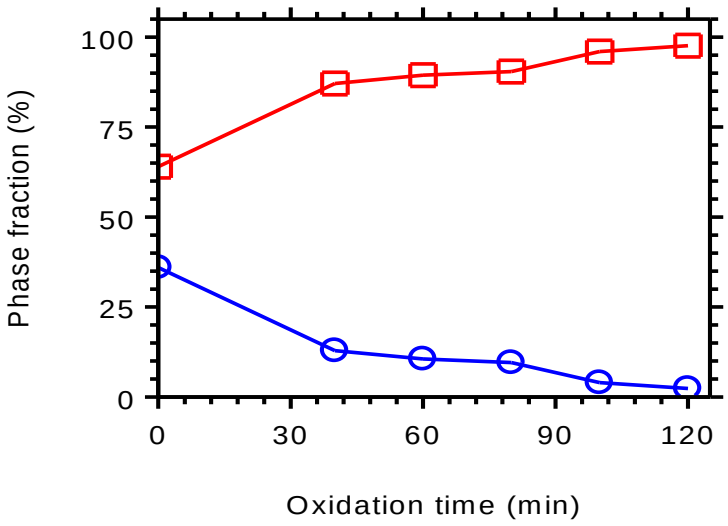

Figure 4.79 Comparison of phase ratios of pristine and stabilized bamboo fibers for different oxidation times. (O) crystalline phase; (□) amorphous phase.

Figure 4.80(a) presents the X-ray stabilization index values of the oxidized bamboo fibers for different oxidation times evaluated by using Equation 2. Once the oxidation time was raised from 40 to 120 minutes, the X-ray oxidation index rose from 64 to 97.6%. Evaluation of X-ray stabilization index is regarded as a dependable way to assess the proportion of aromatic or cyclized and cross-linked structures produced in the oxidation stage [219, 223, 275]. The experimental outcomes noticeably point out that DAP-SMSU impregnated and oxidized bamboo fibers resulted in the gradual disappearance of cellulose I crystal structure and growth in the disordered phase along with an enhancement in the ratio of aromatic structure possessing cross-linked ladder-like structural species.

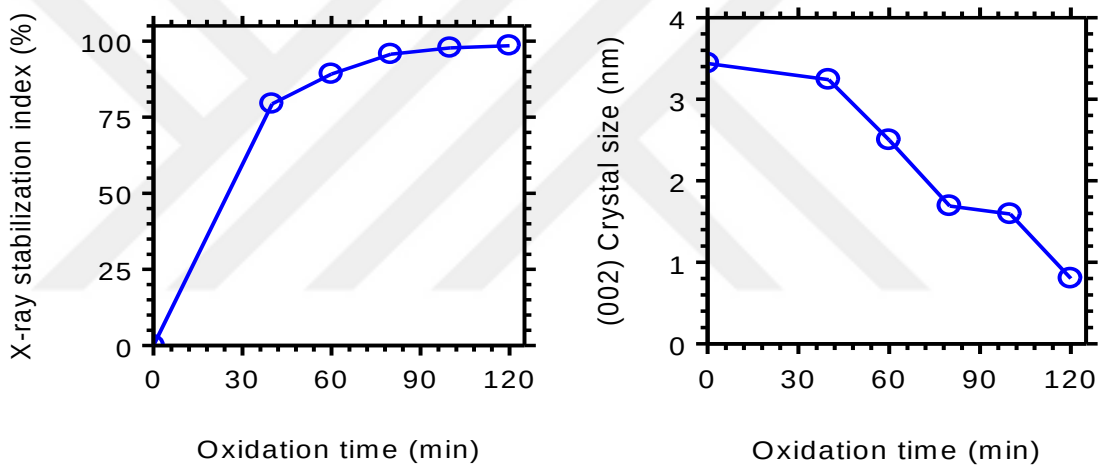

Figure 4.80 Comparison of X-ray stabilization index (a), and the crystal size for (002) planes (b) of pristine and oxidized bamboo fibers for different oxidation times.

During the oxidation reactions, 101 reflection disappeared as a result of ongoing oxidation reactions. The most prominent and strongest (002) peak kept its presence during the oxidations reactions. The half-height widths of the reflections increased with growing oxidation times, indicating a progressive reduction in the crystal dimensions. This is considered to be owing to the structure collapsing during the decrystallization processes [275]. The gradual disappearance of the $10\bar{1}$, 002 and 040 peaks is likely owing to the decrystallization or amorphization reactions collapsing the cellulose I crystal structure.

Since the (002) reflection kept its presence during the oxidation process, it was utilized for the assessment of lateral crystal size during the oxidation process. Evaluation of crystal sizes due to raw and oxidized bamboo fibers was performed using Equation 4. Figure 4.80(b) shows the variation of crystal size corresponding to prominent (002) peak as a function of oxidation time. Crystal size for the (002) reflection was lowered from 3.4 to 0.8 nm with growing oxidation time due to ongoing decrystallization processes.

Following the curve-fitting procedure, an amorphous peak was observed at around 25.5° 2θ attributed to pre-graphitic carbon structure. It is mentionable that the presence of amorphous carbon peak was observed after the oxidation time of 60 minutes. Assuming that the interlayer distance between graphene planes is 0.3354 nm, the corrected crystallite sizes using Equation 4 for this peak vary between 1.5 and 1.7 nm, and the corresponding number of graphene layers vary from 0 to 5 (Figure 4.81). There is no doubt that the presence of the amorphous carbon structure will lead to further enhanced carbonization reactions with increasing temperature during the carbon fiber processing.

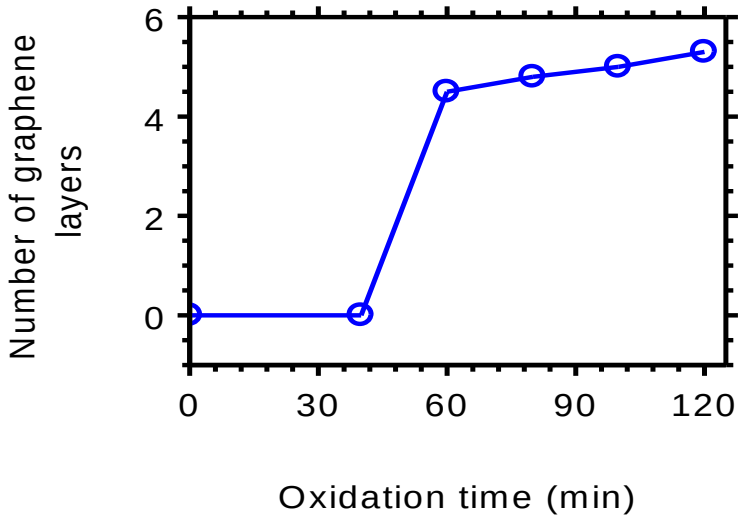

Figure 4.81 Comparison of the number of graphene layers as a function of oxidation time for the amorphous carbon reflection.

4.4.3.2 Evaluation of Differential Scanning Calorimetry Analysis (DSC)

DSC thermograms were used to investigate the structural alterations occurring in the oxidation stage of the DAP-SMSU impregnated bamboo fibers for different oxidation times. The DSC traces of raw bamboo fiber illustrated in Figure 4.82(a) reveals a wide endotherm occurring immediately 100 °C owing to the presence of water vapor. The depolymerization and decomposition reactions of cellulose, hemicellulose, and lignin are followed by processes leading to the production of levoglucosan and its decomposition components, resulting in an endotherm spanning from 245 to 345 °C with a maximum temperature of 330 °C [285]. The intensity of this peak weakened and broadened with increasing oxidation times. The DSC thermogram of raw bamboo fiber also showed an extra peak as a wide exotherm ranging from 350 to 400 °C with a maximum temperature of 345 °C resulted from the stabilization of levoglucosan-based volatile pyrolysis intermediates [286].

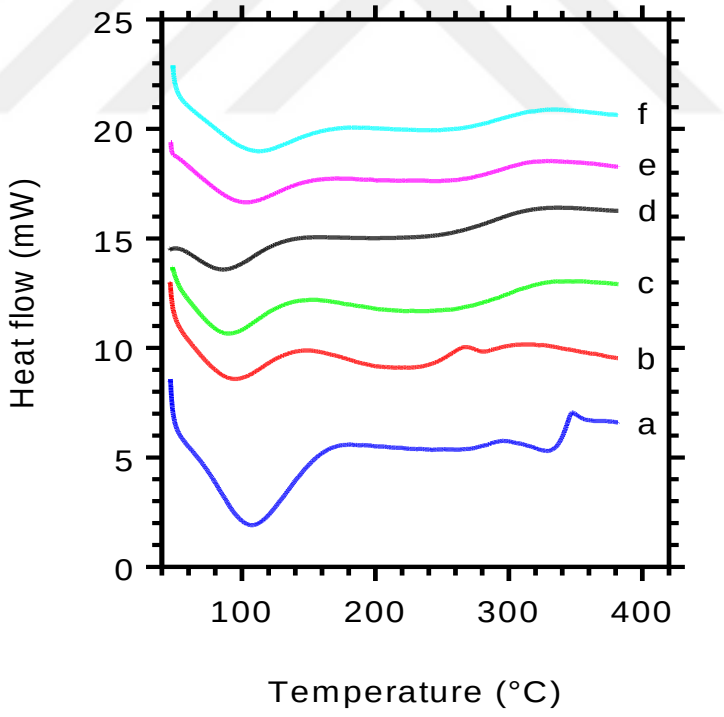

Figure 4.82 DSC thermograms of original (a) and DAP-SMSU incorporated-stabilized bamboo fibers for different oxidation periods. (b) 40 min; (c) 60 min; (d) 80 min; (e) 100 min; (f) 120 min.

DAP-SMSU integration followed by thermal treatment in an air atmosphere seemed to have a significant impact on the DSC thermograms of oxidized bamboo fibers as shown in Figure 4.82(b–f). The DSC patterns of the sample stabilized for 40 minutes at 245 °C shifted to 280 °C because of the depolymerization reactions of remaining cellulose, hemicellulose, and lignin. The decomposition temperature of bamboo fiber that has been oxidized for 40 minutes is 65 °C lesser than that of raw bamboo fiber. As an influential flame-retardant, DAP-SMSU impregnation resulted in a serious depletion of the cellulose decomposition temperature [287]. The chemical interactions occurring within the hydroxyl groups of the cellulose, hemicellulose, and lignin structural units accelerated dehydration reactions of cellulose structural units, resulting in a decrease in decomposition temperature. The substantial decrease in cellulose-hemicellulose-lignin decomposition temperature following DAP-SMSU treatment is often thought to be due to a decrease in crystallinity as stabilization duration increases [277].

The region beneath the primary endothermic peak is observed to be smaller after the oxidation time of 40 minutes and disappeared completely between 60 and 120 minutes, respectively; this behavior is attributed to the dehydration process that occurred by the chemical reactions in the central hydroxyl groups (-CH_2-OH) of cellulose rings, hemicellulose, and lignin. The removal of hydroxyl groups from cellulose, hemicellulose, and lignin chains, as well as the loss of hydrogen bonds (H-bonds) within the hydroxyl groups, is believed to result in the formation of water, and also causes double bonds formation, mostly C=O and C=C. By the dehydration process, the generation of volatile compounds is avoided, the structure of cellulose-hemicellulose-lignin is preserved, and weight loss is typically restricted to water loss alone [5].

After 40 minutes of oxidation at 245 °C, the region relating to the decomposition endotherm has decreased and vanished (Table 4.15). The disappearance of the endotherm indicates that the depolymerization processes are suppressed, and the generation of levoglucosan is halted. This tendency might be the cause of higher carbon yields and prolonged oxidation durations after DAP-SMSU pretreatment. The disappearing of the decomposition endotherm for 40 minutes oxidation time and beyond also indicates the formation of high temperature resistant and thermally stabilized structural units. The DSC profiles of the bamboo fibers oxidized for 40 minutes and

beyond reveal the complete vanishing of the decomposition endotherms originating from the cellulose I-hemicellulose-lignin structure loss and the development of extremely thermally stable and cross-linked structural units.

Table 4.15 Thermal properties of raw and DAP-SMSU incorporated and oxidized bamboo fibers.

Oxidation time (min)	Decomposition temperature (°C)	Area of (ΔH) decomposition (J/g)	Exotherm due to levoglucosan oxidation (°C)
0	345	31.77	345
40	280	-	-
60	-	-	-
80	-	-	-
100	-	-	-
120	-	-	-

4.4.3.3 Evaluation of Thermogravimetric Analysis (TGA)

The TGA technique continuously evaluates the weight loss of specimens for variable time or temperature at a linear rate. Various steps in the TGA thermogram provide valuable information on thermal stability, original sample composition, the thermal stability of intermediates formed, and kinetic data. Essentially, the TGA method is dynamic in nature and offers quantitative information about the thermal stability of the samples under study. Thermal analysis is one of the most important techniques to observe and analyze the thermal behavior of samples under investigation. The thermogravimetric analysis method in the present investigation has been utilized to study the thermal behavior of bamboo fibers.

In the case of bamboo fibers, the weight loss occurring during TGA scanning was due to the decomposition of cellulose, hemicellulose, and lignin structural units. Usually, higher decomposition temperatures result in higher thermal stability [288]. In cellulosic fibers, there is no glass transition or melting temperatures. The only temperature is that of decomposition around 365-370 °C at a heating rate of 10 °C/min. It should be

emphasized that the exact positions of these temperatures are greatly dependent on the rate of heating and the impurities present in the material. According to published literature [289], the heating rate is an important factor for differentiating the relative features of good quality fibers. The results indicated that increasing heating rates from 5 to 150 °C/min, decomposition peak position increased from 321 to 394 °C for water-retted lignocellulosic based flax fibers [289].

According to Liodakis [290], the range of transition temperatures was observed in a typical TGA scan of lignocellulosic fibers are 200-280 °C for hemicellulose, 320-370 °C for cellulose, and 370-550 °C for lignin. TGA measurements showed that the temperature corresponding to 10% weight loss for bamboo fiber is 285 °C and that of 20% weight loss is 305 °C. The main characteristic of the TGA scan of the raw bamboo fibers is the rapid weight loss from 300 to 600 °C. This trend continues right up to the final scan temperature of 800 °C.

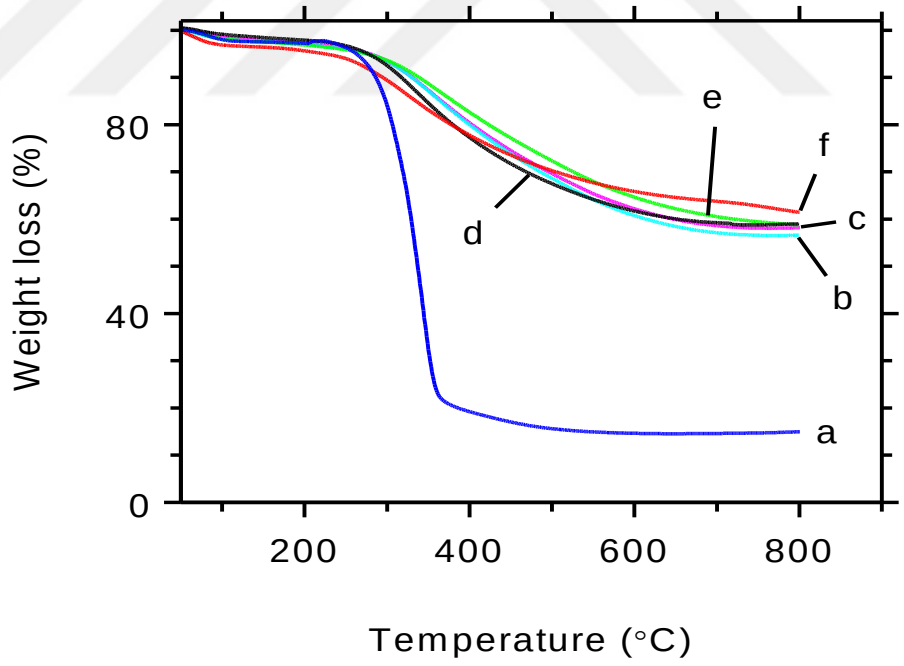

Figure 4.83: TGA thermograms of pristine (a) and DAP-SMSU incorporated-stabilized bamboo fibers for different stabilization periods. (b) 40 min; (c) 60 min; (d) 80 min; (e) 100 min; (f) 120 min.

TGA was employed to investigate the oxidative thermal stability of original and DAP-SMSU pretreated bamboo fibers that had been oxidized in the air atmosphere. For the

production of bamboo-based ACFs, rapid pyrolysis (i.e., carbonization) in the inert environment is unfavorable. It is expected to promote secondary reactions that result in the low carbon yield and the release of carbon-containing volatile compounds [146]. A substantial amount of carbon dioxide, organic acids, and aldehydes were generated as volatile derivatives during rapid pyrolysis, leading to poor carbon yield. The abundance of oxygen in the air is also critical to achieving a higher carbon yield.

TGA could be used to quantify the effect of DAP-SMSU incorporation on the decomposition characteristic of bamboo yarn oxidized in air at various temperatures. To assess the comparative yields of the carbonization phase for different oxidation duration, the carbonization yield and the weight loss values can be utilized. The TGA thermograms of original and DAP-SMSU incorporated-oxidized bamboo samples are illustrated in Figure 4.83. At about 100 °C, all TGA thermograms revealed weight losses, indicating moisture evaporation due to physically bonded water. Raw bamboo fibers exhibited no significant weight loss after this point, up to 250 °C [Figure 4.83(a)]; afterward, the frequency of weight loss rose significantly between 250 and 350 °C, following a gradual weight loss up to 800 °C.

In contrast, DAP-SMSU incorporated-oxidized bamboo fibers [Figure 4.83(b–h)] demonstrated notable deviations in thermal properties. The TGA profiles of the stabilized bamboo fibers revealed lower weight loss for higher stabilization time, indicating growing carbon yields attributable to the enhanced cross-linking and aromatization (ladder-like structure formation) reactions between the cellulose-hemicellulose and lignin chains. Because of enhanced cross-linking and aromatization reactions, raw bamboo fibers lost weight across a limited temperature span, while stabilized specimens lost weight across a wide temperature span.

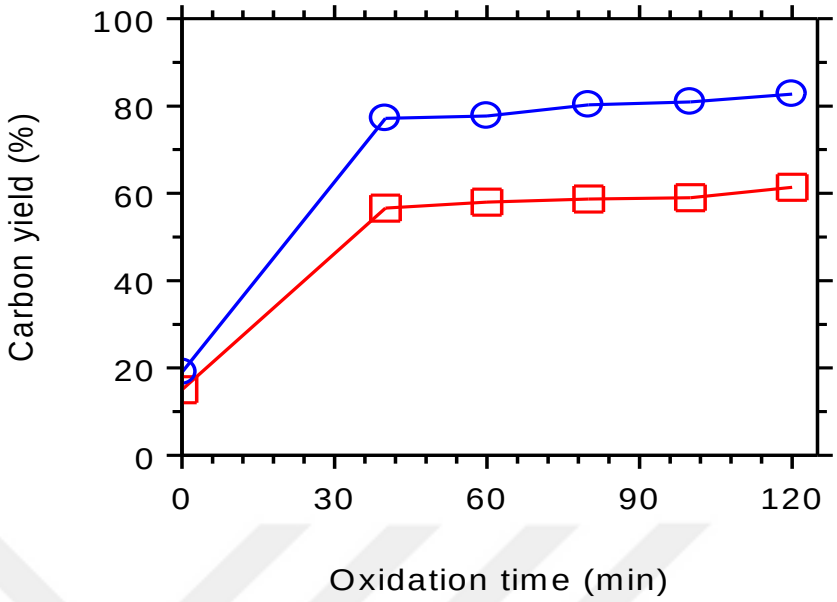

Figure 4.84 Carbon yields fractions of pristine and DAP-SMSU incorporated-oxidized bamboo fibers at the temperature of 400 °C (O) and 800 °C (□).

For the original and DAP-SMSU incorporated-oxidized bamboo fibers, an evaluation of the carbon yield values at temperatures of 400 and 800 °C are presented in Figure 4.84. The results indicate the continuous increase of carbon yield percentage by the intensification of the stabilization period. At 400 °C temperature, the value of carbon yield was noticed to be greater than that of 800 °C, ranging from 19% and 83%. The results showed the highest carbon yield value of DAP-SMSU impregnated 120 minutes stabilized bamboo yarns by 61% at 800 °C.

4.4.3.4 Evaluation of Infrared Spectroscopy Analysis (FT-IR)

FT-IR spectroscopy analysis is one of the most practical and valuable approaches for assessing the structure of cellulose, mainly for analyzing the structure and properties of hydrogen bonding in cellulose crystalline structure. In the infrared spectra of cellulose, the range of 4000-2000 cm^{-1} is assigned to the OH and C-H stretching vibrations, and the range of 2000-400 cm^{-1} is known to be the most valuable segment for both quantitative and qualitative analysis (Figure 4.85). The 1500-1200 cm^{-1} region is

attributed to methylene (CH_2) bonds. The bands positioned at 1420, 1160, 1102, and 895 cm^{-1} are known as crystallinity spectra.

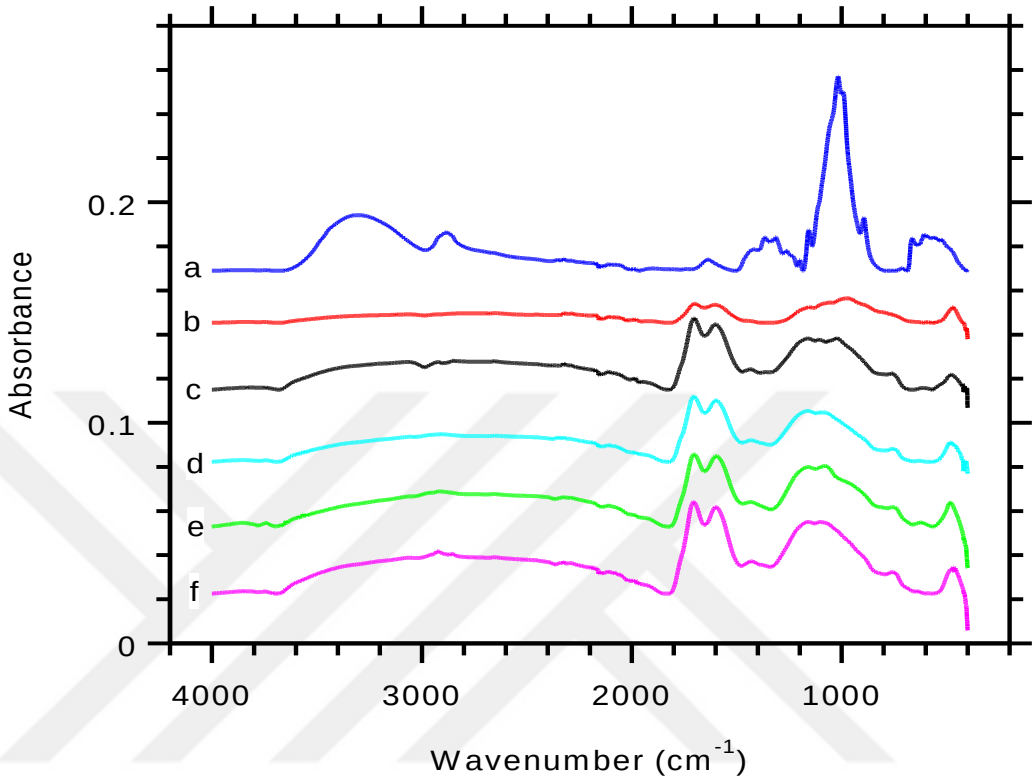

Figure 4.85 Infrared spectra in the range of 4000–400 cm^{-1} of original (a) and DAP-SMSU incorporated-oxidized bamboo fibers for different oxidation periods. (b) 40 min; (c) 60 min; (d) 80 min; (e) 100 min; (f) 120 min.

The band positioned at 2900 cm^{-1} is attributed to methyl (C-H) and methylene (CH_2) vibrations (Figure 4.85). This vibration has also been used as an internal standard due to the unchanging relative intensity in the present investigation, as it is clearly well-defined and prominent vibration in pristine bamboo fiber. The use of standard internal vibration makes it easy to make comparisons between different samples for different oxidation times. The vibration at 3300 cm^{-1} due to hydrogen-bonded OH stretching vibrations is also taken into consideration during the quantitative analysis. Detailed assignments for the bands in the spectra of cellulose I are listed in Table 4.16. The band assignments are based on published literature [279–281].

Table 4.16 Band assignments for the 3300-800 cm^{-1} region of the infrared spectrum of bamboo fiber [279–281].

Wavenumber (cm^{-1})	**Assignment**
3300	OH stretching (intermolecular hydrogen bonding in the 101 plane)
2920	CH_2 asymmetrical stretching
2885	CH and CH_2 stretching
2860	CH stretching
1700	C=O stretch in unconjugated ketones, carbonyls, and ester groups of hemicellulose structure
1637	H-O-H expanding and contracting vibration adsorbed H_2O
1605	Lignin (aromatic skeletal vibrations, C=C stretch + C=O stretch)
1420	CH_2 symmetric bending
1316	CH_2 wagging
1235	C–O stretching in acetyl group
1205	OH in-plane bending
1160	Asymmetrical in-phase ring stretching (crystalline) (well defined)
1110	Asymmetrical in-phase ring stretching (crystalline)
1015	C=O stretching (strong)
895	Asymmetrical out of phase ring stretching (C-O-C) (crystalline)
800	Ring breathing vibration

Intermolecular H-bonded OH stretching positioned at 3300 cm^{-1} loses its intensity with progressing oxidations reactions. In the present work, the absorbance ratio of A_{3300}/A_{2900} is defined as a dehydrogenation index and is presented in Figure 4.86(a). The results suggest that with increasing oxidation time, the dehydrogenation index decreases indicating the loss of hydrogen from the bamboo fibers. Carbonyl stretching vibration positioned at 1740 cm^{-1} allotted to C=O stretching vibration is shifted to 1700 cm^{-1} indicating strong interaction with OH groups in the creation of H-bonds.

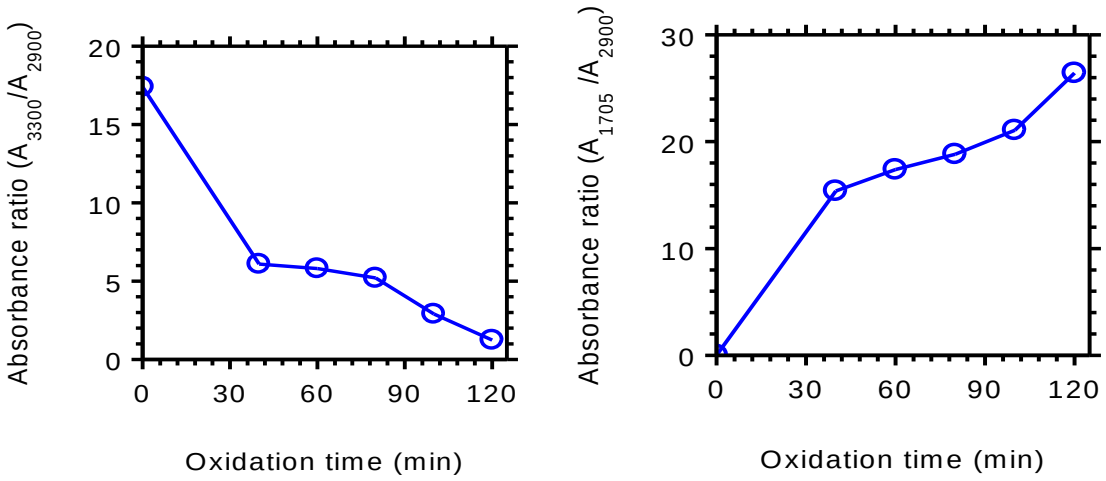

Figure 4.86 Changing of absorbance ratio (a) A_{3300}/A_{2900} (dehydrogenation index), and (b) A_{1705}/A_{2900} (oxidation index) for different oxidation times.

The absorbance ratio of A_{1705}/A_{2900} is defined as the oxidation index in the present investigation. The results presented in Figure 4.86(b) show the increasing oxidation index with increasing oxidation time suggesting increased oxygen uptake during the oxidation reactions. A completely new band placed about 1600 cm^{-1} seemed as a strong vibration assigned to C=C stretching became major in the samples oxidized for 40 minutes and higher, suggesting the formation of a highly aromatic structure during the oxidation process. The absorbance ratio of A_{1600}/A_{2900} is defined as the aromatization or cyclization index in the present investigation (Figure 4.87(a)).

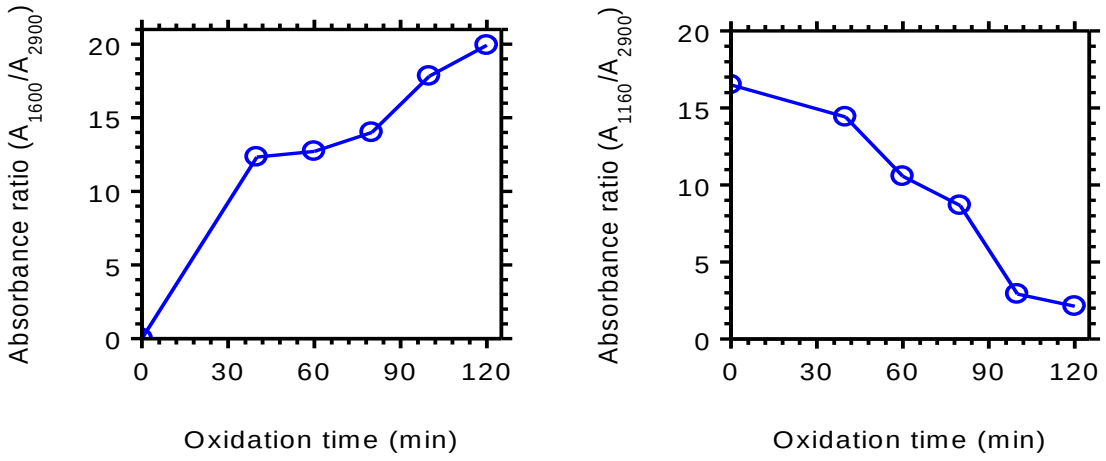

Figure 4.87 Changing of absorbance ratio (a) (A_{1600}/ A_{2900}) (aromatization or cyclization index), and (b) A_{1160}/A_{2900} (decrystallization index) for different oxidation times.

The IR vibration located at 1160 cm^{-1} assigned to asymmetrical in-phase ring stretching in crystalline phase loses maximum intensity with growing oxidation time, indicating the gradual loss of crystalline structure as a result of amorphization reactions. The absorbance ratio of A_{1160}/A_{2900} is defined as the decrystallization index. Figure 4.87(b) shows that the decrystallization index decreases with increasing oxidation time, demonstrating the crystalline structure loss as oxidation time progresses. The spectrum at 895 cm^{-1} assigned to asymmetrical out of phase cellulose ring stretching (C-O-C) loses its intensity with progressing oxidation reactions as oxidation time increased, indicating the replacement of hydrogen atoms from the cellulose structures by functional groups or due to the ring structure formation [275]. The absorbance ratio of A_{895}/A_{2900} is also defined as the decrystallization index. Figure 4.88 indicates that the crystallization index decreases with increasing oxidation time, showing the crystalline structure loss with increasing oxidation time.

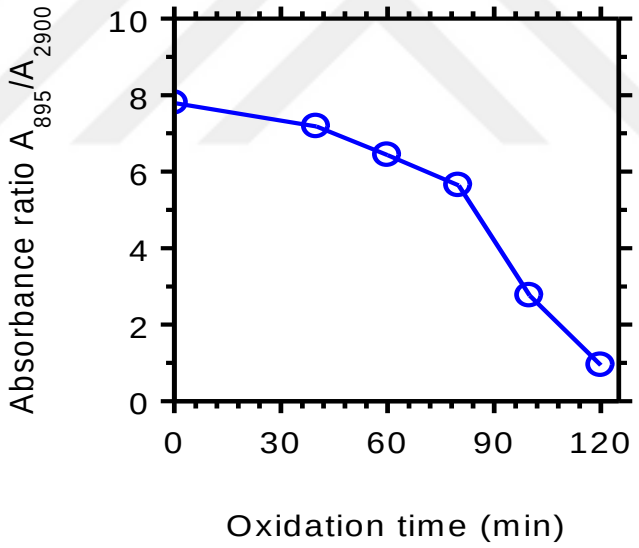

Figure 4.88 Changing of absorbance ratio (A_{895}/A_{2900}) (decrystallization index) for different oxidation times.

4.4.3.5 Scanning electron microscopy (SEM)

SEM was employed to assess the surface features of pristine and oxidized bamboo fiber samples. The surface characteristics of the oxidized bamboo fiber samples do not appear to alter significantly for variable oxidation durations, according to SEM analysis.

According to the available literature [219], the surface area temperature prevails lesser than the internal temperature of the precursor fiber. As a result, the heat transmitted during the stabilization phase is expected to drive the cyclization reaction and result in the formation of a disordered ladder-like pattern in the center of the oxidized specimens.

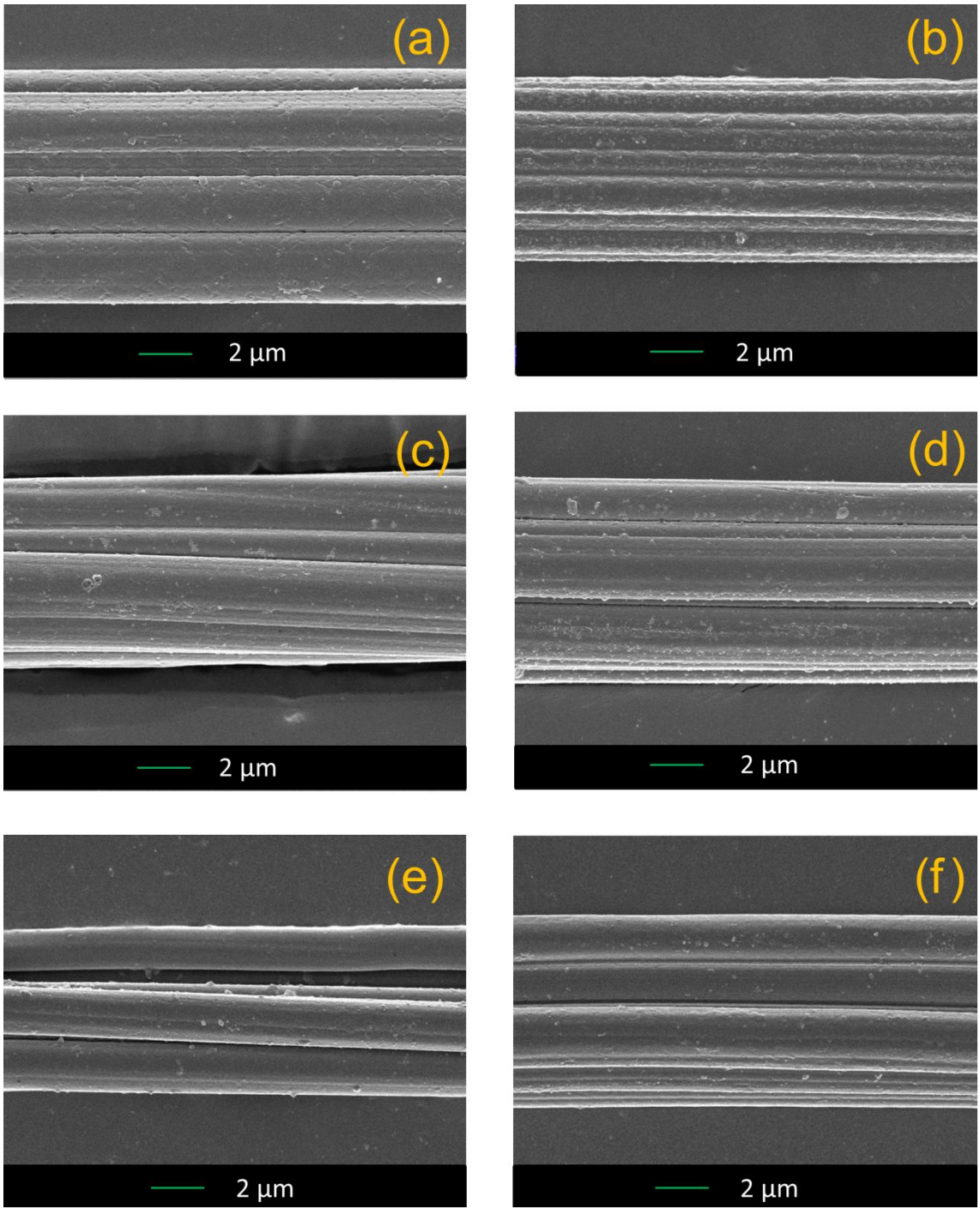

Figure 4.89 Longitudinal SEM images of pristine (a) and oxidized bamboo fiber samples for different oxidation times. (b) 40 min; (c) 60 min; (d) 80 min; (e) 100 min; (f) 120 min.

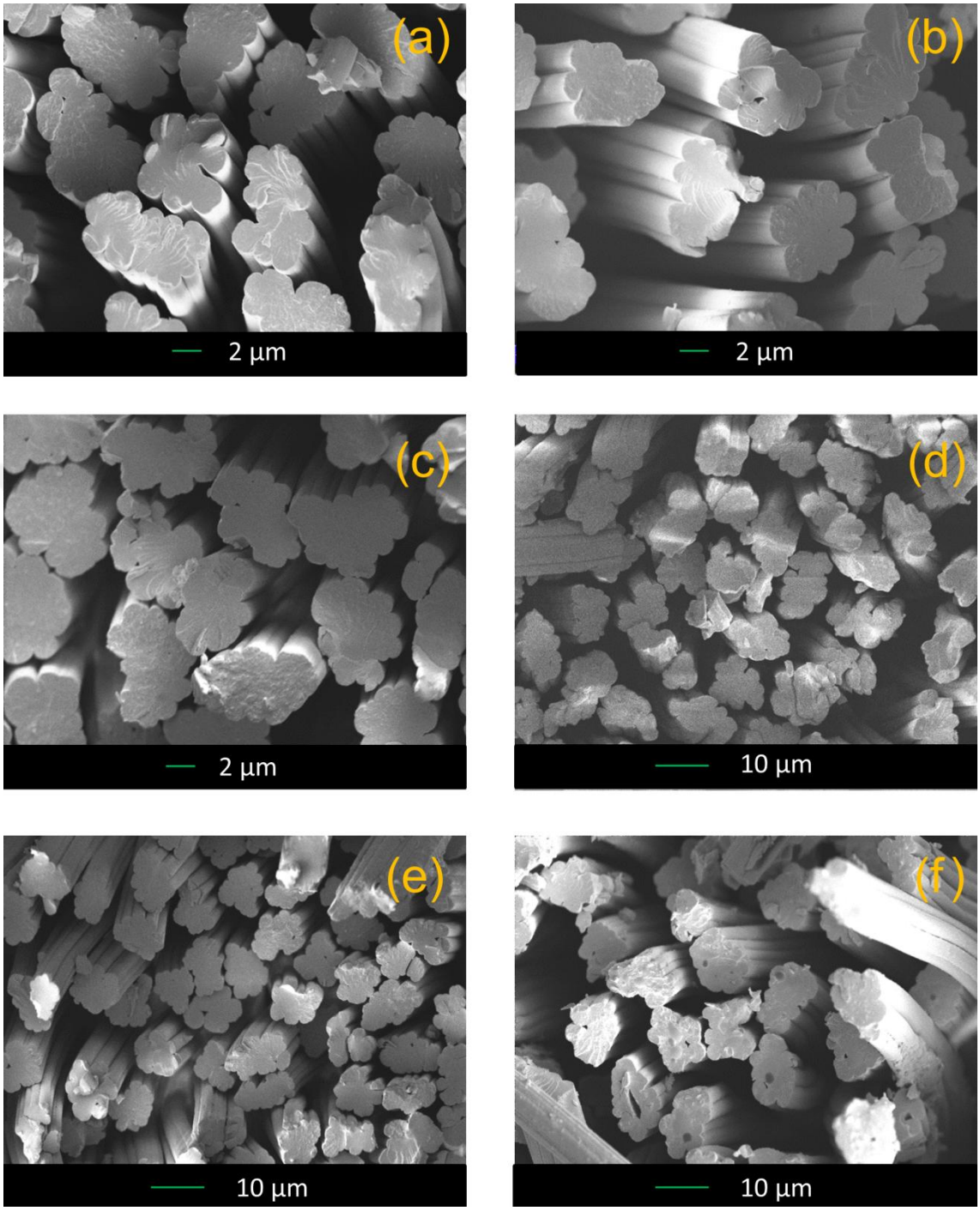

Figure 4.90 Cross-sectional SEM images of pristine (a) and oxidized bamboo fiber samples for different oxidation times. (b) 40 min; (c) 60 min; (d) 80 min; (e) 100 min; (f) 120 min.

4.5 Flax Fiber

4.5.1 Characterization of Original Flax Fiber

Naturally available flax yarn was used in this work to obtain thermal stability. The linear density of the original flax samples was 51.45 tex, and the fiber thickness was 9.76±0.34 μm. Tensile strength was found as 464.56±39.44 MPa of the flax yarn.

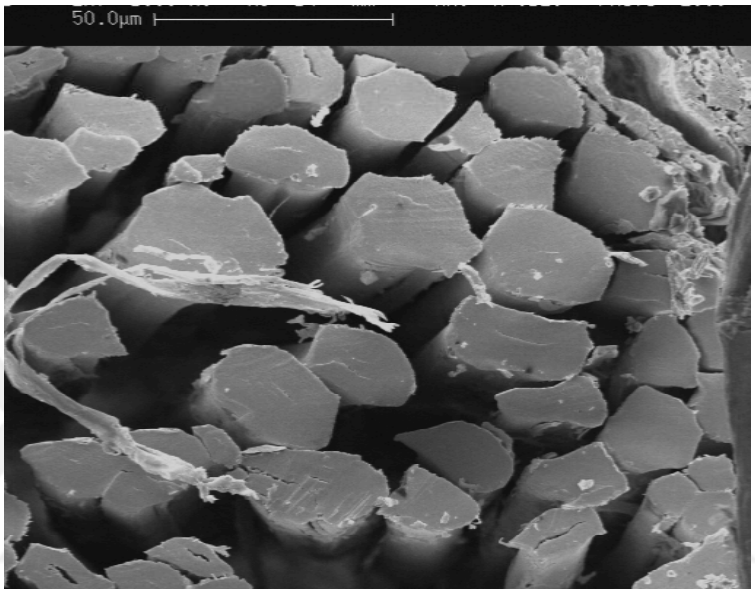

Figure 4.91 Cross-sectional SEM image of original flax fiber.

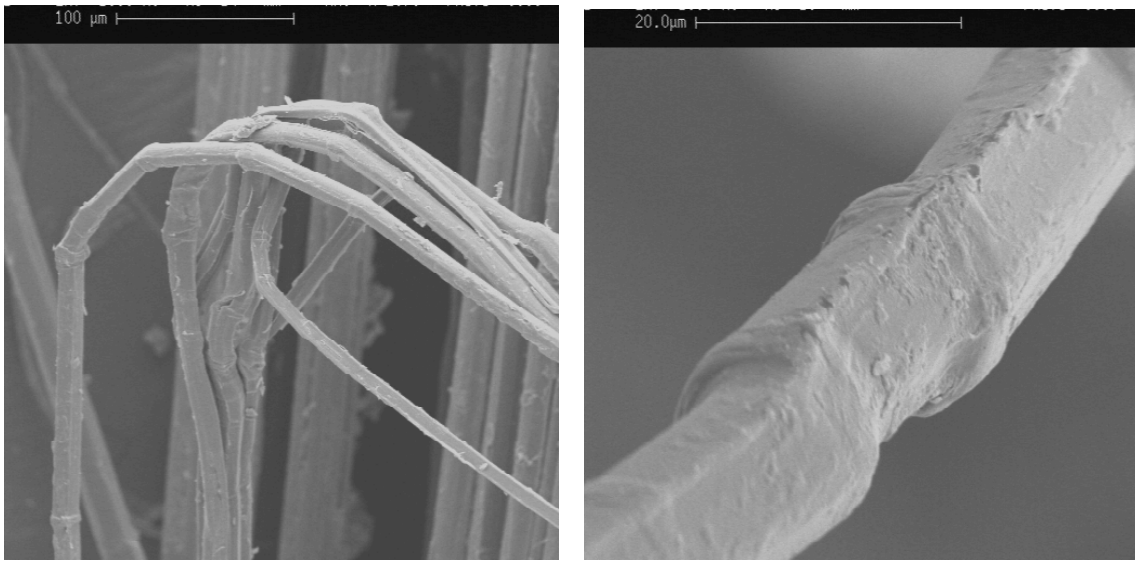

Figure 4.92 Longitudinal SEM images of original flax fiber.

4.5.2 Physical and Mechanical Characterization of Original and Thermally Stabilized Flax Fiber Impregnated with DAP-BAU

The volume density of the original flax fiber was 1.460 g/cm^3. DAP-BAU incorporation and thermal oxidation result in continuing rise of volume density values. This value reached 1.59 g/cm^3 for the 125 minutes oxidized flax samples by growing a total of 8.9%.

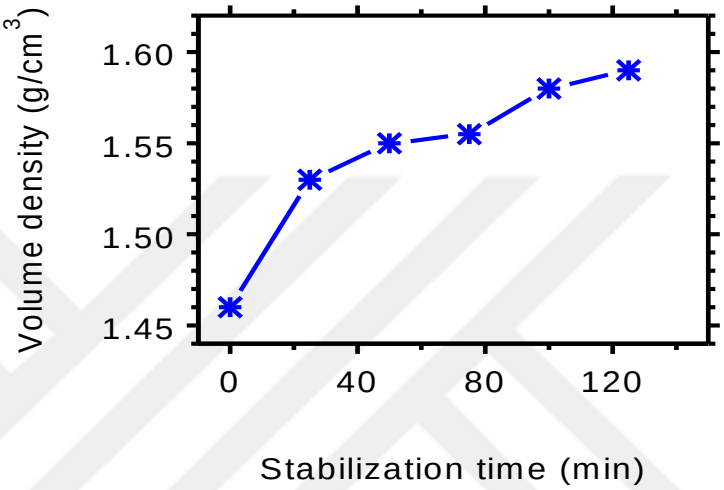

Figure 4.93 Volume density (g/cm^3) of original and oxidized flax fiber.

Figure 4.94 shows the linear density values of the original and oxidized flax samples, which were impregnated with DAP-BAU and stabilized for variable periods ranging from 25 to 125 minutes. A continuous rise of linear density values was observed between this period. The linear density value for the 125 minutes oxidized flax sample was 39.98 tex.

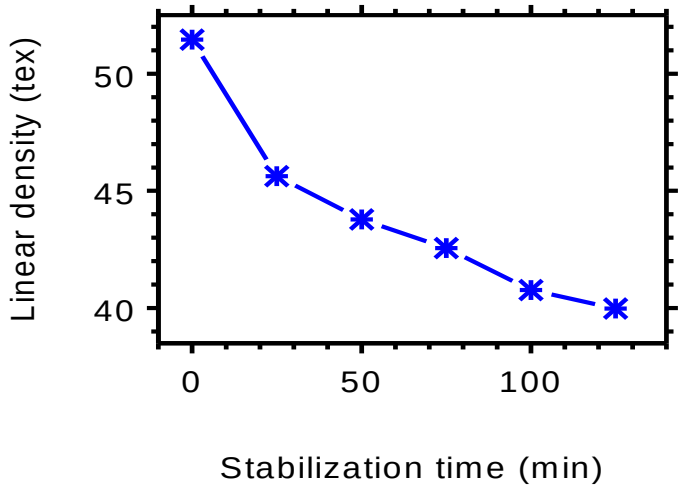

Figure 4.94 Linear density (tex) of original and oxidized flax fiber.

Variations of fiber diameter of the oxidized flax fibers are depicted in Figure 4.95 for the variable oxidation periods. The fiber diameter of the oxidized flax samples was diminished from 9.76 µm of the original sample to 6.86 µm for 125 minutes oxidation duration. The fiber diameter constantly declined with the growing oxidation duration. The highest decrease in fiber diameter was seen after 125 minutes of oxidation with nearly 29.7% loss compared to the original flax sample. The prime cause for decreasing fiber diameter is the weight loss of the thermally oxidized sample.

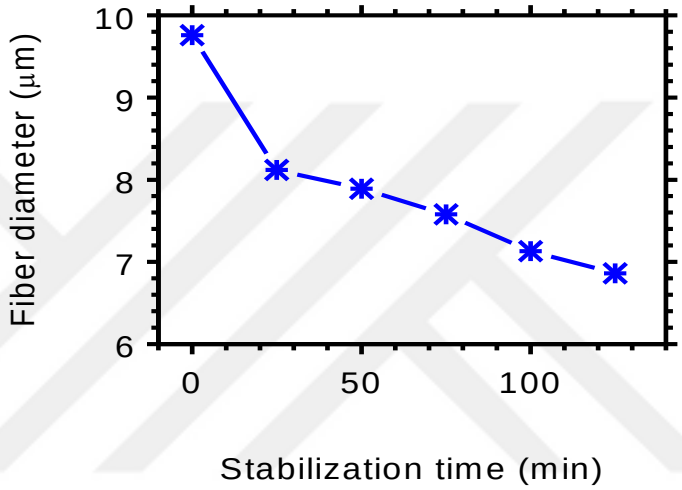

Figure 4.95 Fiber diameter (µm) of original and oxidized flax fiber.

4.5.3 Thermal and Structural Characterization of Original and Thermally Stabilized Flax Fiber Impregnated with DAP-BAU

4.5.3.1 Evaluation of Differential Scanning Calorimetry Analysis (DSC)

DSC thermograms were utilized to investigate the structural changes occurring in the oxidation reactions of flax fibers impregnated with DAP-BAU for different oxidation duration. The DSC profile of raw flax fiber illustrated in Figure 4.96a represents a wide endotherm immediate 100 °C due to the presence of water vapor. A wider and stronger endotherm between 340 and 370 °C, having a peak temperature of 360 °C, ascribed to depolymerization and decomposition reactions of cellulose and hemicellulose following the reactions resulting in the development of levoglucosan and its decomposition constituents [285]. The intensity of this peak weakened and broadened in intensity with

growing oxidation times. The DSC thermogram of raw flax fiber also showed an extra peak as a wide exotherm between 350 and 400 °C, having 373 °C peak temperature owing to the oxidation of levoglucosan-based volatile pyrolysis compounds [286]. DAP-BAU pretreatment and thermal stabilization in the air atmosphere seemed to show a major impact on the DSC profiles of oxidized flax fibers. Figure 4.96b–f represents the DSC traces of DAP-BAU integrated flax fibers oxidized for 25 to 125 minutes oxidation durations.

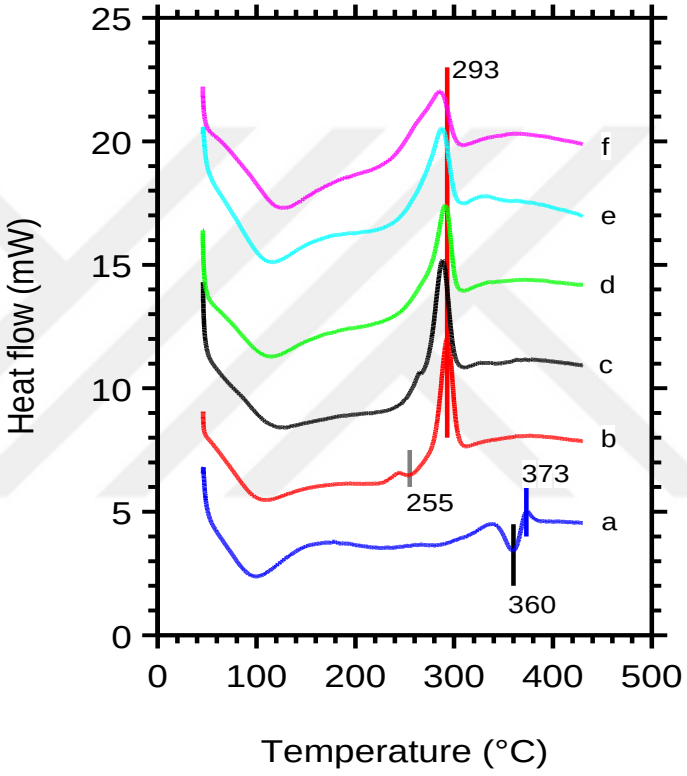

Figure 4.96 DSC profiles of raw (a) and DAP-BAU pretreated-oxidized flax fibers for variable oxidation durations. (b) 25 min; (c) 50 min; (d) 75 min; (e) 100 min; (f) 125 min.

The DSC profiles of the sample oxidized for 50 min at 245 °C shifted to 255 °C owing to the depolymerization reactions of remaining cellulose and hemicellulose. The decomposition temperature of the flax fiber oxidized for 50 min is 105 °C, which is lesser than the raw flax fiber. As a potent fire retardant, DAP-BAU resulted in a severe depletion of the decomposition temperature of cellulose [287]. Decomposition temperature reduction attributes to the catalyzed dehydration reactions of cellulosic structural units by the chemical processes occurring within the hydroxyl groups of cellulose, hemicellulose, lignin, and DAP-BAU. The substantial decrease of cellulose-

hemicellulose-lignin decomposition temperature after the DAP-BAU treatment is also thought to be due to the drop of the degree of crystallinity with escalating oxidation time [277].

The extent below the central endothermic peak is noticed to be dropped after the oxidation time of 25 minutes and disappeared completely between 50 and 125 minutes, respectively; this behavior is accredited to the dehydration process that occurred by the chemical reactions occurring in the core hydroxyl groups of cellulose (-CH_2-OH) rings, hemicellulose, and lignin. This process is estimated to cause the removal of -OH groups from cellulose, hemicellulose, and lignin chains and in the loss of H-bonds from the -OH groups in producing water. The development of double-bonded groups, typically C=O and C=C, also takes place. Due to the dehydration process, the structure of cellulose-hemicellulose-lignin is sustained, the development of volatile derivatives is prohibited, and the weight loss is typically restricted to water loss alone. [5].

Table 4.17 Thermal properties of raw and oxidized flax fibers pretreated in DAP-BAU.

Oxidation time (min)	Decomposition temperature (ºC)	Area of (ΔH) decomposition (J/g)	Carbon formation exotherm (ºC)	Area of carbon formation exotherm (J/g)	Exotherm due to levoglucosan oxidation (ºC)
0	360	24.739	-	-	373
25	255	6.322	293	-67.267	-
50	-	-	288	-81.579	-
75	-	-	290	-81.055	-
100	-	-	288	-71.046	-
125	-	-	286	-68.659	-

After 50 minutes of oxidation at 245 °C, the region associated with the decomposition endotherm is decreased and then eliminated (Table 4.17). DAP-BAU pretreatment limits the depolymerization processes and prevents the synthesis of levoglucosan, which results in the diminution and final removal of the endotherm. This outcome is thought due to the higher carbon yield in the samples generated for DAP-BAU pretreatment and

increased oxidation times. The vanishing of the decomposition endotherm for 50 minutes oxidation time and beyond also shows the formation of high temperature resistant and thermally stabilized structural units. The DSC traces of the 50 minutes and above timed oxidized samples also represented the complete vanishing of the decomposition endotherms originated from the cellulose I-hemicellulose-lignin structure loss and the development of thermally stabilized and crosslinked structural units.

The DSC traces of DAP-BAU treated flax fibers stabilized at 245 °C for oxidation times of 25 minutes and beyond showed a strong intensity exotherm at around 286-293 °C. This exotherm kept its presence at the oxidation times between 25 and 125 minutes (Figure 4.96 and Table 4.17), and is accredited to the crosslinking process of cellulose-hemicellulose-lignin rings occurring in the decomposition and dehydration reactions. The exothermic heat below this peak did keep its presence but gradually lessened in intensity at the oxidation times between 25 and 125 minutes, while the entire cellulose structure was fully converted into greatly cyclized and crosslinked groups of chains.

4.5.3.2 Evaluation of thermogravimetric analysis (TGA)

The TGA method continuously measures the weight loss of samples as a function of time or temperature at a linear rate. The various steps in the TGA analysis provide important information on thermal stability, original sample composition, the thermal stability of intermediates formed, and kinetic data. Essentially, the TGA method is dynamic in nature and offers quantitative information about the thermal stability of the samples under investigation. Thermal analysis is one of the most important techniques to observe and analyze the thermal behavior of samples under investigation. In the present investigation, the TGA method has been employed to investigate the thermal behavior of flax fibers. The weight loss occurring during TGA scanning of flax fibers is attributed to the decomposition of cellulose, hemicellulose, and lignin structural components. Usually, higher decomposition temperatures result in higher thermal stability [196].

In cellulosic fibers, there is no glass transition or melting transitions. The only transition is that of decomposition around 340-380 °C at a heating rate of 10 °C/min. It should be emphasized that the exact positions of these transitions heavily depend on the rate of heating and the impurities present in the material. According to published literature [289], the heating rate is an important factor for differentiating the relative characteristics of fibers. It seems that when the heating rates increased from 5 to 150 °C/min, decomposition maxima increased from 321 to 394 °C for water-retted lignocellulosic flax fibers [289].

Thermogravimetric analysis was utilized for characterizing the thermal stability of pristine and DAP-BAU incorporated and oxidized flax fibers. An initial evaluation of the pyrolysis processes can be carried out based on comparative decomposition temperatures and dTGA curve patterns. Comparatively higher and steeper peaks indicate quicker reactions; and, greater weight loss results in lower carbon yield. On the other hand, broader pyrolytic peaks result in rational reactions and therefore generate higher carbon yield. For flax-based activated carbon fiber production, faster pyrolysis (such as carbonization) in the inert environment is unfavorable. It is expected to accelerate side reactions, resulting in lower-carbon yields and the constituents having volatile carbon [146]. Large quantities of organic acids, aldehydes, and carbon dioxide are released as volatile derivatives during faster pyrolysis leading to poor carbon yields. The oxygen-containing air environment is also essential in obtaining higher carbon yields. Under an inert atmosphere, the thermal decomposition of flax fibers shows a single-step decomposition which results in one dTGA curve. This decomposition pattern is attributed to the combination of the main structural components of hemicellulose, cellulose, and lignin in flax fibers. According to Thuault et al. [291], the following transition temperatures were observed in a typical TGA scan of flax fiber; hemicellulose at 250-320 °C, cellulose at 340-400 °C, and lignin at 400-470 °C.

Carbon yield and weight loss could be used in comparing the relative yield values of the carbonization stage for variable oxidation times. The TGA profiles of pristine and DAP-BAU incorporated flax fibers oxidized in the air for oxidation times of 0 and 125

minutes are illustrated in Figure 4.97. All the TGA curves show weight loss at about 50-120 °C indicating the presence of water on the surface of the samples. The TGA profile of pristine flax fiber indicated that the weight loss occurs in a small temperature range of 250 to 400 °C. The thermal decomposition process of pristine flax fibers was initiated at 250 °C and sustained until 400 °C (Figure 4.97a).

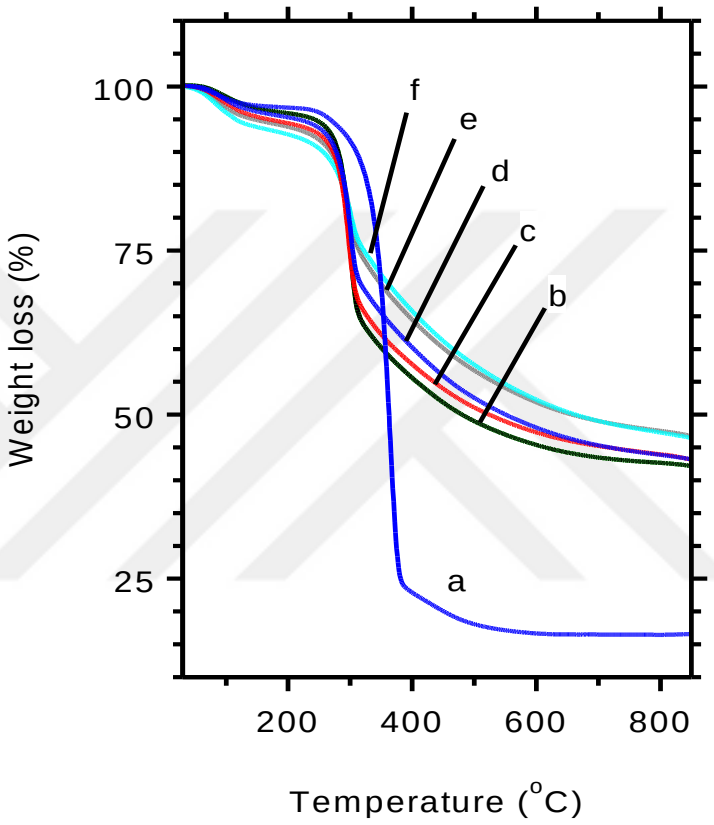

Figure 4.97 TGA thermograms of raw (a) and DAP-BAU pretreated-oxidized flax fibers for variable oxidation durations. (b) 25 min; (c) 50 min; (d) 75 min; (e) 100 min; (f) 125 min.

Faster weight loss occurring in the range of 250 to 400 °C in the inert environment indicates the occurrence of higher thermal decomposition. The highest weight loss was observed at 355 °C, the carbon yield value was 42.5% at 1000 °C. In contrast, the TGA profiles of DAP-BAU incorporated and oxidized flax fibers demonstrated a reduced weight loss ratio with growing oxidation time, signifying escalating carbon yield due to the greater crosslinking and aromatization reactions among the flax cellulose-hemicellulose-lignin chains. The TGA curves of the DAP-BAU incorporated-oxidized

flax fibers exhibited slower weight loss at temperatures between 250 and 500 °C owing to aromatization and crosslinking processes.

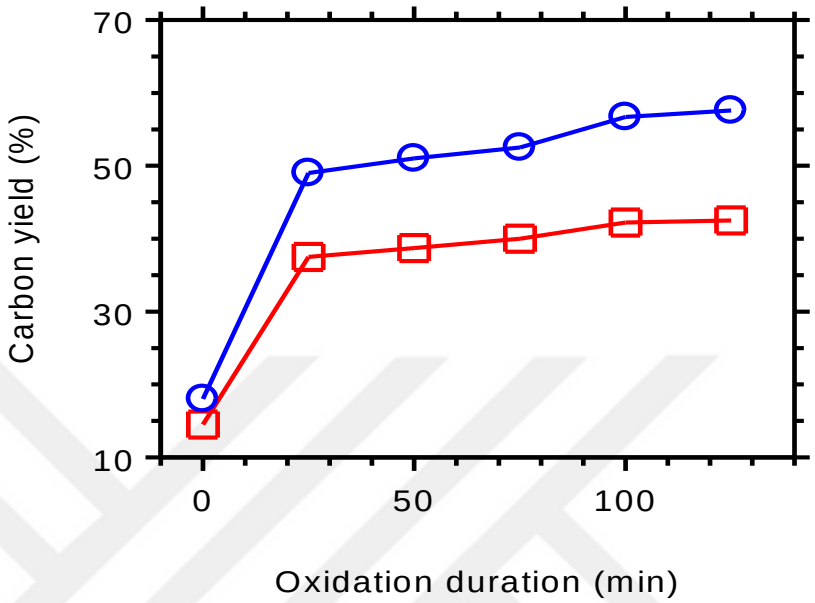

Figure 4.98 Variation of carbon yields at scanning temperatures 500 °C (O), and 1000 °C (□) of the raw and oxidized flax fibers.

The carbon yield (%) at 500 and 1000 °C temperatures attained from the original and DAP-BAU incorporated flax fibers for variable oxidation times are presented in Figure 4.98. The outcomes indicated a steady growth of carbon yield for higher oxidation times. Carbon yield ratios are higher at 500 °C than those at the temperature of 1000 °C growing from 49% to 58%. The carbon yield ratio increased to a maximum value of 42.5% at 1000°C for the DAP-BAU incorporated and 125 minutes oxidized flax fibers.

dTGA curves of TGA thermograms are presented in Figure 4.99. The dTGA curve of the original flax fibers (Figure 4.99a) exhibits two exothermic peaks. The peak appearing as a broad shoulder centered around 290 °C is assigned to the decomposition of hemicellulose, and a well-defined peak centered around 365 °C is attributed to the decomposition of cellulose. Lignin decomposition peak did not appear in the dTGA thermograms.

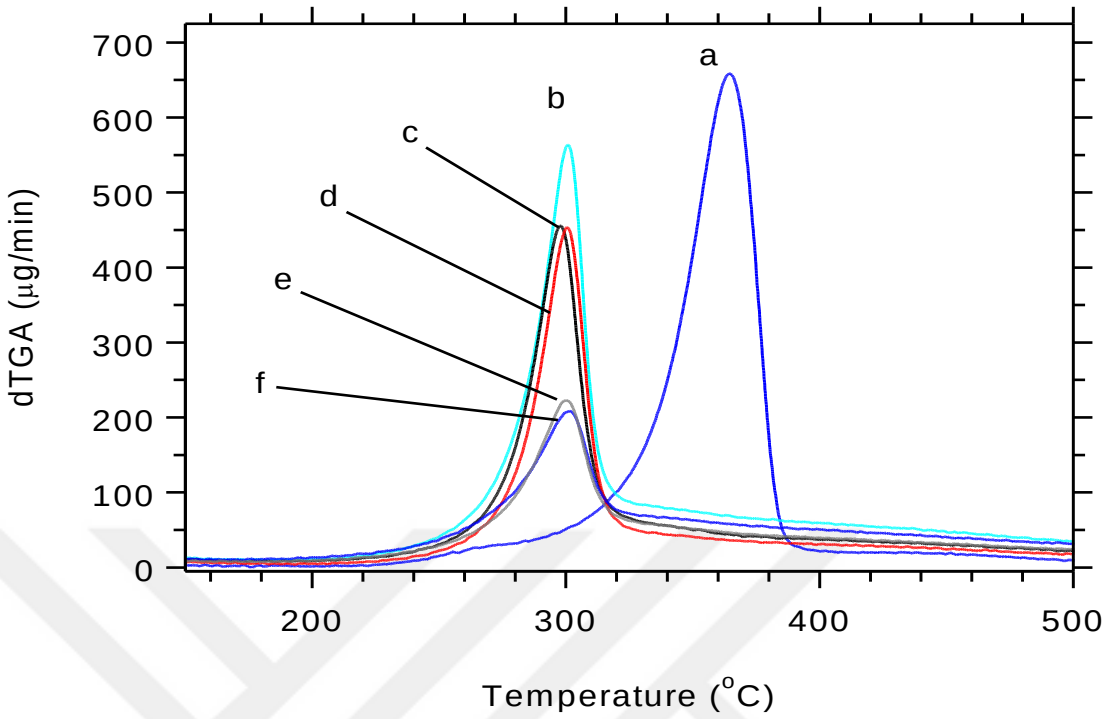

Figure 4.99 dTGA thermograms of raw (a) and DAP-BAU pretreated-oxidized flax fibers for variable oxidation durations. (b) 25 min; (c) 50 min; (d) 75 min; (e) 100 min; (f) 125 min.

Following the oxidation reactions, the dTGA peak for the oxidized samples shifts from 365 °C due to the decomposition of cellulose to 300 °C. Hemicellulose decomposition peak was located at 290 °C but disappeared in the oxidized samples. Lignin decomposition peak was not detected in the samples, possibly due to its lower existence.

4.5.3.3 Evaluation of Infrared Spectroscopy Analysis (FT-IR)

In the present investigation, infrared spectroscopy was extensively utilized to investigate structural changes occurring during the oxidation reactions. Structural changes happening during the oxidation process were monitored and followed as a function of oxidation time. Information from infrared spectroscopy is one of the most useful and fundamental approaches for the understanding of the structure of cellulose, hemicellulose, and lignin, mainly for identifying the network of hydrogen bonds in the molecular structure of flax fibers. The infrared bands of pristine and oxidized flax fibers are presented in Figure 4.100 for different oxidation times between 4000 and 2000 cm^{-1} region.

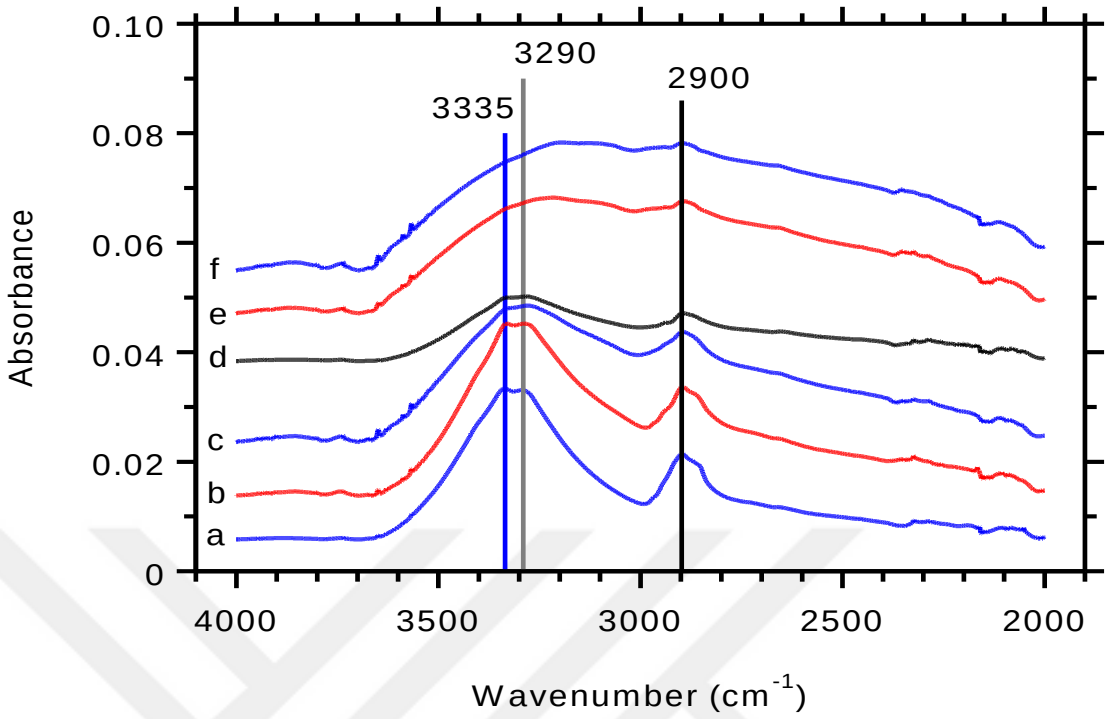

Figure 4.100 IR spectra in the range 4000–2000 cm^{-1} of raw (a) and DAP-BAU pretreated-oxidized flax fibers for variable oxidation durations. (b) 25 min; (c) 50 min; (d) 75 min; (e) 100 min; (f) 125 min.

The IR range 4000 to 3000 cm^{-1} is considered to be due to intramolecular and intermolecular H-bonded OH group bands. The OH groups available in the molecular structure of cellulose, hemicellulose, and lignin readily form intra- and intermolecular hydrogen bonds, which results in the formation of crystalline regions [5, 277, 278]. In the infrared spectrum of cellulose, the 3000-2000 cm^{-1} region is assigned to the methine (C-H) and methylene (CH_2) stretching bands. The IR spectrum of pristine flax fiber contains vibrations due to cellulose, hemicellulose, and lignin components [276]. Band assignments for the 4000-500 cm^{-1} region of the IR spectrum of flax fiber are listed in Table 4.18. Following DAP-BAU pretreatment and oxidation in an air atmosphere, noticeable deviations in comparative intensity values were observed as H-bonding and CH stretching vibrations in the area spanning 4000 to 3000 cm^{-1}.

Table 4.18 Band assignments for the 4000-500 cm^{-1} region of the infrared spectrum of flax fiber.

Wavenumber (cm^{-1})	**Assignment** [158, 279–281, 292, 293]
3540	Free OH vibrations
3540, 3480, 3435, 3340, 3290, 3235, 3105	OH stretching intermolecular hydrogen bonding
2922	CH_2 asymmetrical stretching
2900	CH and CH_2 stretching
2870	CH and CH_2 symmetrical stretching
1730	C=O stretch (before oxidation), hemicellulose
1715	C=O stretch in unconjugated ketones, carbonyls, and ester groups of hemicellulose structure (after oxidation)
1635	adsorbed H_2O
1610	C=C stretching, aromatic skeletal mode (lignin)
1455	CH-deformation and CH_2 bending
1430	CH_2 and O-C-H in-plane bending, crystalline cellulose
1370	CH_2 bending (the crystalline phase from cellulose)
1317	CH_2 wagging
1235	C–O stretching in acetyl group
1205	OH in-plane bending
1155	C-O-C asymmetrical stretching of cellulose and hemicellulose (crystalline phase mainly from cellulose); A decrease in the intensity of this vibration is attributed to a decrease in the degree of crystallinity.
1102	Asymmetrical in-phase ring stretching of cellulose (crystalline)
1054	C-O bond stretching and C-O deformation
1030	CO stretching
1007	C-O stretching
895	Cellulose-based asymmetrical out of phase ring stretching (C-O-C)
800	Cellulose-based ring breathing mode
663	OH, out of plane bending

The IR spectrum of original flax fiber covering 3700 and 3000 cm^{-1} regions illustrated in Figure 4.101 was analyzed and fitted with nine peaks using a peak separation procedure. Peak separation procedure was performed using band positions located at 3540, 3480, 3435, 3380, 3340, 3290, 3235, 3175, and 3105 cm^{-1}. The infrared peak located at 3540 cm^{-1} is attributed to free OH vibrations. On the other hand, the IR bands located at 3540, 3480, 3435, 3380, and 3340 cm^{-1} are attributed to the OH vibration of the intramolecular H-bonds (Table 4.18).

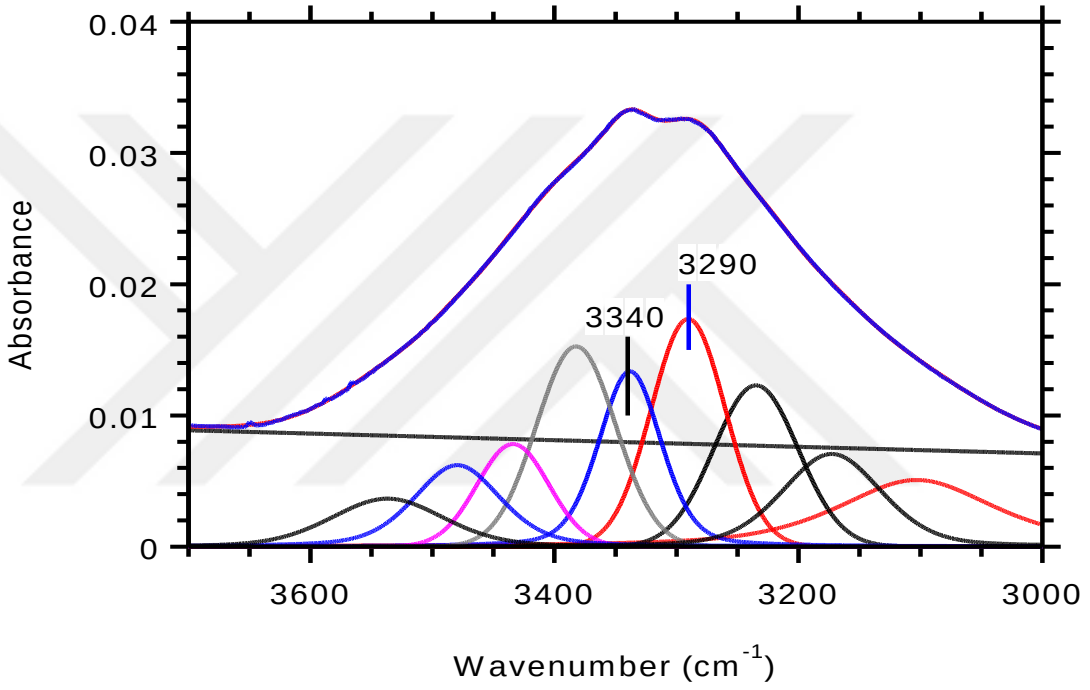

Figure 4.101 Curve-fitting of the infrared spectrum of pristine flax fibers in the 3700-3000 cm^{-1} region.

Intermolecular H-bonded bands are positioned at 3290, 3235, 3175, and 3105 cm^{-1}, respectively. It seems that intermolecular H-bonding shows a higher delicacy to temperature fluctuations than intramolecular H-bonding [283]. OH, CH, and CH_2 bands positioned in the range from 3700 to 3000 cm^{-1} progressively lost intensities yet never vanished entirely. OH spectra attributed to oxidized flax fibers primarily exposed broadening but lost maximum intensity for higher oxidation time. The dehydration process resulted from the interaction of hydroxyl and boron phosphate (BPO_4) groups in the initial steps of oxidation reactions, the intensities of the vibrations located at 3290, 3235, 3175, and 3105 cm^{-1} involved in the intermolecular H-bonding and the OH

groups gradually weakened with increasing oxidation time. This behavior indicated an interruption in intermolecular H-bonding. The IR spectra located at 3520, 3450, 3405, and 3350 cm^{-1} attributed to the intramolecular H-bonded OH groups also lost their intensity yet never vanished entirely. This outcome suggests that maximum oxidation reactions occurred within OH-groups of cellulose, hemicellulose, and lignin with boron phosphate (BPO_4) groups. The disorder of the intermolecular H-bonding system during the oxidation process is thought for the gradual crystallinity loss together with the development of the amorphous phase for increased oxidation time.

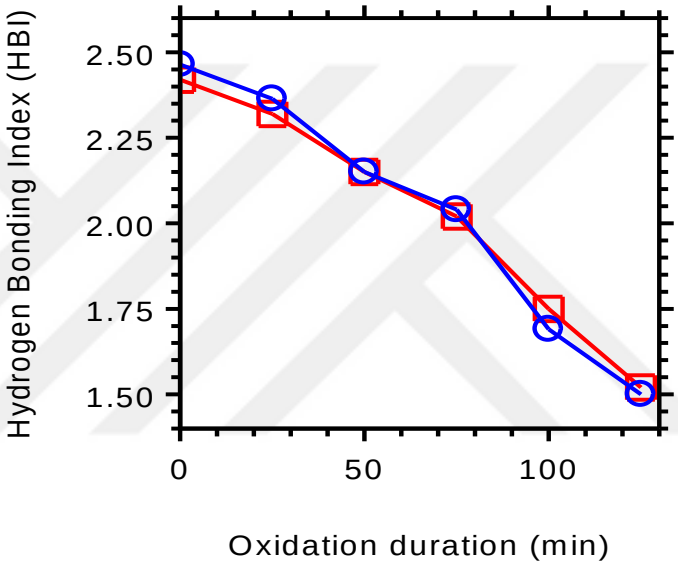

Figure 4.102 Changing of absorbance ratio (A_{3290}/A_{2900}) marked as (□), and (A_{3340}/A_{2900}) marked as (O) for variable oxidation durations. The absorbance value of 2900 cm^{-1} was considered as an internal standard.

The methine (CH) and methylene (CH_2) bands located at 2922, 2900, and 2860 cm^{-1} also lost most of their intensities, but a minor amount still remained, demonstrating that all H-species are not involved in dehydrogenation and dehydration processes. It is clear that the gradual loss of the H-bonded OH groups and H of the CH groups with growing oxidation time is a clear indication that dehydrogenation and dehydration processes took place in the oxidation process. Gradual reduction of intermolecular hydrogen bonding between OH groups of flax fibers using intensity ratios of (A_{3290}/A_{2900}) and (A_{3240}/A_{2900}) defined as hydrogen-bonding index (HBI) for different oxidation duration is presented quantitatively in Figure 4.102. The infrared spectrum located at 2900 cm^{-1} was taken as an internal standard for normalization purposes [158]. The vibration located at 2900 cm^{-1} is clearly

well-defined and prominent vibration in the pristine flax fiber. The use of the internal standard vibration makes it easy to make comparisons between different specimens for different oxidation duration.

The infrared spectra of the raw and oxidized flax fibers in the range 2000-400 cm^{-1} of raw and DAP-BAU incorporated-stabilized flax fibers for different oxidation periods are presented in Figure 4.103. The wavenumber range 2000 to 400 cm^{-1} of the cellulose infrared spectra is known to be the most suitable portion for both quantitative and qualitative analysis. The physically absorbed water gives a distinctive spectrum at approximately 1640 cm^{-1}, while the infrared spectra of original flax fibers located around 1428, 1370, 1337, 1315, 1280, 1220, 1160, and 895 cm^{-1} are stated as delicate to crystallinity and lattice-category [292].

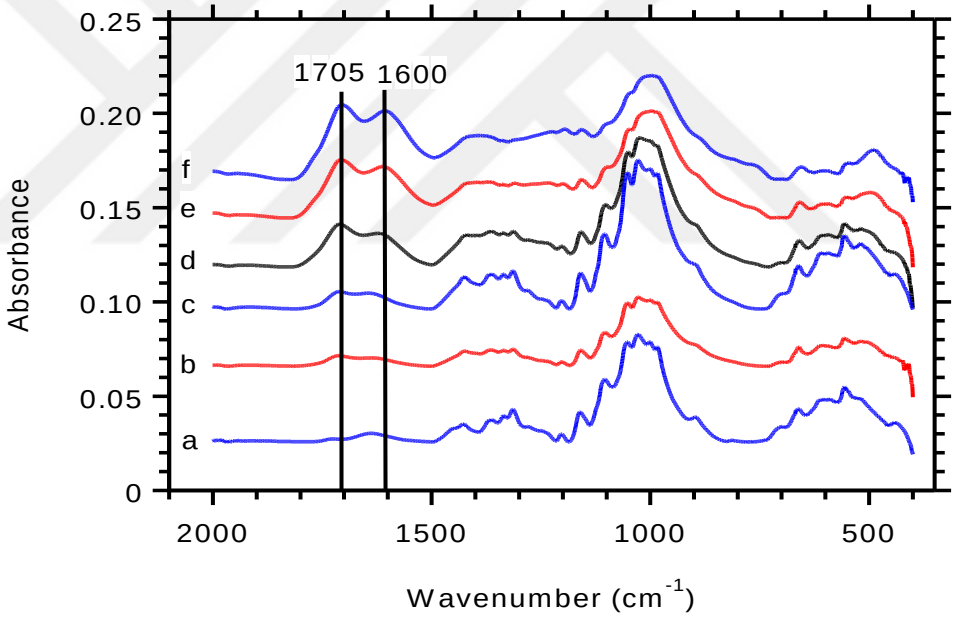

Figure 4.103 IR spectra in the range 2000–400 cm^{-1} of raw (a) and DAP-BAU pretreated-oxidized flax fibers for variable oxidation durations. (b) 25 min; (c) 50 min; (d) 75 min; (e) 100 min; (f) 125 min.

Infrared spectra of pristine and oxidized flax fibers in the presence of DAP-BAU impregnation in the range 1850-1200 cm^{-1} for 25 minutes oxidation time are presented in Figure 4.104. Carbonyl stretching vibration located at 1730 cm^{-1} allocated to C=O stretching band is moved to 1715 cm^{-1} indicating strong interaction with OH groups in forming H-bonds [282].

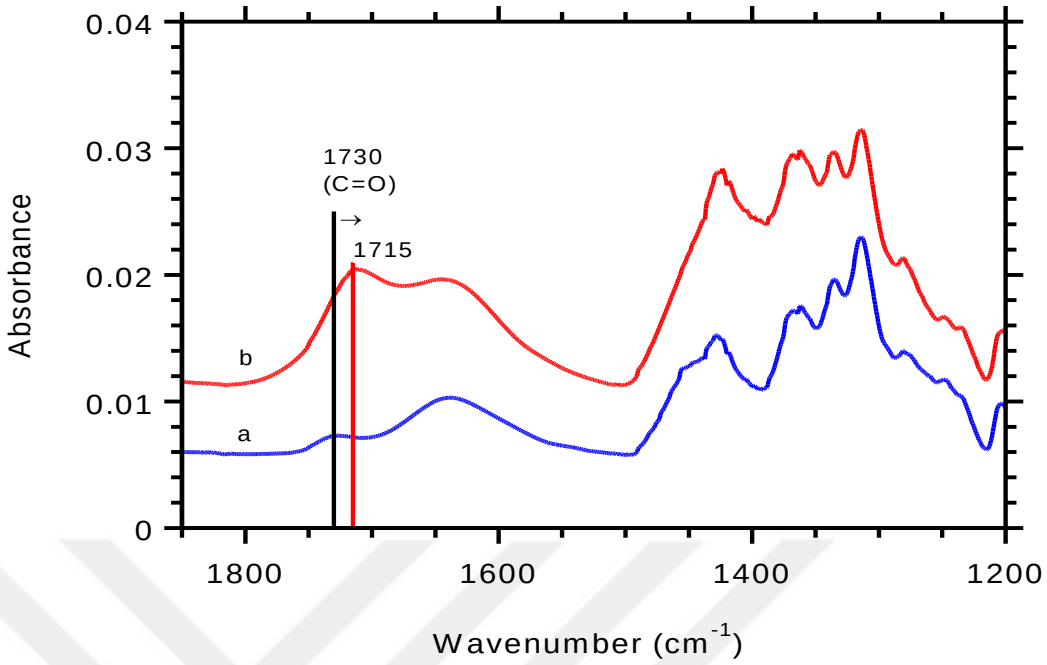

Figure 4.104 Infrared spectra of raw (a) and DAP-BAU pretreated-oxidized (25 min) flax fibers in the range 1850-1200 cm^{-1}.

IR spectra in Figure 4.103 indicate that the carbonyl (C=O) intensity grows with increasing oxidation time. This outcome strongly suggests that oxygen-containing functional groups are incorporated in the oxidation reactions. The ratio of the absorbance value of the carbonyl (C=O) band at 1715 to 2900 cm^{-1} is defined as an oxidation index, where 2900 cm^{-1} is used here for comparison purposes. The results presented in Figure 4.105 suggest that the oxidation index increases with increasing oxidation time suggesting increased oxygen content.

A completely new band at approximately 1610 cm^{-1} seemed like a strong vibration assigned to C=C stretching come to be prime in the samples oxidized at 25 minutes oxidation time and higher, suggesting the formation of the highly aromatic structure during the oxidation procedure. The infrared spectrum at 1610 cm^{-1} appeared as a shoulder in the IR spectrum obtained after the oxidation time of 25 minutes but became stronger with increasing oxidation time. The absorbance ratio of A_{1610}/A_{2900} is defined as the IR-aromatization index, and the values are presented in Figure 4.106 that shows increasing aromatization index values with increasing oxidation time.

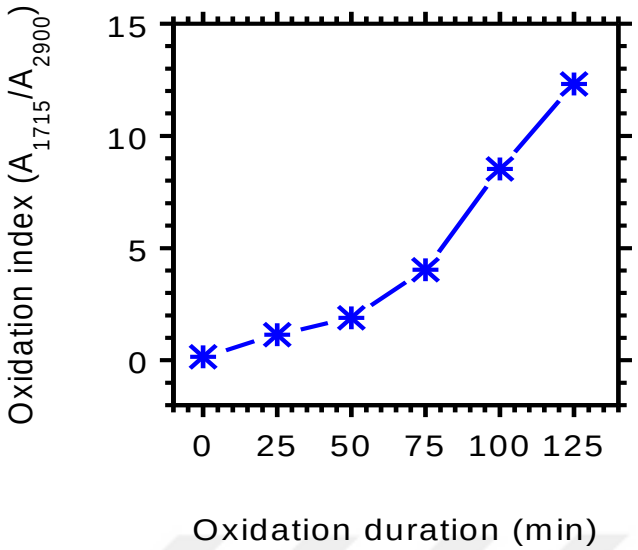

Figure 4.105 Changing of oxidation index (A_{1715}/A_{2900}) for variable oxidation durations.

The spectrum at 895 cm^{-1} allotted to asymmetrical out of phase cellulose ring stretching (C-O-C) lost intensity for the oxidation reactions with increasing oxidation time, indicating the replacement of hydrogen atoms from the cellulose, hemicellulose, and lignin structures by functional groups or owing to the creation of ring structures [292].

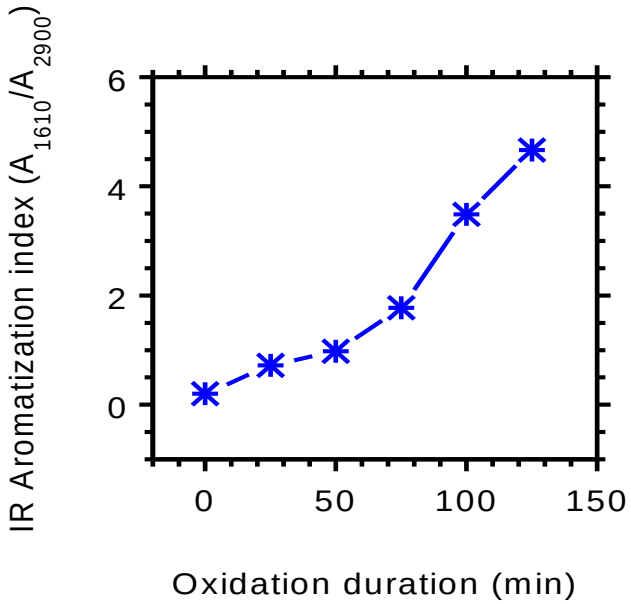

Figure 4.106 Changing of IR aromatization index (A_{1610}/A_{2900}) for variable oxidation durations.

The IR spectrum located at 1370 cm^{-1} assigned to the CH_2 bending mode of crystalline cellulose is used for the evaluation of the degree of total crystallinity index (TCI) values

using the intensity ratios of A_{1370}/A_{2900} for the pristine and oxidized flax samples [292]. The variation of the total crystallinity index is presented in Figure 4.107 for variable oxidation duration. The outcomes demonstrate reduced crystallinity and increasing amorphous content for increased oxidation duration.

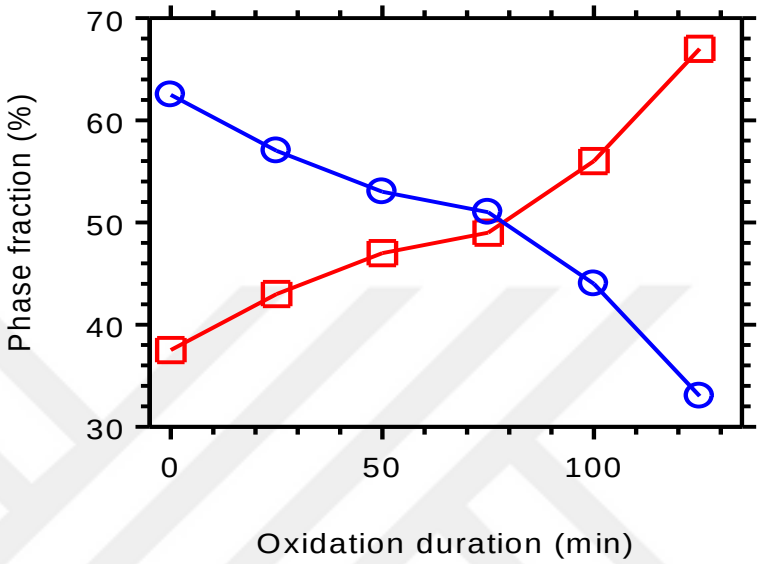

Figure 4.107 Comparison of infrared crystallinity and amorphous fraction of raw and DAP-BAU pretreated-oxidized flax fibers for variable oxidation durations. (O) crystalline phase, (□) amorphous phase.

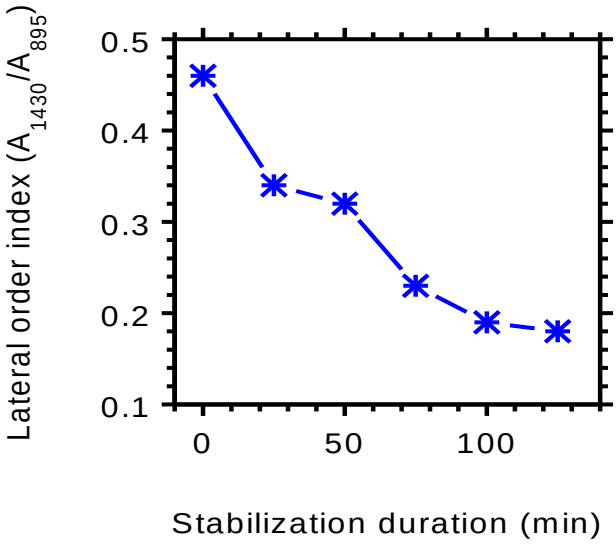

Figure 4.108 Lateral order index (LOI) values of raw and DAP-BAU pretreated-oxidized flax fibers for variable oxidation durations. (Here, 1430 cm^{-1} as a crystalline band, and 895 cm^{-1} as a reference band).

The IR spectroscopy was also used to assess the values of lateral index values using the absorbance ratios of A_{1430}/A_{895} as suggested in the published literature [292]. Figure 4.108 shows the changing values of the lateral order index for the pristine and oxidized flax samples as a function of oxidation time. The outcomes point to a continuous decrease in the values of lateral order index for the pristine and oxidized flax samples. It is clear that the values of the total crystallinity index are higher as expected than the lateral order index.

4.5.3.4 Evaluation of X-ray Diffraction Analysis (XRD)

Equatorial X-ray diffraction traces of pristine and thermally oxidized flax fibers are plotted in Figure 4.109. Investigation of the equatorial XRD profile of raw flax fibers shows the availability of four distinct crystalline peaks as the most prominent reflections.

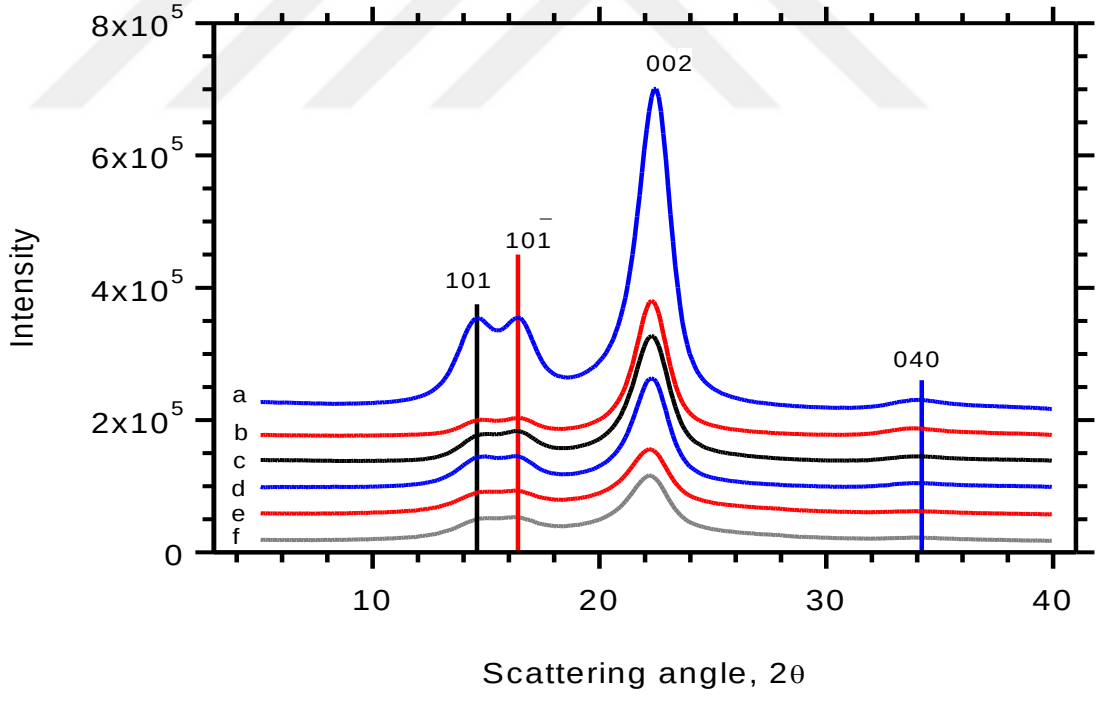

Figure 4.109 Equatorial X-ray diffraction profiles of raw (a) and DAP-BAU pretreated-oxidized flax fibers for variable oxidation durations. (b) 25 min; (c) 50 min; (d) 75 min; (e) 100 min; (f) 125 min.

A curve-fitting technique has been utilized to acquire precise peak parameters for the equatorial X-ray diffraction profiles. Curve-fitting was used to evaluate amorphous

ratio, apparent X-ray crystallinity, crystal size, and X-ray oxidation index for variable oxidation durations. The equatorial XRD profile of flax fibers presented in Figure 4.110 can be determined from five crystalline peaks of cellulose I structure located at about 14.7±0.3, 16.4±0.3, 21.4±0.2, 22.4±0.2 and 34.8±0.3 attributed to (101), (10$\bar{1}$), (120/200), (002) and (040) reflections. These bands relate to a monoclinic unit cell. It is obvious that the 002 peak intensity is the sturdiest comparing with (101), (10$\bar{1}$), (120/200), and (040) peak intensities. The peak parameters acquired from the curve-fitting technique of raw flax fibers are presented in Table 4.19, along with the comparative assessment of the calculated and observed d-spacing values.

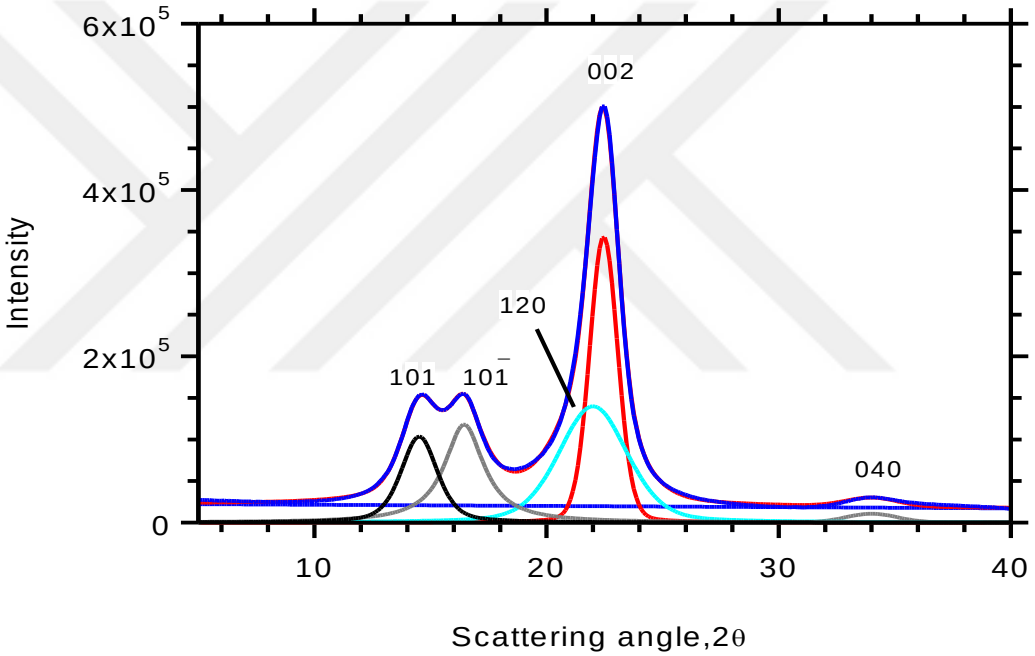

Figure 4.110 Curve-fitting of equatorial X-ray diffraction trace of raw flax fiber.

Table 4.19 Resolved peak parameters of curve-fitted XRD trace of raw flax fiber.

hkl	f	A	W	P (2θ)	d_{obs} (nm)	d_{calc} (nm)
101	0.47	103580	1.85	14.75	0.600	0.603
10$\bar{1}$	0.99	118047	2.04	16.35	0.542	0.543
120/200	0.29	139975	3.47	21.43	0.414	0.415
002	0.13	343929	1.43	22.55	0.394	0.392
040	0.00	10576	2.62	34.4	0.260	0.258

DAP-BAU incorporation followed by oxidation in the air atmosphere at 245 °C and oxidation times ranging from 25 to 125 minutes showed an impressive influence on the crystalline structure of flax fiber as the degree of apparent crystallinity of the cellulose I structure. A close investigation of the XRD profiles presented in Figure 4.109 exhibited a steady loss of crystal structure for higher oxidation times. The loss of the intensity of the XRD profiles indicates the development of amorphization (i.e., decrystallization) reactions with growing oxidation time. The findings presented in Table 4.20 demonstrate that all of the crystalline peaks seem to survive with progressing oxidation reactions due to ongoing oxidation reactions through the oxidation time from 25 to 125 minutes.

Table 4.20 The presence and absence of X-ray diffraction reflections of raw and DAP-BAU pretreated-oxidized flax fibers.

Stabilization duration (min)	**101**	**$10\bar{1}$**	**002**	**040**
0	+	+	+	+
25	+	+	+	+
50	+	+	+	+
75	+	+	+	+
100	+	+	+	+
125	+	+	+	+

Key: (+) : Reflection is present

(-) : Reflection is absent

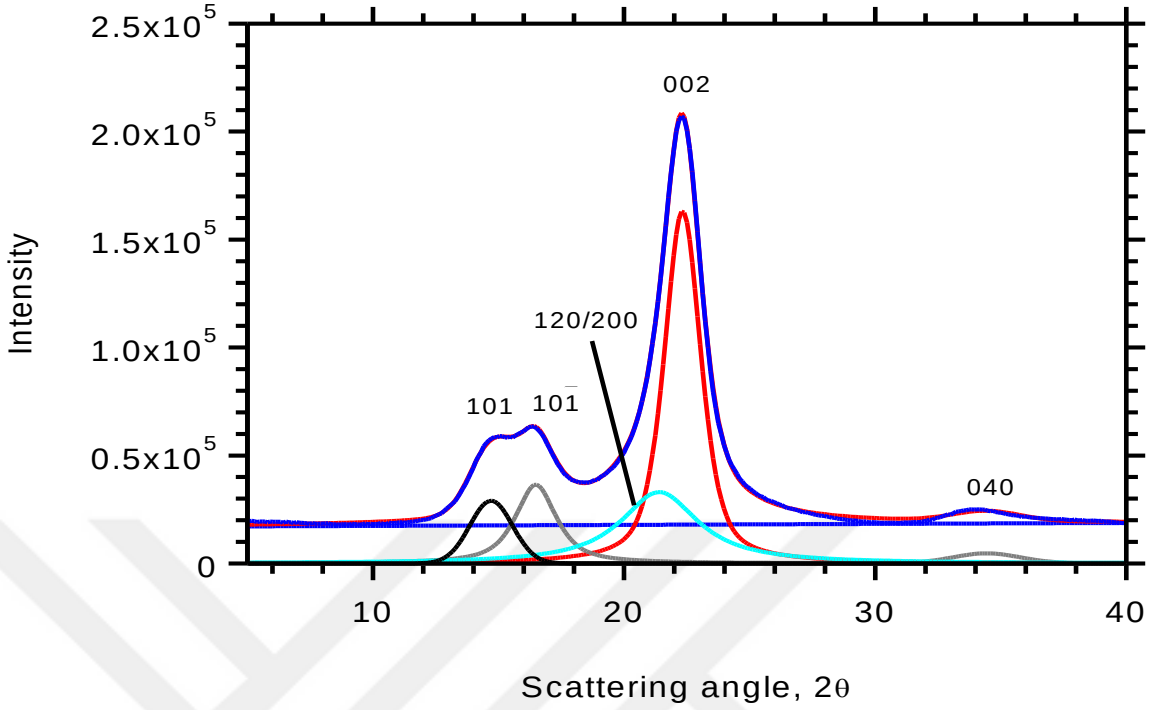

Figure 4.111 Curve-fitting of equatorial XRD trace of 50 min thermally stabilized flax fiber.

Curve-fitting of XRD profile of 50 minutes oxidized flax fiber is presented in Figure 4.111. Peak areas acquired from the curve-fitting of XRD traces were utilized to assess the ratios of amorphous and crystalline (i.e., cellulose I) structures employing Equation 3. The findings presented in Figure 4.112 indicate that the X-ray crystallinity was reduced from 68.8 to 38.9% after 125 minutes of oxidation duration. In contrast, the amorphous fraction increased from 31.2 to 61.1% after the oxidation time of 125 minutes.

X-ray oxidation index was evaluated employing the intensity of the (002) as a prominent reflection. The outcomes showed in Figure 4.113 illustrate the X-ray oxidation indices for the oxidized flax samples for variable oxidation durations. With increasing oxidation duration from 25 to 125 minutes, the X-ray oxidation index was increased from 0 to 88%.

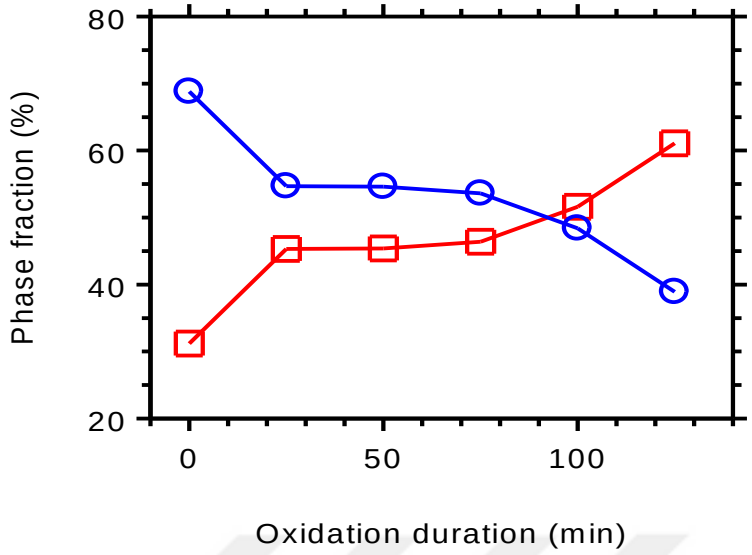

Figure 4.112 Comparison X-ray crystallinity and amorphous fraction of raw and oxidized flax fibers for variable oxidation durations. (O) crystalline phase; (□) amorphous phase.

Evaluation X-ray oxidation index is considered as a dependable way in assessing the fraction of aromatic and crosslinked structures formed in the course of oxidation reactions [275]. The experimental outcomes point out that DAP-BAU impregnated and oxidized flax fibers in an air atmosphere resulted in the gradual disappearance of cellulose I crystal structure and a rise in the disordered fraction along with the improvement in the ratio of the cyclized structure comprising crosslinked ladder-like structural units.

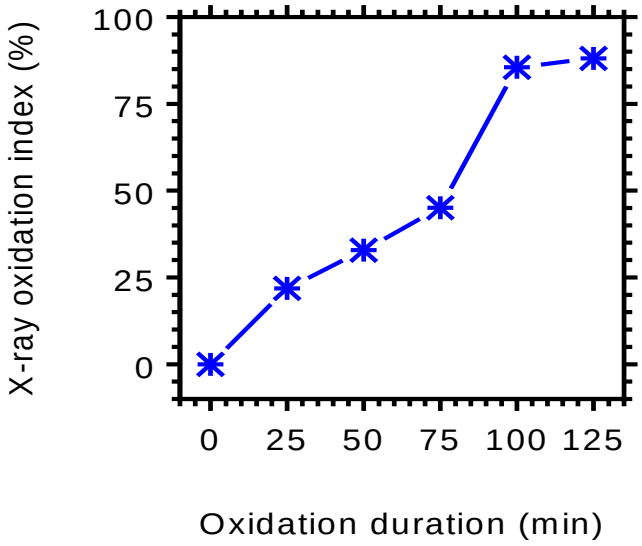

Figure 4.113 Comparison of X-ray oxidation index of raw and oxidized flax fibers for variable oxidation durations.

During the oxidation reactions, 101, $10\bar{1}$, 120/200, and 040 reflections kept their presence during the oxidation reactions. The most prominent (002) peak also kept its presence during the oxidations reactions. The half-height widths of the reflections broadened with growing oxidation times, indicating the progressive reduction in the crystal dimensions. This result comes as a result of the breaking up structure in the decrystallization reactions [275]. The gradual intensity decrease of the 101, $10\bar{1}$, 120/200, 002, and 040 peaks are supposed as a result of breaking the cellulose I crystal structure due to the ongoing decrystallization reactions.

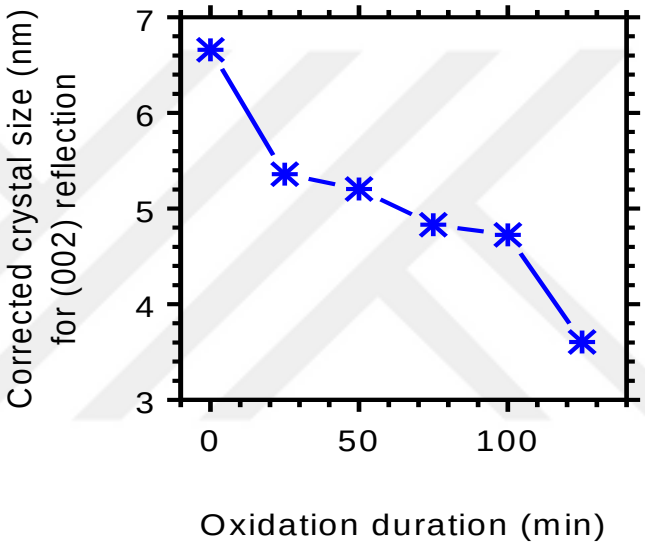

Figure 4.114 Comparison of the crystal size for (002) peak of raw and oxidized flax fibers for variable oxidation durations.

Since the (002) reflection kept its presence during the oxidation process, it was used for the evaluation of crystal size during the oxidation process. Evaluation of crystal sizes of the raw and oxidized flax fibers was performed using Equation 4. Figure 4.114 shows the values of corrected crystal size corresponding to prominent (002) peak as a function of oxidation time. Crystal size for (002) reflection was reduced from 6.6 to 3.6 nm with growing oxidation durations due to the ongoing decrystallization process.

CHAPTER 5
CONCLUSION AND SUGGESTIONS

5.1 CONCLUSION

In this study, process optimization of the thermal oxidative stabilization stage in carbon fiber manufacturing was performed. Five different natural and synthetic textile fibers were utilized as carbon fiber precursors, including polyacrylonitrile (PAN) multifilament, polyamide 66 (PA66) multifilament, jute fiber, bamboo fiber, and flax fiber. Chemical pretreatment of these precursor fibers was executed using different chemicals and chemical combinations having flame retardance and tensile retention properties. Following chemical impregnation to the precursor fibers, the thermal oxidative stabilization process was performed employing different multistep strategies to achieve thermal stability within the quickest possible time. The finest alternative was chosen from the chemical pretreatment option choosing and stabilization strategy selecting to utilize for further analysis process that offers the best thermal and tensile features in the thermally stabilized precursor samples.

Stabilized specimens were characterized using different characterization tools. The thermal and structural properties of the stabilized samples were obtained utilizing a set of measurements, including thermogravimetric analysis (TGA), X-ray diffraction (XRD), Fourier-transform infrared spectroscopy (FTIR), and scanning electron microscopy (SEM). Characterization of physical changes was accomplished by observing fiber burning behavior, change of color, linear density, volume density, fiber thickness, and mechanical properties for the different stabilization periods.

Prior to the thermal stabilization stage, a 15% ammonium persulfate (APS) aqueous solution was impregnated with PAN multifilaments. According to the experimental results, APS treatment decreases stabilization duration and speeds up the formation of the cyclized structure, which is crucial to tolerate higher temperatures in the following stages. The APS impregnated PAN multifilaments experienced significant physical, structural, and thermal changes as a result of thermal stabilization in the air environment. Infrared outcomes demonstrated a quicker and simultaneous cyclization and dehydrogenation process as the stabilization time was increased. The rapid intensity decrease of the nitrile band at 2242 cm^{-1} and the methylene band at 2920 cm^{-1} confirm this change. The conversion indices obtained from IR spectroscopy and X-ray diffraction findings revealed that the open structure of the PAN fiber was quickly converted into a strongly cross-linked and cyclized polymer structure. The TGA thermograms showed a comparative improvement in thermal stability as the stabilization time progressed, which was measured by the rise in carbon yield.

In the thermal stabilization process, the heating rate impacts greatly on the resultant precursor fiber properties. Different heating rates were tested in the stabilization process of PAN samples to make a comparison, and the best outcomes were obtained when 2 °C/min heating rate was employed to reach from room temperature to 200 °C and afterward 1 °C/min to reach 250 °C in the multistep TOS process. Additional load application or tensile stretching during the TOS process also helps to improve the tensile properties significantly, as the results obtained in this study. However, along with other parameters, the optimization of tensile stretching is also essential to obtain the best outcomes in the TOS process.

The impact of an eco-friendly chemical combination (phosphoric acid, boric acid, and urea or in brief, PBU) impregnation on the TOS process of PA66 multifilaments was studied. The TGA thermograms revealed the comparative enhancement in thermal stability of the PBU impregnated PA66 multifilament samples as directed by the growth of carbon yield with increasing stabilization period. By the 150 minutes thermal stabilization at 245 °C, PBU impregnated PA66 multifilaments attained complete stability and non-burning property, and showed the highest carbon yield value of 47% at 1000 °C. The obtained outcomes from the IR spectroscopy and XRD revealed a steady

loss of crystallinity due to the breakage of H-bonds by the increase of the stabilization duration.

The structure and characteristics of jute fibers were studied after SMSPH-U impregnation and oxidation by a multi-stepped annealing approach at temperatures up to 245 °C. The progressive loss of crystallinity was observed by examining the equatorial X-ray diffraction traces, resulting from the amorphization processes occurring in oxidation induced by the breakage of interchain H-bonding. With increasing oxidation time, X-ray diffraction results indicated the formation of a greater percentage of ladder-like structures containing aromatic moieties. The disintegration of crystalline structure with advancing oxidation time was noticed in infrared measurements in the 1800-850 cm^{-1} region, validating the findings of X-ray diffraction outcomes. The development of C=C bonds was also observed in infrared studies, which was ascribed to the creation of ladder-like structures. The analyses of all the obtained results confirm the jute fibers, oxidized at 245 °C for a 175 minutes multistep annealing process, were properly oxidized, and ready for employing in the subsequent stages.

Bamboo fibers impregnated with DAP-SMSU attained complete infusibility at the temperature of 245 °C for 120 minutes of oxidation time, employing a multistep strategy. The equatorial X-ray diffraction patterns indicated a progressive loss of crystallinity as a result of the amorphization mechanism caused by the rupture of interchain hydrogen bonds during the oxidation stage. DSC analysis revealed that DAP-SMSU impregnation enhanced thermal stability and inhibited the development of volatile compounds by obstructing the fundamental hydroxyl groups. TGA results demonstrated that the highest carbon yield value of DAP-SMSU impregnated 120 minutes stabilized bamboo fibers by 61% at 800 °C. Infrared spectroscopy analysis showed that the intensity of OH stretching of intermolecular and intramolecular H-bonds, as well as methine (CH) bands, decreased gradually during the dehydrogenation and dehydration processes.

DAP-BAU aqueous solution impregnation and multistep thermal oxidation of flax fiber were performed in the air atmosphere at temperatures up to 245 °C. The investigation of DSC profiles showed that DAP-BAU pretreatment enhanced thermal stability by inhibiting the fundamental hydroxyl groups and restricted the development of volatile

byproducts. In the initial stages of oxidation, the DSC traces revealed a notable decrease in the decomposing temperature and then slowed decomposition reactions in the following steps. TGA thermograms have demonstrated an improvement in thermal stability, as seen by increased char yield with increasing oxidization times. The findings of the XRD investigation indicated that the crystalline structure had been lost and that the original cellulose structures had been converted to a strongly cyclized and crosslinked structure at increased oxidation duration. Intermolecular and intramolecular H-bonds and methine (CH) bands related to hydrogenation and dehydration reactions were shown to have a steady decrease of intensity of OH stretching in the infrared spectroscopy analysis. In the wavenumber range between 1900 and 800 cm^{-1}, IR data analysis indicated the interference of the crystalline structure for higher oxidation duration confirms the findings of X-ray diffraction analyses.

5.2 SUGGESTIONS

Oxidative thermal stabilization is a major stage in carbon fiber and activated carbon fiber manufacturing. However, this is a very time-consuming stage that requires around longer waiting time at temperatures around 200-300 °C, which in terms results in a more significant amount of energy consumption. This thesis work utilized different process optimization tools to achieve complete thermal stability in the precursor fibers within the quickest possible time. Chemical impregnation that includes different flame retardant and tensile properties retaining chemicals and chemical combinations to the precursor fibers was accomplished prior to the stabilization stage to accelerate the process. The chemical integration with the precursor fibers (synthetic fibers, including polyacrylonitrile, polyamide 66, etc.) might be performed prior to the continuous filament spinning processes (either melt or solution spinning). This strategy might offer higher acceleration in the thermal stabilization process. However, this approach is not applicable for the nature-originated precursor fibers (for example, jute, bamboo, and flax fibers).

Carbonization of stabilized precursor fibers is a compulsory stage in carbon fiber manufacturing which is generally performed after the thermal stabilization stage at

temperatures between 1000 to 1500 °C in an inert atmosphere to develop various physical, mechanical, and thermal properties. Carbonization eliminates most non-carbon components from the precursor fiber, compacts the aromatic ring structures, and transforms them into a turbostratic graphitic structure to produce carbon fiber. Carbonization and graphitization (usually done up to 3000 °C temperature) or activation (employed to produce activated carbon fiber) could be performed of the chemically impregnated and stabilized fiber samples (obtained in this study) to see any further impact in these stages.

All the fibers and filaments utilized for thermal stabilization in this study had diameters in the micrometer range. However, nanometer-diameter precursor fibers could be used in producing carbon fiber employing different optimization strategies. Nano-dimension fibers are produced by the electrospinning method, which is based on electrostatic forces for spinning fibers from either melts or polymer solutions.

REFERENCES

1. Balandin, A.A., 2011. Thermal properties of graphene and nanostructured carbon materials. **Nature Materials**, **10** (8): 569–581.
2. Borca-Tasciuc WL Liu, G. Chen, H.-W. Ren, C.-H. Lin, SS Pei, T, D.A., 2001. Thermal conductivity of InAs/AlSb superlattices. **Microscale Thermophysical Engineering**, **5** (3): 225–231.
3. Fitzer, E., 1990. Carbon fibres—present state and future expectations. In: Carbon Fibers Filaments Composites, Springer, Dordrecht, pp. 3–41.
4. Bhatt, P., Goe, A., 2017. Carbon Fibres: Production, properties and potential use. **Material Science Research India**, **14** (1): 52–57.
5. Dumanlı, A.G., Windle, A.H., 2012. Carbon fibres from cellulosic precursors: a review. **Journal of Materials Science**, **47** (10): 4236–4250.
6. Morita, K., Murata, Y., Ishitani, A., Murayama, K., Ono, T., Nakajima, A., 1986. Characterization of commercially available PAN (polyacrylonitri1e)-based carbon fibers. **Pure and Applied Chemistry**, **58** (3): 455–468.
7. MInus, M., Kumar, S., 2005. The processing, properties, and structure of carbon fibers. **The Journal of The Minerals, Metals & Materials Society**, **57** (2): 52–58.
8. Rahaman, M.S.A., Ismail, A.F., Mustafa, A., 2007. A review of heat treatment on polyacrylonitrile fiber. **Polymer Degradation and Stability**, **92** (8): 1421–1432.
9. Mainka, H., Täger, O., Körner, E., Hilfert, L., Busse, S., Edelmann, F.T., et al., 2015. Lignin–an alternative precursor for sustainable and cost-effective automotive carbon fiber. **Journal of Materials Research and Technology**, **4** (3): 283–296.
10. Mainka, H., Täger, O., Stoll, O., Körner, E., Herrmann, A.S., 2013. Alternative Precursors for Sastainable and Cost: Effective Carbon Fibers Usable Within the Automotive Industry. In: SPE Automative, pp. 1–10.
11. Suzuki, T., Takahashi, J., 2005. LCA of lightweight vehicles by using CFRP for mass-produced vehicles. in: Fifteenth Int. Conf. Compos. Mater. Durban, South Africa, pp. 1–4.

12. Mayyas, A., Qattawi, A., Omar, M., Shan, D., 2012. Design for sustainability in automotive industry: A comprehensive review. **Renewable and Sustainable Energy Reviews**, **16** (4): 1845–1862.
13. Witik, R.A., Payet, J., Michaud, V., Ludwig, C., Månson, J.-A.E., 2011. Assessing the life cycle costs and environmental performance of lightweight materials in automobile applications. **Composites Part A: Applied Science and Manufacturing**, **42** (11): 1694–1709.
14. Park, S.-J., 2015. Carbon fibers. Springer, Singapore.
15. Jain, M.K., Abhiraman, A.S., 1987. Conversion of acrylonitrile-based precursor fibres to carbon fibres. **Journal of Materials Science**, **22** (1): 278–300.
16. Damodaran, S., Desai, P., Abhiraman, A.S., 1990. Chemical and physical aspects of the formation of carbon fibres from PAN-based precursors. **Journal of the Textile Institute**, **81** (4): 384–420.
17. Ogawa, H., Saito, K., 1995. Oxidation behavior of polyacrylonitrile fibers evaluated by new stabilization index. **Carbon**, **33** (6): 783–788.
18. Clarke, A.J., Bailey, J.E., 1973. Oxidation of acrylic fibres for carbon fibre formation. **Nature**, **243** (5403): 146–150.
19. Morgan, P., 2005. Carbon fibers and their composites. 1st Edition CRC press, Boca Raton.
20. Holmes, M., 2013. Carbon fibre reinforced plastics market continues growth path. **Reinforced Plastics**, **57** (6): 24–29.
21. Warren, C.D., 2011. Low cost carbon fiber overview. Oak Ridge National Laboratory, Oak Ridge, Tennessee.
22. Taherian, R., Ghorbani, M.M., Nasr, M., Kiahosseini, S.R., 2018. Fabrication and investigation of polymer-based carbon composite as gas diffusion layer of proton exchange membrane of fuel cells. **Materials Science**, **2** (1): 1–12.
23. Dirk, H., Lukaszewicz, J.A., 2013. Automotive composite structures for crashworthiness. in: Adv. Compos. Mater. Automot. Appl. Struct. Integr. Crashworthiness, Wiley Online Library, Munich, pp. 99–127.
24. Pandey, J.K., Ahn, S.H., Lee, C.S., Mohanty, A.K., Misra, M., 2010. Recent advances in the application of natural fiber based composites. **Macromolecular Materials and Engineering**, **295** (11): 975–989.

25. Maghe, M., Creighton, C., Henderson, L.C., Huson, M.G., Nunna, S., Atkiss, S., et al., 2016. Using ionic liquids to reduce energy consumption for carbon fibre production. **Journal of Materials Chemistry A**, **4** (42): 16619–16626.

26. Golkarnarenji, G., Naebe, M., Badii, K., Milani, A.S., Jazar, R.N., Khayyam, H., 2018. Support vector regression modelling and optimization of energy consumption in carbon fiber production line. **Computers & Chemical Engineering**, **109:** 276–288.

27. Badii, K., Naebe, M., Golkarnarenji, G., Dhami, N., Atkiss, S., Buckmaster, D., et al., 2014. Energy saving in electric heater of carbon fiber stabilization oven. in: 2014 4th International Conference on Artificial Intelligence with Applications in Engineering and Technology, IEEE, pp. 109–114.

28. Golkarnarenji, G., Naebe, M., Badii, K., Milani, A.S., Jazar, R.N., Khayyam, H., 2018. Production of low cost carbon-fiber through energy optimization of stabilization process. **Materials**, **11** (3): 385.

29. Hirschler, M.M., 2001. Fire performance of organic polymers, thermal decomposition, and chemical composition. In: Fire and Polymers, ACS Publications, pp. 293–306.

30. Edie, D.D., 1990. Pitch and mesophase fibers. In: Carbon Fibers Filaments and Composites, Springer, Dordrecht, pp. 43–72.

31. Frank, E., Hermanutz, F., Buchmeiser, M.R., 2012. Carbon fibers: precursors, manufacturing, and properties. **Macromolecular Materials and Engineering**, **297** (6): 493–501.

32. Council, N.R., 1992. High Performance Synthetic Fibers for Composites. National Academies Press, Washington, DC.

33. Chung, D.D.L., 1994. Carbon fiber composites. Heinemann, Newton, MA.

34. Onishi, M., 2020. Carbon Fiber Composite Materials | Our Businesses | TORAY. https://www.toray.com/products/prod_004.html, Accessed 24 Jun 2020

35. Guo, Y., Rockstraw, D.A., 2006. Physical and chemical properties of carbons synthesized from xylan, cellulose, and Kraft lignin by H3PO4 activation. **Carbon**, **44** (8): 1464–1475.

36. Su, C.-I., Peng, C.-C., Lee, C.-Y., 2011. Performance of viscose rayon based activated carbon fabric modified by sputtering silver and continuous plasma treatment. **Textile Research Journal**, **81** (7): 730–737.

37. Aber, S., Khataee, A., Sheydaei, M., 2009. Optimization of activated carbon fiber preparation from Kenaf using K2HPO4 as chemical activator for adsorption of phenolic compounds. **Bioresource Technology**, **100** (24): 6586–6591.

38. Phan, N.H., Rio, S., Faur, C., Le Coq, L., Le Cloirec, P., Nguyen, T.H., 2006. Production of fibrous activated carbons from natural cellulose (jute, coconut) fibers for water treatment applications. **Carbon**, **44** (12): 2569–2577.

39. Williams, P.T., Reed, A.R., 2006. Development of activated carbon pore structure via physical and chemical activation of biomass fibre waste. **Biomass and Bioenergy**, **30** (2): 144–152.

40. Zhang, S., Shao, T., Kose, H.S., Karanfil, T., 2010. Adsorption of aromatic compounds by carbonaceous adsorbents: a comparative study on granular activated carbon, activated carbon fiber, and carbon nanotubes. **Environmental Science & Technology**, **44** (16): 6377–6383.

41. Maciá-Agulló, J.A., Moore, B.C., Cazorla-Amorós, D., Linares-Solano, A., 2004. Activation of coal tar pitch carbon fibres: Physical activation vs. chemical activation. **Carbon**, **42** (7): 1367–1370.

42. Altenor, S., Carene, B., Emmanuel, E., Lambert, J., Ehrhardt, J.-J., Gaspard, S., 2009. Adsorption studies of methylene blue and phenol onto vetiver roots activated carbon prepared by chemical activation. **Journal of Hazardous Materials**, **165** (1–3): 1029–1039.

43. Ko, Y.G., Choi, U.S., Kim, J.S., Park, Y.S., 2002. Novel synthesis and characterization of activated carbon fiber and dye adsorption modeling. **Carbon**, **40** (14): 2661–2672.

44. Su, C.-I., Wang, C.-L., 2007. Optimum manufacturing conditions of activated carbon fiber absorbents. I. Effect of flame retardant reagent concentration. **Fibers and Polymers**, **8** (5): 477–481.

45. Sun, J., Wu, L., Wang, Q., 2005. Comparison about the structure and properties of PAN-based activated carbon hollow fibers pretreated with different compounds containing phosphorus. **Journal of Applied Polymer Science**, **96** (2): 294–300.

46. Ayranci, E., Hoda, N., 2004. Adsorption of bentazon and propanil from aqueous solutions at the high area activated carbon-cloth. **Chemosphere**, **57** (8): 755–762.

47. Ayranci, E., Hoda, N., 2005. Adsorption kinetics and isotherms of pesticides onto activated carbon-cloth. **Chemosphere**, **60** (11): 1600–1607.

48. Morley, J.G., n.d. High-performance fiber composites (1987). Academic Press, London.

49. Donnet, J.-B., Bansal, R.C., 1998. Carbon fibers. 3rd ed. Crc Press, London New York.

50. Johnson, W., Watt, W., 1967. Structure of high modulus carbon fibres. **Nature**, **215** (5099): 384–386.

51. Bennett, S.C., Johnson, D.J., Johnson, W., 1983. Strength-structure relationships in PAN-based carbon fibres. **Journal of Materials Science**, **18** (11): 3337–3347.

52. Johnson, W., 1979. Optical anisotropy of carbon fibres. **Nature**, **279** (5709): 142–145.

53. Edison, T.A., 1880. Electric lamp. US Patent 223,898.

54. Frohs, W., Jaeger, H., 2012. Carbon fiber & composite material–Landscape Germany. **Carbon**, **2** (50): 737.

55. Park, S.-J., Lee, S.-Y., 2015. History and structure of carbon fibers. in: Carbon Fibers, 2nd ed., Springer, Singapore, pp. 1–30.

56. Abbott, W.F., 1962. Method for carbonizing fibers. US Patent 3,053,775.

57. Houtz, R.C., 1950. "Orlon" Acrylic Fiber: Chemistry and Properties. **Textile Research Journal**, **20** (11): 786–801.

58. Carrott, P.J.M., Nabais, J.M. V, Carrott, M.M.L.R., Pajares, J.A., 2001. Preparation of activated carbon fibres from acrylic textile fibres. **Carbon**, **39** (10): 1543–1555.

59. Qiao, W.M., Yoon, S.-H., Korai, Y., Mochida, I., Inoue, S., Sakurai, T., et al., 2004. Preparation of activated carbon fibers from polyvinyl chloride. **Carbon**, **42** (7): 1327–1331.

60. Buchmeiser, M.R., Unold, J., Schneider, K., Anderson, E.B., Hermanutz, F., Frank, E., et al., 2013. A new carbon precursor: synthesis and carbonization of triethylammonium-based poly (p-phenylenevinylene)(PPV) progenitors. **Journal of Materials Chemistry A**, **1** (42): 13154–13163.

61. Ying, Y.-G., Pan, Y.-P., Ren, R., Dang, J.-M., Liu, C.-L., 2013. Effect of the molecular structure of phenolic novolac precursor resins on the properties of phenolic fibers. **Materials Chemistry and Physics**, **143** (1): 455–460.

62. Dong, C., Davies, I.J., 2014. Flexural and tensile strengths of unidirectional hybrid epoxy composites reinforced by S-2 glass and T700S carbon fibres. **Materials & Design (1980-2015)**, **54:** 955–966.

63. Das, S., Warren, J., West, D., Schexnayder, S.M., 2016. Global carbon fiber composites supply chain competitiveness analysis. Oak Ridge National Laboratory; The University of Tennessee, Knoxville.

64. Mittal, J., Bahl, O.P., Mathur, R.B., Sandle, N.K., 1994. IR studies of PAN fibres thermally stabilized at elevated temperatures. **Carbon**, **32** (6): 1133–1136.

65. Mittal, J., Mathur, R.B., Bahl, O.P., 1997. Post spinning modification of PAN fibres—a review. **Carbon**, **35** (12): 1713–1721.

66. Jie, L., Wangxi, Z., 2005. Structural changes during the thermal stabilization of modified and original polyacrylonitrile precursors. **Journal of Applied Polymer Science**, **97** (5): 2047–2053.

67. Johnson, W., Phillips, L.N., Watt, W., 1968. Production of carbon fibres and compositions containing said fibres. US Patent 3,412,062.

68. Edie, D.D., 1998. The effect of processing on the structure and properties of carbon fibers. **Carbon**, **36** (4): 345–362.

69. Johnson, J.W., Potter, W., Rose, P.G., Scott, G., 1972. Stabilisation of polyacrylonitrile by oxidative transformation. **British Polymer Journal**, **4** (6): 527–540.

70. Hou, Y., Sun, T., Wang, H., Wu, D., 2008. Influence of ozone on chemical reactions during the stabilization of polyacrylonitrile as a carbon fiber precursor. **Journal of Applied Polymer Science**, **108** (6): 3990–3996.

71. Bahl, O.P., Manocha, L.M., 1975. Effect of preoxidation conditions on mechanical properties of carbon fibres. **Carbon**, **13** (4): 297–300.

72. Gupta, A., Harrison, I.R., 1997. New aspects in the oxidative stabilization of PAN-based carbon fibers: II. **Carbon**, **35** (6): 809–818.

73. Manocha, L.M., Bahl, O.P., 1980. Role of oxygen during thermal stabilisation of PAN fibres. **Fibre Science and Technology**, **13** (3): 199–212.

74. Ezekiel, H.M., Spain, R.G., 1967. Preparation of graphite fibers from polymeric fibers. In: Journal of Polymer Science Part C: Polymer Symposia, Wiley Online Library, pp. 249–265.

75. Rašković, V., Marinković, S., 1978. Processes in sulfur dioxide treatment of PAN fibers. **Carbon**, **16** (5): 351–357.

76. Błażewicz, S., 1989. Carbon fibres from a SO2 treated PAN precursor. **Carbon**, **27** (6): 777–783.

77. Bahl, O.P., Mathur, R.B., Kundra, K.D., 1980. Treatment of pan fibres with SO2 and development of carbon fibres therefrom. **Fibre Science and Technology**, **13** (2): 155–162.

78. Bhat, G.S., Peebles Jr, L.H., Abhiraman, A.S., Cook, F.L., 1993. Rapid stabilization of acrylic fibers using ammonia: effect on structure and morphology. **Journal of Applied Polymer Science**, **49** (12): 2207–2219.

79. Bhat, G.S., Cook, F.L., Abhiraman, A.S., Peebles Jr, L.H., 1990. New aspects in the stabilization of acrylic fibers for carbon fibers. **Carbon**, **28** (2–3): 377–385.

80. Konkin, A., 1985. Properties of carbon fibres and fields of their application. In: Elsevier Science Publishers BV, Handbook of Composites, pp. 241–273.

81. Montes-Morán, M.A., Martınez-Alonso, A., Tascón, J.M.D., Paiva, M.C., Bernardo, C.A., 2001. Effects of plasma oxidation on the surface and interfacial properties of carbon fibres/polycarbonate composites. **Carbon**, **39** (7): 1057–1068.

82. Manocha, L.M., Yasuda, E., Tanabe, Y., Kimura, S., 1988. Effect of carbon fiber surface-treatment on mechanical properties of C/C composites. **Carbon**, **26** (3): 333–337.

83. Song, W., Gu, A., Liang, G., Yuan, L., 2011. Effect of the surface roughness on interfacial properties of carbon fibers reinforced epoxy resin composites. **Applied Surface Science**, **257** (9): 4069–4074.

84. Parker, B.M., Waghorne, R.M., 1982. Surface pretreatment of carbon fibre-reinforced composites for adhesive bonding. **Composites**, **13** (3): 280–288.

85. Watt, W., 1970. Production and properties of high modulus carbon fibres. **Proceedings of the Royal Society of London. A. Mathematical and Physical Sciences**, **319** (1536): 5–15.

86. Hunter, B., 2014. Toray Develops High Tensile Strength and Modulus Carbon Fiber TORAYCA® T1100G. https://cs2.toray.co.jp/news/toray/en/newsrrs02.nsf/0/B126D9D8433675EE49257D11001770C5, Accessed 2 Oct 2021.

87. Hawthorne, H.M., Baker, C., Bentall, R.H., Linger, K.R., 1970. High strength, high modulus graphite fibres from pitch. **Nature**, **227** (5261): 946–947.

88. McHenry, E., 1976. Process for producing carbon fibers from mesophase pitch. US Patent 3,974,264-A.

89. Wortberg, G., De Palmenaer, A., Beckers, M., Seide, G., Gries, T., 2015. Polyethylene-based carbon fibers by the use of sulphonation for stabilization. **Fibers**, **3** (3): 373–379.

90. Sudo, K., Shimizu, K., 1992. A new carbon fiber from lignin. **Journal of Applied Polymer Science**, **44** (1): 127–134.

91. Huang, X., 2009. Fabrication and properties of carbon fibers. **Materials**, **2** (4): 2369–2403.

92. Bright, A.A., Singer, L.S., 1979. The electronic and structural characteristics of carbon fibers from mesophase pitch. **Carbon**, **17** (1): 59–69.

93. Ishida, O., Kim, D.-Y., Kuga, S., Nishiyama, Y., Brown, R.M., 2004. Microfibrillar carbon from native cellulose. **Cellulose**, **11** (3–4): 475–480.

94. Sun, T., Hou, Y., Wang, H., 2009. Effect of atmospheres on stabilization of polyacrylonitrile fibers. **Journal of Macromolecular Science®, Part A: Pure and Applied Chemistry**, **46** (8): 807–815.

95. Chae, H.G., Kumar, S., 2008. Making strong fibers. **Science**, **319** (5865): 908–909.

96. Li, W., Long, D., Miyawaki, J., Qiao, W., Ling, L., Mochida, I., et al., 2012. Structural features of polyacrylonitrile-based carbon fibers. **Journal of Materials Science**, **47** (2): 919–928.

97. Nunna, S., Creighton, C., Hameed, N., Naebe, M., Henderson, L.C., Setty, M., et al., 2017. Radial structure and property relationship in the thermal stabilization of PAN precursor fibres. **Polymer Testing**, **59:** 203–211.

98. Huang, Y., Young, R.J., 1995. Effect of fibre microstructure upon the modulus of PAN-and pitch-based carbon fibres. **Carbon**, **33** (2): 97–107.

99. Edie, D.D., Diefendorf, R.J., 1993. Carbon fiber manufacturing. **Carbon-Carbon Materials and Composites**, 19–37.

100. Masson, J., 1995. Acrylic fiber technology and applications. 1st Edition, CRC Press, Boca Raton London New York Washington D.C.

101. Petrie, C.S., 1978. Fundamentals of fibre formation: A. Ziabicki, John Wiley & Sons, London, August 1976, 502 pages, price£ 19.50 ($39.00). **Journal of Non-Newtonian Fluid Mechanics**, **3** (3): 306–308.

102. Ram, M.J., Riggs, J.P., 1972. Process for the production of acrylic filaments. US Patent 3,657,409.

103. Knudsen, J.P., 1963. The influence of coagulation variables on the structure and physical properties of an acrylic fiber. **Textile Research Journal**, **33** (1): 13–20.

104. Riggs, D.M., Shuford, R.J., Lewis, R.W., 1982. Graphite fibers and composites. in: Handb. Compos., Springer, pp. 196–271.

105. Freytag, R., Donze, J.J., 1983. Handbook of fiber science and technology. Volume 1 Chemical Processing of Fibers and Fabrics: Part A Fundamental and Preparation, Marcel Dekker Inc., New York and Basel, pp. 93–166.

106. Watt, W., Perov, B. V, 1985. Handbook of Composites Vol. 1 Strong Fibres. North-Holland Publishing Company, Oxford.

107. Fitzer, E., Muller, D.J., 1972. Reaction technique observation for continuous production of carbon fibers from polyacrylonitrile. **Chemiker-Zeitung**, **96** (1–2): 20.

108. Grassie, N., Hay, J.N., 1962. Thermal coloration and insolubilization in polyacrylonitrile. **Journal of Polymer Science**, **56** (163): 189–202.

109. Fitzer, E., Frohs, W., Heine, M., 1986. Optimization of stabilization and carbonization treatment of PAN fibres and structural characterization of the resulting carbon fibres. **Carbon**, **24** (4): 387–395.

110. Fitzer, E., Müller, D.J., 1975. The influence of oxygen on the chemical reactions during stabilization of pan as carbon fiber precursor. **Carbon**, **13** (1): 63–69.

111. Coleman, M.M., Sivy, G.T., 1981. Fourier transform ir studies of the degradation of polyacrylonitrile copolymers—III: Acrylonitrile/vinyl acetate copolymers. **Carbon**, **19** (2): 133–135.

112. Xue, Y., Liu, J., Liang, J., 2013. Correlative study of critical reactions in polyacrylonitrile based carbon fiber precursors during thermal-oxidative stabilization. **Polymer Degradation and Stability**, **98** (1): 219–229.

113. Dunham, M.G., Edie, D.D., 1992. Model of stabilization for pan-based carbon fiber precursor bundles. **Carbon**, **30** (3): 435–450.

114. Xiao, S., Cao, W., Wang, B., Xu, L., Chen, B., 2013. Mechanism and kinetics of oxidation during the thermal stabilization of polyacrylonitrile fibers. **Journal of Applied Polymer Science**, **127** (4): 3198–3203.

115. Grassie, N., McGuchan, R., 1970. Pyrolysis of polyacrylonitrile and related polymers—I. Thermal analysis of polyacrylonitrile. **European Polymer Journal**, **6** (9): 1277–1291.

116. Schurz, J., 1958. Discoloration effects in acrylonitrile polymers. **Journal of Polymer Science**, **28** (117): 438–439.

117. Thompson, E. V, 1966. The thermal behavior of acrylonitrile polymers. I. On the decomposition of polyacrylonitrile between 250 and 325° C. **Journal of Polymer Science Part B: Polymer Letters**, **4** (5): 361–366.

118. Friedlander, H.N., Peebles Jr, L.H., Brandrup, J., Kirby, J.R., 1968. On the chromophore of polyacrylonitrile. VI. Mechanism of color formation in polyacrylonitrile. **Macromolecules**, **1** (1): 79–86.

119. Peebles Jr, L.H., Thompson Jr, R.B., Kirby, J.R., Gibson, M.E., 1972. Basic dyeability and acid content of high- conversion polyacrylonitrile. **Journal of Applied Polymer Science**, **16** (12): 3341–3351.

120. Peebles Jr, L.H., Peyser, P., Snow, A.W., Peters, W.C., 1990. On the exotherm of polyacrylonitrile: pyrolysis of the homopolymer under inert conditions. **Carbon**, **28** (5): 707–715.

121. Bajaj, P., Roopanwal, A.K., 1997. Thermal stabilization of acrylic precursors for the production of carbon fibers: an overview. **Journal of Macromolecular Science, Part C: Polymer Reviews**, **37** (1): 97–147.

122. Ko, T., 1991. Influence of continuous stabilization on the physical properties and microstructure of PAN- based carbon fibers. **Journal of Applied Polymer Science**, **42** (7): 1949–1957.

123. Dalton, S., Heatley, F., Budd, P.M., 1999. Thermal stabilization of polyacrylonitrile fibres. **Polymer**, **40** (20): 5531–5543.

124. Jain, M.K., Balasubramanian, M., Desai, P., Abhiraman, A.S., 1987. Conversion of acrylonitrile-based precursors to carbon fibres. **Journal of Materials Science**, **22** (1): 301–312.

125. Oberlin, A., Bonnamy, S., Lafdi 3rd, K., 1998. In Carbon Fibers ; Donnet, JB; Wang, TK; Rebouillat, S.; Peng, JCM Ed, Marcel Dekker, New York.

126. Liu, Y., Chae, H.G., Kumar, S., 2011. Gel-spun carbon nanotubes/polyacrylonitrile composite fibers. Part I: Effect of carbon nanotubes on stabilization. **Carbon**, **49** (13): 4466–4476.

127. Fitzer, E., Heine, M., Metzler, W., 1986. Gaseous products during heat treatment of polyacrylonitrile. Fourth International Carbon Conference, Baden-Baden, Germany.

128. Fitzer, E. and Frohs, W., 1988. The influence of carbonization and post treatment conditions on the properties of PAN based carbon fibers. International Carbon Conference, U.K., pp. 298–300.

129. Fitzer, E., 1989. Pan-based carbon fibers—present state and trend of the technology from the viewpoint of possibilities and limits to influence and to control the fiber properties by the process parameters. **Carbon**, **27** (5): 621–645.

130. Fedorov, V.B., Shorshorov, M.K., Khakimova, D.K., 1978. Carbon and its interaction with metals. Metallurgija-Publishers, Moscow.

131. J. B. Donnet and R. C. Bansal, 1990. Carbon fibers. 2nd edition, Marcel Dekker, New York.

132. Bahl, O.P., Shen, Z., Lavin, J.G., Ross, R.A., 1998. Manufacture of carbon fibers. Marcel Dekker, New York.

133. Bacon, R., 1980. Carbon fibres from mesophase pitch. **Philosophical Transactions of the Royal Society of London. Series A, Mathematical and Physical Sciences**, **294** (1411): 437–442.

134. Otani, S., Fukuoka, Y., Igarashi, B., Sasaki, K., 1969. Method for producing carbonized lignin fiber. US Patent 3461082A.

135. Sudo, K., Shimizu, K., Nakashima, N., Yokoyama, A., 1993. A new modification method of exploded lignin for the preparation of a carbon fiber precursor. **Journal of Applied Polymer Science**, **48** (8): 1485–1491.

136. Uraki, Y., Kubo, S., Nigo, N., Sano, Y., Sasaya, T., 1995. Preparation of carbon fibers from organosolv lignin obtained by aqueous acetic acid pulping. **Holzforschung-International Journal of the Biology, Chemistry, Physics and Technology of Wood**, **49** (4): 343–350.

137. Kubo, S., Uraki, Y., Sano, Y., 1998. Preparation of carbon fibers from softwood lignin by atmospheric acetic acid pulping. **Carbon**, **36** (7–8): 1119–1124.

138. Kadla, J.F., Kubo, S., Venditti, R.A., Gilbert, R.D., Compere, A.L., Griffith, W., 2002. Lignin-based carbon fibers for composite fiber applications. **Carbon**, **40** (15): 2913–2920.

139. Krutchen, C., 1974. Melt extrudable polyacetylene copolymer blends. US Patent 3852235A.

140. Mavinkurve, A., Visser, S., Pennings, A.J., 1995. An initial evaluation of poly (vinylacetylene) as a carbon fiber precursor. **Carbon**, **33** (6): 757–761.

141. Horikiri, S., Iseki, J., Minobe, M., 1978. Process for producing carbon fibre. US Patent 4070446A.

142. Newell, J.A., Edie, D.D., 1996. Factors limiting the tensile strength of PBO-based carbon fibers. **Carbon**, **34** (5): 551–560.

143. Williams, P.T., Reed, A.R., 2004. High grade activated carbon matting derived from the chemical activation and pyrolysis of natural fibre textile waste. **Journal of Analytical and Applied Pyrolysis**, **71** (2): 971–986.

144. Rosas, J.M., Bedia, J., Rodríguez-Mirasol, J., Cordero, T., 2009. HEMP-derived activated carbon fibers by chemical activation with phosphoric acid. **Fuel**, **88** (1): 19–26.

145. Fu, R., Liu, L., Huang, W., Sun, P., 2003. Studies on the structure of activated carbon fibers activated by phosphoric acid. **Journal of Applied Polymer Science**, **87** (14): 2253–2261.

146. Zeng, F., Pan, D., Pan, N., 2005. Choosing the impregnants by thermogravimetric analysis for preparing rayon-based carbon fibers. **Journal of Inorganic and Organometallic Polymers and Materials**, **15** (2): 261–267.

147. You, S.Y., Park, Y.H., Park, C.R., 2000. Preparation and properties of activated carbon fabric from acrylic fabric waste. **Carbon**, **38** (10): 1453–1460.

148. Worasuwannarak, N., Hatori, S., Nakagawa, H., Miura, K., 2003. Effect of oxidation pre-treatment at 220 to 270 C on the carbonization and activation behavior of phenolic resin fiber. **Carbon**, **41** (5): 933–944.

149. Zhang, S.-J., Yu, H.-Q., Feng, H.-M., 2006. PVA-based activated carbon fibers with lotus root-like axially porous structure. **Carbon**, **44** (10): 2059–2068.

150. Suárez-García, F., Martínez-Alonso, A., Tascón, J.M.D., 2004. Activated carbon fibers from Nomex by chemical activation with phosphoric acid. **Carbon**, **42** (8–9): 1419–1426.

151. Villar-Rodil, S., Martinez-Alonso, A., Tascon, J.M.D., 2005. Nanoporous carbon fibres by pyrolysis of nomex polyaramid fibres. **Journal of Thermal Analysis & Calorimetry**, **79** (3): 529–532.

152. López, M.C.B., Martínez-Alonso, A., Tascon, J.M.D., 2000. N2 and CO2 adsorption on activated carbon fibres prepared from Nomex chars. **Carbon**, **38** (8): 1177–1182.

153. Gilardo, L., Ladino, Y., Pirajanc, J.C.M., Rodriguez, M.P., 2007. Ecletica Quimica. Sao Paulo.

154. Villar-Rodil, S., Suarez-Garcia, F., Paredes, J.I., Martinez-Alonso, A., Tascon, J.M.D., 2005. Activated carbon materials of uniform porosity from polyaramid fibers. **Chemistry of Materials**, **17** (24): 5893–5908.

155. Byrne, N., De Silva, R., Ma, Y., Sixta, H., Hummel, M., 2018. Enhanced stabilization of cellulose-lignin hybrid filaments for carbon fiber production. **Cellulose**, **25** (1): 723–733.

156. Baker, D.A., Rials, T.G., 2013. Recent advances in low-cost carbon fiber manufacture from lignin. **Journal of Applied Polymer Science**, **130** (2): 713–728.

157. Senthilkumaar, S., Varadarajan, P.R., Porkodi, K., Subbhuraam, C. V, 2005. Adsorption of methylene blue onto jute fiber carbon: kinetics and equilibrium studies. **Journal of Colloid and Interface Science**, **284** (1): 78–82.

158. Roy, A., Chakraborty, S., Kundu, S.P., Basak, R.K., Majumder, S.B., Adhikari, B., 2012. Improvement in mechanical properties of jute fibres through mild alkali treatment as demonstrated by utilisation of the Weibull distribution model. **Bioresource Technology**, **107:** 222–228.

159. Asadullah, M., Kabir, M.S., Ahmed, M.B., Razak, N.A., Rasid, N.S.A., Aezzira, A., 2013. Role of microporosity and surface functionality of activated carbon in methylene blue dye removal from water. **Korean Journal of Chemical Engineering**, **30** (12): 2228–2234.

160. Ku, H., Wang, H., Pattarachaiyakoop, N., Trada, M., 2011. A review on the tensile properties of natural fiber reinforced polymer composites. **Composites Part B: Engineering**, **42** (4): 856–873.

161. Ramesh, M., Palanikumar, K., Reddy, K.H., 2013. Mechanical property evaluation of sisal–jute–glass fiber reinforced polyester composites. **Composites Part B: Engineering**, **48:** 1–9.

162. Davidson, J.A., Jung, H.-T., Hudson, S.D., Percec, S., 2000. Investigation of molecular orientation in melt-spun high acrylonitrile fibers. **Polymer**, **41** (9): 3357–3364.

163. Paiva, M.C., Kotasthane, P., Edie, D.D., Ogale, A.A., 2003. UV stabilization route for melt-processible PAN-based carbon fibers. **Carbon**, **41** (7): 1399–1409.

164. Zabihi, O., Ahmadi, M., Li, Q., Shafei, S., Huson, M.G., Naebe, M., 2017. Carbon fibre surface modification using functionalized nanoclay: A hierarchical interphase for fibre-reinforced polymer composites. **Composites Science and Technology**, **148:** 49–58.

165. Kraus, T., Kühnel, M., Witten, E., 2016. Composites market report 2016-market developments, trends, outlook and challenges. Carbon Composites EV.

166. Gates, D., 2007. Spirit Aerosystems in "The Seattle Times." .

167. Dominic Gates, 2007. Dreamliner nose shows the face of future plane factories | The Seattle Times.

168. Adam, H., 1997. Carbon fibre in automotive applications. **Materials & Design**, **18** (4–6): 349–355.

169. Park, S.-J., Seo, M.-K., 2011. Interface science and composites. Academic Press, Great Britain.

170. Othman, R., Ismail, N.I., Pahmi, M.A.A.H., Basri, M.H.M., Sharudin, H., Hemdi, A.R., 2018. Application of Carbon fiber reinforced plastics in automotive industry: A review. **Journal of Mechanical Manufacturing, 1:** 144–154.

171. Kelly, G., 2004. Joining of carbon fibre reinforced plastics for automotive applications, Phd Thesis, KTH-Royal Institute of Technology, Sweden, 2004.

172. Park, S.-J., 2018. Recent Uses of Carbon Fibers. In: Carbon Fibers, Springer, pp. 241–277.

173. Bunsell, A.R., Renard, J., 2005. Fundamentals of fibre reinforced composite materials. CRC Press, Boca Raton.

174. Piancastelli, L., Frizziero, L., Zanuccoli, G., Daidzic, N.E., Rocchi, I., 2013. A comparison between CFRP and 2195-FSW for aircraft structural designs. **International Journal of Heat and Technology**, **31** (1): 17–24.

175. Kapidžić, Z., Nilsson, L., Ansell, H., 2014. Finite element modeling of mechanically fastened composite-aluminum joints in aircraft structures. **Composite Structures**, **109:** 198–210.

176. Deo, R.B., Starnes Jr, J.H., Holzwarth, R.C., 2003. Low-cost composite materials and structures for aircraft applications. RTO Applied Vehicle Technology Panel (AVT) Specialists' Meeting on "Low Cost Composite Structures", Loen, Norway.

177. Tenney, D.R., Davis Jr, J.G., Pipes, R.B., Johnston, N., 2009. NASA composite materials development: lessons learned and future challenges. NATO RTO AVT-164 Workshop on support of composite systems, Bonn, Germany.

178. Paton, W., 1970. Carbon fibre in sports equipment. **Composites**, **1** (4): 221–226.

179. Huntley, M.P., Davis, C.L., Strangwood, M., Otto, S.R., 2006. Comparison of the static and dynamic behaviour of carbon fibre composite golf club shafts. **Proceedings of the Institution of Mechanical Engineers, Part L: Journal of Materials: Design and Applications**, **220** (4): 229–236.

180. Miyano, Y., Nakada, M., Ichimura, J., Hayakawa, E., 2008. Accelerated testing for long-term strength of innovative CFRP laminates for marine use. **Composites Part B: Engineering**, **39** (1): 5–12.

181. Biswas, S., Mittal, A., Srikanth, G., 2002. Composites: a vision for the future. ICERP Conference IIT, Madras, pp. 25–36.

182. Kimpara, I., 1991. Use of advanced composite materials in marine vehicles. **Marine Structures**, **4** (2): 117–127.

183. Grogg, K., 2005. Harvesting the wind: the physics of wind turbines. **Physics and Astronomy Comps Papers**, **7:** 1–41.

184. Brøndsted, P., Lilholt, H., Lystrup, A., 2005. Composite materials for wind power turbine blades. **Annual Review of Materials Research**, **35:** 505–538.

185. Walczyk, D., 2010. An overview of composite wind turbine blade manufacturing. Workshop on Next-Generation Wind Power, Rensselaer Polytechnic Institute Fangfang Song.

186. Kovacevic, M., Markovic, L., 2015. Application of carbon fibre in construction industry. "New Technologies NT-2015" – Development and Application, Kosovo, pp. 217–226.

187. Rujitanaroj, P., Pimpha, N., Supaphol, P., 2010. Preparation, characterization, and antibacterial properties of electrospun polyacrylonitrile fibrous membranes containing silver nanoparticles. **Journal of Applied Polymer Science**, **116** (4): 1967–1976.

188. Tsafack, M.J., Levalois-Grützmacher, J., 2006. Plasma-induced graft-polymerization of flame retardant monomers onto PAN fabrics. **Surface and Coatings Technology**, **200** (11): 3503–3510.

189. Dunn, P., Ennis, B.C., 1970. Thermal analysis of polyacrylonitrile. Part I. The melting of polyacrylonitrile. **Journal of Applied Polymer Science**, **14** (7): 1795–1798.

190. Mark, H.F., Kroschwitz, J.I., 1985. Encyclopedia of polymer science and engineering. 2nd edition, Wiley, New York.

191. Ivanovska, A., Asanovic, K., Jankoska, M., Mihajlovski, K., Pavun, L., Kostic, M., 2020. Multifunctional jute fabrics obtained by different chemical modifications. **Cellulose**, **27** (14): 8485–8502.

192. Cai, Y., David, S.K., Pailthorpe, M.T., 2000. Dyeing of jute and jute/cotton blend fabrics with 2: 1 pre-metallised dyes. **Dyes and Pigments**, **45** (2): 161–168.

193. Alves, C., Silva, A.J., Reis, L.G., Freitas, M., Rodrigues, L.B., Alves, D.E., 2010. Ecodesign of automotive components making use of natural jute fiber composites. **Journal of Cleaner Production**, **18** (4): 313–327.

194. Ray, D., Sarkar, B.K., 2001. Characterization of alkali- treated jute fibers for physical and mechanical properties. **Journal of Applied Polymer Science**, **80** (7): 1013–1020.

195. Compere, A.L., Griffith, W.L., 2009. Preparation and analysis of biomass lignins. 1st edition, Springer, Totowa, NJ, USA, pp. 185-212.

196. Kabir, M.M., Islam, M.M., Wang, H., 2013. Mechanical and thermal properties of jute fibre reinforced composites. **Journal of Multifunctional Composites**, **1** (1): 71–77.

197. Bengtsson, A., Bengtsson, J., Sedin, M., Sjöholm, E., 2019. Carbon fibers from lignin-cellulose precursors: effect of stabilization conditions. **ACS Sustainable Chemistry & Engineering**, **7** (9): 8440–8448.

198. Chatterjee, S., Saito, T., 2015. Lignin-derived advanced carbon materials. **ChemSusChem**, **8** (23): 3941–3958.

199. Stark, N.M., Yelle, D.J., Agarwal, U.P., 2016. Techniques for characterizing lignin. Lignin in polymer composites, Elsevier Inc., pp. 49–66.

200. Vu, T.H.M., Pakkanen, H., Alén, R., 2004. Delignification of bamboo (Bambusa procera acher): Part 1. Kraft pulping and the subsequent oxygen delignification to pulp with a low kappa number. **Industrial Crops and Products**, **19** (1): 49–57.

201. Mir, B.J., Tajvidi, M., Ghasemi, E., Hermanson, J.C., 2007. Prediction of the elastic modulus of wood flour/kenaf fibre/polypropylene hybrid composites. **Iranian Polymer Journal**, **16** (4): 271–278.

202. Scurlock, J.M.O., Dayton, D.C., Hames, B., 2000. Bamboo: an overlooked biomass resource?. **Biomass and Bioenergy**, **19** (4): 229–244.

203. Zhang, Q., Zeng, Y., Xiao, X., Deng, P., He, Q., Zhang, T., 2019. Investigation on the preparation and adsorption performance of bamboo fiber based activated carbon. **Fibers and Polymers**, **20** (2): 293–301.

204. Khalil, H.P.S.A., Bhat, I.U.H., Jawaid, M., Zaidon, A., Hermawan, D., Hadi, Y.S., 2012. Bamboo fibre reinforced biocomposites: A review. **Materials & Design**, **42:** 353–368.

205. Albano, C., Gonzalez, J., Ichazo, M., Kaiser, D., 1999. Thermal stability of blends of polyolefins and sisal fiber. **Polymer Degradation and Stability**, **66** (2): 179–190.

206. Juárez, A.G.V., Rost, G., Heitmann, U., Heger, E., Müller, R., 2011. Development of a biotechnological process for the production of high quality linen fibers. **Bioprocess and Biosystems Engineering**, **34** (8): 913–921.

207. Mascheroni, E., Rampazzo, R., Ortenzi, M.A., Piva, G., Bonetti, S., Piergiovanni, L., 2016. Comparison of cellulose nanocrystals obtained by sulfuric acid hydrolysis and ammonium persulfate, to be used as coating on flexible food-packaging materials. **Cellulose**, **23** (1): 779–793.

208. Zeng, Z., Shao, Z., Xiao, R., Lu, Y., 2017. Structure evolution mechanism of poly (acrylonitrile/itaconic acid/acrylamide) during thermal oxidative stabilization process. **Chinese Journal of Polymer Science**, **35** (8): 1020–1034.

209. Karacan, I., Erdŏgan, G., 2012. The effect of ethylenediamine pretreatment on the molecular structure of thermally stabilized polyacrylonitrile fibers before carbonization. **Polymer Engineering & Science**, **52** (3): 467–480.

210. Karacan, I., Erdoğan, G., 2012. An investigation on structure characterization of thermally stabilized polyacrylonitrile precursor fibers pretreated with guanidine carbonate prior to carbonization. **Polymer Engineering & Science**, **52** (5): 937–952.

211. Rahman, M.M., Karacan, I., 2021. The impact of eco-friendly chemical incorporation on the thermal oxidation process of flax fiber prior to carbonization and activation. **Journal of Materials Science**.

212. Erzurumluoglu, L., Rahman, M.M., Demirel, T., Karacan, I., 2021. Fabrication of carbon fibers from the cupric ion impregnated and thermally stabilized poly(hexamethylene adipamide) precursor. **Journal of Industrial Textiles, 0** (0): 1-31.

213. Karacan, I., Erzurumluoğlu, L., 2015. The effect of carbonization temperature on the structure and properties of carbon fibers prepared from poly (m-phenylene isophthalamide) precursor. **Fibers and Polymers**, **16** (8): 1629–1645.

214. Karacan, I., Tunçel, K.Ş., 2013. Thermal stabilization of poly (hexamethylene adipamide) fibers in the presence of ferric chloride prior to carbonization. **Polymer Degradation and Stability**, **98** (9): 1869–1881.

215. Hindeleh, A.M., Johnson, D.J., Montague, P.E., 1980. Computational methods for profile resolution and crystallite size evaluation in fibrous polymers. ACS Symposium Series, pp. 149–182.

216. Karacan, I., Tunçel, K.Ş., 2013. An assessment of the impact of cupric ion complexation on thermal stabilization of polyamide 66 as carbon fiber precursor. **Recent Res. Devel. Appl. Polym. Sci.**, **5** (1): 1–33.

217. Karacan, I., Meşeli, H., 2018. Characterization of amorphous carbon fibers produced from thermally stabilized polyamide 6 fibers. **Journal of Industrial Textiles**, **47** (6): 1185–1211.

218. Karacan, I., Baysal, G., 2012. Investigation of the effect of cupric chloride on thermal stabilization of polyamide 6 as carbon fiber precursor. **Fibers and Polymers**, **13** (7): 864–873.

219. Rahman, M.M., Demirel, T., Tunçel, K.Ş., Karacan, I., 2021. The effect of the ammonium persulfate and a multi-step annealing approach during thermal stabilization of polyacrylonitrile multifilament prior to carbonization. **Journal of Materials Science**, **56** (26): 14844–14865.

220. Miao, M., McDonnell, J., Vuckovic, L., Hawkins, S.C., 2010. Poisson's ratio and porosity of carbon nanotube dry-spun yarns. **Carbon**, **48** (10): 2802–2811.

221. Hindeleh, A.M., Johnson, D.J., Montague, P.E., 1983. In Fibre Diffraction Methods ACS Symp. No. 141, French, AD, Gardner, KH, Eds., American Chemical Society, Washington DC, pp. 149-182.

222. Zhu, Y., Wilding, M.A., Mukhopadhyay, S.K., 1996. Estimation, using infrared spectroscopy, of the cyclization of poly (acrylonitrile) during the stabilization stage of carbon fibre production. **Journal of Materials Science**, **31** (14): 3831–3837.

223. Yu, M.-J., Bai, Y.-J., Wang, C.-G., Xu, Y., Guo, P.-Z., 2007. A new method for the evaluation of stabilization index of polyacrylonitrile fibers. **Materials Letters**, **61** (11–12): 2292–2294.

224. Hindeleh, A.M., Johnson, D.J., 1978. Crystallinity and crystallite size measurement in polyamide and polyester fibres. **Polymer**, **19** (1): 27–32.

225. Stokes, A.R., 1948. A numerical Fourier-analysis method for the correction of widths and shapes of lines on X-ray powder photographs. **Proceedings of the Physical Society**, **61** (4): 382–391.

226. Ko, T., 1993. Characterization of PAN- based nonburning (nonflammable) fibers. **Journal of Applied Polymer Science**, **47** (4): 707–715.

227. Sun, J., Wang, Q., 2005. Effects of the oxidation temperature on the structure and properties of polyacrylonitrile- based activated carbon hollow fiber. **Journal of Applied Polymer Science**, **98** (1): 203–207.

228. Sun, J., He, C., Zhu, S., Wang, Q., 2007. effects of oxidation time on the structure and properties of polyacrylonitrile- based activated carbon hollow fiber. **Journal of Applied Polymer Science**, **106** (1): 470–474.

229. Bahl, O.P., Manocha, L.M., 1976. Methods of determining optimum preoxidation time of PAN fibres. **Fibre Science and Technology**, **9** (1): 77–80.

230. Ko, T., Chiranairadul, P., Ting, H., Lin, C., 1989. The effect of modification on structure and dynamic mechanical behavior during the processing of acrylic fiber to stabilized fiber. **Journal of Applied Polymer Science**, **37** (2): 541–552.

231. Mathur, R.B., Gupta, D., Bahl, O.P., Dhami, T.L., 1984. Infrared spectral studies of preoxidized PAN fibres incorporated with cuprous chloride additive. **Fibre Science and Technology**, **20** (3): 227–234.

232. Takaku, A., Hashimoto, T., Miyoshi, T., 1985. Tensile properties of carbon fibers from acrylic fibers stabilized under isothermal conditions. **Journal of Applied Polymer Science**, **30** (4): 1565–1571.

233. Karacan, I., Erdoğan, G., 2012. The role of thermal stabilization on the structure and mechanical properties of polyacrylonitrile precursor fibers. **Fibers and Polymers**, **13** (7): 855–863.

234. Touheed, A., Maab, H., 2012. Preparation and Characterization of Sulfonated Polyacrylamide from Polyacrylonitrile for Proton Conductive Membranes. **Journal of the Chinese Chemical Society**, **59** (12): 1541–1547.

235. Yamadera, R., Tadokoro, H., Murahashi, S., 1964. Normal vibrations of polyacrylonitrile and deuterated polyacrylonitriles. **The Journal of Chemical Physics**, **41** (5): 1233–1247.

236. Tadokoro, H., Murahashi, S., Yamadera, R., Kamei, T., 1963. Infrared absorption spectra of polyacrylonitrile and deuterated polyacrylonitriles. **Journal of Polymer Science Part A: General Papers**, **1** (10): 3029–3042.

237. Liang, C.Y., Krimm, S., 1958. Infrared spectra of high polymers. VII. Polyacrylonitrile. **Journal of Polymer Science**, **31** (123): 513–522.

238. Stupp, S.I., Carr, S.H., 1977. Chemical origin of thermally stimulated discharge currents in polyacrylonitrile. **Journal of Polymer Science: Polymer Physics Edition**, **15** (3): 485–499.

239. Grassie, N., McGuchan, R., 1972. Pyrolysis of polyacrylonitrile and related polymers—VI. Acrylonitrile copolymers containing carboxylic acid and amide structures. **European Polymer Journal**, **8** (2): 257–269.

240. Rafalko, J.J., 1984. Fourier- transform infrared studies of the thermal degradation of isotopically labeled polyacrylonitriles. **Journal of Polymer Science: Polymer Physics Edition**, **22** (7): 1211–1222.

241. Grassie, N., McGuchan, R., 1971. Pyrolysis of polyacrylonitrile and related polymers—II: The effect of sample preparation on the thermal behaviour of polyacrylonitrile. **European Polymer Journal**, **7** (8): 1091–1104.

242. Fochler, H.S., Mooney, J.R., Ball, L.E., Boyer, R.D., Grasselli, J.G., 1985. Infrared and NMR spectroscopic studies of the thermal degradation of polyacrylonitrile. **Spectrochimica Acta Part A: Molecular Spectroscopy**, **41** (1–2): 271–278.

243. Shimada, I., Takahagi, T., Fukuhara, M., Morita, K., Ishitani, A., 1986. FT- IR study of the stabilization reaction of polyacrylonitrile in the production of carbon fibers. **Journal of Polymer Science Part A: Polymer Chemistry**, **24** (8): 1989–1995.

244. Ouyang, Q., Cheng, L., Wang, H., Li, K., 2008. Mechanism and kinetics of the stabilization reactions of itaconic acid-modified polyacrylonitrile. **Polymer Degradation and Stability**, **93** (8): 1415–1421.

245. Loginova, E. V, Mikheev, I. V, Volkov, D.S., Proskurnin, M.A., 2016. Quantification of copolymer composition (methyl acrylate and itaconic acid) in polyacrylonitrile carbon-fiber precursors by FTIR-spectroscopy. **Analytical Methods**, **8** (2): 371–380.

246. Chung, T., Schlesinger, Y., Etemad, S., Macdiarmid, A.G., Heeger, A.J., 1984. Optical studies of pyrolyzed polyacrylonitrile. **Journal of Polymer Science: Polymer Physics Edition**, **22** (7): 1239–1246.

247. Grassie, N., McGuchan, R., 1971. Pyrolysis of polyacrylonitrile and related polymers—III. Thermal analysis of preheated polymers. **European Polymer Journal**, **7** (10): 1357–1371.

248. Coleman, M.M., Petcavich, R.J., 1978. Fourier transform infrared studies on the thermal degradation of polyacrylonitrile. **Journal of Polymer Science: Polymer Physics Edition**, **16** (5): 821–832.

249. Layden, G.K., 1972. Retrograde core formation during oxidation of polyacrylonitrile filaments. **Carbon**, **10** (1): 59–63.

250. Ko, T., Chiranairadul, P., Lin, C., 1991. The influence of continuous stabilization on the properties of stabilized fibers and the final activated carbon fibers. Part I. **Polymer Engineering & Science**, **31** (22): 1618–1626.

251. Skrovanek, D.J., Howe, S.E., Painter, P.C., Coleman, M.M., 1985. Hydrogen bonding in polymers: infrared temperature studies of an amorphous polyamide. **Macromolecules**, **18** (9): 1676–1683.

252. Dunn, P., Sansom, G.F., 1969. The stress cracking of polyamides by metal salts. Part II. Mechanism of cracking. **Journal of Applied Polymer Science**, **13:** 1641–1655.

253. Vasanthan, N., Kotek, R., Jung, D.-W., Shin, D., Tonelli, A.E., Salem, D.R., 2004. Lewis acid–base complexation of polyamide 66 to control hydrogen bonding, extensibility and crystallinity. **Polymer**, **45** (12): 4077–4085.

254. Wu, Y., Xu, Y., Wang, D., Zhao, Y., Weng, S., Xu, D., et al., 2004. FT- IR spectroscopic investigation on the interaction between nylon 66 and lithium salts. **Journal of Applied Polymer Science**, **91** (5): 2869–2875.

255. Cooper, S.J., Coogan, M., Everall, N., Priestnall, I., 2001. A polarised μ-FTIR study on a model system for nylon 6 6: implications for the nylon Brill structure. **Polymer**, **42** (26): 10119–10132.

256. Sengupta, R., Tikku, V.K., Somani, A.K., Chaki, T.K., Bhowmick, A.K., 2005. Electron beam irradiated polyamide-6, 6 films—I: characterization by wide angle X-ray scattering and infrared spectroscopy. **Radiation Physics and Chemistry**, **72** (5): 625–633.

257. Cannon, C.G., Harris, P.H., 1969. Chain folding and the structure of nylon 6.6 spherulites. **Journal of Macromolecular Science, Part B: Physics**, **3** (2): 357–364.

258. Jakeš, J., Krimm, S., 1971. A valence force field for the amide group. **Spectrochimica Acta Part A: Molecular Spectroscopy**, **27** (1): 19–34.

259. Elzein, T., Brogly, M., Schultz, J., 2002. Crystallinity measurements of polyamides adsorbed as thin films. **Polymer**, **43** (17): 4811–4822.

260. Peak, D., Luther III, G.W., Sparks, D.L., 2003. ATR-FTIR spectroscopic studies of boric acid adsorption on hydrous ferric oxide. **Geochimica et Cosmochimica Acta**, **67** (14): 2551–2560.

261. Baykal, A., Kizilyalli, M., Gözel, G., Kniep, R., 2000. Synthesis of strontium borophosphate, SrBPO5 by solid state and hydrothermal methods and characterisation. **Crystal Research and Technology: Journal of Experimental and Industrial Crystallography**, **35** (3): 247–254.

262. Puziy, A.M., Poddubnaya, O.I., Martınez-Alonso, A., Suárez-Garcıa, F., Tascón, J.M.D., 2002. Synthetic carbons activated with phosphoric acid: I. Surface chemistry and ion binding properties. **Carbon**, **40** (9): 1493–1505.

263. Petric, M., Grozav, M., Ilia, G., 2010. Boron phosphate flame-retardant for certain resins. **Revista de Chimie**, **61:** 1183–1185.

264. Sun, J., Gu, X., Dong, Q., Zhang, S., Liu, W., Li, L., et al., 2013. Durable flame-retardant finishing for polyamide 66 fabrics by surface hydroxymethylation and crosslinking. **Polymers for Advanced Technologies**, **24** (1): 10–14.

265. Hornsby, P.R., Wang, J., Rothon, R., Jackson, G., Wilkinson, G., Cossick, K., 1996. Thermal decomposition behaviour of polyamide fire-retardant compositions containing magnesium hydroxide filler. **Polymer Degradation and Stability**, **51** (3): 235–249.

266. Levchik, S. V, Weil, E.D., Lewin, M., 1999. Society of Chemical Industry. **Polymer International**, **48:** 532.

267. Bunn, C.W., Garner, E. V, Bragg, W.L., 1947. The crystal structures of two polyamides (‘nylons’). **Proceedings of the Royal Society of London. Series A. Mathematical and Physical Sciences**, **189** (1016): 39–68.

268. Standage, A.E., Matkowsky, R.D., 1971. Thermal oxidation of polyacrylonitrile. **European Polymer Journal**, **7** (7): 775–783.

269. Archibald, L.B., 1992. Quality in flax fibre. In: The Biology and Processing of Flax, M Publications, Belfast, UK, pp. 297–309.

270. Sarkar, J.K., Wang, Q., 2020. Characterization of pyrolysis products and kinetic analysis of waste jute stick biomass. **Processes**, **8** (7): 1–15.

271. Meyer, K.H., Misch, L., 1937. Positions des atomes dans le nouveau modele spatial de la cellulose. **Helvetica Chimica Acta**, **20** (1): 232–244.

272. Gardner, K.H., Blackwell, J., 1974. The structure of native cellulose. **Biopolymers: Original Research on Biomolecules**, **13** (10): 1975–2001.

273. Sarko, A., Muggli, R., 1974. Packing analysis of carbohydrates and polysaccharides. III. Valonia cellulose and cellulose II. **Macromolecules**, **7** (4): 486–494.

274. Helms, C.R., Poindexter, E.H., 1994. The silicon-silicon dioxide system: Its microstructure and imperfections. **Reports on Progress in Physics**, **57** (8): 791–852.

275. Karacan, I., Soy, T., 2013. Enhancement of oxidative stabilization of viscose rayon fibers impregnated with ammonium sulfate prior to carbonization and activation steps. **Journal of Applied Polymer Science**, **128** (2): 1239–1249.

276. Khan, M.A., Hassan, M.M., Drzal, L.T., 2005. Effect of 2-hydroxyethyl methacrylate (HEMA) on the mechanical and thermal properties of jute-polycarbonate composite. **Composites Part A: Applied Science and Manufacturing**, **36** (1): 71–81.

277. Mwaikambo, L.Y., Ansell, M.P., 2002. Chemical modification of hemp, sisal, jute, and kapok fibers by alkalization. **Journal of Applied Polymer Science**, **84** (12): 2222–2234.

278. Kondo, T., 1997. The assignment of IR absorption bands due to free hydroxyl groups in cellulose. **Cellulose**, **4** (4): 281–292.

279. Nelson, M.L., O'Connor, R.T., 1964. Relation of certain infrared bands to cellulose crystallinity and crystal lattice type. Part II. A new infrared ratio for estimation of crystallinity in celluloses I and II. **Journal of Applied Polymer Science**, **8** (3): 1325–1341.

280. Liang, C.Y., Marchessault, R.H., 1959. Infrared spectra of crystalline polysaccharides. I. Hydrogen bonds in native celluloses. **Journal of Polymer Science**, **37** (132): 385–395.

281. Tsuboi, M., 1957. Infrared spectrum and crystal structure of cellulose. **Journal of Polymer Science**, **25** (109): 159–171.

282. Abdelmouleh, M., Boufi, S., Belgacem, M.N., Duarte, A.P., Salah, A. Ben, Gandini, A., 2004. Modification of cellulosic fibres with functionalised silanes: development of surface properties. **International Journal of Adhesion and Adhesives**, **24** (1): 43–54.

283. Dadashian, F., Yaghoobi, Z., Wilding, M.A., 2005. Thermal behaviour of lyocell fibres. **Polymer Testing**, **24** (8): 969–977.

284. Yaman, N., 2009. Preparation and flammability properties of hybrid materials containing phosphorous compounds via sol-gel process. **Fibers and Polymers**, **10** (4): 413–418.

285. Arseneau, D.F., 1971. Competitive reactions in the thermal decomposition of cellulose. **Canadian Journal of Chemistry**, **49** (4): 632–638.

286. Shafizadeh, F., Bradbury, A.G.W., 1979. Thermal degradation of cellulose in air and nitrogen at low temperatures. **Journal of Applied Polymer Science**, **23** (5): 1431–1442.

287. Nam, S., Condon, B.D., Parikh, D. V, Zhao, Q., Cintrón, M.S., Madison, C., 2011. Effect of urea additive on the thermal decomposition of greige cotton nonwoven fabric treated with diammonium phosphate. **Polymer Degradation and Stability**, **96** (11): 2010–2018.

288. Kabir, M.M., Islam, M.M., Wang, H., 2013. Mechanical and Thermal Properties of Jute Fibre Reinforced Composites. **Journal of Multifunctional Composites**, **1** (1): 71–77.

289. Sharma, H.S.S., Sumere, C.F. van, 1992. The Biology and processing of flax. M Publications, Belfast.

290. Liodakis, S., Bakirtzis, D., Dimitrakopoulos, A.P., 2003. Autoignition and thermogravimetric analysis of forest species treated with fire retardants. **Thermochimica Acta**, **399** (1–2): 31–42.

291. Thuault, A., Eve, S., Blond, D., Bréard, J., Gomina, M., 2014. Effects of the hygrothermal environment on the mechanical properties of flax fibres. **Journal of Composite Materials**, **48** (14): 1699–1707.

292. Carrillo, F., Colom, X., Valldeperas, J., Evans, D., Huson, M., Church, J., 2003. Structural characterization and properties of lyocell fibers after fibrillation and enzymatic defibrillation finishing treatments. **Textile Research Journal**, **73** (11): 1024–1030.

293. Fanti, G., Baraldi, P., Basso, R., Tinti, A., 2013. Non-destructive dating of ancient flax textiles by means of vibrational spectroscopy. **Vibrational Spectroscopy**, **67:** 61–70.

APPENDICES

Table 1 Fiber diameter (in μm) of original PAN multifilament.

Observation no	1. Sample	2. Sample	3. Sample	4. Sample	5. Sample
1	16.62	22.06	23.38	22.53	15.77
2	16.71	22.25	22.81	21.03	15.87
3	16.71	21.97	23.09	20.65	15.58
4	16.52	21.31	23.00	20.37	15.30
5	16.43	21.31	22.91	20.09	15.77
6	16.71	20.65	23.19	20.18	16.05
7	16.99	21.03	22.81	20.28	15.68
8	17.18	21.12	22.91	20.46	16.05
9	17.65	21.50	22.53	20.56	16.43
10	17.74	21.31	23.00	20.37	16.24
11	18.21	21.31	23.00	20.46	16.15
12	17.93	21.31	23.56	20.84	15.68
13	18.40	21.40	24.13	20.37	15.87
14	18.12	21.50	23.84	20.46	15.87
15	17.84	21.59	24.03	20.28	16.05
16	17.46	21.31	23.94	20.46	15.77
17	17.74	21.12	23.38	20.00	15.30
18	17.65	21.40	23.56	20.28	15.11
19	17.37	21.59	23.66	20.00	16.05
20	17.55	21.31	23.38	19.81	16.15
Mean X	17.38	21.42	23.31	20.47	15.84
Std. Dev.	0.61	0.36	0.45	0.56	0.33
Avg. Mean					**19.68**
Avg. Std. Dev.					**0.46**

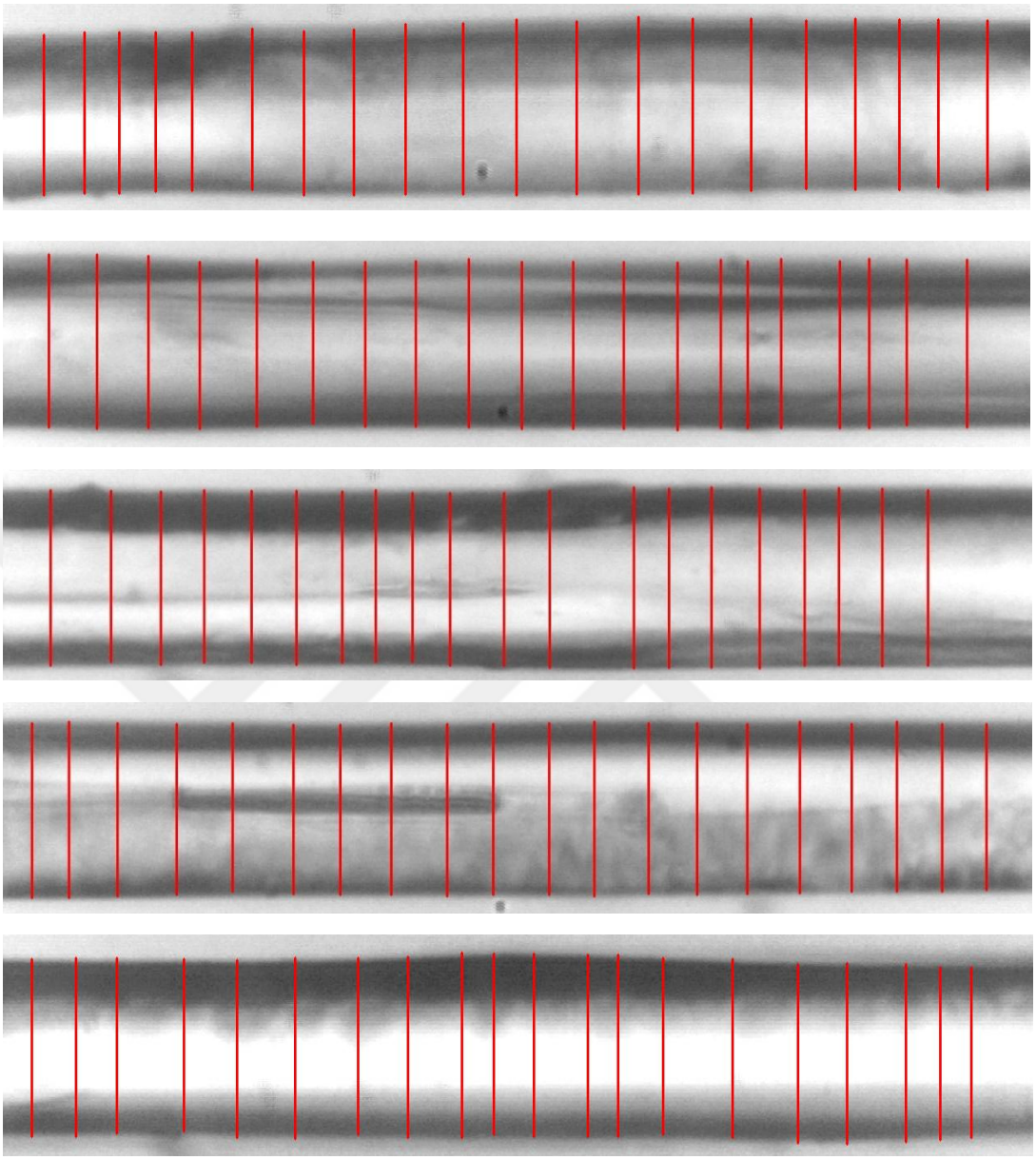

Figure 1 Optical microscopic image of PAN filament (40X).

Table 2 Mechanical properties of original PAN multifilament.

Strain rate	**:**	50%
Gauge length	**:**	26 mm
Test speed	**:**	13 mm/min
Linear density	**:**	59.95 Tex
Density	**:**	1.179 g/cm^3

Obs. no	Breaking force (N)	Tensile strength (N/Tex)	Tensile strength (MPa)	Extension at break (%)	Tensile modulus (N)	Tensile modulus (N/Tex)	Tensile modulus (GPa)
1	12.93	0.22	254.29	7.156	641.11	10.69	12.61
2	14.4	0.24	283.20	7.494	715.14	11.93	14.06
3	14.63	0.24	287.72	6.955	721.06	12.03	14.18
4	12.95	0.22	254.68	11.829	624.39	10.42	12.28
5	14.96	0.25	294.21	11.89	857.71	14.31	16.87
6	15.01	0.25	295.19	11.704	755.93	12.61	14.87
7	12.99	0.22	255.47	6.679	776.95	12.96	15.28
8	12.58	0.21	247.40	10.761	473.89	7.90	9.32
9	15.35	0.26	301.88	14.136	394.96	6.59	7.77
10	15.17	0.25	298.34	7.851	740.76	12.36	14.57
11	14.62	0.24	287.52	7.612	598.58	9.98	11.77
12	12.5	0.21	245.83	7.073	663.38	11.07	13.05
13	12.31	0.21	242.09	6.705	642.17	10.71	12.63
14	12.06	0.20	237.18	7.218	630.39	10.52	12.40
15	12.05	0.20	236.98	8.606	557.26	9.30	10.96
16	14.94	0.25	293.82	12.215	622.33	10.38	12.24
17	16.45	0.27	323.51	11.866	724.52	12.09	14.25
18	12.37	0.21	243.27	6.409	829.01	13.83	16.30
19	16.02	0.27	315.06	9.968	640.29	10.68	12.59
20	13.84	0.23	272.18	7.465	600.16	10.01	11.80
X	**13.91**	**0.23**	**273.49**	**9.08**	**660.50**	**11.02**	**12.99**
SD	**1.40**	**0.02**	**27.63**	**2.43**	**111.31**	**1.86**	**2.19**

Table 3 Mechanical properties of 15% APS impregnated and 5 minutes stepped annealed PAN multifilament.

Strain rate : 50%

Gauge length : 26 mm

Test speed : 13 mm/min

Linear density : 65.26 Tex

Density : 1.305 g/cm^3

Obs. no	Breaking force (N)	Tensile strength (N/Tex)	Tensile strength (MPa)	Extension at break (%)	Tensile modulus (N)	Tensile modulus (N/Tex)	Tensile modulus (GPa)
1	7.52	0.12	150.38	3.610	496.86	7.61	7.94
2	7.88	0.12	157.58	3.570	720.00	11.03	10.30
3	8.04	0.12	160.78	3.983	620.69	9.51	8.41
4	7.07	0.11	141.38	2.939	522.76	8.01	11.71
5	6.88	0.11	137.58	3.425	388.29	5.95	7.76
6	8.21	0.13	164.17	3.665	639.27	9.80	8.78
7	8.84	0.14	176.77	3.950	593.63	9.10	7.87
8	8.77	0.13	175.37	3.822	715.04	10.96	8.30
9	8.98	0.14	179.57	4.677	679.63	10.41	6.59
10	8.91	0.14	178.17	4.091	532.75	8.16	10.65
X	**8.11**	**0.12**	**162.18**	**3.77**	**590.89**	**9.05**	**8.83**
SD	**0.77**	**0.01**	**15.45**	**0.46**	**105.99**	**1.62**	**1.57**

Table 4 Mechanical properties of 15% APS impregnated and 15 minutes stepped annealed PAN multifilament.

Strain rate **:** 50%
Gauge length **:** 26 mm
Test speed **:** 13 mm/min
Linear density **:** 64.79 Tex
Density **:** 1.32 g/cm^3

Obs. no	Breaking force (N)	Tensile strength (N/Tex)	Tensile strength (MPa)	Extension at break (%)	Tensile modulus (N)	Tensile modulus (N/Tex)	Tensile modulus (GPa)
1	7.73	0.12	177.86	2.572	646.88	9.98	13.18
2	7.97	0.12	162.38	3.567	429.91	6.64	8.76
3	6.5	0.10	173.17	3.422	315.69	4.87	6.43
4	8.03	0.12	163.60	3.030	584.55	9.02	11.91
5	6.86	0.11	139.76	2.292	557.14	8.60	11.35
6	7.53	0.12	153.41	3.476	420.48	6.49	8.57
7	6.58	0.10	134.06	2.703	421.37	6.50	8.58
8	6.55	0.10	174.19	1.990	662.71	10.23	13.50
9	7.46	0.12	151.99	2.726	415.93	6.42	8.47
10	8.81	0.14	177.66	4.299	414.29	6.39	8.44
X	**7.40**	**0.11**	**160.81**	**3.01**	**486.89**	**7.51**	**9.92**
SD	**0.77**	**0.01**	**15.66**	**0.69**	**116.69**	**1.80**	**2.38**

Table 5 Mechanical properties of 15% APS impregnated and 30 minutes stepped annealed PAN multifilament.

Strain rate **:** 50%
Gauge length **:** 26 mm
Test speed **:** 13 mm/min
Linear density **:** 64.12 Tex
Density **:** 1.33 g/cm^3

Obs. no	Breaking force (N)	Tensile strength (N/Tex)	Tensile strength (MPa)	Extension at break (%)	Tensile modulus (N)	Tensile modulus (N/Tex)	Tensile modulus (GPa)
1	7.89	0.12	163.66	3.39	483.10	7.53	10.02
2	7.27	0.11	150.80	2.596	705.77	11.01	14.64
3	7.58	0.12	157.23	3.014	658.81	10.27	13.67
4	7.58	0.12	157.23	2.339	414.59	6.47	8.60
5	8.2	0.13	170.09	3.367	496.65	7.75	10.30
6	6.97	0.11	144.57	3.215	476.19	7.43	9.88
7	6.81	0.11	141.26	2.825	400.37	6.24	8.30
8	8.35	0.13	173.20	2.590	389.52	6.07	8.08
9	8.07	0.13	167.39	2.227	534.80	8.34	11.09
10	8.01	0.12	166.15	3.774	558.30	8.71	11.58
X	**7.67**	**0.12**	**159.16**	**2.93**	**511.81**	**7.98**	**10.62**
SD	**0.52**	**0.01**	**10.87**	**0.50**	**105.97**	**1.65**	**2.20**

Table 6 Mechanical properties of 15% APS impregnated and 45 minutes stepped annealed PAN multifilament.

Strain rate **:** 50%
Gauge length **:** 26 mm
Test speed **:** 13 mm/min
Linear density **:** 63.40 Tex
Density **:** 1.355 g/cm^3

Obs. no	Breaking force (N)	Tensile strength (N/Tex)	Tensile strength (MPa)	Extension at break (%)	Tensile modulus (N)	Tensile modulus (N/Tex)	Tensile modulus (GPa)
1	7.21	0.11	154.09	2.312	650.28	10.26	13.90
2	7.83	0.12	167.34	2.46	631.25	9.96	13.49
3	7.66	0.12	163.71	3.315	422.33	6.66	9.03
4	7.3	0.12	156.02	1.995	680.75	10.74	14.55
5	7.18	0.11	153.45	3.181	347.21	5.48	7.42
6	8.26	0.13	176.53	3.373	719.14	11.34	15.37
7	6.46	0.10	138.06	1.668	611.90	9.65	13.08
8	6.47	0.10	138.28	2.594	403.51	6.36	8.62
9	6.58	0.10	140.63	1.684	610.67	9.63	13.05
10	6.35	0.10	135.71	2.329	545.19	8.60	11.65
X	**7.13**	**0.11**	**152.38**	**2.49**	**562.22**	**8.87**	**12.02**
SD	**0.66**	**0.01**	**14.03**	**0.63**	**127.93**	**2.02**	**2.73**

Table 7 Mechanical properties of 15% APS impregnated and 60 minutes stepped annealed PAN multifilament.

Strain rate **:** 50%
Gauge length **:** 26 mm
Test speed **:** 13 mm/min
Linear density **:** 62.12 Tex
Density **:** 1.395 g/cm^3

Obs. no	Breaking force (N)	Tensile strength (N/Tex)	Tensile strength (MPa)	Extension at break (%)	Tensile modulus (N)	Tensile modulus (N/Tex)	Tensile modulus (GPa)
1	5.45	0.09	122.39	1.041	618.03	9.95	13.88
2	7.27	0.12	163.26	1.844	529.81	8.53	11.90
3	5.2	0.08	116.77	1.378	551.52	8.88	12.39
4	6.32	0.10	141.93	1.738	614.49	9.89	13.80
5	4.94	0.08	110.94	0.914	682.03	10.98	15.32
6	6.03	0.10	135.41	1.275	688.73	11.09	15.47
7	6.14	0.10	137.88	1.575	495.84	7.98	11.13
8	5.38	0.09	120.82	1.057	467.80	7.53	10.51
9	5.06	0.08	113.63	1.811	498.77	8.03	11.20
10	6.56	0.11	147.31	1.723	545.66	8.78	12.25
X	**5.84**	**0.09**	**131.03**	**1.44**	**569.27**	**9.16**	**12.78**
SD	**0.75**	**0.01**	**16.92**	**0.35**	**77.81**	**1.25**	**1.75**

Table 8 Mechanical properties of 15% ammonium persulfate impregnated and 45 minutes stepped annealed PAN (Heating rate 1-1 °C/min).

Strain rate **:** 50%
Gauge length **:** 26 mm
Test speed **:** 13 mm/min
Linear density **:** 62.208 Tex
Density **:** 1.375 g/cm^3

Obs. no	Breaking force (N)	Tensile strength (N/Tex)	Tensile strength (MPa)	Extension at break (%)	Tensile modulus (N)	Tensile modulus (N/Tex)	Tensile modulus (GPa)
1	4.15	0.07	91.73	1.08	740.00	11.90	16.36
2	5.86	0.09	129.52	1.617	714.00	11.48	15.78
3	4.92	0.08	108.74	1.183	547.00	8.79	12.09
4	3.7	0.06	81.78	1.2	587.00	9.44	12.97
5	7.25	0.12	160.24	1.63	532.00	8.55	11.76
6	6.11	0.10	135.05	1.868	665.00	10.69	14.70
7	6.44	0.10	142.34	1.275	433.00	6.96	9.57
8	4.83	0.08	106.76	1.043	499.00	8.02	11.03
9	4.61	0.07	101.89	1.239	462.00	7.43	10.21
10	5.98	0.10	132.17	1.684	536.00	8.62	11.85
X	**5.39**	**0.09**	**119.02**	**1.38**	**571.50**	**9.19**	**12.63**
SD	**1.11**	**0.02**	**24.64**	**0.29**	**104.10**	**1.67**	**2.30**

Table 9 Mechanical properties of 15% APS impregnated and 45 minutes stepped annealed PAN (Heating rate 1-2 °C/min).

Strain rate **:** 50%
Gauge length **:** 26 mm
Test speed **:** 13 mm/min
Linear density **:** 63.88 Tex
Density **:** 1.375 g/cm^3

Obs. no	Breaking force (N)	Tensile strength (N/Tex)	Tensile strength (MPa)	Extension at break (%)	Tensile modulus (N)	Tensile modulus (N/Tex)	Tensile modulus (GPa)
1	4.97	0.08	106.98	1.292	693.00	10.85	14.92
2	4.89	0.08	105.26	1.628	463.00	7.25	9.97
3	4.93	0.08	106.12	1.165	439.00	6.87	9.45
4	5.41	0.08	116.45	1.237	488.00	7.64	10.50
5	5.03	0.08	108.27	1.131	712.00	11.15	15.33
6	4.52	0.07	97.29	1.021	635.00	9.94	13.67
7	5.52	0.09	118.82	1.185	698.00	10.93	15.02
8	4.86	0.08	104.61	1.505	586.00	9.17	12.61
9	5.47	0.09	117.74	2.062	537.00	8.41	11.56
10	4.4	0.07	94.71	1.094	497.00	7.78	10.70
X	**5.00**	**0.08**	**107.62**	**1.33**	**574.80**	**9.00**	**12.37**
SD	**0.38**	**0.01**	**8.14**	**0.32**	**104.18**	**1.63**	**2.24**

Table 10 Mechanical properties of 15% APS impregnated and 45 minutes stepped annealed PAN (Heating rate 2-1 °C/min).

Strain rate : 50%
Gauge length : 26 mm
Test speed : 13 mm/min
Linear density : 63.4 Tex
Density : 1.355 g/cm^3

Obs. no	Breaking force (N)	Tensile strength (N/Tex)	Tensile strength (MPa)	Extension at break (%)	Tensile modulus (N)	Tensile modulus (N/Tex)	Tensile modulus (GPa)
1	7.21	0.11	154.09	2.312	650.28	10.26	13.90
2	7.83	0.12	167.34	2.46	631.25	9.96	13.49
3	7.66	0.12	163.71	3.315	422.33	6.66	9.03
4	7.3	0.12	156.02	1.995	680.75	10.74	14.55
5	7.18	0.11	153.45	3.181	347.21	5.48	7.42
6	8.26	0.13	176.53	3.373	719.14	11.34	15.37
7	6.46	0.10	138.06	1.668	611.90	9.65	13.08
8	6.47	0.10	138.28	2.594	403.51	6.36	8.62
9	6.58	0.10	140.63	1.684	610.67	9.63	13.05
10	6.35	0.10	135.71	2.329	545.19	8.60	11.65
X	**7.13**	**0.11**	**152.38**	**2.49**	**562.22**	**8.87**	**12.02**
SD	**0.66**	**0.01**	**14.03**	**0.63**	**127.93**	**2.02**	**2.73**

Table 11 Mechanical properties of 15% APS impregnated and 45 minutes stepped annealed PAN (Heating rate 2-2 °C/min).

Strain rate : 50%
Gauge length : 26 mm
Test speed : 13 mm/min
Linear density : 64.53 Tex
Density : 1.37 g/cm^3

Obs. no	Breaking force (N)	Tensile strength (N/Tex)	Tensile strength (MPa)	Extension at break (%)	Tensile modulus (N)	Tensile modulus (N/Tex)	Tensile modulus (GPa)
1	5.08	0.08	107.85	1.308	640.00	9.92	13.59
2	5.56	0.09	118.04	2.261	573.00	8.88	12.17
3	5.95	0.09	126.32	2.227	562.00	8.71	11.93
4	5.39	0.08	114.43	1.598	657.00	10.18	13.95
5	5.32	0.08	112.95	1.167	687.00	10.65	14.59
6	5.52	0.09	117.19	1.241	676.00	10.48	14.35
7	6.04	0.09	128.23	2.028	607.00	9.41	12.89
8	5.85	0.09	124.20	3.6	471.00	7.30	10.00
9	6.17	0.10	130.99	2.407	619.00	9.59	13.14
10	6.06	0.09	128.66	1.958	650.00	10.07	13.80
X	**5.69**	**0.09**	**120.89**	**1.98**	**614.20**	**9.52**	**13.04**
SD	**0.37**	**0.01**	**7.84**	**0.73**	**64.89**	**1.01**	**1.38**

Table 12 Mechanical properties of 15% APS impregnated and 45 minutes stepped annealed PAN (Heating rate 3-1 °C/min).

Strain rate : 50%
Gauge length : 26 mm
Test speed : 13 mm/min
Linear density : 64.91 Tex
Density : 1.36 g/cm^3

Obs. no	Breaking force (N)	Tensile strength (N/Tex)	Tensile strength (MPa)	Extension at break (%)	Tensile modulus (N)	Tensile modulus (N/Tex)	Tensile modulus (GPa)
1	7.24	0.11	151.69	1.72	659.00	10.15	13.81
2	6.88	0.11	144.15	1.98	667.00	10.28	13.98
3	7.14	0.11	149.60	2.08	715.00	11.02	14.98
4	6.64	0.10	139.12	1.58	623.00	9.60	13.05
5	6.22	0.10	130.32	1.64	651.00	10.03	13.64
6	6.49	0.10	135.98	1.69	629.00	9.69	13.18
7	7.25	0.11	151.90	1.87	732.00	11.28	15.34
8	7.32	0.11	153.37	1.59	694.00	10.69	14.54
9	6.95	0.11	145.62	1.76	653.00	10.06	13.68
10	6.45	0.10	135.14	1.99	599.00	9.23	12.55
X	**6.86**	**0.11**	**143.69**	**1.79**	**662.20**	**10.20**	**13.87**
SD	**0.39**	**0.01**	**8.14**	**0.18**	**41.56**	**0.64**	**0.87**

Table 13 Mechanical properties of 15% APS impregnated and 45 minutes stepped annealed PAN (Heating rate 3-2 °C/min).

Strain rate : 50%
Gauge length : 26 mm
Test speed : 13 mm/min
Linear density : 65.26 Tex
Density : 1.36 g/cm^3

Obs. no	Breaking force (N)	Tensile strength (N/Tex)	Tensile strength (MPa)	Extension at break (%)	Tensile modulus (N)	Tensile modulus (N/Tex)	Tensile modulus (GPa)
1	6.64	0.10	138.38	1.759	732.00	11.22	15.25
2	5.75	0.09	119.83	1.114	789.00	12.09	16.44
3	7.68	0.12	160.05	1.671	756.00	11.58	15.75
4	5.04	0.08	105.03	0.879	785.00	12.03	16.36
5	7.71	0.12	160.67	1.525	495.00	7.59	10.32
6	5.76	0.09	120.04	2.005	584.00	8.95	12.17
7	7.24	0.11	150.88	1.943	687.00	10.53	14.32
8	7.21	0.11	150.25	1.919	783.00	12.00	16.32
9	5.83	0.09	121.50	1.921	731.00	11.20	15.23
10	6.78	0.10	141.29	2.633	562.00	8.61	11.71
X	**6.56**	**0.10**	**136.79**	**1.74**	**690.40**	**10.58**	**14.39**
SD	**0.92**	**0.01**	**19.22**	**0.49**	**105.90**	**1.62**	**2.21**

Table 14 Mechanical properties of 15% APS impregnated and 45 minutes stepped annealed PAN (Heating rate 3-3 °C/min).

Strain rate : 50%
Gauge length : 26 mm
Test speed : 13 mm/min
Linear density : 66.64 Tex
Density : 1.37 g/cm^3

Obs. no	Breaking force (N)	Tensile strength (N/Tex)	Tensile strength (MPa)	Extension at break (%)	Tensile modulus (N)	Tensile modulus (N/Tex)	Tensile modulus (GPa)
1	4.93	0.07	101.35	1.542	565.00	8.48	11.62
2	6	0.09	123.35	1.543	758.00	11.37	15.58
3	7.18	0.11	147.61	2.405	664.00	9.96	13.65
4	6.29	0.09	129.31	1.722	681.00	10.22	14.00
5	5.89	0.09	121.09	2.362	528.00	7.92	10.85
6	5.13	0.08	105.46	1.237	583.00	8.75	11.99
7	6.56	0.10	134.86	1.743	618.00	9.27	12.70
8	5.76	0.09	118.42	1.382	711.00	10.67	14.62
9	4.97	0.07	102.17	1.258	712.00	10.68	14.64
10	5.2	0.08	106.90	1.062	793.00	11.90	16.30
X	**5.79**	**0.09**	**119.05**	**1.63**	**661.30**	**9.92**	**13.60**
SD	**0.75**	**0.01**	**15.36**	**0.45**	**86.40**	**1.30**	**1.78**

Table 15 Fiber diameter (in μm) of original PA66 multifilament.

Observation no	1. Sample	2. Sample	3. Sample	4. Sample	5. Sample
1	12.33	11.65	11.55	10.58	11.94
2	11.84	11.36	11.46	10.58	12.04
3	12.04	11.17	11.26	10.68	11.36
4	11.84	11.17	11.17	10.39	11.36
5	11.94	11.26	11.46	10.29	11.84
6	11.55	11.46	11.46	10.19	11.26
7	11.17	11.46	11.55	10.39	10.87
8	11.36	11.55	11.55	10.29	10.87
9	10.97	11.46	11.55	10.68	10.97
10	11.17	11.75	11.36	10.97	11.07
11	10.97	11.65	11.36	10.58	10.97
12	11.17	12.14	11.46	10.78	11.07
13	10.78	11.75	11.36	10.68	10.97
14	10.97	12.14	11.55	10.97	10.97
15	11.07	11.94	11.65	11.07	11.07
16	11.46	12.14	11.65	11.07	10.97
17	11.46	12.14	11.46	11.17	11.26
18	11.65	11.94	11.55	11.17	11.46
19	11.94	11.65	11.65	11.07	11.46
20	11.36	11.94	11.46	11.07	11.75
Mean	11.45	11.69	11.48	10.73	11.28
Std. Dev.	0.43	0.33	0.13	0.32	0.37
Avg. Mean					**11.32**
Avg. Std. Dev.					**0.31**

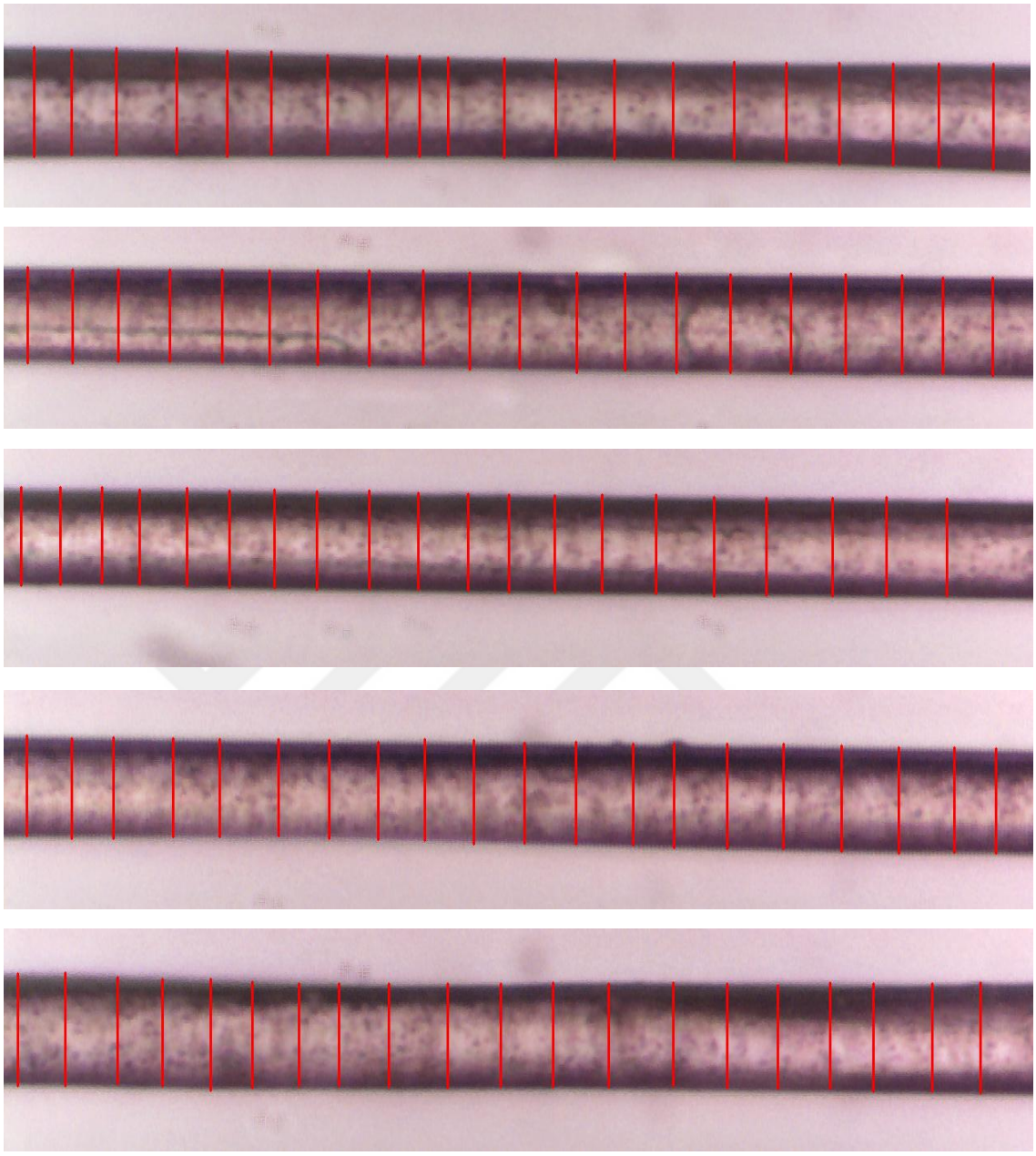

Figure 2 Optical microscopic image of original PA66 filament (40X).

Table 16 Mechanical properties of original PA66 multifilament.

Strain Rate	**:**	50%
Gauge Length	**:**	26 mm
Test Speed	**:**	13 mm/min
Linear Density	**:**	16.28 Tex
Density	**:**	1.160 g/cm^3

Obs. no	**Breaking force (N)**	**Tensile strength (N/Tex)**	**Tensile strength (MPa)**	**Extension at break (%)**	**Tensile modulus (N)**	**Tensile modulus (N/Tex)**	**Tensile modulus (GPa)**
1	4.01	0.25	282.03	27.344	192.00	11.79	13.68
2	4.10	0.25	288.36	28.824	299.00	18.37	21.30
3	4.22	0.26	296.80	30.543	200.00	12.29	14.25
4	4.27	0.26	300.32	28.731	218.00	13.39	15.53
5	3.99	0.25	280.62	30.514	172.00	10.57	12.26
6	4.24	0.26	298.21	31.274	262.00	16.09	18.67
7	3.85	0.24	270.78	35.332	175.00	10.75	12.47
8	3.92	0.24	275.70	20.592	304.00	18.67	21.66
9	3.81	0.23	267.96	30.124	207.00	12.71	14.75
10	4.15	0.25	291.88	26.545	206.00	12.65	14.68
X	**4.06**	**0.25**	**285.27**	**28.98**	**223.50**	**13.73**	**15.93**
SD	**0.17**	**0.01**	**11.61**	**3.81**	**48.10**	**2.95**	**3.43**

Table 17 Fiber diameter (in μm) of original jute fiber.

Observation no	1. Sample	2. Sample	3. Sample	4. Sample	5. Sample
1	50.69	54.64	53.04	43.65	49.75
2	50.97	54.45	53.32	43.09	49.57
3	51.16	53.51	53.32	42.81	49.94
4	51.16	53.32	52.95	42.53	51.54
5	50.88	53.13	52.66	41.96	50.13
6	50.69	52.95	53.04	43.00	52.20
7	50.69	52.48	52.85	43.18	52.20
8	50.60	52.57	52.85	42.34	52.57
9	50.88	52.57	52.76	42.53	52.66
10	51.16	52.76	52.66	42.43	53.13
11	51.16	53.04	52.95	42.43	54.17
12	51.54	53.04	52.20	42.15	54.17
13	51.35	53.98	52.38	42.06	54.73
14	51.54	52.76	52.20	42.15	54.73
15	51.73	53.60	52.57	41.96	54.92
16	51.73	53.88	52.38	42.24	51.35
17	51.82	53.42	52.66	41.49	49.38
18	51.82	53.42	53.23	40.65	49.75
19	51.73	54.54	53.23	40.74	49.94
20	51.26	54.73	52.57	41.02	52.66
Mean X	51.23	53.44	52.80	42.22	51.97
Std. Dev.	0.41	0.72	0.35	0.79	1.93
Avg. Mean					**50.33**
Avg. Std. Dev.					**0.84**

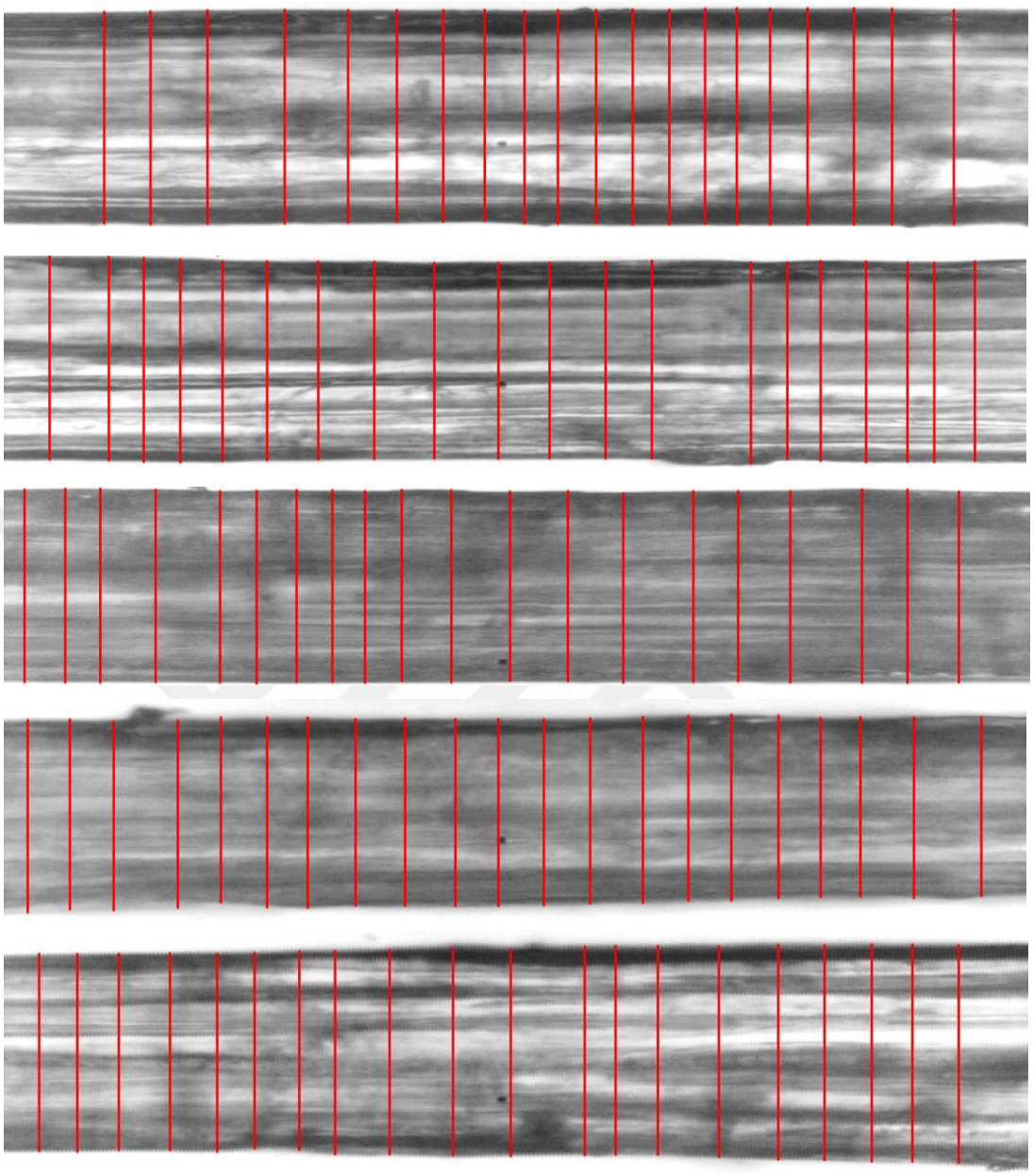

Figure 3 Optical microscopic image of original jute fiber (40X).

Table 18 Mechanical properties of original jute yarn.

Strain rate	:	50%
Gauge length	:	26 mm
Test speed	:	13 mm/min
Linear density	:	332.28 Tex
Density	:	1.37 g/cm^3

Obs. no	Breaking force (N)	Tensile strength (N/Tex)	Tensile strength (MPa)	Extension at break (%)	Tensile modulus (N)	Tensile modulus (N/Tex)	Tensile modulus (GPa)
1	40.55	0.12	167.19	1.73	2405.14	7.24	9.92
2	41.68	0.13	171.85	1.59	2892.90	8.71	11.93
3	36.64	0.11	151.07	1.44	2839.60	8.55	11.71
4	39.82	0.12	164.18	1.73	2317.25	6.97	9.55
5	57.63	0.17	237.61	2.02	2183.22	6.57	9.00
6	52.77	0.16	217.57	2.26	2987.01	8.99	12.32
7	46.97	0.14	193.66	2.23	2517.06	7.58	10.38
8	42.84	0.13	176.63	1.79	2861.62	8.61	11.80
9	42.82	0.13	176.55	2.02	2500.73	7.53	10.31
10	38.12	0.11	157.17	2.13	2940.05	8.85	12.12
11	43.23	0.13	178.24	1.69	2943.10	8.86	12.13
12	38.57	0.12	159.03	1.62	3072.14	9.25	12.67
13	40.77	0.12	168.10	2.06	2096.18	6.31	8.64
14	44.62	0.13	183.97	1.51	2597.38	7.82	10.71
15	44.78	0.13	184.63	2.17	2149.08	6.47	8.86
16	46.21	0.14	190.53	1.81	2970.13	8.94	12.25
17	40.17	0.12	165.62	1.37	3428.17	10.32	14.13
18	49.44	0.15	203.84	1.37	3715.23	11.18	15.32
19	47.53	0.14	195.97	2.03	2907.57	8.75	11.99
20	51.93	0.16	214.11	2.14	2761.43	8.31	11.39
X	**44.35**	**0.13**	**182.87**	**1.83**	**2754.25**	**8.29**	**11.36**
SD	**5.43**	**0.02**	**22.41**	**0.30**	**416.41**	**1.25**	**1.72**

Table 19 Fiber diameter results for original bamboo fiber.

Observation no	1. Sample	2. Sample	3. Sample	4. Sample	5. Sample
1	12.52	13.79	9.90	15.24	16.89
2	12.52	13.69	10.19	15.05	16.70
3	12.33	13.88	10.68	15.15	16.50
4	11.94	13.79	10.78	15.44	16.12
5	11.94	13.88	10.10	15.15	16.02
6	12.14	13.69	10.58	15.24	16.31
7	12.23	13.59	9.90	15.34	16.21
8	12.23	13.59	10.10	15.83	16.12
9	12.14	13.50	9.90	15.53	16.12
10	12.23	13.40	9.81	15.53	16.50
11	12.23	13.11	9.81	15.73	16.31
12	12.04	13.50	10.00	16.02	16.50
13	12.43	13.79	10.29	16.02	16.31
14	12.52	13.88	10.29	16.21	16.31
15	12.52	13.88	10.29	16.02	17.09
16	12.52	13.79	10.39	15.83	17.18
17	12.52	13.98	10.19	15.83	16.50
18	12.91	13.98	10.68	15.92	16.89
19	12.82	12.82	10.19	15.44	16.50
20	12.72	13.01	10.68	15.57	16.32
Mean X	12.37	13.63	10.24	15.60	16.47
Std. Dev.	0.27	0.32	0.31	0.35	0.33
Avg. Mean					**13.66**
Avg. Std. Dev.					**0.32**

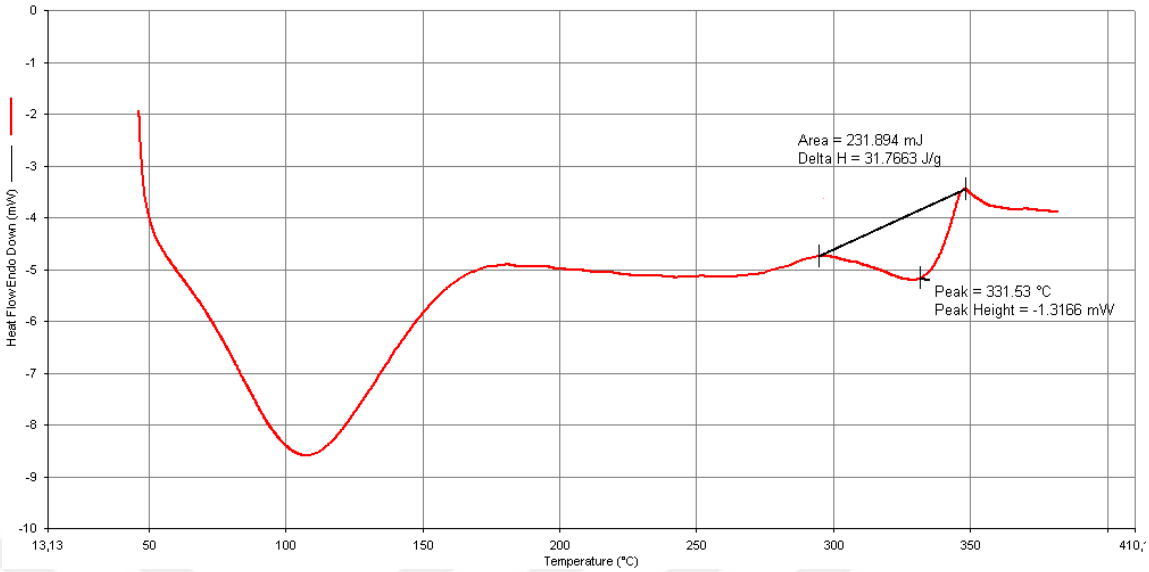

Figure 4 DSC thermogram of original bamboo fiber.

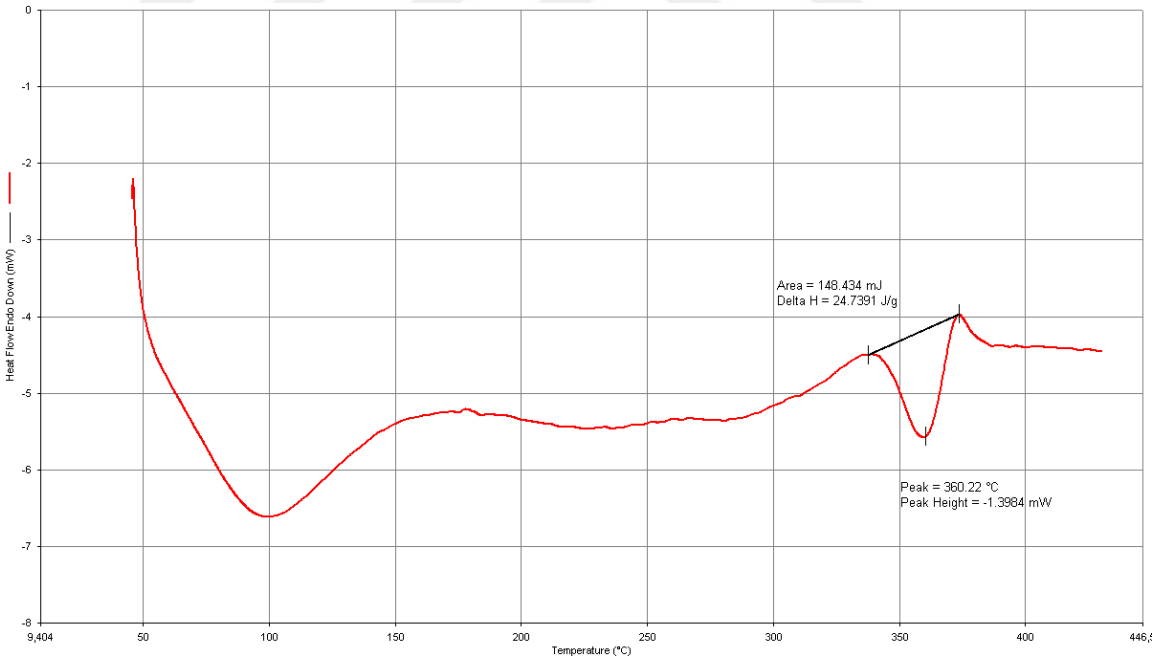

Figure 5 DSC thermogram of original flax fiber.

Table 20 Fiber diameter results for original flax fiber.

Observation no	1. Sample	2. Sample	3. Sample	4. Sample	5. Sample
1	8.06	11.07	12.14	8.35	9.71
2	8.25	10.97	11.55	8.25	9.81
3	7.77	11.17	11.65	8.06	10.29
4	7.57	11.65	12.04	8.45	10.10
5	7.09	11.46	12.14	7.77	10.00
6	7.57	11.46	12.43	7.77	10.19
7	7.67	11.26	12.14	7.38	9.71
8	7.77	11.84	11.75	7.28	9.71
9	7.77	11.65	12.04	7.57	9.51
10	7.38	11.75	12.04	7.57	9.90
11	7.48	11.17	12.04	7.96	9.61
12	7.48	11.26	12.04	7.57	10.00
13	7.18	11.36	12.43	7.57	9.61
14	7.48	11.94	12.33	7.57	10.10
15	7.77	12.23	12.82	7.38	10.10
16	7.57	11.94	12.33	7.67	9.61
17	7.57	11.26	12.52	7.96	9.71
18	7.57	10.49	12.33	8.25	9.90
19	7.57	10.58	12.82	7.86	9.81
20	7.86	10.39	12.47	7.96	9.32
Mean X	7.62	11.35	12.20	7.81	9.84
Std. Dev.	0.27	0.49	0.34	0.34	0.25
Avg. Mean					**9.76**
Avg. Std. Dev.					**0.34**

CURRICULUM VITAE

PERSONAL INFORMATION

Name and Surname : Md. Mahbubor Rahman

Nationality : Bangladeshi

EDUCATION

Degree	Institution	Graduation Year
Doctor of Philosophy (PhD)	Erciyes University (Dept. of Textile Engineering)	2021
Master of Science (M.Sc.)	Bangladesh University of Textiles, (Dept. of Apparel Engineering)	2016
Bachelor of Science (B. Sc.)	Bangladesh University of Textiles, (Dept. of Apparel Engineering)	2010

WORK EXPERIENCE

Year	Institution	Position
2016 - till now	Bangladesh University of Textiles	Assistant Professor
2013 - 2016	Bangladesh University of Textiles	Lecturer

FOREIGN LANGUAGE

English, Turkish

PUBLICATIONS

1) The effect of the ammonium persulfate and a multi-step annealing approach during thermal stabilization of polyacrylonitrile multifilament prior to carbonization.
   (Journal of Materials Science, Springer Nature, June 2021)
   URL: https://doi.org/10.1007/s10853-021-06209-1

2) Fabrication of carbon fibers from the cupric ion impregnated and thermally stabilized poly(hexamethylene adipamide) precursor.
(Journal of Industrial Textiles, SAGE Publishing, December 2021)
URL: https://doi.org/10.1177/15280837211056984

3) The impact of eco-friendly chemical incorporation on the thermal oxidation process of flax fiber prior to carbonization and activation.
(Journal of Materials Science, Springer Nature, January 2022)
URL: https://doi.org/10.1007/s10853-021-06686-4

4) A study on structural characterization of thermally stabilized PAN precursor fibers impregnated with ammonium bromide before carbonization stage.
(Fibers and Polymers, Springer, accepted in December 2021)

5) The beneficial effect of eco-friendly chemical impregnation on the thermal stabilization process of poly(hexamethylene adipamide) multifilament.
(Under Review)

6) Improved thermal stability of jute fiber as an eco-friendly precursor for activated carbon fiber processing.
(Under Review)

7) Structural and thermal characterization of chemically pretreated and thermally oxidized bamboo fiber in activated carbon fiber manufacturing.
(Under Review)

8) The impact of guanidine carbonate incorporation on the molecular structure of PAN precursor fiber stabilized by a multi-step heat treatment strategy.
(Under Review)

CONFERENCES

1) Structural characterization of ammonium persulfate integrated and thermally stabilized poly(acrylonitrile) multifilament for carbon fiber production.
(5^{th} 19 Mayis Conference, Samsun, Turkey)

2) Carbonization behavior of thermally stabilized poly(hexamethylene adipamide) (polyamide 66) precursor fibers in the presence of cupric halide impregnation.
(Istanbul International Modern Scientific Research Congress, Istanbul, Turkey)

3) Thermal stabilization of 1% $FeCl_3$-impregnated polyamide 6 fibers: differential scanning calorimetry (DSC) and thermogravimetric (TGA) analysis.
(1st International Science and Applied Science Congress, Adiyaman, Turkey)

4) Impact of oxidative stabilization of jute fibers prior to carbonization and activation.
(5th Asia Pacific International Modern Sciences Congress, Sydney, Australia)

5) Structure and properties of thermally stabilized poly(hexamethylene adipamide) as carbon fiber precursor: X-ray diffraction, TGA, and FT-IR spectroscopy analysis.
(4th TokyoSUMMIT Conference, Tokyo, Japan)

6) Study on structural transformations occur in the thermal oxidation of bamboo precursor fiber prior to carbonization and activation.
(5th International New York Conference on Evolving Trends in Interdisciplinary Research & Practices, Manhattan, New York city, USA)

7) The effect of heat treatment strategies on thermal stabilization of polyacrylonitrile fibers in carbon fiber production.
(Latin American International Conference on Natural and Applied Sciences, Villahermosa, Mexico)

8) Investigation of thermal and structural changes occur in oxidation phase of flax fiber in activated carbon fiber manufacturing.
(7th International Black Sea Coastline Countries Symposium, Bucharest, Romania)